DISSERTATION

PHYSICS OF ENVIRONMENTAL FLOWS INTERACTING WITH OBSTACLES

Submitted by

Jian Zhou

Department of Civil and Environmental Engineering

In partial fulfillment of the requirements

For the Degree of Doctor of Philosophy

Colorado State University

Fort Collins, Colorado

Fall 2017

Doctoral Committee:

Advisor: Subhas K. Venayagamoorthy

Pierre Y. Julien
Brian P. Bledsoe
Hiroshi Sakurai

ABSTRACT

PHYSICS OF ENVIRONMENTAL FLOWS INTERACTING WITH OBSTACLES

The effects of natural and man-made obstacles on their surrounding environmental flows such as rivers, lakes, estuaries, oceans and the atmosphere has been the subject of numerous studies for many decades. The flow-obstacle interaction can lead to the generation of turbulence which determines local flow dynamics and even large-scale circulations. The characteristic chaotic and enhanced mixing properties of turbulence in conjunction with other environmental conditions such as the clustering of multiple obstacles and density variations raise a number of interesting problems pertaining to both fundamental fluid dynamics and practical engineering applications. Insights into these processes is of fundamental importance for many applications, such as determining the fate of deep water-masses formed in the abyssal ocean, optimizing the productivity and environmental impact of marine farms, predicting the amount of power that a group of turbines can generate, estimating carbon dioxide exchange between the forests and the atmosphere or modeling flood routing in vegetated rivers.

The main aim of this dissertation is to use high-resolution numerical simulations to study environmental flows of different forcing mechanisms interacting with obstacles of different geometries. The objectives are multi-fold: (i) To gain insights into the three-dimensional hydrodynamics of constant-density flows interacting with a finite canopy; (ii) To develop an unambiguous geometrical framework for characterizing canopy planar geometry; (iii) To explore the fundamental differences in the flow dynamics between porous canopies and their solid counterpart; and (iv) To investigate the effect of ambient density stratification on flow-obstacle interactions.

The first part of this dissertation focuses on the mean three-dimensional hydrodynamics in the vicinity of a suspended cylindrical canopy patch with a bulk diameter of D. The patch was made of N_c constituent solid circular cylinders with h in height and d in diameter, and was suspended

in deep water ($H/h \gg 1$ where H is the total flow depth). After the validation against published experimental data, large eddy simulations (LES) were conducted to study the effects of patch density ($0.16 \leq \phi = N_c(d/D)^2 \leq 1$, by varying N_c) and patch aspect ratio ($0.25 \leq AR = h/D \leq 1$, by varying h) on the near-field flow properties. It was observed qualitatively and quantitatively that an increase in either ϕ or AR decreases bleeding velocity along the streamwise direction but increases bleeding velocities along the lateral and vertical directions, respectively. A close examination at the flow inside the patch reveals that despite the similar dependence of vertical bleeding on ϕ and AR, the underlying physics are different. However, in contrast to the bleeding velocity, a flow-rate budget shows that the proportion of the vertical bleeding flow leaving the patch with respect to the total flow entering the patch (i.e. relative vertical bleeding) decreases with increasing AR. Finally, the interlinks between patch geometry, flow bleeding and flow diversion are identified: the patch influences the flow diversion not only directly by its real geometrical dimensions, but also indirectly by modifying flow bleeding which enlarges the size of the near-wake. While loss of flow penetrating the patch increases monotonically with increasing ϕ, its partition into flow diversion around and beneath the patch shows a non-monotonic dependence, highlighting the fundamental differences in the flow dynamics between porous patches and their solid counterpart.

Next, the propagation of full-depth lock-exchange bottom gravity currents over a submerged array of circular cylinders is investigated using laboratory experiments and LES. Firstly, to investigate the front velocity of gravity currents across the whole range of array density ϕ, the array is densified from a flat-bed ($\phi = 0$) towards a solid-slab ($\phi = 1$) under a particular submergence ratio H/h, where H is the flow depth and h is the array height. The time-averaged front velocity in the slumping phase of the gravity current is found to first decrease and then increase with increasing ϕ. Next, a new geometrical framework consisting of a streamwise array density $\mu_x = d/s_x$ and a spanwise array density $\mu_y = d/s_y$ is proposed to account for organized but nonequidistant arrays ($\mu_x \neq \mu_y$), where s_x and s_y are the streamwise and spanwise cylinder spacings, respectively, and d is the cylinder diameter. It is argued that this two-dimensional parameter space can provide a

more quantitative and unambiguous description of the current-array interaction compared with the array density given by $\phi = \left(\frac{\pi}{4}\right)\mu_x\mu_y$. Both in-line and staggered arrays are investigated. Four dynamically different flow regimes are identified: (i) through-flow propagating in the array interior subject to individual cylinder wakes (μ_x: small for in-line array and arbitrary for staggered array; μ_y: small); (ii) over-flow propagating on the top of the array subject to vertical convective instability (μ_x: large; μ_y: large); (iii) plunging-flow climbing sparse close-to-impermeable rows of cylinders with minor streamwise intrusion (μ_x: small; μ_y: large); and (iv) skimming-flow channelized by an in-line array into several sub-currents with strong wake sheltering (μ_x: large; μ_y: small).

Finally, the flow dynamics of intrusive gravity currents past a bottom-mounted obstacle in a continuously stratified ambient was numerically investigated, highlighting the effect of ambient stratification which is not considered in the previous sections. The propagation dynamics of a classic intrusive gravity current was first simulated in order to validate the numerical model with previous laboratory experiments. A bottom-mounted obstacle with a varying non-dimensional height of $\tilde{D} = D/H$, where D is the obstacle height and H is the total flow depth, was then added to the problem in order to study the downstream flow pattern of the intrusive gravity current. For short obstacles, the intrusion re-established itself downstream without much distortion. However, for tall obstacles, the downstream flow was found to be a joint effect of horizontal advection, overshoot-springback phenomenon, and associated Kelvin-Helmholtz instabilities. Analysis of the numerical results show that the relationship between the downstream propagation speed and the obstacle height can be subdivided into three regimes: a retarding regime ($\tilde{D} \approx 0 \sim 0.3$), an impounding regime ($\tilde{D} \approx 0.3 \sim 0.6$), and a choking regime ($\tilde{D} \approx 0.6 \sim 1.0$).

Overall, at a fundamental level, this dissertation aims to contribute to an improved understanding of the physics associated with environmental flows interacting with obstacles. Moreover, the results from this research are expected to facilitate better parameterizations of this important class of flows.

ACKNOWLEDGEMENTS

I sincerely thank my advisor, Dr. Karan Venayagamoorthy for his supportive and indefatigable enthusiasm throughout my PhD studies at CSU. His encouragement, imparted knowledge, and the life he brings to research have made this dissertation possible and have enriched my experience at CSU beyond expectation. I also wish to extend my deepest appreciation to my PhD committee, Drs. Pierre Julien, Brain Bledsoe and Hiroshi Sakurai. I thank all of them for serving on my committee, for their mentorship and encouragement throughout my research. Thanks also to Drs. Timothy Gates, Claudia Cenedese and Roger Nokes for their insightful suggestions and guidance throughout my coursework and research in different stages of my PhD study.

I thank my officemates in EFML with special thanks to my fellow PhD students, Benjamin Mater, Farid Karimpour, Jordan Wilson, Amrapalli Garanaik and Dapo Aseperi. Our various conversations – be they scientific, philosophical, or otherwise – have fostered a camaraderie and friendship which I will always cherish. Thanks also to my friend and officemate, Yishu Zhang, for our mutual help and encouragement.

I am very grateful to my parents, Mr. Zhongyi Zhou and Mrs. Chundi Chen, for their encouragement, instilled ethics, imparted wisdom, and love. This dissertation is dedicated to my family for their unwavering faith in me.

Also, fundings from the National Science Foundation under CAREER grant OCE-1151838 and the Office of Naval Research under grant nos N00014-12-0938 and N00014-16-1-3015 are gratefully acknowledged.

TABLE OF CONTENTS

LIST OF TABLES

LIST OF FIGURES

Chapter 1

Introduction

1.1 Motivation

Turbulence is ubiquitous in environmental flows such as in rivers, lakes, estuaries, oceans and the atmosphere, and it is characterized by chaotic and (supposedly) random motions, with the basic notion that it enhances mixing and transport of both momentum and mass (Pope 2000). The interaction of various natural and man-made obstacles encountered in the real world with the surrounding environmental flows can lead to the generation of turbulence which determines local or even global flow patterns. Some examples include:

- Dense water formed in semi-enclosed seas often has to flow through narrow straits or down continental slopes before it reaches the open ocean (figure 1.1a). Subsequently, such oceanic overflows separate from the slope at their level of neutral buoyancy (Chassignet *et al.* 2012), the subsequent interaction with downstream topographic features such as sills, canyons, banks, seamounts, ridges, underwater volcanos and mountain ranges affects the properties and final fate of the deep water-masses in the abyssal ocean, and thus the localized mixing as well as the large-scale meridional overturning circulation (MOC).

- The hydrodynamic effects of submerged or suspended canopies, including aquatic vegetation patches, offshore aquacultural cages, rafts and long lines (figure 1.1b), have important implications for the fluxes of nutrients and wastes that determine productivity and environmental impacts of the canopy (Plew 2011). For example, nutrient depletion in suspended shellfish culture may limit growth. Under-farm flow accelerations leading to increased bed shear stresses are likely to influence the deposition and resuspension of waste products from shellfish culture. Furthermore, the near-field disposal of wastes tends to affect the far-field water quality (Venayagamoorthy *et al.* 2011).

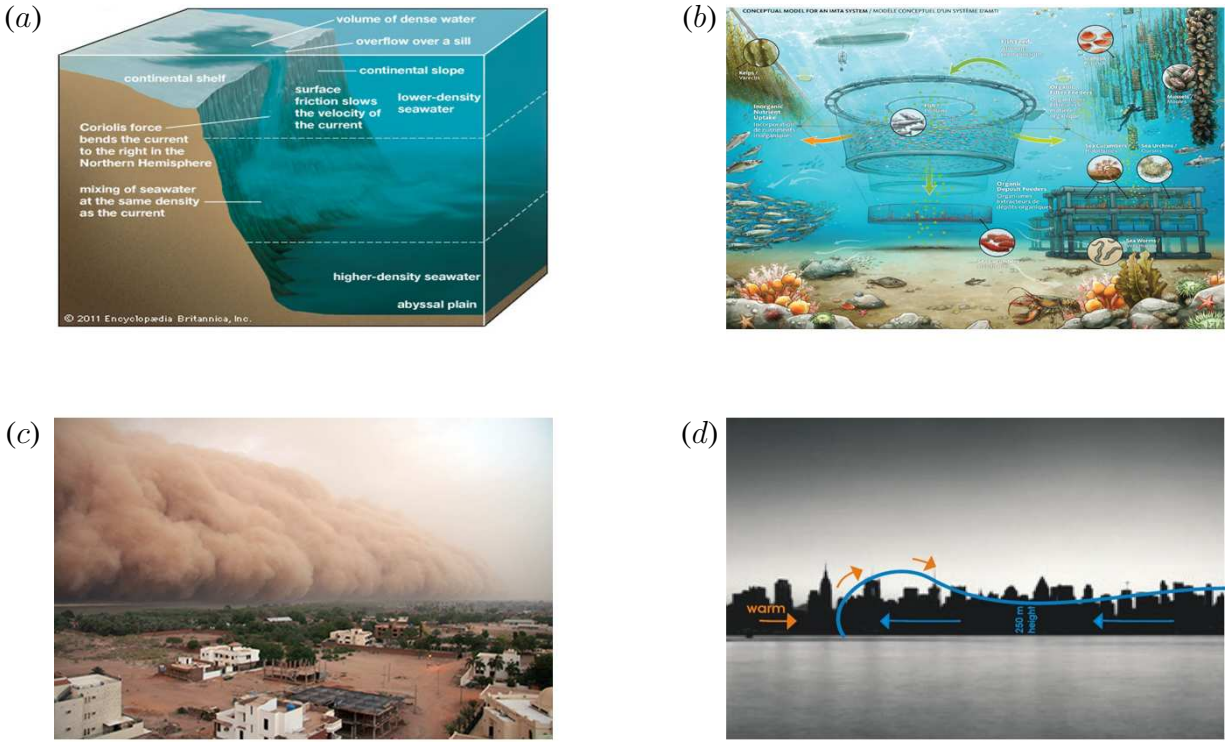

Figure 1.1: Examples of natural and man-made obstacles encountered in environmental flows. (a) Oceanic overflow descending a continental slope; (b) Aquacultural structures suspended in oceanic currents; (c) Haboob advancing over bottom roughness; (d) Seabreeze flowing through urban buildings.

- Gravity currents occur when there are horizontal variations in density in a fluid under the action of gravitational field, such as thermally-driven exchanges, turbidity currents, snow avalanches, haboobs, pyroclastic flows and seabreazes (figure 1.1c, d). A good understanding of their interaction with various types of obstacles (e.g. aquatic and terrestrial canopies) is critical for predicting their propagation dynamics as well as establishing effective preventative measures to mitigate their destructive impacts.

Our current understanding of environmental flows interacting with obstacles have been developed for two limiting conditions: (i) flows impinging on a single isolated obstacle, such as a sphere, a cylinder or a bluff body of any shape (e.g. Williamson 1996; Zdravkovich 1997); and (ii) flows impinging on a uniformly distributed array of elements where the array size is large compared with the characteristic large scales of the flow (e.g. Nepf 2012; Ozan *et al.* 2015). The intermediate condition, where turbulent flows interact with a finite group of obstacles, has received

much less attention and thus remains to be better understood. However, this class of flows is probably the most common in both natural and engineering settings. Examples of such flows include atmospheric boundary layers over a forest patch, groups of wind turbines, groups of outstanding buildings in cities, marine turbines in tidal channels, river flows over patchy vegetated beds and marine currents impinging on offshore structures. For these flows, the estimation of drag forces that the flow exerts on the group and the knowledge of the structure of the turbulent wake occurring behind the obstacles are extremely important for the purpose of, e.g., predicting the amount of power that a group of turbines (wind or marine) can generate (Vennell 2010, 2011), estimating carbon dioxide exchange between the forests and the atmosphere (Irvine *et al.* 1997; Cassiani *et al.* 2008; Huang *et al.* 2011) or modelling flood routing in rivers with a patchy vegetation cover (Nepf 2012, and references therein).

Unlike natural canopies, arrays of obstacles with human intervention such as urban canopies, crop canopies, forest plantations, and engineering retarding facilities, are more often nonuniformly distributed with the spacing between obstacles varying significantly in different directions. However, most existing studies are limited to environmental flows interacting with uniformly distributed arrays (Tanino & Nepf 2008*b*; Cenedese *et al.* 2016). The conventional geometrical characterization consisting of horizontally-averaged bulk parameters, e.g. the array density ϕ (or equivalently, the solid volume fraction), was employed in all these studies. Therefore, the universality of the consensus that a certain value of ϕ can uniquely determine the state of the canopy flows is questionable and needs to be reexamined.

Furthermore, canopies from different systems with different scales exhibit a wide range of array density ϕ. For rooted aquatic vegetation, ϕ ranges from 0.001 for marsh grasses to 0.45 for mangroves. The range of ϕ for terrestrial forests has not been specifically reported in the literature, but is also expected to vary significantly between different circumstances. In industrial settings, however, there is an even wider range of ϕ. For example, the packing density of buildings may reach its minimum ($\phi \approx 0$) in the open country and its maximum ($\phi \approx 1$) in a dense urban center. Other dense porous media may be encountered by environmental flows include sediment

beds, coral reefs and reservoir rocks (Ghisalberti 2009). To date, a very limited range of ϕ has been investigated, with the highest being around 0.36, showing a big gap of data in the range of $0.36 < \phi < 1$ where $\phi = 1$ indicates the limiting case of a solid obstruction. The associated flow transitions within this range that regulate the dynamics of the incoming flows has not yet been adequately explored.

Fundamental difference in the forcing mechanism exists between constant-density flows and density-driven gravity currents. While there is a vast amount of literature on constant-density flows interacting with obstacles, the study of gravity currents is relatively scarce mainly due to the additional complexity associated with the density variations in different directions. On one hand, under a homogeneous ambient, gravity current forms spontaneously due to the hydrostatic pressure force which originates from horizontal density gradient (e.g. Shin *et al.* 2004). On the other hand, natural fluid bodies such as the atmosphere, the oceans and lakes are characteristically stably stratified, i.e. their mean (potential) density decreases as one goes upwards. Gravity currents may propagate into a fluid where the ambient itself is stably stratified (e.g. Maxworthy *et al.* 2002). The effect of these two types of density gradients, either horizontal or vertical, on the flow-obstacle interactions with respect to that in constant-density flows is a subject of ongoing research. Therefore, combining the above motivations, a holistic picture of environmental flows interacting with obstacles is made possible if the influences of obstacle grouping and density variation are both considered. It is with this holistic mindset that the current research seeks to better understand obstacle's effect in environmental flows.

1.2 Objectives

In this dissertation, large-eddy simulations (LES) will be used to study the fundamental physics of environmental flows (constant-density or density-driven) interacting with obstacles (single or multiple). The numerical model will be extensively validated with available experimental and direct numerical simulations (DNS) data. The main objectives of this research are as follows:

1. **To gain insights into the three-dimensional hydrodynamics of constant-density flows interacting with a finite canopy.** The first major contribution of this dissertation is a quantitative evaluation of the flow-bleeding dynamics as presented in chapter 4. This objective is motivated by the need of a systematic understanding of the hydrodynamics of a finite porous patch as a function of its element density and geometrical dimensions. The fundamental interlinks between patch geometry, flow bleeding from the patch and flow diversion around/beneath the patch are suggested for the first time, which have important implications for nutrient uptake and waste disposal in aquacultural structures, and turbulent exchanges between aquatic/terrestrial canopy patches with the surrounding environmental flows.

2. **To develop an unambiguous geometrical framework for characterizing canopy planar geometry.** Herein lies the crux of this dissertation: a two-dimensional parameter space, which features a directional decomposition of the array planar geometry when being impinged by both constant-density and gravity current flows, is developed in chapter 5. Taking the case of bottom-boundary gravity currents over a submerged canopy as an example, this new framework emphasizes, at a fundamental level, the breakdown of the conventional horizontally averaged ϕ-parameterization for canopies whose constituent elements are nonuniformly distributed.

3. **To explore the fundamental differences in the flow dynamics between porous canopies and their solid counterpart.** This objective is motivated by the need for a physical explanation of the observed non-monotonic dependence of flow dynamics on canopy density, which will be presented for constant-density flows in chapter 4 and density-driven currents in chapter 5, respectively. To date, no such in-depth research has been conducted to examine the consensus that the effect of a dense canopy on the surrounding environmental flows will approach asymptotically towards the solid-limit with zero porosity.

4. **To investigate the effect of ambient stratification on flow-obstacle interactions.** In chapter 6, the focus is density-driven intrusions interacting with an isolated bottom-mounted

obstacle, with particular emphasis on the effect of ambient stratification. Orthogonal to the parametric study in objective 3 where we vary the canopy planar geometry, the obstacle height will be varied. This objective is motivated by the need to predict the properties and fate of deep water-masses under the impact of ocean bottom topographies.

1.3 Dissertation Layout

The chapters of this dissertation each include brief discussions of background material so that the chapters may be read as stand-alone works. As such, some concepts and definitions found in the literature review and elsewhere will be repeated in later chapters. The layout of the dissertation is as follows:

- Chapter 2 presents a review of classical literature pertaining to the study of environmental flows interacting with obstacles. Starting from the different types of flow forcings, the scenarios of flow interacting with an isolated obstacle, infinite arrays, finite arrays and partial-depth arrays will be discussed.

- Chapter 3 presents the governing equations and the numerical methodology employed in this dissertation.

- Chapter 4 addresses objectives 1 and 3, discussing the near-field hydrodynamics of a suspended cylindrical canopy patch. No density variations are included in this chapter.

- Chapter 5 addresses objectives 2 and 3, discussing the propagation dynamics of bottom gravity currents encountering a submerged array.

- Chapter 6 addresses objective 4, focusing on the effect of ambient stratification on gravity current-obstacle interactions.

- Finally, chapter 7 briefly summarizes the main findings/relevant contributions of this dissertation, and suggests some directions of future work.

Chapter 2

Literature Review

2.1 Flow Forcings

2.1.1 Constant-density Flow

The incoming uniform constant-density flows can be driven by the potential forcing which is associated with hydrostatic pressure or bed slope. The fluid density is temporally and spatially constant. It is commonly seen in aquatic and atmospheric flows in regions where the effect of stratification is negligible. The pressure gradient is a physical quantity that describes which direction and at what rate the pressure changes the most rapidly around a particular location. The resulting pressure-gradient force, which is always directed from the region of higher-pressure to the region of lower-pressure, can cause an acceleration according to Newton's second law of motion, if there is no additional force to balance it. When a fluid is in an equilibrium state (i.e. there are no net forces), the system is referred to as being in hydrostatic equilibrium, usually balanced by the frictional force.

2.1.2 Gravity Current

2.1.2.1 Definition of Gravity Current

A gravity current appears when fluid of one density ρ_c propagates into another fluid of a different density ρ_a. The fluid motion is predominantly horizontal, in contrast to a buoyant plume. A gravity current is formed when we open the door of a heated house and cold air from outside flows over the floor into the less dense warm air inside. A gravity current is formed when people pour honey on a pancake and let it spread out on its own. Gravity currents originate in many natural and industrial circumstances and are present in the atmosphere, lakes and oceans as winds, cold or warm streams or currents, polluted discharges, etc. The start of quantitative study of gravity currents is attributed to von Karman (1940), but the related dam-break problem was solved by

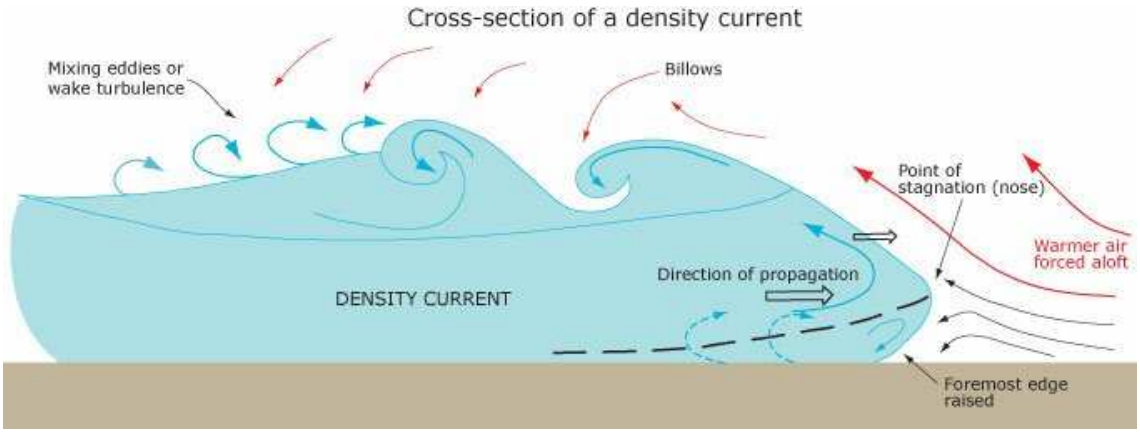

Figure 2.1: Schematic of the typical cross-sectional structure of a bottom-boundary gravity current.

Saint-Venant about a century earlier. To date, the study of gravity currents has generated a large body of work, including some partial review papers (Griffiths 1986; Felix 2002; Huppert 2006; Meiburg & Kneller 2010) and the monographs of Simpson (1997) and Ungarish (2009). Figure 2.1 shows a typical cross section of a gravity current. It shows a characteristic complex head structure, followed by a trailing region where the mean flow properties are relatively constant with horizontal position.

2.1.2.2 Classification of Gravity Current

The basic configurations for various types of gravity currents are sketched in figure 2.2. In a homogeneous ambient (i.e. $\rho_a = \text{constant}$), the gravity current propagates on a well-defined lower (i.e. channel bottom) or upper boundary (i.e. the free surface). A bottom gravity current forms if $\rho_c > \rho_a$ and a surface gravity current forms if $\rho_c < \rho_a$. The gravity current is driven by the gravity body forces, but in a rather subtle way. The fluids under consideration are in almost hydrostatic balance, $\frac{\partial p}{\partial z} \approx -\rho g$, where p and ρ are the pressure and the density, respectively. The difference in ρ between the fluids gives rise to pressure difference in the horizontal direction, which is then balanced by the dynamic reaction (i.e. a non-trivial velocity field with a major horizontal component).

The case of stratified ambient is the most interesting, difficult, and as expected, the least investigated problem. The stratification can be either sharp, i.e. a jump between two relatively thick

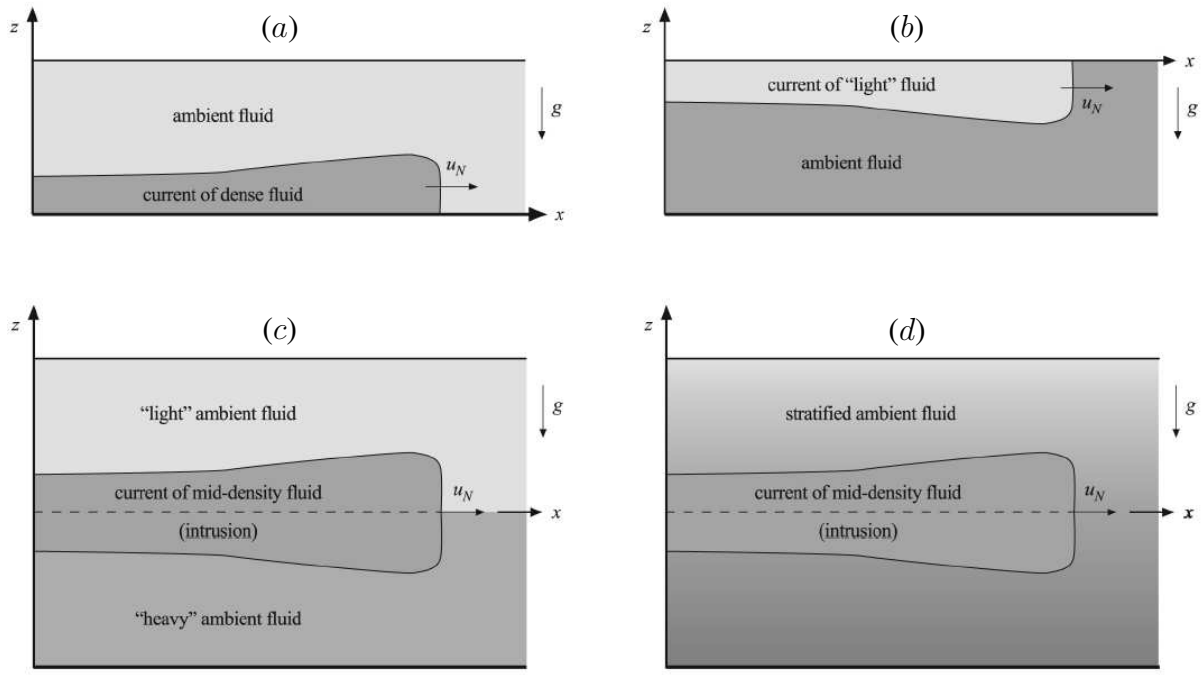

Figure 2.2: Classification of gravity current. (a) bottom current of more dense fluid, $\rho_c > \rho_a$; (b) top (surface) current of less dense fluid, $\rho_c < \rho_a$; (c) intrusion in a sharply (layered) stratified ambient; (d) intrusion in a continuously-stratified ambient, $\rho_c = \rho_a(z = 0)$. Picture is from Ungarish (2009).

layers of homogeneous fluid, or a continuous (typically linear) smooth transition (Simpson 1997). In such systems, an intrusive gravity current (or for brevity, an intrusion) propagates horizontally inside the stratified ambient, typically like an isolated wedge which does not touch the horizontal boundaries. The guiding surface, $z = 0$ say, is the plane of neutral buoyancy for the intruding fluid:

$$\rho_c = \rho_a(z = 0). \tag{2.1}$$

Many results developed for the boundary gravity current can be applied to intrusions, but the difference in flow dynamics can also be significant. The intrusions displaces the isopycnals and thus modifies the prescribed ambient density. Moreover, gravity currents and intrusions in a stratified ambient create, interact, and ultimately combine with internal gravity waves (White & Helfrich 2008).

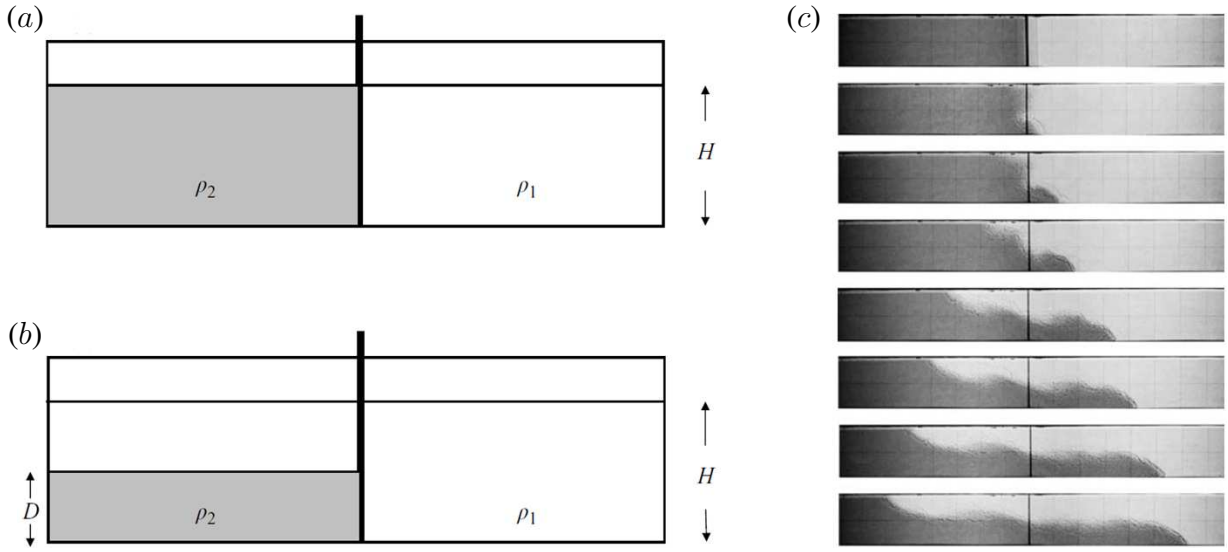

Figure 2.3: Gravity currents produced by lock-release in a homogeneous ambient. The flow is started by removing the gate vertically. The dense fluid $\rho_2 > \rho_1$ occupies the depth H in a full-depth release (a) and a depth $D < H$ in a partial-depth release (b). The temporal evolution of the current propagation after a full-depth release is shown in (c) (Shin *et al.* 2004).

2.1.2.3 Laboratory Generation Methods

Gravity currents are usually generated in the laboratory and numerical simulations by two major configurations. The first type is the constant-flux release where a continuous, constant flux of dense fluid is introduced into the ambient fluid (e.g. Hogg *et al.* 2005). The more common lock-exchange configuration (i.e. constant-volume release) where fluids of different densities initially at rest are separated by a vertical barrier - the lock gate - in a tank (e.g. Shin *et al.* 2004). In figure 2.3, when the gate is removed, differences in the hydrostatic pressure cause the denser fluid to flow in one direction along the bottom boundary of the tank, while the lighter fluid flows in the opposite direction along the top boundary of the tank.

2.1.2.4 Gravity Current's Propagation in a Homogeneous Ambient

The propagation of boundary gravity currents in a homogeneous ambient fluid is the most commonly studied case (figure 2.2a, b). They can be produced with very small density differences (e.g. of a few percent), yet they can still travel for very long distances. The need to predict the arrival time of a gravity current's front and the maximum spreading distance has motivated the

development of relatively simple models (Allen 1985) all the way to detailed simulations (Lee & Wilhelmson 1997*a*,*b*; Härtel *et al.* 2000; Necker *et al.* 2002, 2005; Ozgokmen *et al.* 2004; Cantero *et al.* 2007; Ooi *et al.* 2009; Nogueira *et al.* 2014). The first theoretical attempt to describe the spreading rate of a gravity current using potential flow theory was made in a deep water by von Karman (1940). For a Boussinesq full-depth current with density ρ_2 in an ambient fluid of density ρ_1 (figure 2.3a, c), the dimensionless speed is expressed as a Froude number

$$Fr = \frac{U_f}{\sqrt{g'H}}, \tag{2.2}$$

where U_f is the current speed, H is the channel depth and $g' = g\left(\rho_2 - \rho_1\right)/\rho_2$ is the reduced gravity. The energy-conserving theory of Benjamin (1968) predicts $Fr = 0.5$. Keulegan (1958) found that the speed of the current was independent of the ratio of the channel width and depth, and measured a small increase in Fr with Reynolds number $Re = U_f H/\nu$, from $Fr = 0.42$ at $Re = 600$ to $Fr = 0.48$ at $Re = 150000$.

Following experimental observations, Huppert & Simpson (1980) described the spreading of a gravity current in three phases: an initial *slumping phase* where the current moves at nearly constant speed U_f, followed by an *inertial phase* in which the current moves under the balance of buoyancy and inertial forces, and finally a *viscous phase* where viscous effects dominate and balance buoyancy. Power law expressions for the self-similar evolution of the front have been obtained for the inertial phase where the front speed decays like $U_f \sim t^{-1/3}$ and the viscous phase where $U_f \sim t^{-4/5}$ (Hoult 1972; Rottman & Simpson 1983; Bonnecaze & Lister 1993; Cantero *et al.* 2007; Ooi *et al.* 2009; Ungarish 2009).

2.1.2.5 Gravity Current's Propagation in a Stratified Ambient

An intrusive gravity current (IGC, sometimes referred to as an intrusion) forms when a fluid is released into a non-homogeneous ambient and travels at its level of neutral buoyancy (figure 2.2c, d). The current, however, may still propagate along the boundary if it is lighter (surface gravity current) or denser (bottom-boundary gravity current, BBGC) than the stratified ambient.

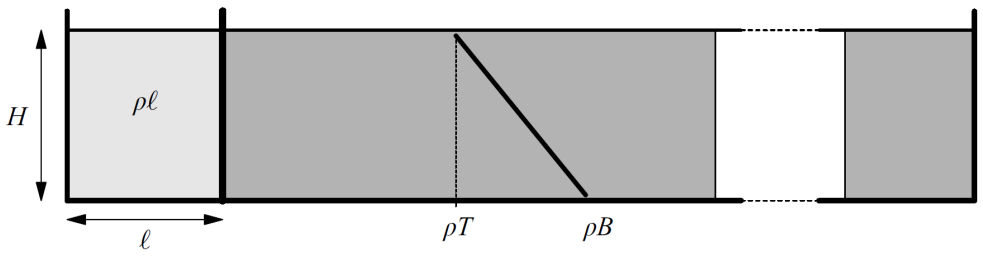

Figure 2.4: Schematic of lock-release configuration with a linearly stratified ambient. ρ_l indicates the lock-fluid density, while ρ_T and ρ_B are the ambient-fluid densities at the top and bottom boundaries, respectively. After the gate removal, an intrusion forms and propagates at its level of neutral buoyancy.

Bottom-boundary gravity currents beneath a two-layer ambient were examined by Rottman & Simpson (1983), and the first experiments and simulations of a gravity current traveling along a rigid bottom under a continuously stratified fluid were performed by Maxworthy *et al.* (2002). The latter found that the front speed of a full-depth BBGC is given by

$$U_f = FrNH, \tag{2.3}$$

where Fr is the Froude number appropriate for gravity currents in a stratified ambient, N is the buoyancy frequency given by $N = \sqrt{(g/\rho_0)\,(-\mathrm{d}\rho/\mathrm{dz})}$, and H is the total fluid depth. For the limiting case of $\rho_l = \rho_B$ (see figure 2.4 for definitions of symbols), they empirically suggested that $Fr = Fr_0 \approx 0.266$, which lies in close agreement with the analytical prediction of $Fr_0 = 0.25$ by Ungarish & Huppert (2002) and Ungarish (2006). Their results also showed good agreement with those from the numerical simulations of Birman *et al.* (2007).

By contrast, the arbitrary-depth intrusions are less understood (Holyer & Huppert 1980; Britter & Simpson 1981; Lowe *et al.* 2002; Sutherland *et al.* 2004; Monaghan 2007; Maurer *et al.* 2010; Holdsworth & Sutherland 2013). By allowing the interface ahead of an intrusion to be vertically displaced, the Benjamin (1968) theory was adapted to predict the propagation speed of intrusions in a two-layer fluid (Flynn & Linden 2006). This speed was predicted on heuristic grounds by Cheong *et al.* (2006), who estimated the speed by relating the available potential energy of the system before the lock fluid was released to the consequent kinetic energy of the intrusion.

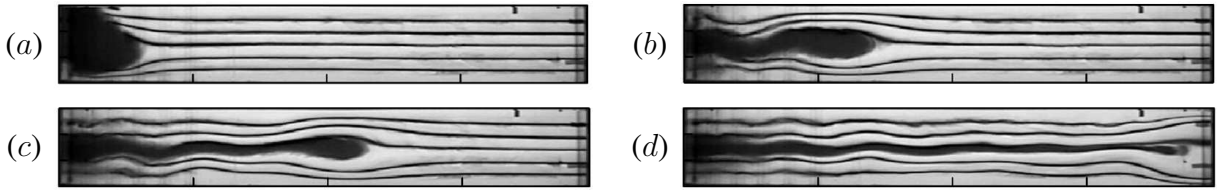

Figure 2.5: Temporal evolution of a mid-depth intrusion (in the sequence of $a \sim d$). Horizontal lines indicate the isopycnals. Picture is from Munroe *et al.* (2009).

Numerous experiments have been performed that examine the speed and structure of intrusions propagating at mid-depth in uniformly stratified ambient (figure 2.5), these resulting either from a full-depth lock-release (e.g. Sutherland & Nault 2007) or from a localized mixed patch (e.g. Sutherland *et al.* 2007). However, only few studies have examined the asymmetric circumstance of intrusions propagating at arbitrary depth in a uniformly stratified fluid. Bolster *et al.* (2008) extended the Cheong *et al.* (2006) result by fitting a quadratic to the mid-depth, top and bottom propagating intrusion speeds, that were predicted by equation (2.3). Thus they heuristically predicted that the speed of an intrusion propagating at depth h_N where the intrusion density matches the ambient density is given by equation (2.3) with a modified Froude number

$$Fr = Fr_0 \sqrt{3\left(\frac{h_N}{H} - \frac{1}{2}\right)^2 + \frac{1}{4}}, \tag{2.4}$$

where Fr_0 is the Froude number in the case where $\rho_l = \rho_B$. Excellent agreement between equation (2.4) with both experimental and numerical simulations has been found.

The presence of ambient stratification allows for a richer set of behaviors than in unstratified gravity currents because the advance of the gravity current forces isopycnal perturbations in the ambient fluid, which may radiate as internal gravity waves (Wu 1969; Schooley & Hughes 1972; Manins 1976; Manins 1976; de Rooij *et al.* 1999, Maxworthy *et al.* 2002, Flynn & Sutherland 2004; Cheong *et al.* 2006; White & Helfrich 2008; Munroe *et al.* 2009; Maurer & Linden 2014). There can be strong interactions between the intrusion and the waves reflected from the back of the lock. In some cases these interactions are sufficient to stop the intrusion propagating. These

reflected waves are the analogue of the finite-amplitude bore generated by reflections from the end wall in a lock-release gravity current. In that case the bore overtakes the current and is responsible for the transition from the constant-velocity phase to the similarity phase.

2.2 Flow Interacting with an Isolated Obstacle

2.2.1 Wake Structure of an Infinitely Long Obstacle

Even the simplest scenario of flow impinging on an infinitely-long isolated obstacle possesses almost the entire complexity of shearing process, such as flow separation, free shear layer and its rolling up, vortex interactions, various shear instabilities, transition to three-dimensional flow and to turbulence, and unsteady turbulent separated flow (Wu *et al.* 2006). In the case of circular cylinder wake alone, there have been hundreds of papers, in part due to its engineering significance, and in part due to the tempting simplicity in setting up such an arrangement in an experimental and computational laboratory. It causes fluctuating drag and lateral force to the body and is a major source of flow-induced structural vibration and noise. After over a century of effort since Strouhal (1878) observed that the frequency of vortex shedding is proportional to U/D with the proportionality constant now being known as the Strouhal number, $St = fD/U$ (U is the incoming velocity and D is the cylinder diameter), and von Karman (1912) constructed the vortex street model and estimated the drag, "the problem of bluff body flow remains almost entirely in the empirical, descriptive realm of knowledge" (Roshko 1993). The great complexity and importance in applications of bluff-body flows are well demonstrated by the comprehensive two-volume monograph of Zdravkovich (1997, 2003).

The various instabilities and flow regimes associated with the wake of an isolated circular cylinder can be discussed using the plot of the base suction coefficient ($-C_{pb}$) versus the Reynolds number (Re). The $-C_{pb}$ is defined as negative of the pressure coefficient at the downstream end of the cylinder:

$$-C_{pb} = -\frac{p_b - p_\infty}{\frac{1}{2}\rho U^2}, \tag{2.5}$$

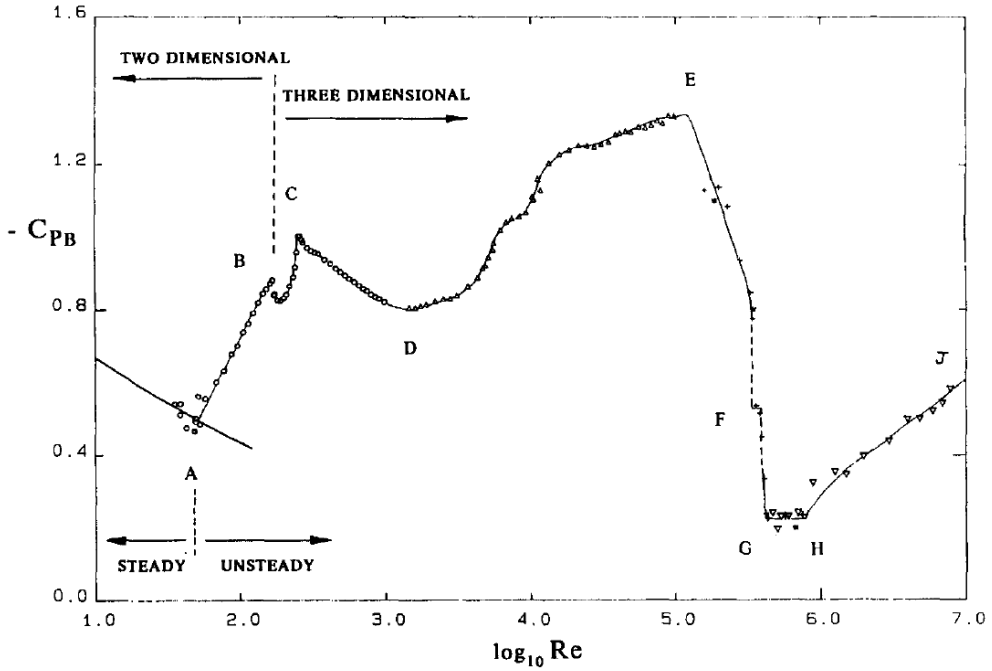

Figure 2.6: Plot of base suction coefficients ($-C_{pb}$) versus Reynolds numbers, as a basis for the discussion of various flow regimes of cylinder wake. Picture is from Williamson (1996).

(a) (b) (c)

Figure 2.7: Visualization of three regimes of cylinder wake with different Re: (a) Steady separation regime at $Re = 26$ (Van Dyke 1982). (b) Periodic laminar regime at $Re = 140$ (Van Dyke 1982). (c) DNS of mode B three-dimensional instabilities at $Re = 250$ (Thompson *et al.* 1996).

which reflects the sensitivity of the flow pattern to Re more adequately than that of the drag coefficient C_D. The physical events divided by the critical Re marked as A, B, ..., J in figure 2.6 are briefly outlined below (Roshko 1993; Williamson 1996; Zdravkovich 1997; Noack 1999).

Regime up to A: Laminar steady regime ($0 < Re < 49$)

The so-called viscously dominated “creeping flow" regime is found to operate in the range $0 < Re < 4$. Creeping flow is firmly attached to the surface of the cylinder all around the circumfer-

ence. The tail of steady and symmetric laminar shear layers does not form a visible wake in this non-separation regime, i.e. no recirculation region exists. Then, separation initiates at $Re = 4$. In the steady separation regime ($4 < Re < 49$), a distinct, symmetric, and closed near-wake (recirculation region) is formed (figure 2.7a), whose length grows as Re increases. The free shear layers meet at the end of the near-wake at the confluence point. The flow is globally stable with respect to all three-dimensional disturbances.

Regime A-B: Periodic laminar regime ($49 < Re < 140 - 194$*)*

At the first critical Reynolds number $Re_{cr1} \approx 49$, the flow becomes linearly unstable with respect to two-dimensional disturbances and experiences a supercritical Hopf bifurcation. A sinusoidal oscillation of free shear layers commences at the confluence point and propagates towards the cylinder, whose amplitude increases with Re. The spontaneous onset of oscillation ($Re \approx 49$) is very sensitive to disturbances and cannot be reliably measured experimentally. The final product is the rolling up of the shear layers and consequently a staggered array of laminar eddies, i.e. the von Karman vortex street (figure 2.7b). The trailing, entrapped, attached vortices periodically become unstable and detached. The oscillating wake induces a lift force on the cylinder with a frequency denoted by St.

Regime B-C: 3D wake-transition regime ($190 < Re < 260$*)*

The cylinder wake becomes intrinsically three-dimensional (not associated with end-effect) due to two bifurcations at $Re_{cr2} = 190$ and $Re_{cr3} = 260$ (Barkley & Henderson 1996; Henderson & Barkley 1996). At Re_{cr2} the flow is linearly unstable with respect to a spanwise wavelength of $\lambda_s/D = 4$, called “mode A" instability, leading to a slightly subcritical onset of three-dimensionality. Then for $Re = 230 - 260$ there is a gradual energy transfer from the mode A shedding to a “mode B" shedding in which finer-scale streamwise vortices of $\lambda_s/D \approx 1$ appear (figure 2.7c) due to a supercritical bifurcation at Re_{cr3}.

Regime beyond C: transitional and turbulent regime ($Re > 260$*)*

As Re increases from 260, the flow starts the transition process to turbulence. The transition first occurs in the wake, where fine-scale three-dimensional structures are more and more disordered.

This causes a reduction of the base suction. Then, in regime D-E the free shear layer transition starts at about $Re \approx 1300$ due to the Kelvin-Helmholtz instability, where $-C_{pb}$ reach a maximum. Around point E ($Re \approx 3 \times 10^5$), the previously laminar boundary layers at one side of the cylinder starts the transition to turbulence. The transition does not occur simultaneously at the other side, implying an asymmetric state with nonzero mean lift. At higher Re the boundary layers at both sides are both turbulent, causing a drastic drop of $-C_{pb}$ down to 0.2 ("drag crisis"). However, the flow is not completely random. Roshko (1961) has discovered the reappearance of periodic turbulent vortex shedding in the H-J regime.

2.2.2 Three-dimensional End Effect

Flow around obstacles with a free end, either bottom-mounted or surface-suspended, is encountered in various engineering applications, such as buildings, cooling towers, fuel and gas storage tanks, chimney stacks, car mirrors, antennas, fastener heads, floating vegetations, and vortex generators (Zdravkovich 2003). Compared with its two-dimensional infinitely-long counterpart, the wake of a bluff body with a free end is complex and strongly three-dimensional, as described in several recent studies that have examined the near-wake vortex structures and von Karman vortex shedding (e.g. Wang *et al.* 2006, 2012; Wang & Zhou 2009; Krajnovic 2011; Sumner 2013; Sumner *et al.* 2015). Key parameters influencing the flow field are the Reynolds number, $Re_d = U_\infty d/\nu$, cylinder aspect ratio $AR = h/d$, and the relative thickness of the boundary layer on the ground plane, δ/h (if bottom mounted), where d is the cylinder width or ortdiameter, h is the cylinder height and δ is the boundary layer thickness.

The general mean flow structures around a bottom-mounted circular cylinder are shown in figure 2.8 and consist of four different mean vortex systems (Sumner *et al.* 2004): a tip vortex system, a von Karman vortex or spanwise vortex system (similar to that described for a two-dimensional cylinder in §2.2.1), a base vortex system and a horseshoe vortex system. The tip region is characterized by separated flow and downwash over the free-end which culminates in complex three-dimensional flow structures from the tip trailing edge. Generally, the mean flow

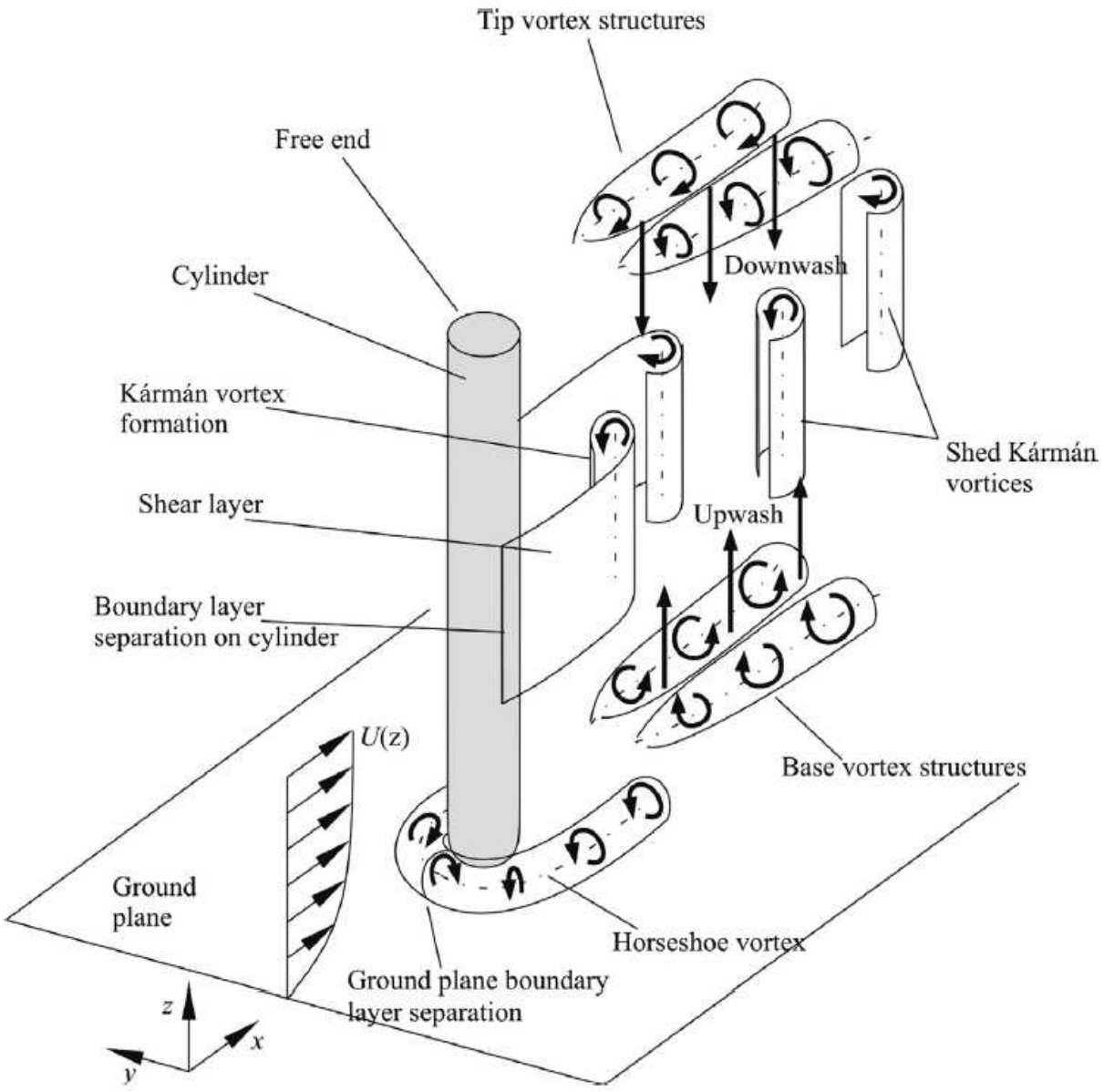

Figure 2.8: Schematic of the flow field for finite circular cylinders greater than the critical aspect ratio, AR_{crit}, based on the work by Sumner *et al.* (2004).

pattern in this range is characterized by a pair of counter rotating vortices which induce downwash into the cylinder wake. A horseshoe vortex system forms at the base due to separation and roll-up of boundary layer vorticity in front of the cylinder, the legs of which wrap around the base of the structure. The base flow also often features a pair of counter-rotating vortices, opposite in direction to the tip vortices, in the recirculation region that induce upwash into the near wake. The base and tip vortices interact with the midspan von Karman vortex system to partially or completely alter the flow field around the body. The influence of the horseshoe vortex on the near wake structure has been found to be considerably milder than the influence of the other vortex systems (Bourgeois *et al.* 2011) and is generally overlooked in near-wake studies.

The cylinder aspect ratio, $AR = h/d$, is the primary geometric characteristic which influences the flow around a cylinder with free ends. The critical aspect ratio, AR_{crit} is defined as the point below which tip vortices dominate the flow and suppress the alternate von Karman vortex shedding. As reviewed by Sumner (2013), most studies of the free-end flow field and its recirculation zone have been performed for relatively small cylinder aspect ratios, within the range of $AR \leqslant 2.5$ (e.g. Roh & Park 2003; Hain *et al.* 2008; Garcia-Villalba *et al.* 2014). These aspect ratios are below AR_{crit} where the familiar antisymmetric Karman vortex shedding is no longer observed. For the higher-aspect ratio cylinders, AR > 2.5, and particularly for cylinders above AR_{crit}, there are fewer studies of the finite-cylinder and free-end flow field in the literature (e.g. $AR = 7$ in Sparrow & Samie 1981; $AR = 6$ and 10 in Afgan *et al.* 2007; $AR = 5$ in Palau-Salvador *et al.* 2010; $AR = 6$ in Krajnovic 2011; $AR = 3 \sim 9$ in Rostamy *et al.* 2012 and Sumner *et al.* 2015).

2.2.3 Gravity Current over an Isolated Obstacle

As shown in figure 2.9, when a BBGC encounters an isolated bottom-mounted obstacle, a proportion of the flow may continue over the obstacle while the remaining flow may be reflected back as a hydraulic jump (HJ). The gravity current head is splashed upwards and then reattaches to the bottom boundary. The plunging of a high-velocity jet-like flow results in an intensified mixing vortex (IMV) directly downstream of the obstacle. Eventually a similar current re-establishes

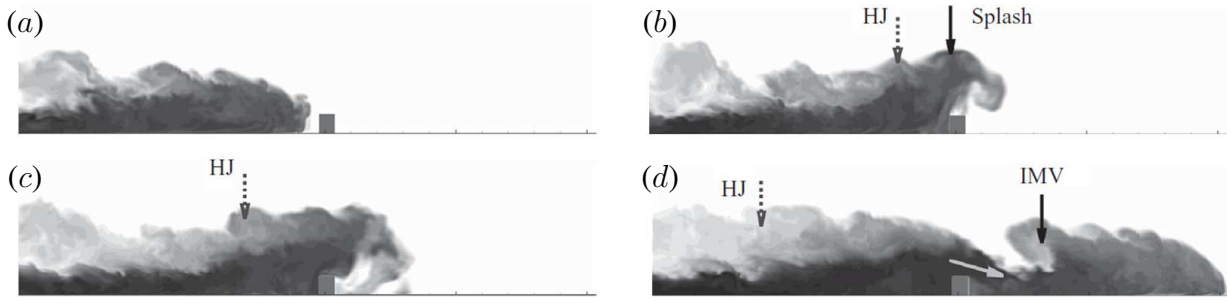

Figure 2.9: Temporal evolution of gravity currents interacting with a bottom-mounted obstacle (in the sequence of $a \sim d$). Picture is from Tokyay *et al.* (2011*b*).

downstream of the obstacle. Lane-Serff *et al.* (1995) theoretically predicted the proportion of the over-passing flux, the speed of the reflected jump, and the depth of the reflected flow. Gonzalez-Juez & Meiburg (2009) extended the shallow-water theory to predict the height and front speed of the downstream re-established current as functions of the upstream Froude number and the ratio of obstacle height to current height. La Rocca *et al.* (2013) used Lattice Boltzmann simulations to simulate the interaction of 3D gravity currents with an emerging cylinder. Tokyay & Constantinescu (2015) investigated the flow induced by a compositional gravity current propagating over a fixed non-erodible triangular bottom-mounted obstacle using 3-D large eddy simulations. Several studies have investigated the time-varying forces on obstacles that result from the impact of gravity currents. The magnitude of the drag increases monotonically with time in an exponential fashion towards a maximum when the current impinges on the obstacle, and goes through a transient phase and eventually reaches a quasi-steady value (Gonzalez-Juez & Meiburg 2009; Gonzalez-Juez *et al.* 2009, 2010). Recently there is also a growing interest in studying sediment-driven turbidity currents over three-dimensional bottom topography for sedimentation-control purpose (Nasr-Azadani & Meiburg 2014*a*,*b*).

2.3 Flow Interacting with an Infinite Array of Obstacles

Infinite arrays of solid bodies fixed relative to an oncoming flow are found in a number of physical situations including fixed bed reactors, porous media, aerosol filtration, building clusters

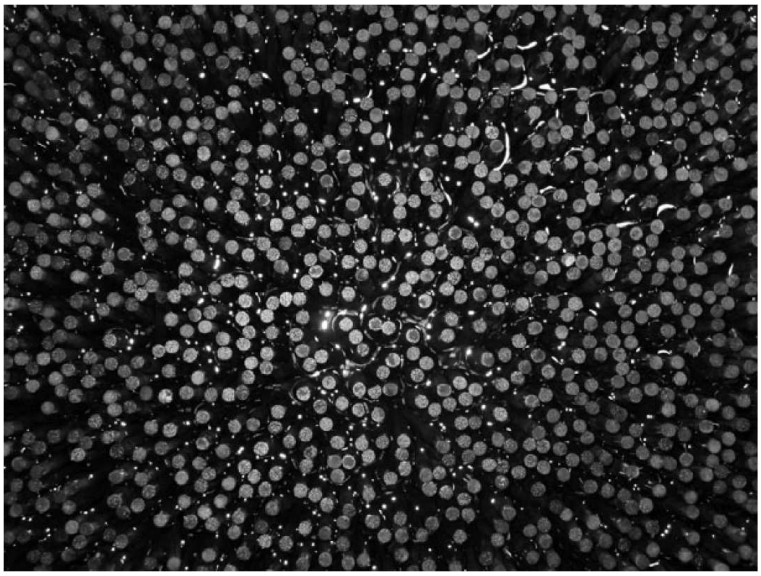

Figure 2.10: Plan view of a section of a random cylinder array with $\phi = 0.27$. Picture is from Tanino & Nepf (2008*b*).

in urban environments, and plant canopies. If the array size is large compared with the characteristic scales of the flow, only the flow behavior within the array is of interest (e.g. figure 2.10).

2.3.1 Array Density

Generally, the planar array geometry is defined by the scale of individual obstacles and the number of these elements per area. If the array elements have a characteristic diameter or width, d, and the average center-to-center spacing between elements is s, then the frontal area per array volume is

$$a = \frac{d}{s^2}. \tag{2.6}$$

In terrestrial canopy literature, this is called the leaf area index (e.g. Kaimal & Finnigan 1994). The array density can also be described by the solid volume fraction occupied by the array elements, ϕ (i.e. array density). If the individual elements approximate a circular cylinder, according to (Nepf 2012):

$$\phi = \left(\frac{\pi}{4}\right) ad, \tag{2.7}$$

where the coefficient of $\pi/4$ accounts for the curvature of circular cylinder.

2.3.2 Constant-density Flow Interacting with an Infinite Array of Obstacles

The existing literature on flow within arrays of obstacles center on aquatic canopies. The reason is that, unlike terrestrial canopies, aquatic canopies can occupy all or a large fraction of the flow depth such that the dynamic impact of the canopy is felt over the entire flow domain, i.e. emergent canopies (Nepf 2012). The dominant turbulent lengthscale within a canopy is shifted downward from analogous conditions without vegetation. In an open channel (with no vegetation), eddies scale with the water depth, H. In a channel with vegetation, the integral lengthscale of the turbulence, l, is set by the smaller of the stem diameter, d, or the averaged distance to the nearest neighboring stem, s_n, regardless of the water depth (Tanino & Nepf 2008*b*). The production of turbulence induced by the stem wakes drains energy from the mean flow (expressed in terms of canopy drag) and feeds it into the turbulent kinetic energy (Pope 2000).

With a cylinder array, flow is forced to move around each element so that the velocity field is spatially heterogeneous. A double-averaging method is used to remove the element-scale spatial heterogeneity, in additional to the more common temporal averaging (Gray & Lee 1977; Raupach & Shaw 1982, and references therein). The instantaneous velocity and pressure fields are first decomposed into a time average (overbar) and deviations from the time average (single prime). The time-averaged quantities are further decomposed into a spatial mean (angle bracket) and deviations from the spatial mean (double prime). For steady, uniform flow within an emergent canopy, the streamwise momentum equation will generally simplify to a balance between potential forcing (associated with hydrostatic pressure or bed slope) and canopy drag (Nepf 2012):

$$g\left(\frac{\partial H}{\partial x}+\sin\theta\right)=-\frac{1}{2}\frac{C_D a}{1-\phi}\langle\overline{u}\rangle|\langle\overline{u}\rangle|=-\frac{\langle\overline{u}\rangle|\langle\overline{u}\rangle|}{L_c} \tag{2.8}$$

where g is the gravitational acceleration, θ is the bed slope, C_D is the canopy drag coefficient, and L_c is the canopy drag lengthscale defined as $L_c = \dfrac{2\,(1-\phi)}{C_D a}$ (Belcher *et al.* 2003), which represents the lengthscale over which the mean and turbulent flow components adjust to canopy drag. For sparse canopies (i.e. small ϕ), L_c is commonly approximated by $(C_D a)^{-1}$. The canopy

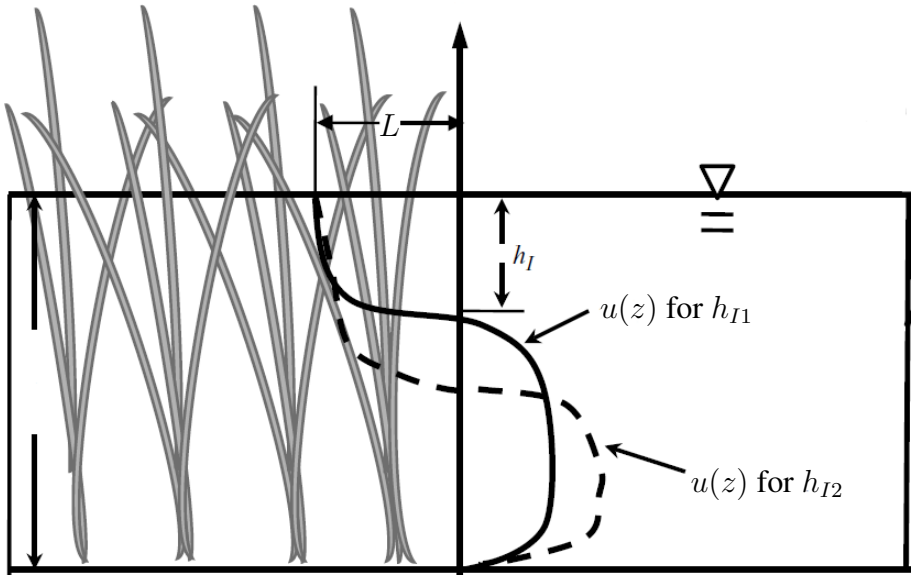

Figure 2.11: Thermally-driven gravity currents in an emergent aquatic canopy. L is the propagated distance of the surface current, and h_I is the intrusion depth of the solar radiation into the canopy. $h_{I1} < h_{I2}$. Picture is from Zhang & Nepf (2009).

drag coefficient, C_D, is affected by the canopy density, a, and the element Reynolds number Re_d. A review of the dependence of C_D on a and Re_d can be found in Tanino & Nepf (2008a).

2.3.3 Gravity Current Interacting with an Infinite Array of Obstacles

The study of gravity currents propagating into a porous medium, such as a channel containing an array of obstacles, is of practical importance for many geophysical and environmental applications. The literature on gravity currents propagating through arrays of emerged obstacles (typically circular cylinders) is limited. Shading by aquatic vegetation can cause differential heating (Chimney *et al.* 2006). For example, dense vegetative stands can reduce incident light by 50% to over 90% (Wetzel 2001). On the other hand, rooted vegetation provides a significant amount of drag, such that we expect rooted plants to both promote, through differential shading, and inhibit, through drag, the thermally driven exchange flow (figure 2.11).

The literature on the propagation dynamics of gravity currents within an array of emergent obstacles (typically circular cylinders) is limited. The classic lock exchange has negligible dissipation and is inertia dominated. It exhibits a predominantly horizontal interface that curves sharply

toward the free surface and the bed at the leading edges of the surface current and undercurrent, respectively (Benjamin 1968). In contrast, exchange flows through sand are drag dominated, and the interface is inclined to the horizontal plane, rotating about its midpoint (Keulegan 1954). Figure 2.12 illustrates these two limits. Hatcher *et al.* (2000) used a one-layer theoretical model and developed similarity solutions for the propagation of gravity currents through an array of obstacles that exert a drag force proportional to $|u|^2$ on the current. They also provide a brief comparison of their similarity solution predictions with their experimental observations for constant-volume currents that propagate through an array of obstacles. Oldham & Sturman (2001), who parameterized vegetative drag using permeability, predicted and observed a reduction in steady, buoyancy-driven, down-slope flow in both the laboratory and field. Tanino *et al.* (2005) applied quadratic and linear drag laws to describe exchange flows occurring entirely within the canopy. They showed that for sparse vegetation the flow has the same interfacial shape as a classic gravity current, but is diminished in magnitude. For dense vegetation, the interface becomes linear. Jamali *et al.* (2008) and Zhang & Nepf (2008, 2009) considered the more natural case of exchange between a model canopy and an adjacent region of unobstructed water. The velocity of the intrusion entering the canopy as well as the total discharge between the open water and the canopy were strongly dependent on the canopy drag. Ozan *et al.* (2015) used LES to study the evolution of lock-exchange gravity currents propagating in a channel containing an array of obstacles. They observed that low-Reynolds-number currents transition to a drag-dominated regime in which the resistance is linearly proportional to the flow speed and, consequently, the front velocity, U_f, is proportional to $t^{-1/2}$, where t is the time measured starting at the gate release time. By contrast, high-Reynolds-number currents, transition first to a quadratic drag-dominated regime in which the front speed is given by $U_f \sim t^{-0.25}$, before undergoing a subsequent transition to the aforementioned linear drag regime in which $U_f \sim t^{-1/2}$. More recently, Testik & Yilmaz (2015) and Testik & Ungarish (2016) investigated the anatomy and propagation dynamics of constant-flux bottom gravity currents within an array of emergent obstacles. All these variations of the propagation characteristics

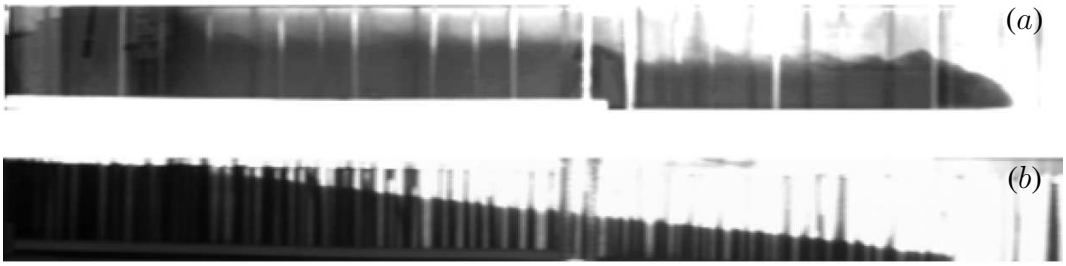

Figure 2.12: Comparison of the interface profile in the inertia-dominated (a) and drag-dominated (b) regimes when a gravity current encounters an emergent canopy. Picture is from Tanino *et al.* (2005).

of the obstructed currents from their unobstructed counterparts were caused by the presence of cylinder-induced drag force, which dominated over the resisting inertia and viscous forces.

2.4 Flow Interacting with a Finite Array of obstacles

Our current understanding of environmental flows interacting with solid obstacles have been developed for two limiting conditions: (i) flows impinging on single isolated obstacles, such as a sphere, a cylinder or a bluff body of any shape (§2.2); and (ii) flows impinging on a uniformly distributed array of elements where the array size is large compared with the characteristic large scales of the flow (§2.3). The intermediate condition, where turbulent flows interact with a small number of obstacles in an isolated group, has received less attention.

2.4.1 Collective Wake Structure

Most of the research on flow past groups of bodies has focused on the offshore industry where cylinders are most commonly used as constituent bodies - for instance as structural members. In the context of offshore risers, there are a number of experimental studies of the force on square groups, e.g., Ball & Hall (1980) investigated larger square arrays of cylinders of up to 9×9 for different angles, but only related this to the total group drag without characterizing the flow field. The number of bodies which forms the group is denoted by N_c as illustrated in figure 2.13. Some numerical studies have examined flow past groups of bodies, usually comprising a small number ($N_c < 10$), with attention usually paid to the structure of the flow. Chang *et al.* (2008)

applied Howe's decomposition method to look at how the flow signature from one cylinder affects downstream cylinders. A few theoretical studies have considered localized fixed arrays of bodies within a uniform flow, with most of the research limited to inviscid descriptions (e.g. Hunt & Eames 2002; Eames *et al.* 2004).

As the number of bodies (N_c) within the array increases, the group begins to resemble a porous medium. The current literature pertaining to this class of flows is mainly focused on the case of arrays of cylinders whose height exceeds the depth of the impinging flow (e.g. Ball *et al.* 1996; Nicolle & Eames 2011; Chen *et al.* 2012; Zong & Nepf 2012, Chang & Constantinescu 2015). In all of these studies, the mean flow around the patch can be considered to be predominantly two-dimensional (2-D) as the vorticity in the wake of the cylinders and the array extends along one dominant direction, i.e. along the vertical axis. Within this context, Chen *et al.* (2012) and Zong & Nepf (2012) have investigated flow properties of circular patches of cylinders piercing the free surface of open channel flows. The number of cylinders and the size of the patches were varied extensively and their effects on the flows around and within the patch were investigated by means of visualization techniques and velocity measurements. The results reported from these studies show that the wake behind a porous obstruction varies strongly with the density of the obstruction. As shown in figure 2.14, downstream of the patch there is a steady wake region where longitudinal velocities were approximately uniform along x. This region is then followed by a recovery region where longitudinal velocities begin to increase with increasing x. The extent of each region increases with decreasing array density and their development is associated with the strength of the shear layers forming along the sides of the array. Further downstream, provided the patch is dense enough, the two shear layers merge and a flow structure resembling a von Karman vortex street can eventually be recovered.

Specifically, for a circular array of circular cylinders, compared with the general definition of array density in equation (2.7), it is more common to define the array density by the number of obstacles within the finite patch, N_c, and the separation of lengthscale between the array and its constituent elements, d/D:

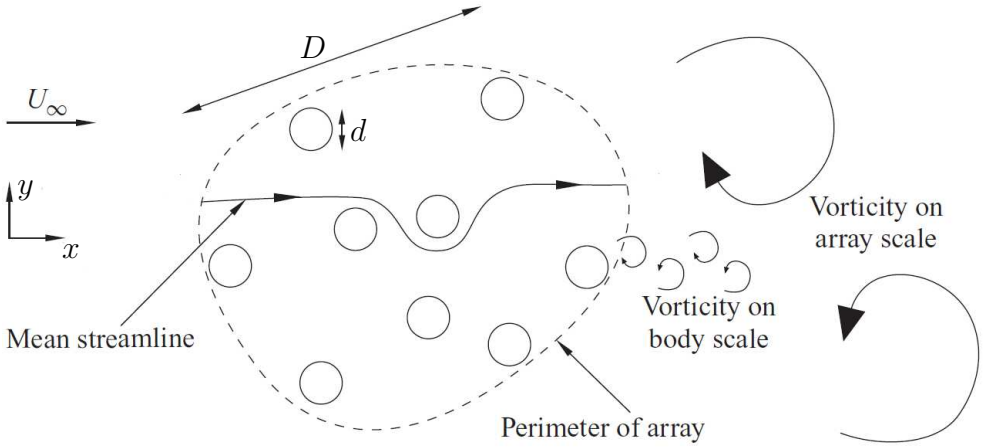

Figure 2.13: A schematic of a finite array of cylinders in a uniform flow showing the body- and array-scale vortices. The array with a bulk diameter of D consists of N_c individual cylinders with a diameter of d.

$$\phi = N_c \left(\frac{d}{D}\right)^2. \tag{2.9}$$

2.4.2 The Three-regime Description

The most noteworthy results pertaining to the problem of flow interacting with a finite array of obstacles should be attributed to the two-dimensional DNS study by Nicolle & Eames (2011). They observed that, depending on the array density, three distinct regimes can be identified:

- At low ϕ ($\phi < 0.05$), the flow interactions are weak within the array and force characteristics on each cylinder are similar to an isolated body. The wake of the group is composed of the identifiable individual wakes of the bodies making up the array. These rapidly dissipate through an annihilation process, as they are advected downstream, leading to a rapid decrease in the maximum vorticity.

- At moderate ϕ ($0.05 < \phi < 0.15$), a stable wake forms behind the array, which is stabilised by a bleed flow. The flow is locally steady and the lift force is negligible. Vorticity annihilation occurs between the cylinders. The maximum vorticity decays slowly with distance by the diffusive thickening of the attached shear layers. The shear layers become unstable some distance downstream and roll up to generate a vortex street (figure 2.14).

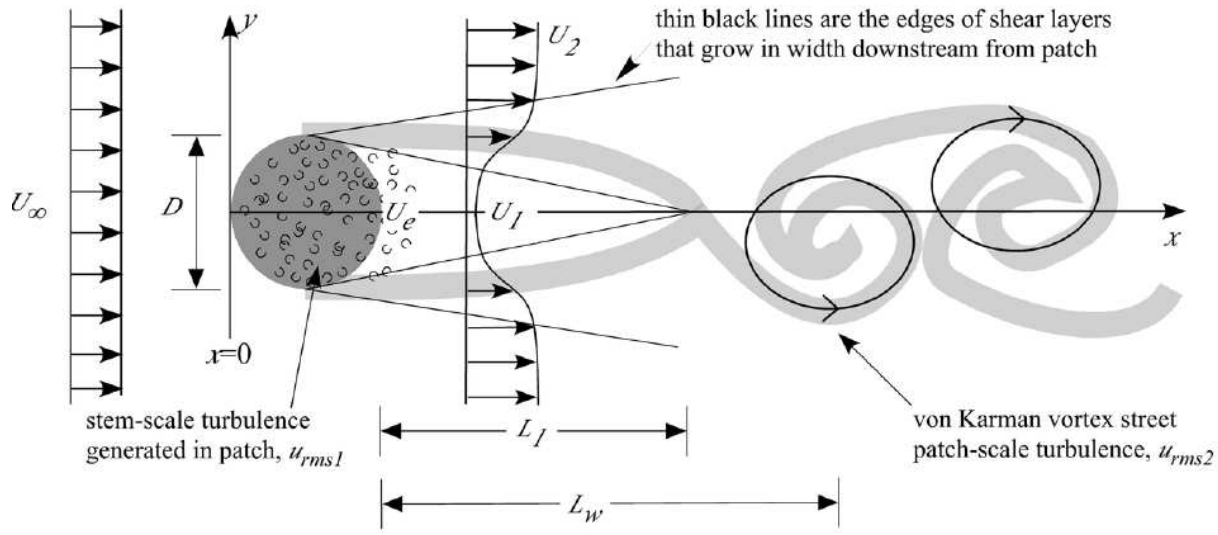

Figure 2.14: Top view of a circular patch of emergent vegetation, shown by dark gray circle of diameter D. Injections of dye at the outer edges of patch (thick gray lines) reveal the evolution of the wake. Velocity exiting the patch ($U_e = u(x = D)$) is diminished relative to upstream velocity (U_∞). The velocity decreases further to the steady wake region (U_1). The flow within the wake delays the onset of von Karman vortex street to the end of the steady wake, $x = L_1 + D$. The wake contains two scales of turbulence: stem-scale turbulence (shown with small thin semicircles), which peaks within the patch, and patch-scale turbulence (black circles with arrows), which peaks at $x = L_w + D$. Picture is from Chen *et al.* (2012).

- At high ϕ ($\phi > 0.15$), the array begins to behave in a similar way to a solid cylinder. The signatures of the individual cylinders within the array are annihilated by wake interactions. The downstream flow consists of a vortex street where the maximum magnitude of vorticity decays slowly downstream.

2.5 Flow Interacting with a Partial-depth Array of Obstacles

The emergent arrays discussed in the previous sections occupy the full depth of the water column ($H/h \leqslant 1$). Another important category is the partial-depth arrays where there is a gap between the array and the vertical boundaries ($H/h > 1$). As shown in figure 2.15, submerged arrays are bottom mounted and extend upward from the bed (e.g. groups of wind turbines; rooted vegetations), while suspended (floating) arrays extend downward from the free surface (e.g. floating vegetations; offshore aquaculture structures). Nevertheless, the interaction between environmental

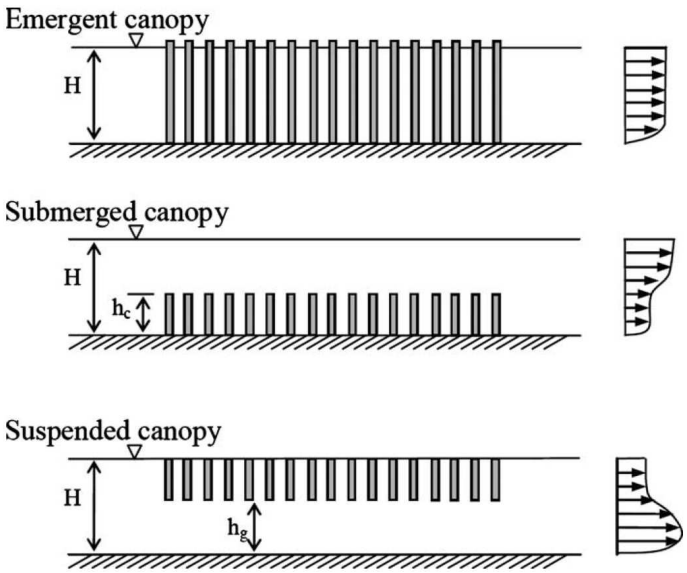

Figure 2.15: Classification of obstacle arrays depending on their vertical sizes and positions. The velocity profiles are shown on the right.

flows and these partial-depth arrays has received much less attention, partly due to the additional complexity arsing from the drag continuity at the array-ambient interface.

2.5.1 Constant-density Flow Interacting with a Partial-depth Array of Obstacles

2.5.1.1 Submerged Infinite Array

Besides the array density, ϕ, the velocity within a submerged canopy has a range of behavior depending on the relative depth of submergence, defined as the ratio of flow depth, H, to array height, h. The flow within the canopy is driven by the turbulent stress at the top of the canopy as well as by the gradients of pressure and gravitational potential (bed slope). The relative importance of these driving forces varies with the depth of submergence (Nepf & Vivoni 2000):

$$\frac{\text{turbulent stress}}{\text{pressure gradient}} \sim \frac{H}{h} - 1. \tag{2.10}$$

Three classes of canopy flow can be defined from equation (2.10): deeply submerged or unconfined ($H/h > 10$), shallow submergence ($H/h < 5$), and emergent ($H/h = 1$). A great deal is known about unconfined canopy flow based on work in terrestrial canopies (e.g. Raupach *et al.* 1996; Finnigan 2000; Belcher *et al.* 2012). When unconfined, the flow within a canopy is driven by the turbulent stress at the top of the canopy, i.e., by the vertical turbulent transport of momentum from the overflow, with negligible contribution from pressure gradients. In this sense, the terrestrial canopy model can be applied to aquatic canopies that are deeply submerged. However, because of the limitation of light penetration, most submerged aquatic canopies occur in the range of shallow submergence, $H/h < 5$ (e.g. Duarte 1991), for which both turbulent stress and potential gradients are important in driving flow in the canopy. For emergent conditions ($H/h = 1$), flow is driven by the potential gradients, as described in the previous sections.

For partial-depth arrays, a nondimensional measure of the array density is the frontal area per bed area, λ_f, known as the roughness density (Wooding *et al.* 1973). For canopy height h, and $z = 0$ at the bed,

$$\lambda_f = \int_{z=0}^{h} a dz = ah, \tag{2.11}$$

with the right-most expression valid for vertically uniform a (defined in equation 2.6). For a submerged canopy, there are two limits of behavior, depending on the relative importance of the bed drag and the canopy drag. If the canopy drag is small compared with the bed drag, then the velocity follows a turbulent boundary-layer profile, with the vegetation contributing to the bed roughness (sparse canopy, figure 2.16a). If the canopy drag is large compared to the bed drag, the discontinuity in drag that occurs at the top of the canopy $z = h$ generates a region of shear resembling a free shear layer with an inflection point near the top of the canopy (dense canopy, figure 2.16b, c). From scaling arguments, Belcher *et al.* (2003) predicted that the transition between the sparse and dense regimes occurs at the roughness density $\lambda_f = ah = 0.1$. Numerical simulations by Coceal & Belcher (2004) suggest that the transition occurs at $\lambda_f = 0.15$. On the basis of measured velocity profiles in aquatic systems (Nepf *et al.* 2007), the profile exhibits a boundary-layer form with no inflection point if $C_D ah < 0.04$, while a pronounced inflection

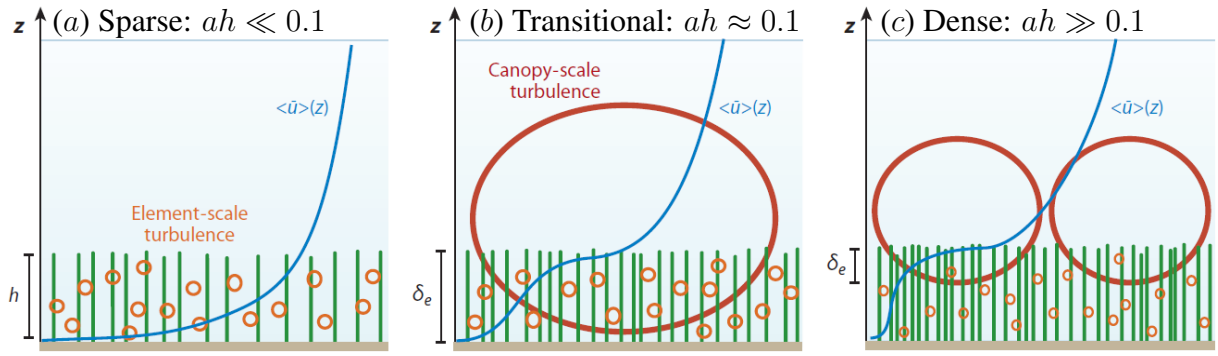

Figure 2.16: Vertical profiles of longitudinal velocity and dominant turbulence scales are shown for (a) a sparse canopy ($ah \ll 0.1$), (b) a transitional canopy ($ah \approx 0.1$), and (c) a dense canopy ($ah \gg 0.1$). For $ah \geqslant 0.1$, a region of strong shear at the top of the canopy generates canopy-scale turbulence. Element-scale (stem-scale) turbulence is generated within the canopy. Picture is from Nepf (2012).

point appears at the top of the canopy for $C_D ah > 0.1$. Because $C_D \approx 1$ in most of the studies considered, the above limits are consistent among each other.

In a free shear layer, the vortices grow continually downstream, predominantly through vortex pairing (Winant & Browand 1974). In canopy shear layers, however, the vortices reach a fixed scale and a fixed penetration into the canopy (δ_e in figure 2.16b, c) at a short distance from the canopy's leading edge (Ghisalberti & Nepf 2004). The fixed vortex and shear-layer scale is reached when the shear production that feeds energy into the canopy-scale vortices is balanced by dissipation by canopy drag. This energy balance predicts the following length scale, which has been verified by laboratory observations (Nepf *et al.* 2007):

$$\delta_e = \frac{0.23 \pm 0.6}{C_D a}, \tag{2.12}$$

which only applies to dense canopies with $C_D ah \geqslant 0.1$. This penetration lengthscale segregates the canopy into: (i) a lower "longitudinal exchange zone" ($z < h - \delta_z$) where the fluid exchanges with surrounding water predominantly through longitudinal advection; and (ii) an upper "vertical exchange zone" ($h - \delta_e < z < h$) where the fluid exchanges with surrounding water through vertical exchange. The extent of each zone is set by the submergence ratio, H/h, and by the canopy morphology, density, and flexibility. Nepf & Vivoni (2000) showed that the vertical exchange zone

deepens between submergence ratio $H/h = 1 \sim 2$. However, for $H/h = 2 \sim 5$, the mixing layer penetration, δ_e, is set by the drag coefficient and canopy density.

Other studies relevant to flow interacting with partial-depth arrays include: turbulence structure near a submerged canopy (e.g. Poggi *et al.* 2004; Chen *et al.* 2013), flexible canopies resembling vegetation (e.g. Ghisalberti & Nepf 2006; Lei & Nepf 2016), flow adjacent to a lateral porous layer (e.g. White & Nepf 2007; Rominger & Nepf 2011), and effect of canopy height heterogeneity (e.g. Hamed *et al.* 2017).

2.5.1.2 Suspended Infinite Array

Common examples of suspended canopies include the cages, rafts and long lines used in aquaculture, and the forests of certain kelp such as *Macrocytis* that have most of the biomass near the surface and low density understories (e.g. Jackson 1998; Rosman *et al.* 2007). The ambient flow is of high importance to aquaculture. It controls the accumulation of waste in the vicinity of the farms (Hartstein & Stevens 2005) and therefore the environmental impact. If artificial feeding is not utilized, it also controls the availability of nutrients for the tissue growth of the organisms (Aure *et al.* 2007; Newell & Richardson 2014). The hydrodynamics of the ambient flow are dependent on the local conditions such as the tidal range (O'Donncha *et al.* 2013), the density stratification (Plew *et al.* 2006), and the partial blockage induced by the aquaculture structures (Plew *et al.* 2005). Field observations have shown that suspended canopies cause flow disturbances such as reduced velocities within the canopy, and increased flow beneath the canopy (Blanco *et al.* 1996; Boyd & Heasman 1998; Plew *et al.* 2005).

Suspended canopies have received little attention in comparison to the more familiar emergent and submerged varieties. At first glance, suspended canopies appear to be an inverted submerged canopy and may be expected to behave in a similar manner. The key difference is the boundary condition: the submerged canopy has a solid boundary at the bottom of the canopy and a free surface at the top of the flow above the canopy; the suspended canopy has the free surface at the top of the canopy while the free-stream flow beneath the canopy is bounded by the solid boundary. Thus, while bottom friction has little effect on velocity profiles in submerged or emergent canopies,

except in highly porous canopies (Nepf *et al.* 1997; Ghisalberti & Nepf 2004; Lightbody & Nepf 2006), bottom friction may have a significant influence on velocities beneath and within suspended canopies (Plew 2011).

2.5.1.3 Partial-depth Finite Array

The most complex scenario, flow impinging on a finite group of obstacles that occupy a portion of the flow depth, has received the least attention. The flow is highly three-dimensional since the porosity of the patch promotes bleeding along all directions. However, this class of flows is probably the most common in both natural and engineering settings. Examples of such flows include atmospheric boundary layers over a forest patch, groups of wind turbines, groups of outstanding buildings in cities, marine turbines in tidal channels, river flows over patchy vegetated beds and marine currents impinging on offshore structures. For these flows, the estimation of drag forces that the flow exerts on the group and the knowledge of the structure of the turbulent wake occurring behind the obstacles are extremely important for the purpose of, e.g., predicting the amount of power that a group of turbines (wind or marine) can generate (Vennell 2010, 2011), estimating carbon dioxide exchange between the forests and the atmosphere (Irvine *et al.* 1997; Cassiani *et al.* 2008; Huang *et al.* 2011) or modelling flood routing in rivers with a patchy vegetation cover (Nepf 2012, and references therein).

To date, only three studies have been conducted on flow interactions with a partial-depth finite array:

- Plew *et al.* (2005) used field observations to investigate the effect of a suspended canopy patch ($2450\mathrm{m} \times 650\mathrm{m} \times 8\mathrm{m}$) on waves, currents and stratification. The submergence ratio H/h varies between 1.25 and 1.5 depending on the tide. They conceptually proposed the hydrodynamics around and behind the patch (figure 2.17).

- Taddei *et al.* (2016) investigated the drag and wake properties of a bottom-mounted cylindrical canopy patch ($0.1\mathrm{m} \times 0.1\mathrm{m} \times 0.1\mathrm{m}$) submerged in a turbulent boundary layer. The

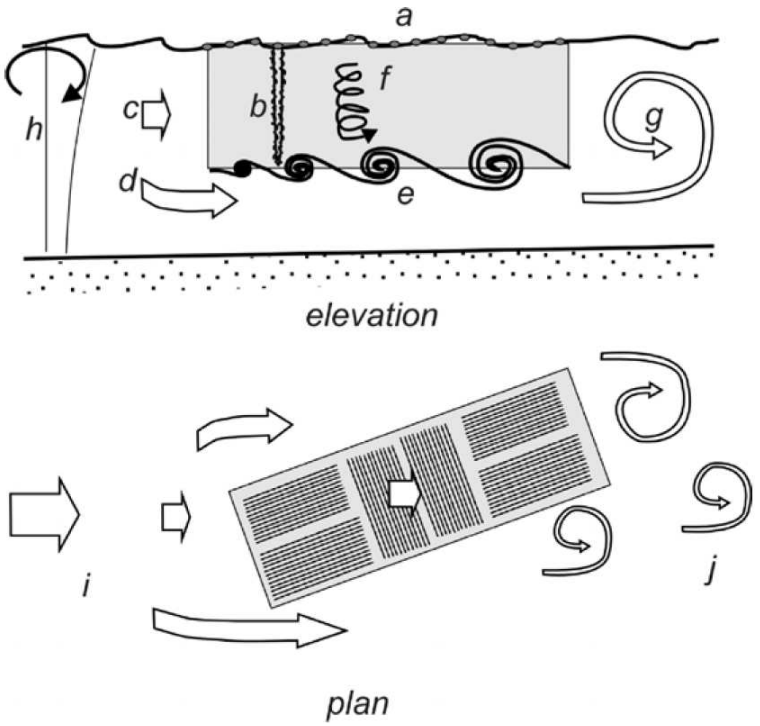

Figure 2.17: Elevation and plan views of a suspended mussel farm indicating various hydrodynamic processes. The (a) floats and (b) vertical dropper loops form a porous barrier to the (c) flow, which generates (d) an accelerating undercurrent. The shear between the undercurrent and the fluid within the farm-proper generates (e) a mixing layer that augments (f) the turbulence due to the droppers. The undercurrent most likely forms a recirculating zone downstream of (g) the farm. The motion of the droppers will also be affected by (h) waves, which in turn are attenuated. In the plan view, the farm can been seen as a number of distinct blocks. These will not necessarily be aligned with the background flow. Flow adjusts (i) upstream and (j) downstream of the farm. The flow is reduced within the farm itself and there is likely a vortex wake (j) downstream.

submergence ratio is $H/h = 6$. It was observed that bleeding along the vertical/horizontal direction increases/decreases with increasing ϕ.

- Tseung *et al.* (2016) investigated the hydrodynamics of a finite canopy patch ($1.08\mathrm{m} \times 0.54\mathrm{m} \times 0.38\mathrm{m}$) suspended at the free surface. The submergence ratio is $H/h = 3.8$. They found similar flow bleeding dynamics as that in Taddei *et al.* (2016).

2.5.2 Gravity Current Interacting with a Partial-depth Array of Obstacles

A series of LES investigations by Tokyay *et al.* (2012, 2011*b*, 2014) have investigated the propagation of gravity currents over a periodic array of submerged obstacles. The array in these

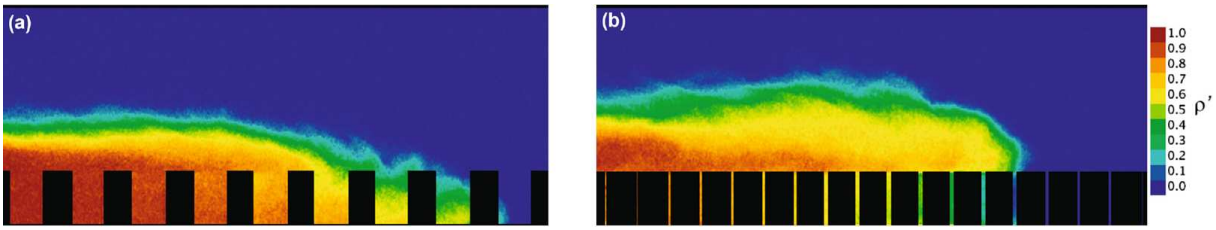

Figure 2.18: Instantaneous non-dimensional density field for a gravity current propagating through and over a (a) sparse and (b) dense array of circular cylinders representing bottom roughness. Picture is from Cenedese *et al.* (2016).

studies is sparse such that the gravity current reattaches to the channel bed after encountering each obstacle. Simulation results show that, similar to an obstructed gravity current, it reaches a constant-speed slumping phase, and then transitions to a drag-dominated phase in which the front speed decays with time.

When the array becomes dense enough to behave like a porous medium, Cenedese *et al.* (2016) experimentally found that enhancement of the dilution of the gravity current by a submerged array can occur due to two different mechanisms. For a sparse array, the vast majority of the gravity current propagates within the array, and the individual cylinder wakes are the main contributor to the current dilution (figure 2.18a). In contrast, for a dense array, the gravity current rides on top of the array and the dilution is enhanced by the vertical convective instability arising from the unstable stratification between the dense current and the ambient lighter fluid within the array (figure 2.18b). The propagation of a surface current beneath a floating (suspended) array of obstacles has been studied experimentally by Zhang & Nepf (2011) and numerically by Ozan *et al.* (2016), which have led to similar results with the studies of bottom currents over a submerged array. A constant-speed slumping phase followed by subsequent self-similar propagation phases are again observed. However, the time-averaged front velocity of the current in the slumping phase, $\overline{U}_f$, decreases with increasing array density in all these studies.

Chapter 3

Numerical Methodology

3.1 Governing Equations

Any motion including fluid flow can be described by the principles of the momentum, mass and energy conservation. In this section, the governing equations are presented for an unsteady, three-dimensional, irrotational, incompressible and stratified flow.

3.1.1 Momentum Equations

The fluid flow is controlled by Newton's second law of motion, relating the imposed force with mass and acceleration. For a three-dimensional, irrotational system with the Boussinesq approximation, the momentum equations (often referred to as the Navier-Stokes equations) are given by

$$\rho\frac{\mathrm{D}u_i}{\mathrm{D}t} = \rho\frac{\partial u_i}{\partial t} + \rho\frac{\partial}{\partial x_j}\left(u_i u_j\right) = -\frac{\partial p}{\partial x_i} + \rho\nu\frac{\partial^2 u_i}{\partial x_j \partial x_j} - \rho g\delta_{i3}, \tag{3.1}$$

where t is the time, g is the gravitational acceleration, ν is the molecular (kinematic) viscosity (assumed as a constant), and δ_{ij} is the Kronecker delta, equal to unity for $i = j$ and zero for $i \neq j$. The Einstein summation convention is used with $i, j = 1, 2, 3$ where x_3 represents the vertical coordinate.

The fluid density can be decomposed into a constant density (ρ_0), local mean value ($\overline{\rho}$) and fluctuation (ρ') give by

$$\rho = \rho_0 + \overline{\rho} + \rho'. \tag{3.2}$$

By inserting the decomposed density in equation (3.1) and rearranging, the momentum equations can be recast as

$$\left(1+\frac{\rho'}{\rho_0+\overline{\rho}}\right)\left(\frac{\mathrm{D}u_i}{\mathrm{D}t}\right) = -\left(\frac{1}{\rho_0+\overline{\rho}}\right)\frac{\partial p}{\partial x_i} + \left(1+\frac{\rho'}{\rho_0+\overline{\rho}}\right)\nu\frac{\partial^2 u_i}{\partial x_j \partial x_j} - \left(\frac{\rho_0+\overline{\rho}+\rho'}{\rho_0+\overline{\rho}}\right)g\delta_{i3}. \tag{3.3}$$

In stratified water bodies, the ratio $\rho'/\left(\rho_0+\overline{\rho}\right) \ll 1$ and can be neglected in the acceleration (inertial) and viscosity terms, but should be retained in the gravity term as it is the primary contributor to buoyancy. This assumption is known as the Boussinesq approximation. Moreover, as $\overline{\rho} \ll \rho_0$ then the mean density is negligible compared with the background density. In addition, if $\rho_r = \rho_0 + \overline{\rho}$ and $p_r = p_0 + \overline{p}$ are considered as the reference density and pressure, and the hydrostatic relation holds, then the reference pressure and density are related as $\partial p_r/\partial x_3 = -\rho_r g$. This assumption helps in numerical simulations when starting from the rest, as the pressure field is taken as the initial hydrostatic pressure field. However, for an irrotational, incompressible and stratified fluid, the Navier-Stokes equation (equation 3.1) can be rewritten as

$$\frac{\partial u_i}{\partial t} + \frac{\partial}{\partial x_j}\left(u_i u_j\right) = -\frac{1}{\rho_0}\frac{\partial p}{\partial x_i} + \nu\frac{\partial^2 u_i}{\partial x_j \partial x_j} - \left(\frac{\rho}{\rho_0}\right)g\delta_{i3}. \tag{3.4}$$

3.1.2 Continuity Equation

In fluid mechanics, mass is absolutely conserved and can be described by a mass conservation equation. The continuity equation using an Eulerian point of view is given by

$$\frac{\partial \rho}{\partial t} + \frac{\partial \rho u_i}{\partial x_i} = 0, \tag{3.5}$$

or from a Lagrangian point of view is as

$$\frac{\mathrm{D}\rho}{\mathrm{D}t} + \rho\frac{\partial u_i}{\partial x_i} = 0, \tag{3.6}$$

where $\mathrm{D}/\mathrm{D}t$ is the total or material derivative. For the flows under Boussinesq approximation, $\rho^{-1}(\mathrm{D}\rho)/(\mathrm{D}t)$ is negligible compared with $\partial u_i/\partial x_i$, therefore the continuity equation reduces to

$$\frac{\partial u_i}{\partial x_i} = 0, \tag{3.7}$$

which implies that the flow field is divergence free.

3.1.3 Density Transport Equation

In unstratified flows, the density is constant and acts as a “passive" quantity in the momentum equation, but in stratified flows the density field evolves with the flow and is coupled with the momentum equation through the buoyancy term in the vertical momentum equation. This highlights the importance of considering the evolution of density transport as one of the flow governing equations. The density transport is depicted through an advection-diffusion equation based on the energy equation as

$$\frac{\partial \rho}{\partial t} + \frac{\partial}{\partial x_j}\left(\rho u_j\right) = \kappa \frac{\partial^2 \rho}{\partial x_j \partial x_j}, \tag{3.8}$$

where κ is the molecular diffusivity.

3.2 Turbulence Modelling

Turbulence is the chaotic, unstable motion of fluids that occurs when there are insufficient stabilizing viscous forces. At high Reynolds numbers, the natural instabilities that occur within the flow are not dampened and they manifest in the formation of eddies of various sizes. In general, there are three main approaches for solving the governing equations numerically, namely: Direct Numerical Simulation (DNS), Large-Eddy Simulation (LES) and Reynolds-averaged Navier-Stokes Simulation (RANS). DNS resolves tha whole spatial and temporal scales of the flow without employing any “turbulent model", while LES uses a spatial filter to simulate large scales explicitly and uses a turbulence model for small scales. RANS simulations just model the mean field of the flow

by using turbulence closure schemes. Figure 3.1 compares the performance of these turbulence schemes in simulating flow over a backward facing step.

Ideally, we would be able to simulate, with the equations of mass and momentum conservation, the full spectrum of turbulent fluctuations using DNS. However, despite the increase in computational power, DNS is still restricted to simple flows with low-to-moderate Reynolds numbers and regular geometries. These shortcomings have made DNS to be more of a valuable technique employed to understand the fundamental physics of turbulent flows rather than a tool for industrial applications. On the other hand, the accuracy of the RANS model is always a matter of discussion in turbulence modeling, therefore numerical models with better accuracy, but still feasible for industrial applications are desired. Large-eddy simulations (LES) has gained attention in the past few decades, and has become widely used as a powerful tool in research and industry with reasonable computational cost and accuracy.

As a result, the large-eddy simulation model in FLOW-3D is chosen to study the flow problems in this dissertation, which captures the unsteady and energy-containing motions of large eddies, but still relies on a turbulence closure scheme to model the effect of small subgrid scales (Pope 2000). A spatial decomposition called "filtering" is applied to the governing equations, splitting the velocity field into a filtered or mean value, $\langle U \rangle$, and a residual or subgrid scale value, $\langle u' \rangle$. The LES filtered governing equations for unsteady, three-dimensional, stratified flows with the Boussinesq approximation are given in tensor notation by

$$\frac{\partial \langle U_i \rangle}{\partial t} + \frac{\partial \langle U_i U_j \rangle}{\partial x_j} = -\frac{1}{\rho_0}\frac{\partial \langle p \rangle}{\partial x_i} + \nu \frac{\partial^2 \langle U_i \rangle}{\partial x_j \partial x_j} - g\frac{\langle \rho \rangle}{\rho_0}\delta_{i3} - \frac{\partial \tau_{ij}^{SGS}}{\partial x_j}, \tag{3.9}$$

subject to the filtered continuity equation

$$\frac{\partial \langle U_i \rangle}{\partial x_i} = 0, \tag{3.10}$$

and the filtered density transport equation

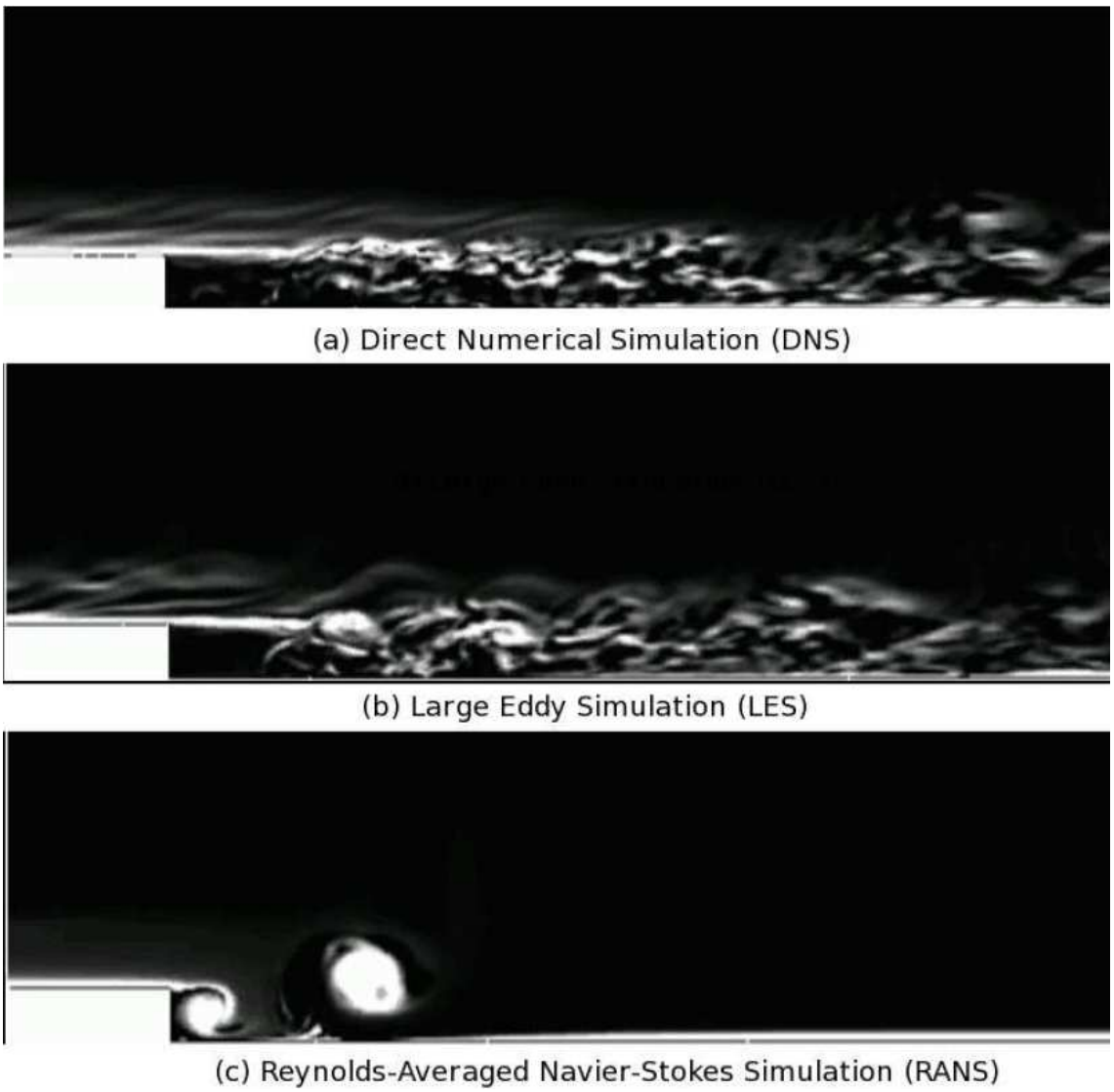

Figure 3.1: Flow over a back-ward facing step (spanwise vorticity) obtained from : (a) Direct Numerical Simulation (DNS), (b) Large-Eddy Simulation (LES) and (c) Reynolds-averaged Navier-Stokes Simulation (RANS). Figure is from Wu, Homsy & Moin: Gallery of Turbulent Flows, Center for Turbulence Research.

$$\frac{\partial \langle \rho \rangle}{\partial t} + \frac{\partial \langle \rho U_j \rangle}{\partial x_j} = \kappa \frac{\partial^2 \langle \rho \rangle}{\partial x_j \partial x_j} - \frac{\partial \chi_j^{SGS}}{\partial x_j}, \tag{3.11}$$

where $\langle U_i \rangle$ is the Cartesian components of the filtered velocity field, $\langle p \rangle$ is the filtered pressure, $\langle \rho \rangle$ is the filtered density, ρ_0 is the reference density, and τ_{ij}^{SGS} and χ_j^{SGS} are the subgrid scale (SGS) stress tensor and subgrid scalar flux vector, respectively, and are defined as

$$\tau_{ij}^{SGS} = \langle U_i U_j \rangle - \langle U_i \rangle \langle U_j \rangle , \tag{3.12}$$

$$\chi_j^{SGS} = \langle \rho U_j \rangle - \langle \rho \rangle \langle U_j \rangle . \tag{3.13}$$

The accuracy of LES models depends on the efficiency of the SGS closure model that is used to define the subgrid scale motions. FLOW-3D employs the well-known but simple LES model proposed by Smagorinsky (1963). This model uses a linear turbulent eddy viscosity, ν_t, to model the SGS motions as

$$\tau_{ij}^{SGS} = -2\nu_t \langle S_{ij} \rangle , \tag{3.14}$$

with the eddy viscosity defined as

$$\nu_t = (C_S \Delta)^2 \langle S \rangle = (C_S \Delta)^2 \sqrt{2 \langle S_{ij} \rangle \langle S_{ij} \rangle}, \tag{3.15}$$

where Δ is usually taken as the grid size, C_S is the Smagorinsky constant having a typical value in the range of 0.1 - 0.2, and $\langle S \rangle$ is the characteristic rate of strain. The turbulent Schmidt number $Sc_t = \nu_t / \Gamma_t$, where ν_t and Γ_t are the turbulent viscosity and diffusivity respectively, is kept at unity. This assumption is common in numerical studies of turbulent flows, and provides closure for the SGS scalar flux, χ_j^{SGS}.

3.3 Volume-of-Fluid (VOF) technique

An interface between a gas and liquid is often referred to as a free surface. The reason for the “free" designation arises from the large difference in the densities of the gas and liquid (e.g.

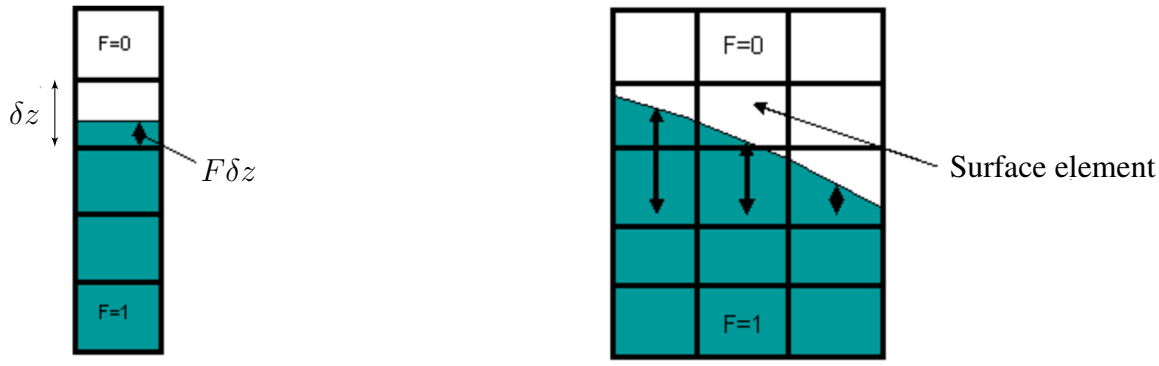

Figure 3.2: Locating the free surface using the VOF technique. Left panel: one-dimensional free surface. Right panel: two-dimensional free surface.

the ratio of density for water to air is about 1000). A low gas density means that its inertia can generally be ignored compared to that of the liquid. In this sense the liquid moves independently, or freely, with respect to the gas. The only influence of the gas is the pressure it exerts on the liquid surface. In other words, the gas-liquid interface is not constrained, but free.

Several types of numerical approaches have been used to model free surfaces, e.g. the Lagrangian grid method (Hirt *et al.* 1974, 1970), the surface height method (Nichols & Hirt 1971) and the marker-and-cell (MAC) method (Harlow & Welch 1965). FLOW-3D differs from other computational fluid dynamics code in its treatment of flows fluid surfaces. In FLOW-3D, free surfaces are modeled with the Volume-of-Fluid (VOF) technique that was first developed by a group of scientists, including Flow Science's founder, Dr. C. W. Hirt, at the Los Alamos National Laboratory. The idea for this approach originated as a way to have the powerful volume-tracking feature of the MAC method without its large memory and CPU costs. Within each grid cell (control volume) it is customary to retain only one value for each flow quantity (e.g. pressure, velocity, temperature, etc.). For this reason, it makes little sense to retain more information for locating a free surface. Following this reasoning, the use of a single quantity, the fluid volume fraction F in each grid cell, is consistent with the resolution of the other flow quantities. The VOF method in FLOW-3D possesses the three essential features needed to accurately model free surfaces:

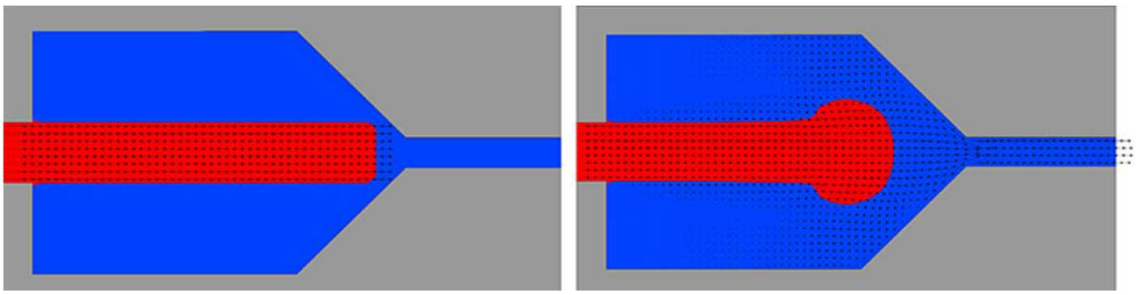

Figure 3.3: Comparison of VOF and Pseudo-VOF methods in modelling a jet of water issuing into air. Left panel: correct jet shape predicted by VOF technique in FLOW-3D. Right panel: Incorrect jet shape predicted by pseudo-VOF technique.

- *A scheme to describe the shape and location of a surface*. The fluid volume fraction function F represents the volume of fluid per unit volume. Therefore, fluid exists where $F = 1$, and void regions correspond to locations where $F = 0$. Any element having an F value lying between 0 and 1 must contain a surface. For accuracy purposes, it is desirable to have a way to locate a free surface within an element. In figure 3.2, we compute the exact location of the one-dimensional free surface as lying above the bottom edge of the surface element by a distance equal to F times the vertical size of the element, δz. For the two-dimensional free surface, the local height of the surface in the column containing the surface element gives the location of the surface in that element, while the other two heights can be used to compute the local surface slope and curvature. In three-dimensional flows (not shown), the same procedure is used although column heights must be evaluated for nine columns around the surface element, thus a little more computation is needed.

- *A means of applying boundary conditions at the surface*. Most pseudo-VOF methods use a fluid volume fraction to locate surfaces, but they then attempt to compute flow in both liquid and gas regions instead of accounting for the gas by a boundary condition. This practice produces an incorrect motion of the surface since it is assumed to move with the average velocity of gas and liquid. By contrast, the VOF method of FLOW-3D computes the two fluids as moving independently of one another except for a thin viscous boundary layer. In figure 3.3, imagine a jet of water issuing at a constant velocity from a long silt into air. If we

neglect gravity and keep the velocity of the jet low (say 0.1 m/s), we expect the jet to move more or less unimpeded by the air, as predicted by the VOF method. However, pseudo-VOF method produces a numerically induced growth at the tip of the jet.

- *An algorithm to evolve the surface shape and location with time*. Although the VOF technique can locate the free surfaces very well, the method is worthless unless an algorithm can be devised for accurately computing the evolution of the F field. The time dependence of F is governed by the equation:

$$\frac{\partial F}{\partial t} + \frac{\partial}{\partial x_j}\left(F u_j\right) = 0, \tag{3.16}$$

This equation states that F moves with the fluid. In a Lagrangian mesh, equation (3.16) reduces to the statement that F remains constant in each cell. In this case, F serves solely as a flag identifying cells that contain fluid. In an Lagrangian-Eulerian mesh, the flux of F moving with the fluid through a cell must be computed. The standard finite-difference approximations would lead to a smearing of the F function and interfaces would lose their definition. Fortunately, the fact that F is a step function with values of zero or one permits the use of a flux approximation that preserves its discontinuous nature (refer to Hirt & Nichols 1981 for details).

3.4 FAVOR$^{\mathrm{TM}}$ Technique

3.4.1 Geometrical Representation

Geometry is constructed in FLOW-3D by assembling solid geometric objects to define the flow region for a simulation. The flow geometry is then embedded in the computation grid by the preprocessor using a technique called $\mathrm{FAVOR}^{\mathrm{TM}}$, an acronym for Fractional Area/Volume Obstacle Representation. This method computes the open area functions on the cell faces (A_x,A_y,A_z) along with the open volume functions V_F, and reconstructs the geometry based on these parameters. This approach offers a simple and accurate way to represent complex surfaces in the domain without requiring a body-fitted grid.

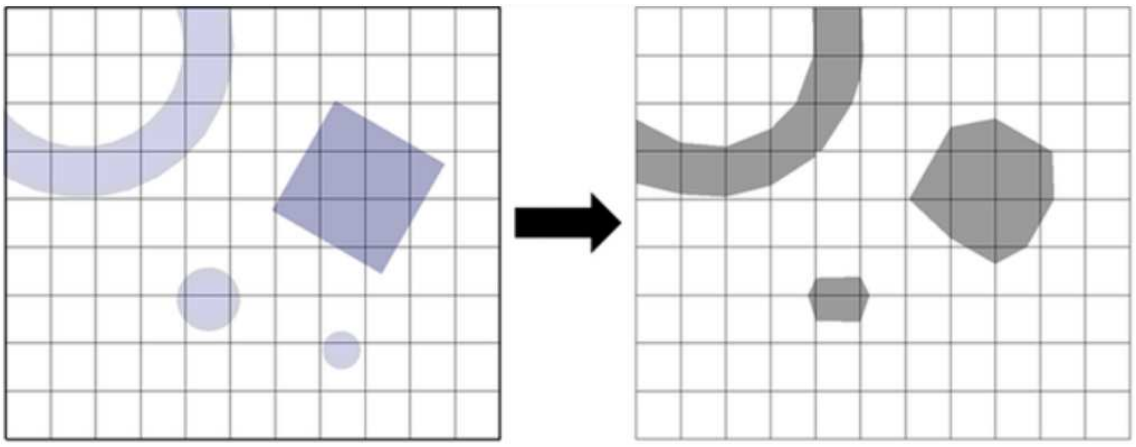

Figure 3.4: Geometrical representation using FAVOR$^{\mathrm{TM}}$. Left panel: object defined. Right panel: object represented.

FAVOR$^{\mathrm{TM}}$ is a very powerful method for incorporating geometry effects into the governing equations (see 3.4.2), but like all discrete methods, it is affected by the resolution of the computational grid. This is because the preprocessor generates area fractions for each cell face in the grid by determining which corners of the face are inside of a defined geometry. If all four corners of a cell face are inside the geometry, then the entire face is defined to be within the geometry. Similarly, if all corners lie outside, then the entire face is assumed to be outside the geometry. When some face corners are inside a geometry and some are outside, the intersection of the geometry with face edges are computed. Area fractions (A_x,A_y,A_z) are then computed from these intersection points assuming straight-line connections between intersection points within the face. The straight-line assumption introduces a small error in the fractional area when the geometry boundary is curved inside the cell. The approximation is consistent with the other assumptions in the development of the equations and improves as the grid resolution is refined. The implication of this construction is that features that are smaller than the cell size are not resolved. More specifically, any piece of a geometry that extends across a cell face but does not including a corner of that cell face is not recognized by the area fraction generator. For instance, a small spherical object (say smaller than a mesh cell) will not be recorded unless it covers at least one grid vertex, as illustrated by the circle

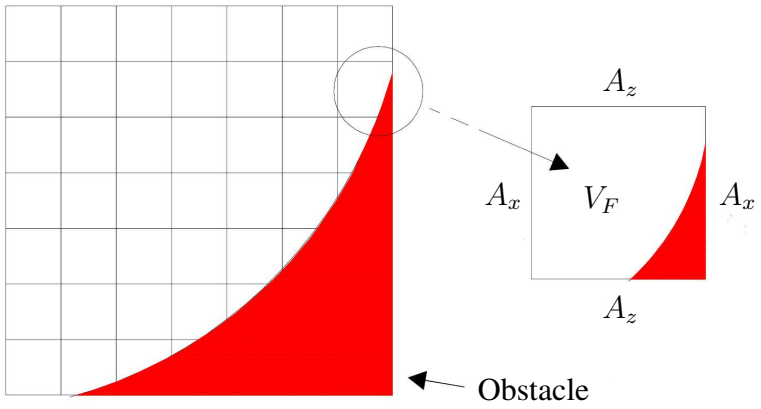

Figure 3.5: Definition of area/volume fractions in the x-z plane. V_F is the fractional volume open to flow, and A_x, A_y, A_z are the fractional areas open to flow.

in the lower right corner of the mesh shown in figure 3.4. The representation is improved as the mesh resolution is increased.

3.4.2 FAVOR$^{\text{TM}}$-modified Governing Equations

The governing equations formulated with the area and volume porosity functions based on the FAVOR$^{\text{TM}}$ technique are the real equations that the FLOW-3D solver is dealing with. Specifically, in figure 3.5, A_x, A_y and A_z are respectively the fractional areas open to flow in the x, y and z directions, and V_F is the fractional volume open to flow. The modified governing equations with the Boussinesq approximation (equations 3.4, 3.7, 3.8, and 3.16) are given by:

- Momentum equations

$$\frac{\partial u_i}{\partial t} + \left(\frac{1}{V_F}\right)\frac{\partial}{\partial x_j}\left(u_i u_j A_j\right) = -\frac{1}{\rho_0}\frac{\partial p}{\partial x_i} + \nu\frac{\partial^2 u_i}{\partial x_j \partial x_j} - \left(\frac{\rho}{\rho_0}\right) g\delta_{i3}, \tag{3.17}$$

- Continuity equation

$$\frac{\partial\left(u_i A_i\right)}{\partial x_i} = 0, \tag{3.18}$$

- Density transport equation

$$\frac{\partial \rho}{\partial t} + \left(\frac{1}{V_F}\right) \frac{\partial}{\partial x_j} \left(\rho u_j A_j\right) = \left(\frac{1}{V_F}\right) \kappa \frac{\partial^2 \rho A_j}{\partial x_j \partial x_j}, \tag{3.19}$$

- Fluid fraction transport equation

$$\frac{\partial F}{\partial t} + \left(\frac{1}{V_F}\right) \frac{\partial}{\partial x_j} \left(F u_j A_j\right) = 0. \tag{3.20}$$

Generally, the area and volume fractions are time independent. However, these quantities may vary with time when the moving obstacle model is employed.

3.5 Numerical Approximations

FLOW-3D numerically solves the equations described in the previous sections using finite-difference (or finite-volume) approximations. Fluid velocities and pressures are located at staggered mesh locations as shown for a typical cell in figure 3.6: velocities (u, v, w) and fractional areas (A_x, A_y, A_z) are located at the center of cell faces. Pressures (p), fluid fractions (F), fractional volumes (V_F), densities (ρ), internal energy (I), turbulence quantities for energy (q), dissipation (D), and viscosity (ν) are at cell centers.

The finite-difference notation used corresponds to that used in the code where fractional index values cannot be used. The convention is that all fractional indexes are decreased to the nearest whole integer. For example, the u velocity at $i + 1/2$ which is located on the cell face between cells (i, j, k) and $(i + 1, j, k)$ is denoted by $u^n_{i,j,k}$. A superscript n refers to the n-th time-step value.

3.5.1 Outline of Finite Difference Solution Method

The basic procedure for advancing a solution through one increment in time, δt, consists of three steps:

1. Explicit approximations of the momentum equations (3.17) are used to compute the first guess for new time-level velocities using the initial conditions or previous time-level values

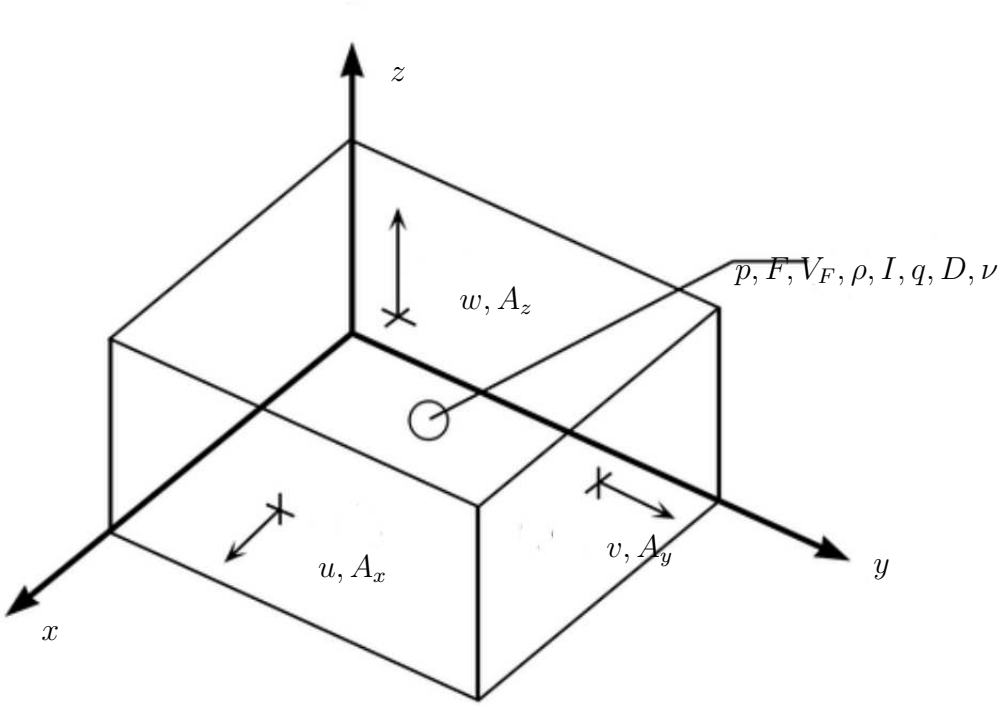

Figure 3.6: Location of variables in a mesh cell.

for all advective, pressure, and other accelerations. The density transport equation (3.19) is coupled with the momentum equations (3.17) through the buoyancy term.

2. To satisfy the continuity equation (3.18) when the implicit option is used, the pressures are iteratively adjusted in each cell and the velocity changes induced by each pressure change are added to the velocities computed in Step (1). An iteration is needed because the change in pressure needed in one cell will upset the balance in the six adjacent cells. In explicit calculations, an iteration may still be performed within each cell to satisfy the equation-of-state for compressible problems.

3. Finally, when there is a free-surface or fluid interface, it must be updated using equation (3.20) to give the new fluid configuration. Turbulence quantities and wall temperatures are also updated in this step.

3.5.2 Momentum Equation Approximations

A generic form for the finite-difference approximation of equation (3.17) is:

$$
\begin{aligned}
u_{i,j,k}^{n+1} &= u_{i,j,k}^{n} + \delta t^{n+1}\left[-\frac{p_{i+1,j,k}^{n+1} - p_{i,j,k}^{n+1}}{(\rho\delta x)_{i+1/2,j,k}^{n}} + G_x - \mathrm{FUX} - \mathrm{FUY} - \mathrm{FUZ} + \mathrm{VISX}\right], \\
v_{i,j,k}^{n+1} &= v_{i,j,k}^{n} + \delta t^{n+1}\left[-\frac{p_{i,j+1,k}^{n+1} - p_{i,j,k}^{n+1}}{(\rho\delta y)_{i,j+1/2,k}^{n}} + G_y - \mathrm{FVX} - \mathrm{FVY} - \mathrm{FVZ} + \mathrm{VISY}\right], \\
w_{i,j,k}^{n+1} &= w_{i,j,k}^{n} + \delta t^{n+1}\left[-\frac{p_{i,j,k+1}^{n+1} - p_{i,j,k}^{n+1}}{(\rho\delta z)_{i,j,k+1/2}^{n}} + G_z - \mathrm{FWX} - \mathrm{FWY} - \mathrm{FWZ} + \mathrm{VISZ}\right].
\end{aligned}
\tag{3.21}
$$

where, for example,

$$
(\rho\delta x)_{i+1/2,j,k}^{n} = \frac{\rho_{i,j,k}^{n}\delta x_i + \rho_{i+1,j,k}^{n}\delta x_{i+1}}{2}. \tag{3.22}
$$

The other right-hand-side terms have an obvious meaning, e.g. G_x is the gravitational acceleration, FUX means the advective flux of u in the x-direction, and VISX is the x-component viscous acceleration.

In FLOW-3D, there are three approximation schemes for the momentum equations, including first-order method, second-order method, and second-order monotonicity preserving method. A modified donor-cell approximation has been developed that retains its accuracy in a variable mesh and reduces to a conservative difference expression when the mesh is uniform. This method approximates advective fluxes in the non-conservative form, $u\nabla u$. The general form of this approximation for FUX is

$$
\mathrm{FUX} = \frac{0.5}{\mathrm{VFC}}\left[(\mathrm{UAR} - \alpha|\mathrm{UAR}|)\cdot\mathrm{DUDR} + (\mathrm{UAL} + \alpha|\mathrm{UAL}|)\cdot\mathrm{DUDL}\right], \tag{3.23}
$$

where

$$
\begin{aligned}
\mathrm{DUDL} &= \frac{u_{i,j,k} - u_{i-1,j,k}}{\delta x_i}, \\
\mathrm{DUDR} &= \frac{u_{i+1,j,k} - u_{i,j,k}}{\delta x_{i+1}}, \\
\mathrm{UAR} &= 0.5\left(u_{i+1,j,k}\mathrm{AFR}_{i+1,j,k} + u_{i,j,k}\mathrm{AFR}_{i,j,k}\right), \\
\mathrm{UAL} &= 0.5\left(u_{i,j,k}\mathrm{AFR}_{i,j,k} + u_{i-1,j,k}\mathrm{AFR}_{i-1,j,k}\right), \\
\mathrm{VFC} &= \frac{\delta x_i VF_{i,j,k} + \delta x_{i+1} VF_{i+1,j,k}}{\delta x_i + \delta x_{i+1}},
\end{aligned}
\tag{3.24}
$$

In these equations, fractional areas and volumes appear with the following notations:

$$
\begin{aligned}
&\mathrm{AFR}_{i,j,k} = \text{fractional area } A_x \text{ for flow in } x-\text{direction at } i+1/2 \text{ cell} - \text{face}, \\
&\mathrm{VF}_{i,j,k} = \text{fractional volume for flow at center of cell } (i,j,k).
\end{aligned}
\tag{3.25}
$$

If the mesh is uniform, this approximation reduces to a spatially second-order accurate, centered-difference approximation when $\alpha = 0$. When $\alpha = 1$, the first-order, donor-cell approximation is recovered. In either case, the method reduces to the correct zeroth order expression in a variable mesh. In a uniform mesh the advective flux approximations can be shown to reduce to a conservative approximation form ∇uu. The basic idea underlying equation (3.23) is to weight the upstream quantity being fluxed more than the downstream value. The weighting factors are $(1+\alpha)$ and $(1-\alpha)$ for the upstream and downstream directions, respectively. This type of first-order approximation scheme is used for all advective flux terms appearing in equations (3.21). All other acceleration terms in the momentum equations are approximated by standard centered differences.

3.5.2.1 First-order Method

The simplest FLOW-3D finite-difference approximation is first-order accurate in both space and time increments. In this case the advective and viscous terms are all evaluated using old-time level (n) values for velocities. Because the pressures at time level $n+1$ are generally unknown at the beginning of the cycle, these equations cannot be used directly to evaluate the $n+1$ level velocities but must be combined with the continuity equation. In the first step of a solution, the p^{n+1} values in these equations are replaced by p^n values to get a first guess for the new velocities. In

an explicit approximation the pressure gradient in equations (3.21) is evaluated at time n, therefore further adjustment to p does not influence the evaluation of u^{n+1}.

3.5.2.2 Second-order Method

Two optional second-order approximation schemes for the momentum equations can be requested through the input data. The essence of the first scheme is a double pass through the advection and viscous subroutines. In the first pass, the first-order method is used with the donor cell parameter $\alpha = 1$. These new velocities are then stored in the arrays for the previous time velocities. The first-order calculations are then repeated, but this time the parameter is set to $\alpha = -1$. Finally, the results of the two calculations are averaged to give the desired second-order approximation to the new time-level velocities. These approximations are second-order in time because the first pass uses time-n velocities, while the second pass uses (first-order) approximations for velocities at time $n+1$. The average then has level $n+1/2$, which is second-order in δt. Likewise, using $\alpha = 1$ in the first pass and $\alpha = -1$ in the second results in an average α-value of zero, which is second-order in δx, δy and δz if the mesh is uniform.

This algorithm is the least numerically diffusive of the three advection methods available in FLOW-3D. However, it does not possess the transportive property, which in standard upstream differencing schemes ensures that a flow disturbance only propagates downstream from its initial location. In addition, this method is the most CPU intensive. Finally, this method may occasionally generate a numerically unstable solution for flows with transient free-surfaces.

3.5.2.3 Second-order Monotonicity Preserving Method

The other higher-order advection algorithm in FLOW-3D is based on a second-order, monotonicity-preserving upwind-difference method (van Leer 1977). It is as robust as the original first-order advection scheme. It requires slightly more CPU time than the first-order method, although in most cases the difference is insignificant. This method may be applied in FLOW-3D to approximate momentum advection, as well as density, energy and fluid fraction advection. The higher-order discretization scheme is derived by using second-order polynomial approximations to the advected

quantity in each of the coordinate directions. For a variable Q advected in the x-direction, the value fluxed through a cell-face, Q^*, is computed as

$$Q^* = Q_i + \frac{1}{2} A \left(1 - C\right) \delta x_i, \tag{3.26}$$

where Q_i is the cell-centered value, C is the Courant number, δx_i is the cell size, and A is a second-order approximation to the first derivative of Q at the location

$$x_0 = \frac{1}{6} \left(1 - 2C\right) \delta x_i, \tag{3.27}$$

within the cell. Coefficient A can easily be computed from two neighboring first derivatives by linear interpolation, provided these derivatives are second-order accurate. The latter can be achieved by computing the derivatives at the midpoints between Q_i locations. For example,

$$\frac{\mathrm{d}Q}{\mathrm{d}x_{i+1/2}} = 2 \cdot \frac{Q_{i+1} - Q_i}{\delta x_{i+1} + \delta x_i} \tag{3.28}$$

is a second-order accurate first derivative of Q at the point between Q_i and Q_{i+1}.

To ensure monotonicity, it is necessary to restrict the value of A. According to van Leer (1977), the value of A is not allowed to exceed twice the minimum magnitude of the centered Q derivatives used in its computation:

$$A \leq 2 \min \left(\frac{\mathrm{d}Q}{\mathrm{d}x_i}, \frac{\mathrm{d}Q}{\mathrm{d}x_{i+1}} \right). \tag{3.29}$$

Furthermore, if Q_i is a local minimum or maximum value, i.e., if the two centered derivatives appearing in equation (3.29) are of opposite sign, then A is set to zero and the donor-cell approximation is used.

3.5.3 Pressure Solution Algorithm

Equations (3.17) and (3.18) are coupled to each other, hence iteration solution procedures are needed to solve them. They can be equivalently cast into the following discretized form using the

global cell indices in the FORTRAN subroutines and functions:

$$\begin{aligned}
&\frac{u^*_{ijk}-u^n_{ijk}}{\delta t} = -\left(\mathrm{FUX}+\mathrm{FUY}+\mathrm{FUZ}\right)^n_{ijk} - \frac{1}{\rho}\frac{p^n_{ipjk}-p^n_{ijk}}{\delta x} \\
&-\nu\left[\frac{u^{*/n}_{ipjk}-2u^{*/n}_{ijk}+u^{*/n}_{imjk}}{\delta x^2}+\frac{u^{*/n}_{ijpk}-2u^{*/n}_{ijk}+u^{*/n}_{ijmk}}{\delta y^2}+\frac{u^{*/n}_{ijkp}-2u^{*/n}_{ijk}+u^{*/n}_{ijkm}}{\delta z^2}\right]+\mathrm{FX}^n_{ijk}, \\
&\frac{v^*_{ijk}-v^n_{ijk}}{\delta t} = -\left(\mathrm{FVX}+\mathrm{FVY}+\mathrm{FVZ}\right)^n_{ijk} - \frac{1}{\rho}\frac{p^n_{ijpk}-p^n_{ijk}}{\delta y} \\
&-\nu\left[\frac{v^{*/n}_{ipjk}-2v^{*/n}_{ijk}+v^{*/n}_{imjk}}{\delta x^2}+\frac{v^{*/n}_{ijpk}-2v^{*/n}_{ijk}+v^{*/n}_{ijmk}}{\delta y^2}+\frac{v^{*/n}_{ijkp}-2v^{*/n}_{ijk}+v^{*/n}_{ijkm}}{\delta z^2}\right]+\mathrm{FY}^n_{ijk}, \\
&\frac{w^*_{ijk}-w^n_{ijk}}{\delta t} = -\left(\mathrm{FWX}+\mathrm{FWY}+\mathrm{FWZ}\right)^n_{ijk} - \frac{1}{\rho}\frac{p^n_{ijkp}-p^n_{ijk}}{\delta z} \\
&-\nu\left[\frac{w^{*/n}_{ipjk}-2w^{*/n}_{ijk}+w^{*/n}_{imjk}}{\delta x^2}+\frac{w^{*/n}_{ijpk}-2w^{*/n}_{ijk}+w^{*/n}_{ijmk}}{\delta y^2}+\frac{w^{*/n}_{ijkp}-2w^{*/n}_{ijk}+w^{*/n}_{ijkm}}{\delta z^2}\right]+\mathrm{FZ}^n_{ijk}.
\end{aligned} \tag{3.30}$$

$$\begin{aligned}
\frac{u^{n+1}_{ijk}-u^*_{ijk}}{\delta t} &= -\frac{1}{\rho}\frac{p'_{ipjk}-p'_{ijk}}{\delta x}, \\
\frac{v^{n+1}_{ijk}-v^*_{ijk}}{\delta t} &= -\frac{1}{\rho}\frac{p'_{ijpk}-p'_{ijk}}{\delta y}, \\
\frac{w^{n+1}_{ijk}-w^*_{ijk}}{\delta t} &= -\frac{1}{\rho}\frac{p'_{ijkp}-p'_{ijk}}{\delta z},
\end{aligned} \tag{3.31}$$

where i, j and k are cell indices in x, y and z directions respectively; $imjk$, $ipjk$, $ijmk$, $ijpk$, $ijkm$ and $ijkp$ are the global indices of the cell to left, right, front, back, bottom and top of cell ijk, respectively; FX, FY and FZ include all the force terms; the superscript $*/n$ indicates the related terms can be treated either implicitly or explicitly; p' is equal to $p^{n+1}-p^n$ and represents pressure change in the cell. Equations (3.30) are solved for velocities u^*, v^* and w^* which are called intermediate velocities. Substituting equations (3.31) into equation (3.18) yields the following equation for pressure change:

$$\nabla\cdot U^* - \frac{\delta t}{\rho}\nabla^2 p' = 0, \tag{3.32}$$

where U^* is intermediate velocity vector with components defined by u^*, v^* and w^*. Equation (3.32) is then solved by the general minimum residual method (GMRES). It is an iterative method designed to solve nonsymmetric linear systems due to its high accuracy, rapid convergence and

parallel efficiency (Yao 2004). The method approximates the solution by the vector in a Krylov subspace with minimal residual. The Arnoldi iteration is used to find this vector. Detailed information can be found in Ashby *et al.* (1990).

3.5.4 Stability Considerations

Time steps must satisfy the following criteria:

- Fluid must not be permitted to flow across more than one computational cell in one time step. This advective transport depends not only on the velocity but also on the fractional area/volume open to flow. The basic stability condition is

$$\delta t < \mathrm{CON} \cdot \min\left(\frac{V_F \delta x_i}{A_x u}, \frac{V_F \delta y_j}{A_y v}, \frac{V_F \delta z_k}{A_z w}\right), \tag{3.33}$$

  where the stability factor CON is typically set to 0.45 to account for “worst case" situations suggested by a simplified stability analysis.

- The time step size stability condition is associated with the propagation of surface waves. The actual condition is that surface waves should not propagate more than one cell in one time step. For example, if z is the normal direction to the surface and G_z is the acceleration in z direction, then

$$\delta t < \frac{\sqrt{V_F}}{\sqrt{2G_z \delta z_k \left[\frac{A_x}{\delta x_i^2}\max\left(1, \frac{\delta x_i}{\delta z_k}\right) + \frac{A_y}{\delta y_j^2}\max\left(1, \frac{\delta y_j}{\delta z_k}\right)\right]}}. \tag{3.34}$$

  The $\max$ operator in the denominator signifies the distinction between shallow (=1) and deep water ($= \delta x/\delta z$) wave speed. Similar limits must be imposed in the x and y directions for each cell containing a free-surface.

- A linear analysis indicates that the time step must be further limited when a non-zero value of dynamic viscosity is used. This condition is

$$\delta t = \frac{0.25}{\max\left[\mathrm{RM} \cdot \frac{\mu}{\rho}\left(\frac{1}{\delta x_i^2} + \frac{1}{\delta y_j^2} + \frac{1}{\delta z_k^2}\right)\right]}, \tag{3.35}$$

where RM is the maximum multiplier used on μ for all types of diffusional processes. The restriction physically means that no quantity should diffuse more than approximately one mesh cell in one time step. For safety, an extra factor of 0.5 has been incorporated in the right side of equation (3.35) because the limit is otherwise marginal.

- One more parameter controls the relative amounts of donor-cell and centered differencing used for the momentum advection terms shown in equation 3.23. When $\alpha = 1$ is used, the above stability conditions are sufficient. Generally, one should always use a value for α such that

$$\delta t \cdot \max\left(\frac{|u|}{\delta x_i}, \frac{|v|}{\delta y_j}, \frac{|w|}{\delta z_k}\right) < \alpha \leq 1. \tag{3.36}$$

  For instance, if condition of (3.33) is satisfied, then we have have $\alpha > \mathrm{CON}$.

Chapter 4

Constant-density Flow Interacting with a Suspended Cylindrical Canopy Patch[1]

4.1 Introduction

Canopies are essentially porous obstructions consisting of distributed drag elements that cause a partial blockage against the incoming flows. Circular cylinders are often used to model the constituent obstacles due to shape similarity and well-known flow responses (Zdravkovich 1997). The literature on flows past an infinite canopy is extensive (e.g. Nepf 2012, and references therein). However, finite canopy patches with smaller length and width scales than the flow, albeit more commonly seen in both natural and industry, have received much less attention. Typical examples include vegetation patches in river flows (Chen *et al.* 2012), arrays of wind turbines in the atmospheric boundary layer (Kinzel *et al.* 2015) and aquaculture structures in ocean currents (Venayagamoorthy *et al.* 2011). Some examples are shown in figure 4.1.

Depending on their positioning in the water column, canopy patches are classified into emergent patches occupying the whole flow depth and partial-depth patches (bottom-mounted or surface-suspended). The key finding pertaining to emergent canopies is that directly downstream of the patch there is a longitudinally-uniform steady wake region sandwiched by the shear layers at the sides. The steady wake is stabilized by the streamwise bleeding flow through the patch whose strength diminishes with increasing patch density, which has been well documented by a series of studies (Nicolle & Eames 2011; Chen *et al.* 2012; Zong & Nepf 2012; Chang & Constantinescu 2015). The flow can be considered as predominantly two-dimensional with minor variation of

[1]The research presented in this chapter will be submitted in substantial part to *Journal of Fluid Mechanics* under the title "Near-field hydrodynamics of a suspended cylindrical canopy patch" by J. Zhou and S. K. Venayagamoorthy. Background information and literature relevant to this chapter are presented again so the chapter may be read as a stand-alone work. The chapter is written in a collective "we" voice to acknowledge collaboration with the co-author.

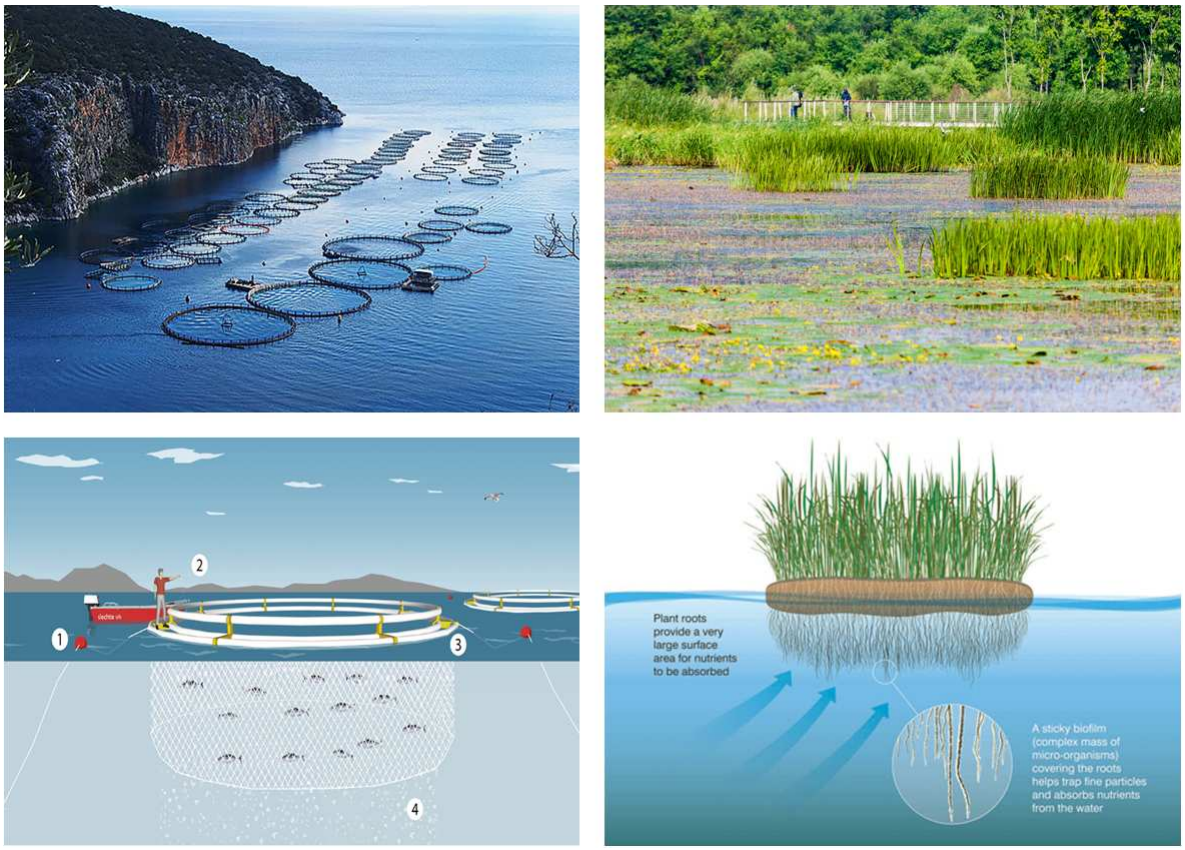

Figure 4.1: Examples of suspended finite canopies. Left panels: marine aquaculture farms. Right panels: floating aquatic vegetations.

the mean flow along the vertical direction. As a result, the planar cylinder configuration uniquely dictates the flow structure.

For partial-depth canopy patches, however, it is conceivable that the vertical dimension of the patch is no longer irrelevant due to its capacity in modifying the three-dimensional features caused by the patch free end as in the case of a solid cylinder (Sumner 2013). Instead, the patch density ϕ and the patch aspect ratio $AR = h/D$ as defined in figure 4.2 are both important (for the convenience of discussion, the patch width is fixed at D in this paper thus $AR \propto h$). The field study of Plew *et al.* (2006) suggested that AR tends to affect the flow diversion either horizontally around or vertically beneath the patch. Taddei *et al.* (2016) and Tseung *et al.* (2016) considered canopy patches with constant AR values and observed that flow bleeding along the vertical/streamwise direction increases/decreases with increasing ϕ. Qiao *et al.* (2016) varied the AR of a spanwise

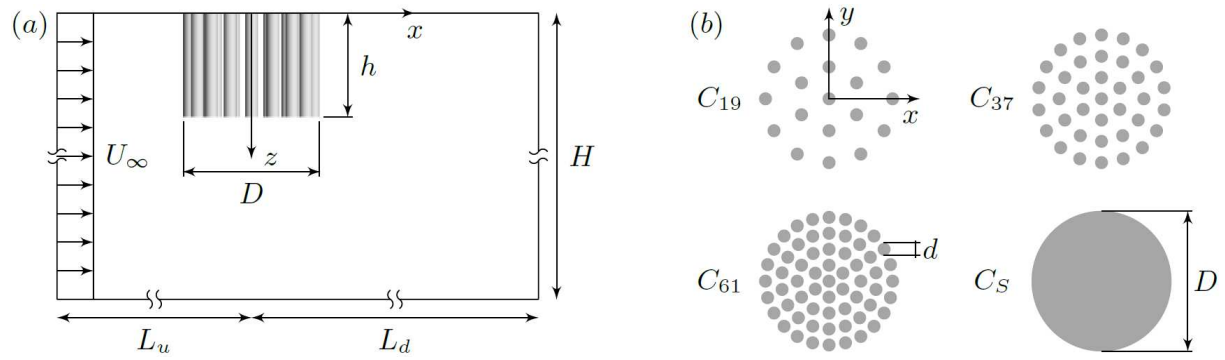

Figure 4.2: (a) Sketch of the computational domain (side view, not to scale). The suspended patch (diameter, D, and height, h) extends downwards from the domain top boundary in a deep water with a depth of H, i.e. $H/h \gg 1$. The origin of the coordinate system is located at the center of the patch top surface, and z is pointing downwards. The domain width (out-of-plane) is $B = 11D$. The distances from the patch center to the upstream and downstream domain extremities are $L_u = 9D$ and $L_d = 45D$, respectively. (b) Plan view of cylinder configurations (C_{19}: $\phi = 0.16$, C_{37}: $\phi = 0.31$, C_{61}: $\phi = 0.50$, C_S: $\phi = 1$).

suspended linear cylinder array with a constant ϕ. Nevertheless, at a fundamental level, it remains unclear what is the complete picture of the interlinks between patch geometry (ϕ and AR), flow bleeding and flow diversion in the vicinity of the patch, which is the focus of this paper. It is noteworthy that the effect of patch aspect ratio AR (varying patch height h at a constant flow depth H) and the effect of submergence ratio H/h (varying H at a constant h) are dynamically different. Therefore, the results of most existing water-flume experimental studies where only H is varied (Nepf & Vivoni 2000; Hamed *et al.* 2017) cannot be applied to predicting the effect of AR.

In this paper, we present results from numerical simulations of a uniform incident flow impinging on a cylindrical canopy patch suspended in deep water. The aim is to systematically investigate the influence of ϕ and AR on the three-dimensional mean hydrodynamics in the vicinity of the patch that is missing in the literature.

4.2 Simulation Setup

The numerical model is validated using a Cartesian mesh with a resolution of $0.125d$ throughout the near-wake region. Firstly, the canonical case of flow past an infinitely-long solid circular cylinder at $Re_d = 1000$ was simulated. The mean drag coefficient predicted by the present LES is $C_D = 1.01$ (figure 4.3a) which agrees well with the value of 1 reported in experiments

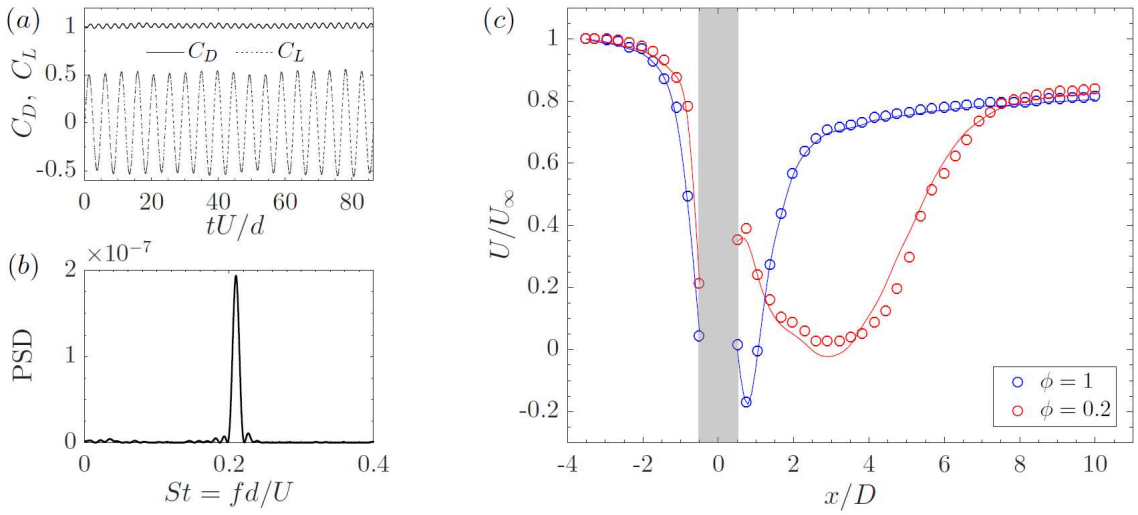

Figure 4.3: Model validation. Left panel (an infinitely-long solid circular cylinder with diameter d at $Re_d = 1000$): (a) time history of the drag and lift coefficients; (b) power density spectrum of the lift coefficient. Right panel (a solid patch with $\phi = 1$ and a porous patch with $\phi = 0.2$, both are emergent): (c) longitudinal profiles of mean streamwise velocity along the patch centerline ($y = 0$). Symbols indicate results from the present LES, and lines represent the data from Chang & Constantinescu (2015). The shaded region depicts the streamwise extent of the patch ($-0.5D \leq x \leq 0.5D$).

(Zdravkovich 1997). The Strouhal number was observed to be $St = 0.209$ (figure 4.3b where f is the vortex shedding frequency), which is also very close to the experimental measurements of 0.21 (Zdravkovich 1997). Secondly, two simulations of flow impinging on an emergent canopy patch having the same cylinder configurations with those in Chang & Constantinescu (2015) were conducted ($d = D/10.4$ and $Re_d = 960$). The agreement in the centerline streamwise velocity is quite good (figure 4.3c). For the porous patch ($\phi = 0.2$), the steady-wake velocity is a little overpredicted which produces a slightly longer steady-wake region.

The main geometrical and flow parameters investigated in this study are shown in figure 4.2. A uniform incident velocity U_∞ was prescribed at the inlet, and a convective boundary condition was used at the outlet. The domain top boundary was modeled as a free-slip rigid lid that coincides with the patch top surface. The patch is suspended in a very large domain ($L = L_u + L_d = 54D$, $B = 11D$ and $H = 9D \sim 36D$ depending on AR). All the solid surfaces were treated as no-slip walls. The patch consists of N_c individual solid cylinders of diameter $d = D/11$, resulting in a patch density of $\phi = N_c(d/D)^2$. All the LES runs were performed with $Re_d = 1000$ and

$Re_D = 11000$. Four patch densities $\phi = N_c(d/D)^2$ were considered (three porous patches plus a limiting case of solid patch). For each ϕ, h was varied to give four patch aspect ratios ($AR = h/D$) as 0.25, 0.50, 0.75 and 1.00 (16 simulations in total). The same mesh resolution as in the model validation was used throughout. After the solution became statistically steady, time-averaging were performed over an interval corresponding to approximately $20D/U_\infty$. In this paper, the mean velocities in the x, y and z directions are denoted as U, V and W, respectively.

4.3 Results and Discussion

4.3.1 Wake Structure

As an overview, we show the instantaneous downstream wake structure in figure 4.4. In the steady wake region, the separated shear layers (SSLs) at the sides and bottom surface of the patch keep growing until they merge at some distance downstream, after which the flow starts to recover to the undisturbed condition. Different with the emergent patches which are predominantly 2-D, the wake length of a suspended patch is shorter at x-y planes closer to the patch free end due to stronger interaction of the SSLs. For this rather dense patch in figure 4.4, the signatures of individual cylinder wakes almost disappear, while the patch-scale vortex shedding is inhibited by the interference of the bottom SSL. This is consistent with previous studies of solid cylinder with a free end (Sumner 2013) since a patch aspect ratio of 0.50 (and actually the whole range of AR investigated in this paper) is way below the critical AR beyond which the von Karman vortex street would appear.

Figure 4.5 shows the effect of array geometry on the streamwise extent of the downstream wake. For a constant $AR = 0.5$ (figure 4.5a), the strength of streamwise bleeding through the patch dictates the wake length: the velocity field behind denser patches recover faster towards the undisturbed free-stream condition due to the weaker stabilizing base bleed. On the other hand, for a constant $\phi = 0.5$ (figure 4.5b), the wake length increases with increasing AR. The reason is two-fold: (i) the effect of bottom SSL is weaker for taller patches along their heights; and (ii) as will be discussed soon below, the increasing vertical bleeding for taller patches pushes the bottom

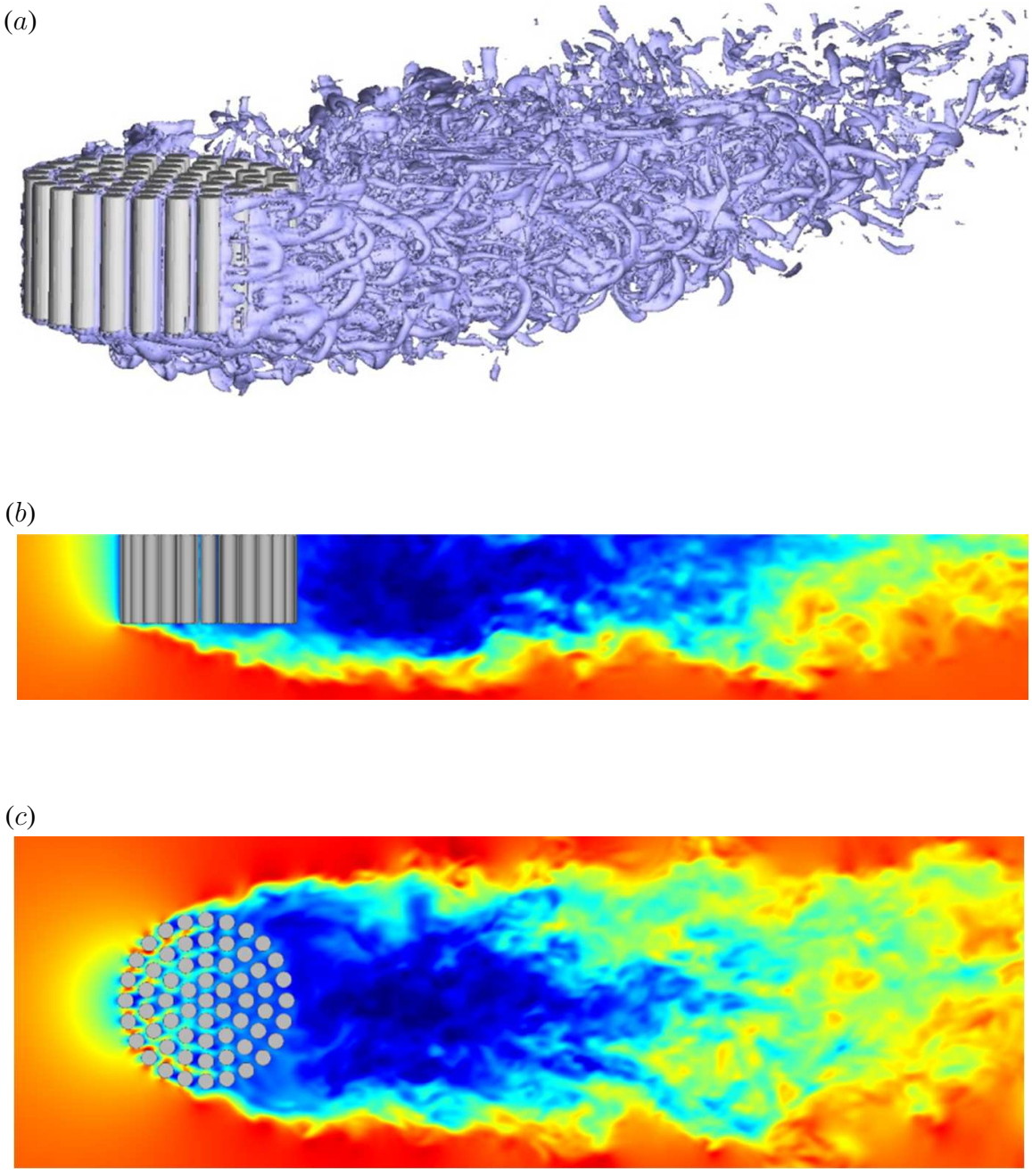

Figure 4.4: Instantaneous flow structures in case $C_{61}AR_{0.50}$. (a) Visualization of the vortex structures using the Q-criterion. (b) Contours of U/U_∞ along the x-z plane at $y = 0$. (c) Contours of U/U_∞ along the x-y plane at $z = h/2$.

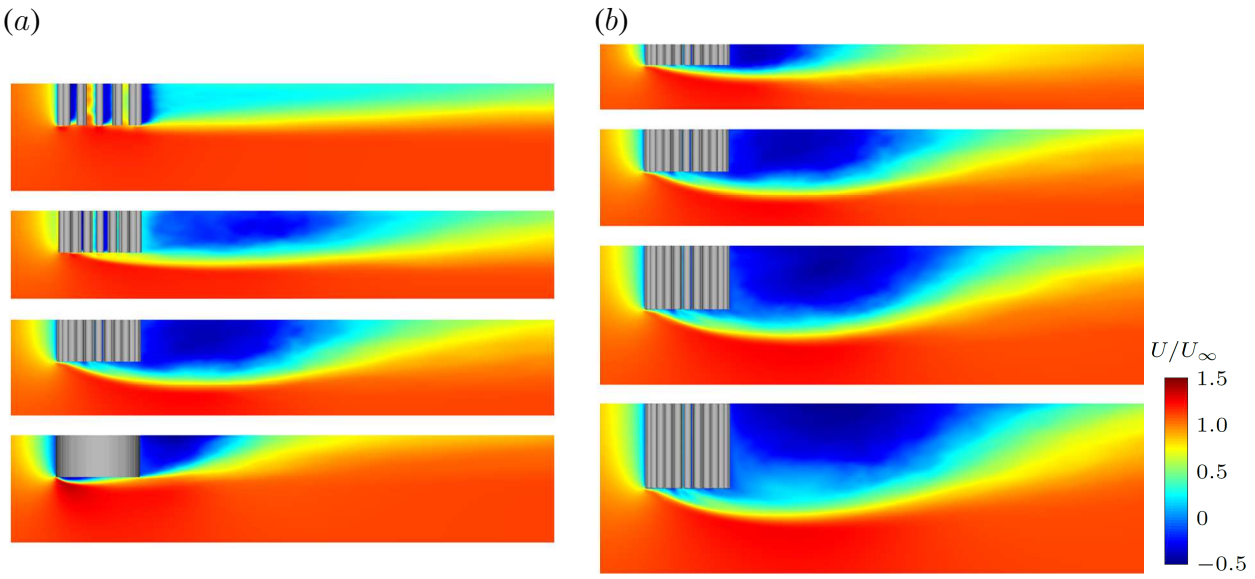

Figure 4.5: Contours of U/U_∞ in the x-z plane at $y = 0$ showing the streamwise extent of the downstream wake. (a) Effect of ϕ. (b) Effect of AR.

SSL downwards, resulting in a even weaker interaction between the lateral and bottom SSLs and thus a longer wake region.

From now on, we focus on the mean flows in the near field of the patch. Figure 4.6 shows the effect of patch density on flow bleeding. For the porous patches, an increase in ϕ leads to weaker streamwise bleeding but stronger vertical and lateral bleeding. As discovered in studies of emergent patches (e.g. Zong & Nepf 2012), the reduced streamwise bleeding contributes to shortening the total wake length, and this is not further discussed in this paper. Vertical bleeding perpendicular to the patch bottom surface pushes the bottom SSL downwards and thus enlarges the vertical size of the near-wake, which is consistent with Taddei *et al.* (2016). Similarly, the lateral bleeding pushes the lateral SSLs to the sides and thus widens the wake, despite the fact that the point of flow separation is fixed at the cylinders situated near the patch lateral extremities. As expected, flow bleeding is completely blocked in the solid-patch case, resulting in a wake region of the smallest height and width.

The patch aspect ratio is found to be another important parameter that influences flow bleeding. As shown in figure 4.7(a), vertical bleeding increases with increasing AR, which effectively presents to the flow as an even taller patch than the actual increase of patch height. There is also

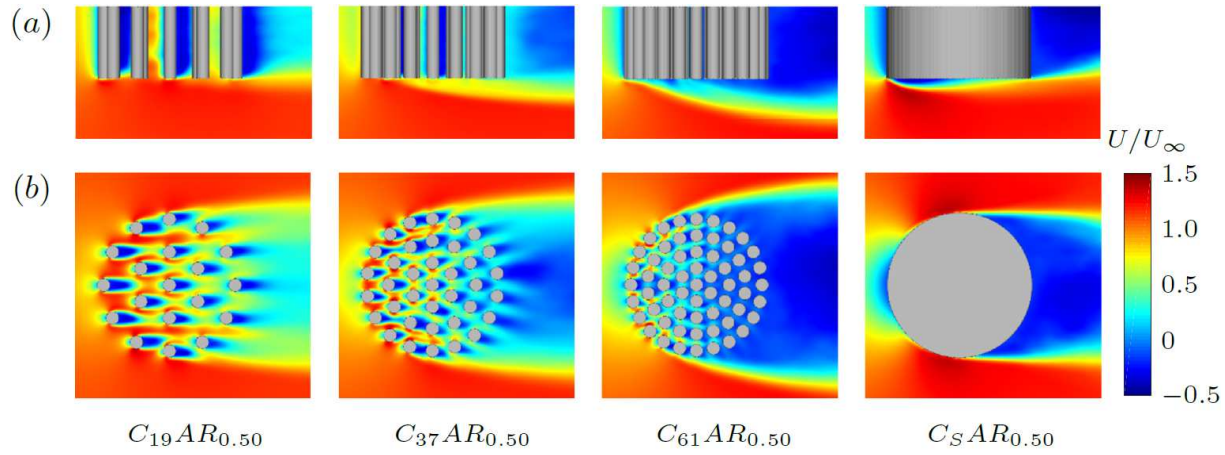

Figure 4.6: Contours of U/U_∞ showing the effect of patch density on flow bleeding. (a) x-z plane at $y = 0$. (b) x-y plane at $z = h/2$.

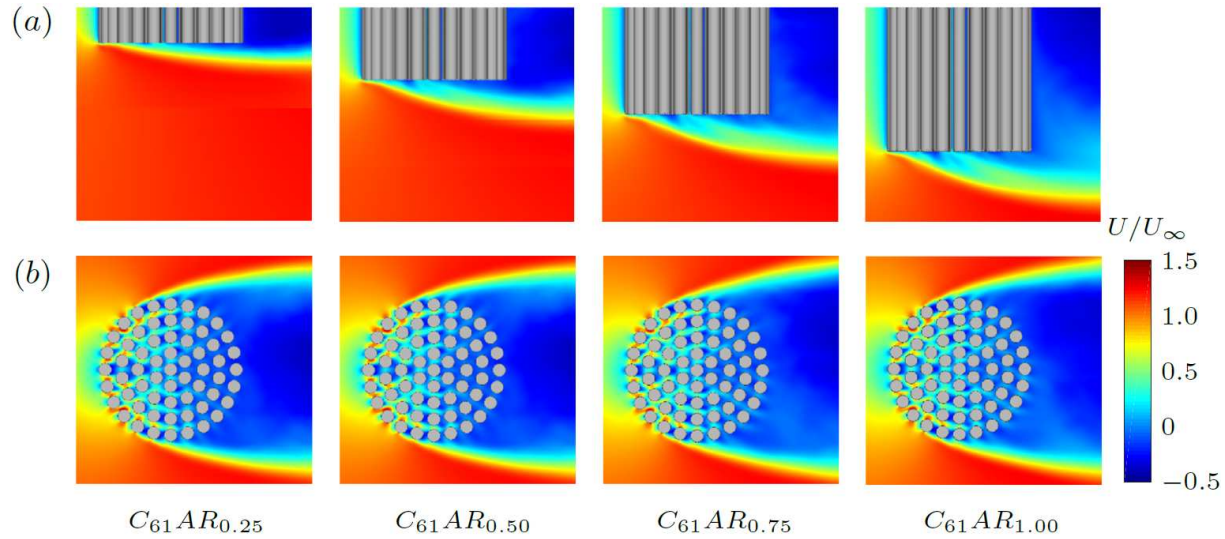

Figure 4.7: Contours of U/U_∞ showing the effect of patch aspect ratio on flow bleeding. (a) x-z plane at $y = 0$. (b) x-y plane at $z = h/2$.

a slight strengthening of the lateral bleeding as AR increases in figure 4.7(b). The streamwise bleeding shows a visually weak dependence on AR.

4.3.2 Vertical Bleeding Inside the Patch

We provide here an explanation for the observed dependence of vertical bleeding on ϕ and AR in §4.3.1. In figure 4.8(a), starting from the patch top surface ($z = 0$) and downwards, the mean vertical bleeding velocity W is horizontally averaged inside the patch at every vertical location.

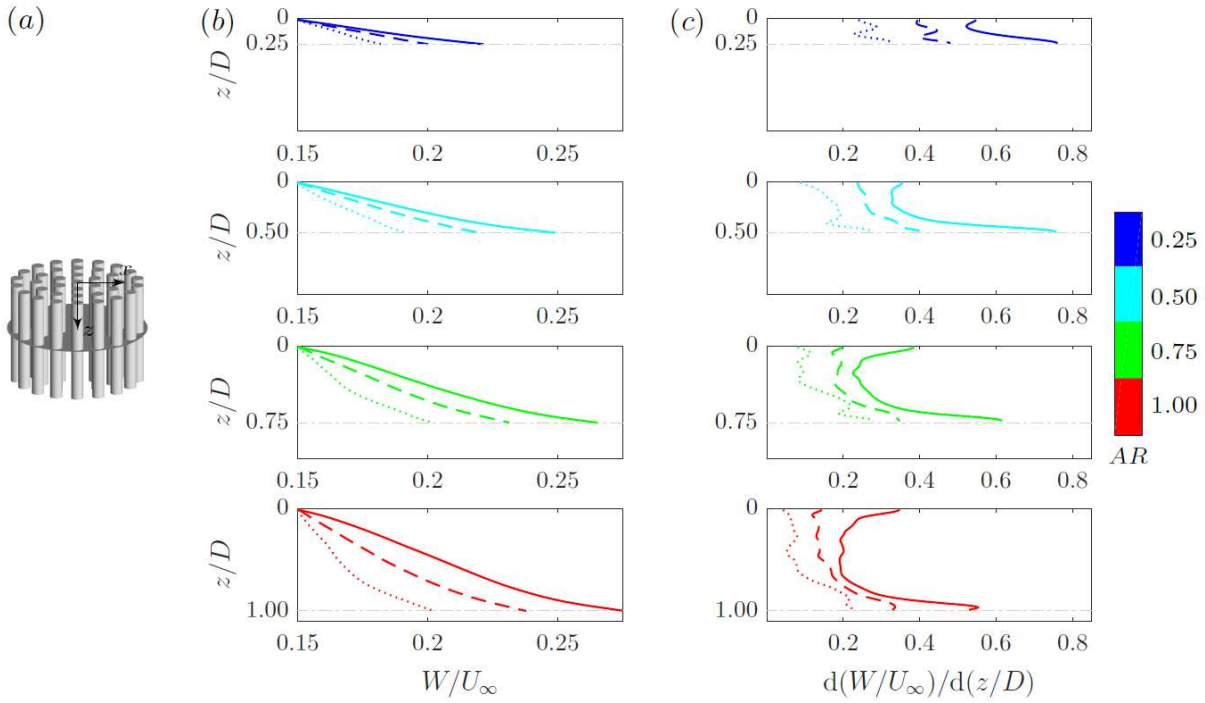

Figure 4.8: (a) Sketch showing the vertically moving x-y planes (dark gray) used for horizontally averaging vertical bleeding velocity W inside the patch. (b) Vertical profiles of W/U_∞. (c) Vertical profiles of $\mathrm{d}(W/U_\infty)/\mathrm{d}(z/D)$. In each plot, the horizontal gray line marks the location of patch bottom surface. The three patch densities are denoted respectively as C_{19} (·····), C_{37} (- - -) and C_{61} (——).

The general varying trend of W with z in figure 4.8(b) is being zero at the impermeable top surface and increasing monotonically towards the patch bottom surface. The vertical gradient of vertical bleeding velocity, $\mathrm{d}(W/U_\infty)/\mathrm{d}(z/D)$, however, exhibits a non-monotonical variation with z. On one hand, it is non-zero at $z = 0$ and decreases downwards due to the gradually attenuated top boundary effect. On the other hand, when approaching the patch free end, there is a significant increase of $\mathrm{d}(W/U_\infty)/\mathrm{d}(z/D)$ because of the abrupt expansion of cross-section below $z = h$. As a result, except for the shortest patches with $AR = 0.25$, an intermediate equilibrium region is observed where the vertical bleeding is almost uniformly accelerating with respect to z, i.e. $\mathrm{d}(W/U_\infty)/\mathrm{d}(z/D)$ is constant.

At a fixed AR, since the cylinder arrangement is heavily staggered in the horizontal directions and aligned in the vertical direction as seen by the flow (figure 4.2b), the variation of ϕ modifies the canopy resistance along different directions to different degrees (Zhou *et al.* 2017). There is a growing priority for the flow entering the patch to be vertically diverted as ϕ increases. As a result,

a denser patch is accompanied by a overall faster acceleration of vertical motions with respect to z (i.e. larger $\mathrm{d}(W/U_\infty)/\mathrm{d}(z/D)$) over the same vertical distance of h, resulting in stronger vertical bleeding through the patch bottom surface.

Although a larger AR also leads to stronger vertical bleeding at the patch bottom surface (figure 4.7a), the way how it is achieved is different. As AR increases while keeping ϕ constant, the effect of cross section expansion below $z = h$ that tends to speed up the vertical motions inside the patch becomes less prominent due to the enlarged patch height, i.e. smaller overall $\mathrm{d}(W/U_\infty)/\mathrm{d}(z/D)$. However, the flow entering the patch has to travel a longer distance (h) to bleed out of its bottom surface, during which the accumulative accelerating effect of the albeit smaller $\mathrm{d}(W/U_\infty)/\mathrm{d}(z/D)$ eventually result in a stronger vertical bleeding at $z = h$.

4.3.3 Quantitative Evaluation of Bleeding Flow Through the Patch Surface

To quantitatively evaluate the bleeding flow along different directions, we created a non-intrusive control volume closely following the patch outer surface as shown in figure 4.9. The total inflow rate entering the patch is defined by

$$Q_{\text{inflow}} = \iint_{S_{l1},S_{l4}} U\boldsymbol{i} \cdot \mathrm{d}\boldsymbol{S}. \tag{4.1}$$

This must be equal to the total ourflow rate leaving the patch surface,

$$Q_{\text{outflow}} = Q_{Bx} + Q_{By} + Q_{Bz}, \tag{4.2}$$

where

$$Q_{Bx} = \iint_{S_{l2},S_{l3}} U\boldsymbol{i} \cdot \mathrm{d}\boldsymbol{S}, \quad Q_{By} = \iint_{S_{l1},S_{l2},S_{l3},S_{l4}} V\boldsymbol{j} \cdot \mathrm{d}\boldsymbol{S}, \quad Q_{Bz} = \iint_{S_b} W\boldsymbol{k} \cdot \mathrm{d}\boldsymbol{S} \tag{4.3}$$

are referred to as the streamwise, lateral and vertical bleeding flow rate, respectively. In these expressions, $\mathrm{d}\boldsymbol{S}$ is the unit normal vector of the surface of the control volume, and $(\boldsymbol{i}, \boldsymbol{j}, \boldsymbol{k})$ are

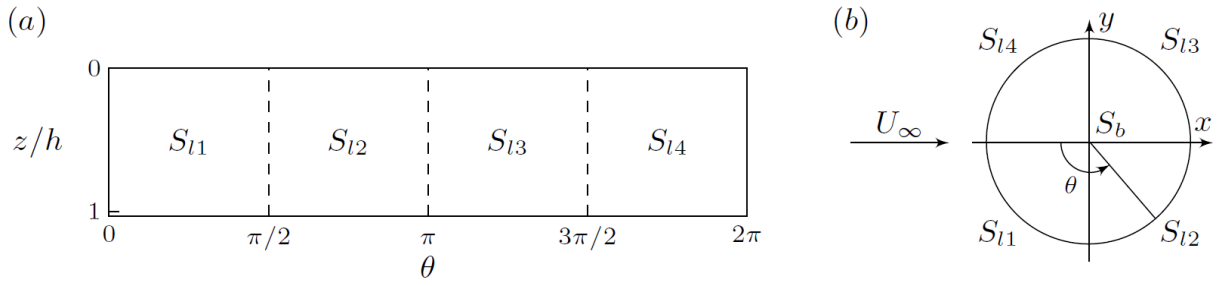

Figure 4.9: Sketch showing the surface of the control volume used to quantitatively evaluate the bleeding flow. (a) Lateral surface composed of four segments: S_{l1}, S_{l2}, S_{l3} and S_{l4} (laid flat). (b) Bottom surface (at $z/h = 1$). The origin of the θ-coordinate is located at the patch leading edge and is positive anticlockwise.

the unit vectors along the (x, y, z) coordinates, respectively. Similarly, the corresponding surface-averaged streamwise, lateral and vertical bleeding velocities can be rendered respectively as $U_B = Q_{Bx}/(Dh)$, $V_B = Q_{By}/(2Dh)$ and $W_B = Q_{Bz}/(\pi D^2/4)$.

Figure 4.10 shows the typical pattern of time-averaged velocity vector fields (U,V,W) following the patch surface. The streamwise velocity U peaks near the latter half of region S_{l1} and the former half of region S_{l4}, and is greatly decreased near the patch's trailing edge (regions S_{l2} and S_{l3}). Strong lateral flow can be observed in most part of regions S_{l1} and S_{l4}, while it weakens considerably in regions S_{l2} and S_{l3} due to flow separation. Noticeably, the vertical velocity W exhibits the most remarkable variation with flow depth (z), expecially in regions S_{l1} and S_{l4}. Moreover, as one moves from the leading edge to the trailing edge along the patch bottom surface S_b, due to the growing effect of wake entrainment occurring immediately downstream of the patch, there is a clear shift from downwash to upwash flow.

Figure 4.11 gives an overview of the three-dimensional bleeding dynamics through the surface area of the twelve porous patches investigated in this paper. In terms of bleeding velocity (figure 4.11a): (i) For a fixed AR, as ϕ increases, U_B drops dramatically while V_B and W_B increase; (ii) For a fixed ϕ, W_B increases with increasing AR. Larger values of AR promotes more horizontal flow inside the patch (because of weaker 3-D end effects), which leads to larger V_B. All of

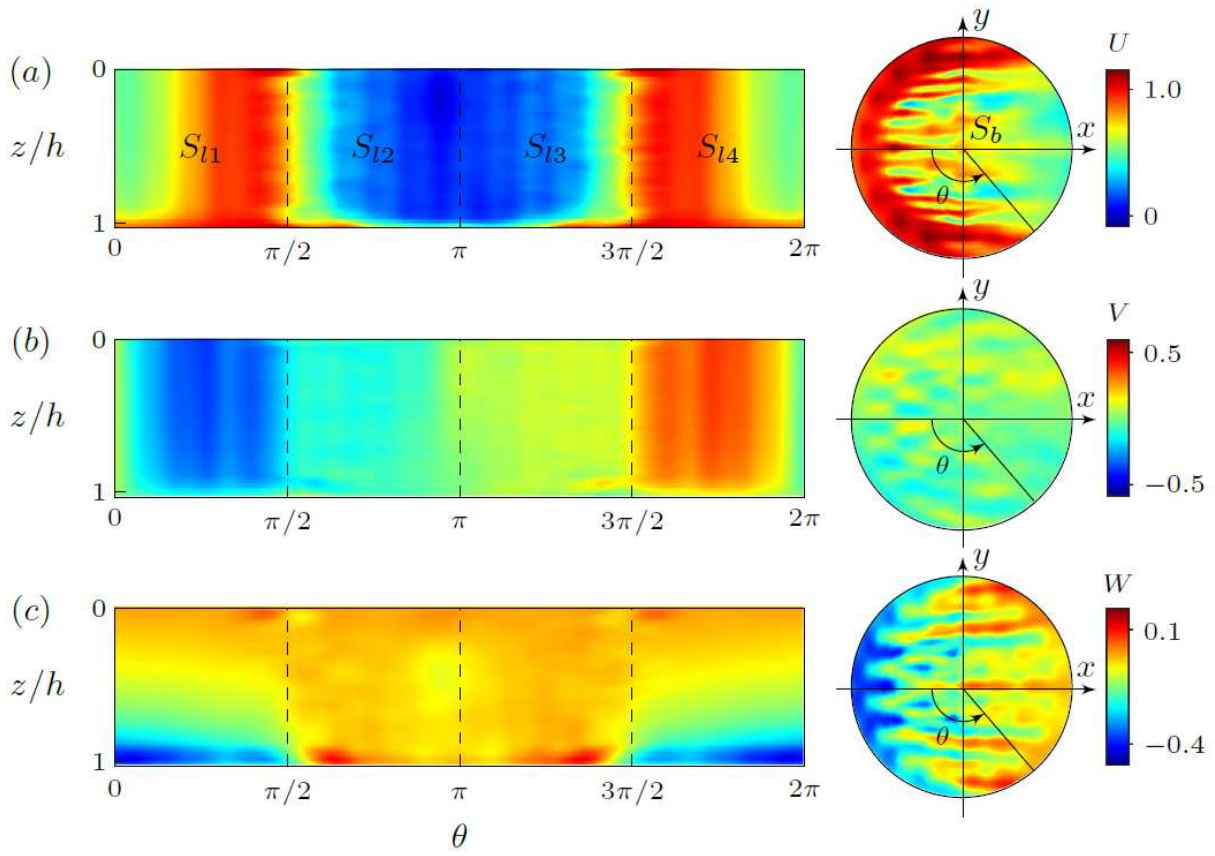

Figure 4.10: Spatial variation of time-averaged velocities in the vicinity of the patch surface ($0.023D$ apart) in case $C_{37}AR_{0.75}$: (a) streamwise velocity, (b) lateral velocity and (c) vertical velocity. Left panel: the lateral surface (laid flat); right panel: the bottom surface at $z = h$. The origin of the θ-coordinate is located at the patch leading edge and is positive anticlockwise. The integral regions in equations (4.1) and (4.3) are denotated in (a). The impermeable top surface at $z = 0$ is not shown.

these quantitative assessments are consistent with the flow structures shown in figures 4.6 and 4.7. Meanwhile, to satisfy flow continuity, there is overall a slight decrease of U_B with increasing AR.

Instead of discussing the absolute strength of bleeding (U_B/U_∞, V_B/U_∞, W_B/U_∞), we define the relative bleeding to be the proportion of bleeding flow rates along different directions relative to the total inflow rate entering the patch. In figure 4.11(b), Q_{Bx}/Q_{inflow} decreases significantly with increasing ϕ, but shows an even weaker dependence on AR than that of U_B. The increase of Q_{By}/Q_{inflow} with increasing ϕ and AR is again observed, and it gradually exceeds Q_{Bx}/Q_{inflow} at large values of ϕ or AR (as large as 64%). The effect of AR on Q_{By}/Q_{inflow} is two-fold. A larger AR promotes 2-D horizontal flows inside the patch and thus larger V_B. More importantly, it also

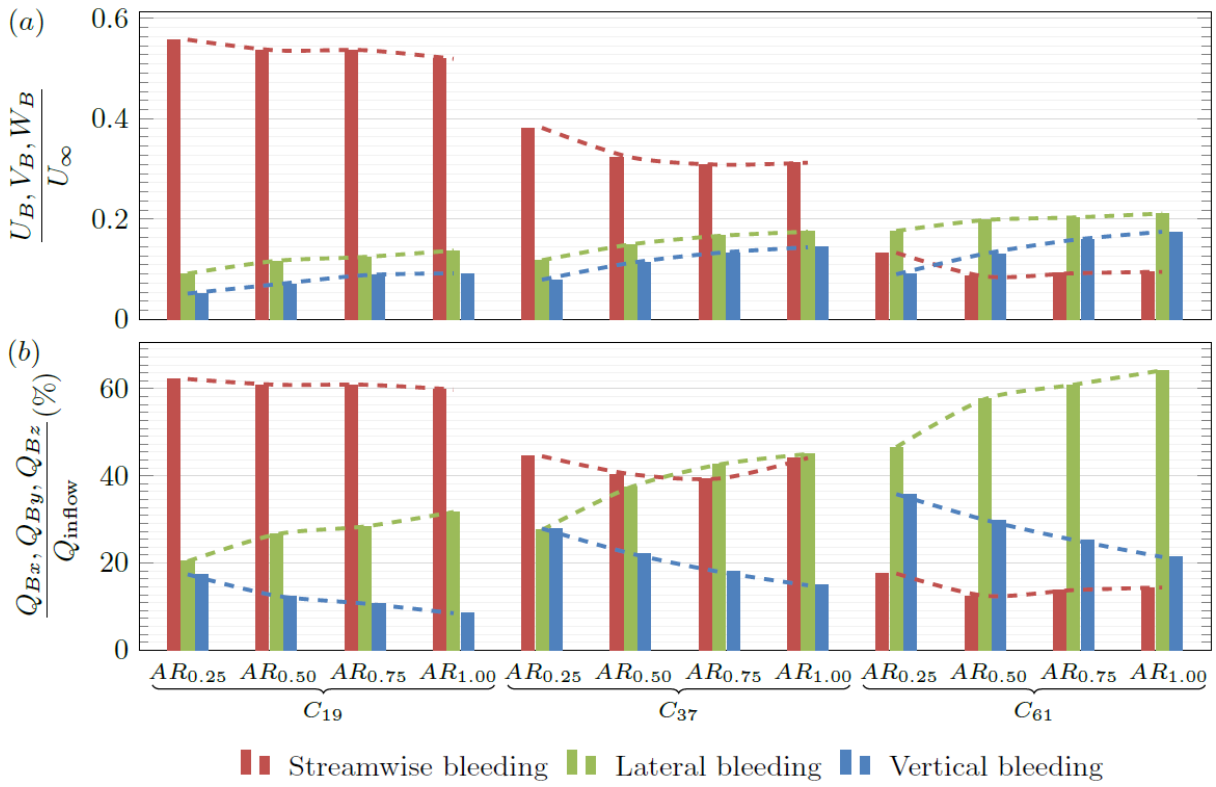

Figure 4.11: Three-dimensional bleeding dynamics through the patch surface. (a) Bleeding velocities normalized by the free-stream velocity. (b) Proportion of bleeding flow rates relative to the total inflow rate. Dashed lines indicate the dependence of bleeding on AR with ϕ being fixed.

generates a larger lateral surface area of the cylindrical patch over which V_B is integrated, resulting a more significant increase of Q_{By}/Q_{inflow} than that of V_B (compare the slopes of the green dashed lines between figures 4.11a and b). By contrast, the bottom surface area stays unchanged with varying AR, and this leads to the most striking difference between figures 4.11(a) and (b): AR has opposite effects on the absolute and relative vertical bleeding.

4.3.4 Flow Diversion Around and Beneath the Patch

An important observation from figures 4.6 and 4.7 is that bleeding flow tends to enlarge the size of the near-wake, presenting to the flow as a wider (lateral bleeding) or taller (vertical bleeding) patch body than its actual dimensions. In what follows, we discuss the interlinks between the patch geometry (ϕ and AR), the aforementioned bleeding flows *perpendicular* to the main stream, and the proportional redistribution of the *streamwise* flow over the domain cross section. As depicted in

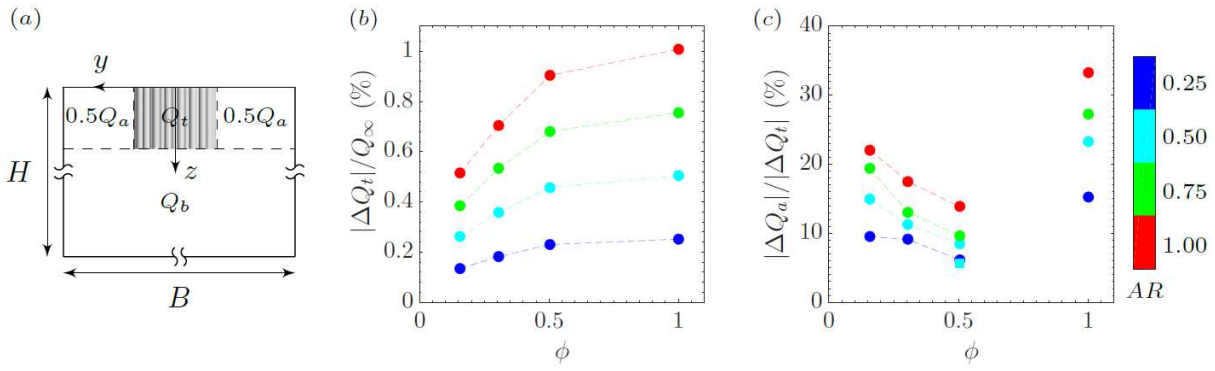

Figure 4.12: (a) Cross-sectional view at the y-z plane at $x = 0$ showing the demarcations (dashed lines) between flow-through (Q_t), flow-around (Q_a) and flow-beneath (Q_b) regions. (b) Effect of patch geometry on $|\Delta Q_t|$ normalized by Q_∞. (c) Effect of patch geometry on the proportion of $|\Delta Q_a|$ in $|\Delta Q_t|$. The square symbol in (c) indicates the special case $C_{61}AR_{0.50}T$ where there is no vertical bleeding.

figure 4.12(a), due to the canopy drag, the otherwise uniform total flow rate $Q_\infty = U_\infty BH$ flushing through the computational domain is redistributed into three pathways: penetrating through the patch (Q_t), horizontally around the patch (Q_a) and vertically beneath the patch (Q_b), i.e. $Q_\infty = Q_t + Q_a + Q_b$. The change of flow rate in region i ($i = t,\ a,$ or b) with respect to the undisturbed condition is defined as $\Delta Q_i = Q_i - Q_{i,\phi=0}$, where $Q_{i,\phi=0}$ is the flow rate in region i without the patch. It directly follows that $|\Delta Q_t| = |\Delta Q_a| + |\Delta Q_b|$. Next, we take the domain cross section at $x = 0$ as an example and analyze the flow-diversion dynamics therein.

Figure 4.12(b) shows the reduction of flow through the patch interior normalized by Q_∞ under the influence of varying patch geometry. On one hand, for a fix ϕ, $|\Delta Q_t|$ is greater for patches with larger AR, mainly due to the growing cross-sectional area of the patch (Dh). On the other hand, for a fix AR, $|\Delta Q_t|$ increases monotonically with patch densification and asymptotically approaches the solid-patch case where $|\Delta Q_t|/Q_\infty = (Dh)/(BH)$. However, it is evident in figure 4.12(c) that the partition of $|\Delta Q_t|$ into flow-around and flow-beneath (quantified by $|\Delta Q_a|/|\Delta Q_t|$ and thus $|\Delta Q_b|/|\Delta Q_t| = 1 - |\Delta Q_a|/|\Delta Q_t|$), although still varies monotonically with AR, possesses a non-monotonic dependence on ϕ. This can be explained by the interrelations between the patch geometry, flow bleeding and flow diversion as follows:

- The patch density ϕ affects flow diversion mainly by means of modifying flow bleeding. In figure 4.6, as ϕ increases from 0.16 to 0.50, both the vertical and lateral sizes of the near-

wake are enlarged. According to figure 4.11, the decrease of $|\Delta Q_a|/|\Delta Q_t|$ with increasing ϕ in figure 4.12(c) must be attributed to the dominating effect of lateral bleeding which promotes flow diversion beneath the patch, compared with the vertical bleeding which promotes lateral diversion. To verify this statement, an additional simulation $C_{61}AR_{0.50}T$ was carried out, where a circular plate of diameter D is placed at the patch bottom surface to eliminate vertical bleeding and presumably enhance lateral bleeding. As expected, $|\Delta Q_a|/|\Delta Q_t|$ drops from 8.5% to 5.6% in figure 4.12(c). Furthermore, the value of $|\Delta Q_a|/|\Delta Q_t|$ associated with the limiting case of a solid patch ($\phi = 1$) turns out to be much larger compared with all the porous patches, due to the absence of bleeding flow. There clearly exists a turning point between $\phi = 0.50$ and 1 after which bleeding along all directions start to recede with increasing ϕ. The associated entirely different flow dynamics precludes a monotonic interpolation over this range in figure 4.12(c). This is beyond the scope of this paper and we leave it to be addressed in future work.

- The patch aspect ratio AR affects flow diversion mainly by changing the real geometrical dimensions of the patch. The disturbances induced by the patch free end is weaker along the patch height at larger AR, therefore the approaching flow is less three-dimensional and favors a lateral diversion other than vertical, i.e. $|\Delta Q_a|/|\Delta Q_t|$ increases. Clearly, the above-mentioned dominance of lateral bleeding over vertical bleeding in terms influencing flow diversion cannot counteract this effect and hence a larger proportion of ΔQ_t is diverted around the patch.

4.3.5 Drag Coefficient

From a momentum balance point of view, the drag coefficient of an obstacle is mainly influenced by the spread of its wake and the intensity of the velocity deficit in the wake itself. For porous patches, there are mainly four flow phenomena which affect the drag coefficient compared with a solid patch:

- The internal cylinders offer some extra resistance to the incident flow, i.e. larger $\overline{C}_D$;

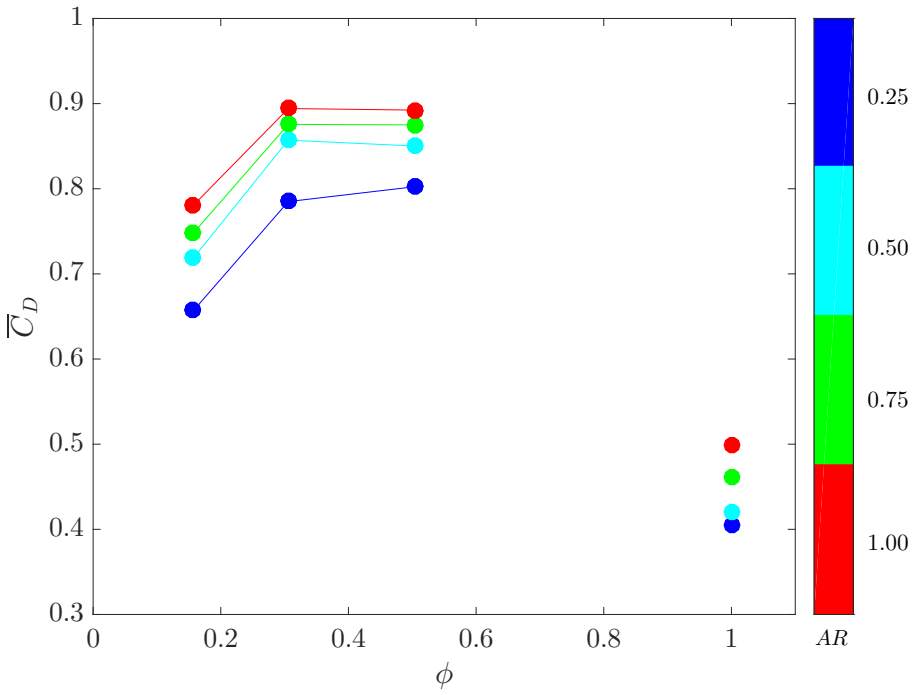

Figure 4.13: Time-averaged drag coefficient versus patch density and aspect ratio.

- The streamwise bleeding contributes to diminishing the velocity deficit in the wake and hence to lower $\overline{C}_D$;
- The lateral bleeding prevents the reattachment of the flow along the sides of the porous patches hence contributing to widening the wake, i.e. larger $\overline{C}_D$;
- The vertical bleeding pushes downwards the shear layer forming at the patch bottom hence enlarging the vertical size the wake, i.e. larger $\overline{C}_D$.

Figure 4.13 shows the variation of the time-averaged drag coefficient with patch density ϕ. It can be seen that the values of $\overline{C}_D$ of patches with a larger aspect ratio AR are generally larger, mainly due to the fact that the bottom shear layer which induces wake entrainment and hence decreases the pressure drag, is weaker for taller patches. This is consistent with previous studies of a solid obstacle (e.g. Inoue & Sakuragi 2008). It is evident in figure 4.13 that the effect of AR plays a dominating role compared with the flow bleeding in the game of drag generation.

On the other hand, for a fixed AR, $\overline{C}_D$ increases as ϕ increases from 0.16 to 0.31, and reaches a plateau between $\phi = 0.31$ and 0.50. During this process, the increase of the number of con-

stituent cylinders, the decrease of streamwise bleeding and increase of lateral/vertical bleeding all contribute to increasing $\overline{C}_D$. However, surprisingly, as ϕ increases further, the $\overline{C}_D$ drops abruptly towards the solid-patch case ($\phi = 1$), which is even smaller than that of the sparsest patch with $\phi = 0.16$. This can be attributed to the absence of internal resistance and the bleeding flows as well. However, it is controversial which of these phenomena is most responsible for the substantial reduction of $\overline{C}_D$ for the solid patch. Nicolle & Eames (2011) and Chang & Constantinescu (2015) argued that the internal resistance is more dominant, while Taddei *et al.* (2016) suggested that the lateral bleeding controls the dynamics. Furthermore, it is noteworthy that in figure 4.13 there is a big gap of data between $0.50 < \phi < 1$. This lack of data calls for more future study to investigate whether for $0.50 < \phi < 1$ the plateau of $\overline{C}_D$ still persists and then abruptly decreases after a threshold value of ϕ, or whether it smoothly decreases towards the solid-case value. Therefore, similar with the discussion of flow diversion in figure 4.12, a monotonic interpolation is not made within this range.

Consistent with the abovementioned previous studies, the results presented in this section suggest that porous obstacles (either emergent, submerged or suspended) act as very efficient momentum sinks when impinged by a incoming uniform flow (i.e. more efficient than their solid counterpart). We suggest that this result could be exploited for engineering applications that require to maximize flow resistance while maintaining low roughness densities. (i.e. number of roughness elements per unit surface). For example, fish passes at steep slopes are commonly built using roughness elements to minimize mean velocities (usually in the form of rocks or artificial baffles) to allow for upstream fish migration. The information contained in figure 4.13 suggests that replacing solid with porous roughness elements (e.g. vegetation-like surfaces) could lead to an enhanced flow resistance and ultimately an improved fish pass efficiency.

4.4 Conclusions

Uniform flow interacting with a suspended cylindrical canopy patch was numerically investigated using large eddy simulations, with the aim of providing a systematic understanding of the

effect of patch density and aspect ratio on the highly three-dimensional mean flow dynamics in the near field. Flow bleeding along all directions was quantitatively evaluated for the first time by integrating the velocity field along the patch outer surface. It was observed that the absolute streamwise(U_B)/lateral(V_B)/vertical (W_B) bleeding decreases/increases/increases with either increasing ϕ or AR. Vertical motions inside the patch was examined to provide an explanation for the similar dependence of W_B on ϕ and AR. In terms of relative vertical bleeding (Q_{Bz}/Q_{inflow}), it is interesting to note that a larger AR causes a smaller proportion of the total flow entering the patch to bleed out vertically. Close interlinks between the patch geometry, flow bleeding and flow diversion were identified, which have important implications for marine farms where fluxes of nutrients and wastes determine productivity and environmental impacts.

Chapter 5

Bottom Gravity Currents Interacting with an Infinite Submerged Array[2]

5.1 Introduction

Gravity currents occur whenever fluid of one density flows primarily horizontally into a fluid of different density. There are many examples of gravity currents, both naturally occurring and man-made (Simpson 1997). Gravity currents propagating along a smooth surface has been extensively studied (Rottman & Simpson 1983; Shin *et al.* 2004; Cantero *et al.* 2007; Ooi *et al.* 2009). However, it is not uncommon for a gravity current to encounter macroscale obstacles or small-scale roughness elements that provide an additional drag and impede its progress (Hatcher *et al.* 2000). The dynamic impact of the obstacles is felt over different fractions of the total flow depth depending on their submergence ratio H/h, where H is the flow depth and h is the array height. A handful of previous studies have dealt with the effect of emergent arrays ($H/h \leqslant 1$) on buoyancy-driven exchange (Tanino *et al.* 2005; Jamali *et al.* 2008; Zhang & Nepf 2008; Ozan *et al.* 2015). Nevertheless, the problem of gravity currents interacting with a partial-depth array ($H/h > 1$) has received less attention, partly due to the additional complexity arising from the drag continuity at the array-ambient interface. The propagation and structure of bottom-boundary gravity currents over a sparse array of two-dimensional submerged obstacles have been investigated by Tokyay *et al.* (2011*a*, 2012, 2014). Cenedese *et al.* (2016) experimentally found that enhancement of the dilution of the bottom currents by a submerged array can occur due to two different mechanisms.

[2]The research presented in this chapter has been published in substantial part in *Journal of Fluid Mechanics* under the title "On the propagation of gravity currents over and through a submerged array of circular cylinders" (J. Zhou *et al.* 2017). Background information and literature relevant to this chapter are presented again so the chapter may be read as a stand-alone work. The chapter is written in a collective "we" voice to acknowledge collaboration with Dr. S. K. Venayagamoorthy from Colorado State University, Dr. Claudia Cenedese from Woods Hole Oceanographic Institution, and Dr. Roger Nokes from University of Canterbury, New Zealand. S. K. V. and C. C. were able to forge this collaborative research at the Workshop on the Mathematics of Layers and Interfaces that was held in Oaxaca, Mexico on November 8-13, 2015.

For a sparse array, the vast majority of the gravity current propagates within the array, and the individual cylinder wakes are the main contributor to the current dilution. In contrast, for a dense array, the gravity current rides on top of the array and the dilution is mainly enhanced by the vertical convective instability arising from the unstable stratification at the interface. The propagation of a surface current beneath a floating array has been studied experimentally by Zhang & Nepf (2011) and numerically by Ozan *et al.* (2016), which have led to similar results with the studies of bottom currents over a submerged array.

Canopies from different systems with different scales exhibit a wide range of solid volume fraction ϕ (defined in equation 5.1 later). For rooted aquatic vegetation, ϕ ranges from 0.001 for marsh grasses to 0.45 for mangroves (Nepf 2012). The range of ϕ for terrestrial forests has not been specifically reported in the literature, but is also expected to vary significantly between different circumstances. In the industrial setting, however, there is an even wider scope of ϕ. For example, the packing density of buildings may reach its minimum ($\phi \approx 0$) in the open country and its maximum ($\phi \approx 1$) in a dense urban center. Other dense porous media over which gravity currents may propagate include sediment beds, coral reefs and reservoir rocks (Ghisalberti 2009). To date, a very limited range of ϕ has been investigated, with the highest being around 0.35 for emergent arrays (Zhang & Nepf 2008) and 0.36 for submerged arrays (Cenedese *et al.* 2016). It has come to an agreement that the front velocity of the gravity current decreases as the array is densified to up to $\phi \approx 0.35$, regardless of the submergence condition. For the emergent case, it seems unnecessary to extend ϕ even higher since a further retarding of the current by the increased array drag can be readily expected until it ceases to advance. In contrast, given the additional flow pathway above a submerged array, one expects the gravity current propagation to approximate the flat-bed case when ϕ reaches unity. The associated dynamics of flow transition occurring within the range of $\phi = 0.36 \sim 1$ that regulates the propagation and structure of the gravity current is nontrivial and has not yet been explored.

Unlike natural canopies, arrays of obstacles with human intervention, including urban canopies, crop canopies, forest plantations, and engineering retarding facilities, are sometimes non-equidistant

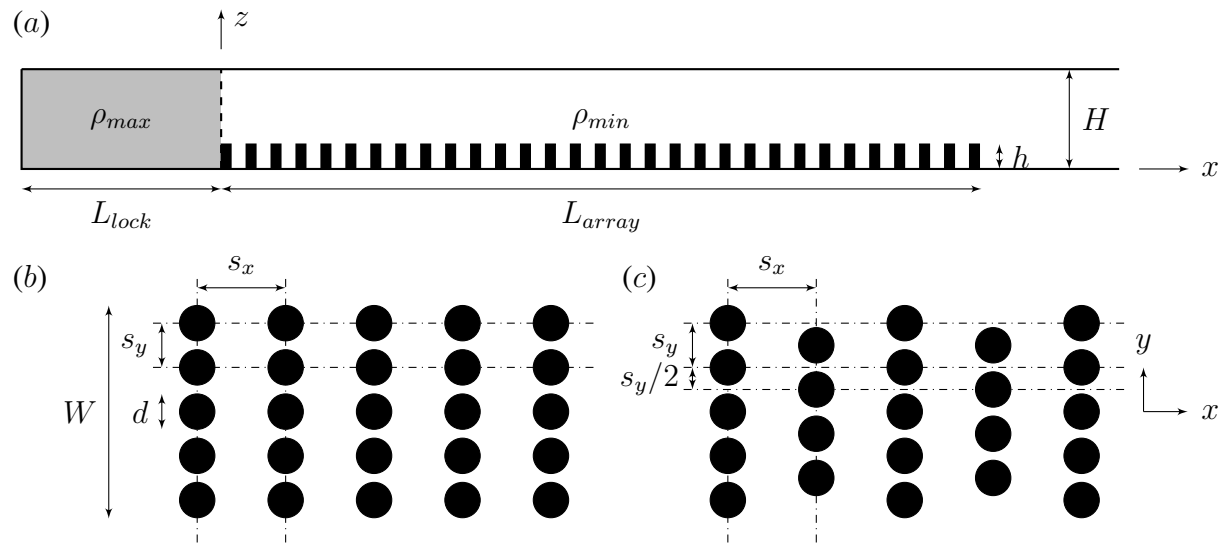

Figure 5.1: Schematic diagram showing the full-depth lock-exchange setup used in this study. (a) elevation view of the channel; (b) plan view of the in-line arrangement; (c) plan view of the staggered arrangement. The vertical dashed line in (a) indicates the gate position at $x = 0$. The rightmost end of the array is far from the channel extremity. Circular cylinders (when present) with a diameter of d and a height of h are mounted on the channel bed, with their axes parallel to the vertical direction. The streamwise and spanwise center-to-center cylinder spacings are denoted as s_x and s_y, respectively. In the staggered case, the offset rows are shifted by $s_y/2$ along the spanwise direction. In both (b) and (c), the array is referred to as equidistant if $s_x = s_y$ and non-equidistant otherwise. Not to scale.

with the obstacles spacings varying significantly in different directions (see equation 5.2 for definition of array non-equidistance). However, most existing studies limit their consideration for gravity currents interacting with equidistant arrays (or similarly, random arrays) where the individual roughness elements are nearly equidistantly distributed (Tanino *et al.* 2005; Cenedese *et al.* 2016). The conventional geometrical characterization consisting of horizontally-averaged bulk parameters, i.e. the solid volume fraction ϕ and the frontal area of solids per unit volume a (defined below), was employed in all these studies. Therefore, whenever there is a nonnegligible degree of array non-equidistance, the universality of the consensus that a certain set of ϕ and a (with all other parameters fixed) uniquely determines the state of the gravity current propagation, is questionable and needs to be reexamined.

Figure 5.1 shows the lock-exchange setup of a bottom-boundary Boussinesq gravity currents propagating over and through a submerged array of circular cylinders used in this study. The initial maximum and minimum fluid densities in the lock and the ambient region before gate

removal are denoted as ρ_{max} and ρ_{min}, respectively. The reduced gravity is defined as $g' = g\left(\rho_{max} - \rho_{min}\right)/\rho_{max}$. The channel depth, H, and the corresponding buoyancy velocity, $u_b = \sqrt{g'H}$, are used as the characteristic length and velocity scales, respectively. Time is rendered dimensionless in terms of $t_0 = H/u_b$. The dimensionless fluid density is defined as $\rho = (\rho_a - \rho_{min})/(\rho_{max} - \rho_{min}) \in [0, 1]$ where ρ_a is the absolute fluid density. The dimensions of each of the circular cylinders is fixed throughout this study, i.e. d in diameter and $h = 2.5d$ in height. This results in an aspect ratio of $h/d = 2.5$. There are N such circular cylinders within the volume of the array ($V_{array} = WhL_{array}$, including pores). The array density (also referred to as the solid volume fraction hereinafter) is given by

$$\phi = \frac{N\left(\pi/4\right)d^2h}{V_{array}}. \tag{5.1}$$

We will present a combined experimental and numerical investigation to provide a comprehensive understanding of the current-array interaction under the impact of array densification and non-equidistance. The results of this study are expected to have great implications for practical applications in a variety of fields. Examples include oceanic turbidity currents over bottom topography (Meiburg & Kneller 2010), thermally-driven exchange flows through aquatic canopies (Oldham & Sturman 2001), sea breezes or haboobs through urban areas (Huppert 2006; Knippertz & Todd 2010) and snow avalanches over mitigative fences (Hopfinger 1983). Taking advantage of the unique obstacle representation technique of our numerical model (Hirt 1993), we are able to vary the embedded array geometry realistically without changing the computational mesh. The resulting freedom of geometrical variation enables us to perform an extensive parametric study to address the following outstanding research questions that are closely related to density-driven gravity currents over groups of obstacles in aquatic/geophysical/atmospheric environments. Specifically:

1. *How does the gravity current behavior vary over the full range of ϕ on encountering a submerged array?* We will start from the classic flat-bed condition ($\phi = 0$), experimentally densify the array to up to $\phi = 0.36$, and then gradually approach the fully-blocked condition

($\phi = 1$) using LES. Across this range, we will present insights into the flow behavior and transitions regulating the initial deceleration and subsequent reacceleration of the gravity current as ϕ increases, which is fundamentally different as compared to the case of emergent-arrays where the front velocity depends monotonically on ϕ.

2. *What is the appropriate geometrical characterization of a non-equidistant array when it affects the gravity current propagation?* We will demonstrate that arrays with the same density ϕ can result in entirely different structures of the gravity current depending on its level of non-equidistance ($s_x \neq s_y$) and cylinder arrangement (either in-line or staggered). A two-dimensional parameter space will be proposed in which the array density ϕ is decomposed into its streamwise and spanwise components respectively as

$$\mu_x = d/s_x \quad \text{and} \quad \mu_y = d/s_y. \tag{5.2}$$

Physically, μ_x can be interpreted as a wake parameter, with large μ_x indicating a strong suppression of the individual cylinder wakes. Meanwhile, μ_y can be interpreted as an intrusion parameter, with large μ_y indicating less intrusive flow through the lateral space between cylinders. Accordingly, the original array density can be expressed as

$$\phi = \left(\frac{\pi}{4}\right) \mu_x \mu_y. \tag{5.3}$$

Similarly, the frontal area of solids per unit volume can be written as $a = (\mu_x \mu_y)/d$ for non-equidistant arrays ($\mu_x \neq \mu_y$). Since d is fixed in this study, the parameter a can be uniquely determined as $\left(\frac{4}{\pi}\right) \phi/d$. We will show that this new geometrical framework, which emphasizes the necessity of directional decomposition of the array density, provides a more unambiguous description of the gravity current propagation especially when the array is highly non-equidistant. Depending on the specific combination of μ_x and μ_y, four dynamically different flow regimes with their mutual transitions are identified. On top of this, the two cylinder arrangement patterns in figure 5.1(b, c) will be analyzed and compared.

The layout of this chapter is as follows. The experimental methodology, numerical model and its validation, as well as the matrix of numerical simulations are given in §5.2. Based on this, the results from a broad-range parametric study using LES are presented in the ensuing sections. We firstly discuss the effect of array geometry on the gravity current under a particular submergence ratio H/h in §5.3, §5.4 and §5.5. In §5.3, a discussion of the gravity current front velocity is provided. In §5.3.1, we present results of the temporal evolution of the current front, while in §5.3.2 we discuss the dependence of the time-averaged front velocities on array geometry during the slumping phase. In §5.4, we describe in detail the various flow regimes identified in this study. The transitional dynamics among different flow regimes for equidistant and non-equidistant arrays is discussed in §5.5.1 and §5.5.2, respectively. In §5.6, with a particular array geometry, the flow depth was varied to investigate the effect of submergence ratio. Finally, §5.7 provides some concluding comments and connects the results to practical situations.

5.2 Descriptions of Experiments and Numerics

5.2.1 Experimental Setup

The experimental work of this study is conducted at University of Canterbury, New Zealand, using a similar apparatus to that of Cenedese *et al.* (2016). As shown in figure 5.1, a gravity current was generated through the classic lock-exchange configuration in a flat flume with perspex lateral walls and a glass bottom. The flume was 620 cm in length, 25 cm in width and 50 cm in height. A stainless steel gate sealed by plastic foam was located $L_{lock} = 100$ cm from the left hand end of the flume, partitioning it into two regions: the lock region and the open region containing the roughness elements which extended $L_{array} = 300$ cm away from the gate. The array consisted of vertical rigid plastic cylinders that were 2 cm in diameter and 5 cm in height which are fixed for all the experiments, resulting in a cylinder aspect ratio of $h/d = 2.5$. The cylinders were held in place by a perforated aluminum base plate and could be screwed in and out to create different geometrical configurations with varying μ_x, μ_y and arrangement patterns as indicated in figure 5.1.

A 4g/l salt solution ($\rho_{max} = 1.0014$ g/cm^3) and a 14.7 ml/l ethanol solution ($\rho_{min} = 0.9963$ g/cm^3) were filled into the lock region and the ambient-fluid region, respectively, resulting in a reduced gravity of $g' = 5\ \mathrm{cm/s^2}$ so that the flow can be considered as Boussinesq. The purpose of using an ethanol solution as opposed to fresh water for the ambient fluid was to match its refractive index with the lock fluid ($n = 1.3337$) in order to eliminate optical distortions. The densities were measured with an Anton Paar DMA 5000 density meter. The experiment was started by pulling the gate vertically out of the tank. The flow evolution was captured using a JAI BB-141GE (Bayer color) CCD camera recording at a frame rate of 30.128 Hz. The 1392×1040 pixel images were transferred directly to a fast hard drive on a PC during capture. A mirror was used to increase the distance between the camera and the field of view, thus decreasing the impact of parallax. Both the light and dense fluids were seeded with approximately neutrally buoyant Pliolite particles sized at 250-300 μm. A LED lightbank generated an approximately 1 cm wide lightsheet which illuminated a slice of the flow from above along the centerline of the tank. The field of view of the camera was from $x = 77.9 \sim 128.1$ cm, which is referred to as the illuminated region. Enough particles were added to ensure that there were at least 1000 particles in the camera window with a volume of roughly 502 mm $\times$ 10 mm $\times$ H. The post-processing of the captured images was undertaken using a Light Attenuation (LA) technique with the *Streams* software system (Nokes 2016).

In this study, a total of 11 laboratory experiments were conducted with bottom roughness present. The streamwise array density was varied as μ_x =0.090, 0.181 and 0.363 while the spanwise array density was fixed at $\mu_y = 0.636$, resulting in a solid volume fraction of ϕ = 0.045, 0.090 and 0.181, respectively. For each array geometry, the water depth was varied to simulate different submergence ratios at H/h = 3, 4, 5.4 and 7. The data of $\phi = 0.045$ associated with $H/h = 7$ was not recorded. It is acknowledged that there are intrinsic problems in obtaining robust time-averaged velocity fields using data recorded by a camera fixed in the laboratory frame of reference. The primary reasons for this are firstly, that it must be assumed that the current is in a quasi-steady state such that the current front propagates at a constant speed and that the internal

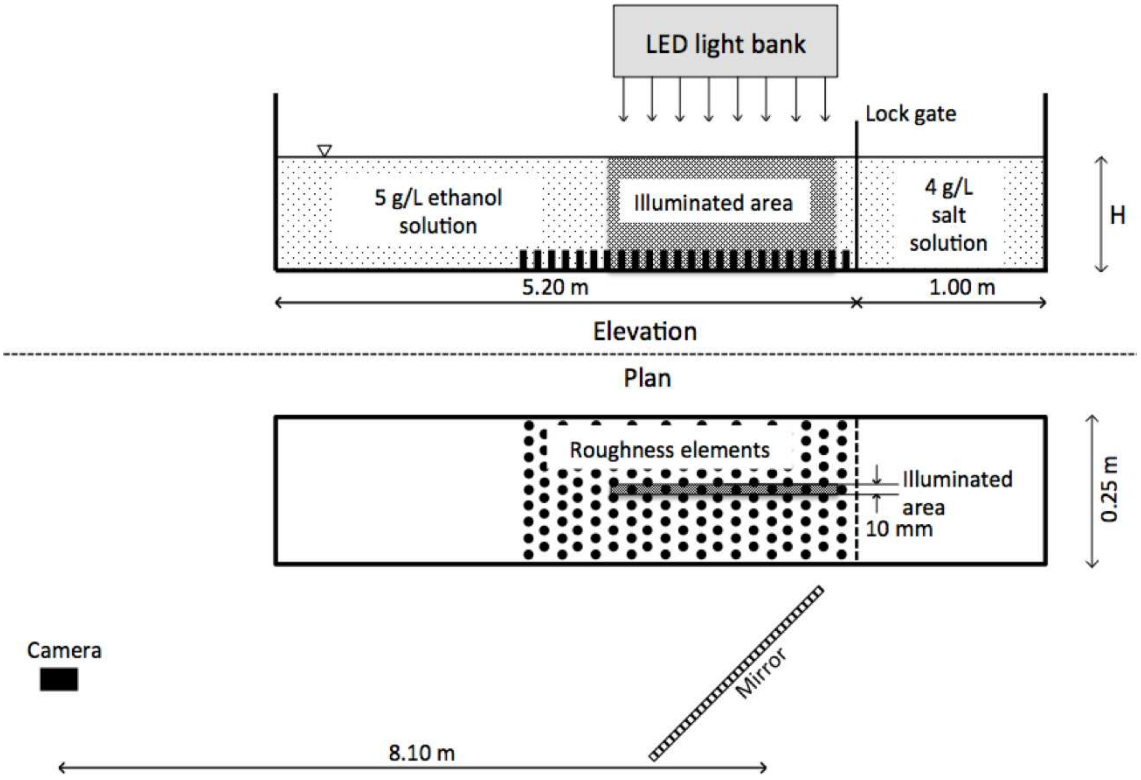

Figure 5.2: Elevation and plan views of the experimental flume and optical system components at University of Canterbury, New Zealand. Upon the gate removal, a BBGC propagates to the left due to a fixed reduced gravity $g' = 5\ \mathrm{cm/s^2}$. Not to scale.

flow is statistically stationary during the recorded motion; and secondly, that the recording period is sufficiently long to be able to compute robust Reynolds averages. However, comparison of the vertical profiles of the horizontal velocity for three repeated experiments with the same initial conditions (not shown) gives us confidence that the results presented in this paper are robust.

5.2.2 Numerical Model and Validation

The LES filtered Navier-Stokes equations for time-dependent, three-dimensional, incompressible stratified flows with the Boussinesq approximation are given in tensor notation by

$$\frac{\partial u_i}{\partial t} + \frac{\partial \left(u_i u_j\right)}{\partial x_j} = -\frac{1}{\rho_0}\frac{\partial p}{\partial x_i} + \nu\frac{\partial^2 u_i}{\partial x_j \partial x_j} - g\frac{\rho}{\rho_0}\delta_{i3} - \frac{\partial \tau_{ij}^{SGS}}{\partial x_j}, \tag{5.4}$$

subject to the filtered continuity equation

$$\frac{\partial u_i}{\partial x_i} = 0, \tag{5.5}$$

and the filtered density transport equation

$$\frac{\partial \rho}{\partial t} + \frac{\partial \left(\rho u_j\right)}{\partial x_j} = \kappa \frac{\partial^2 \rho}{\partial x_j \partial x_j} - \frac{\partial \chi_j^{SGS}}{\partial x_j}, \tag{5.6}$$

where u_i is the Cartesian components of the filtered velocity field, p is the filtered pressure, ρ is the filtered density, ρ_0 is a characteristic reference density, g is the gravitational acceleration, δ_{i3} is the Kronecker delta, ν is the kinematic viscosity, and κ is the molecular diffusivity of the dissolved species that gives rise to the density variation. The spatial-filtering operation is not written explicitly. Time is represented by t and the index $i = 1, 2, 3$ indicates the x (streamwise), y (spanwise), and z (vertical) directions, respectively. Invoking the Boussinesq approximation ($\Delta\rho/\rho \ll 1$), the density differences are only significant in the buoyancy term of the momentum equations. The two flow parameters arising from the non-dimensionalization of the governing equations are the channel Reynolds number $Re_H = u_b H/\nu$ and the molecular Schmidt number $Sc = \nu/\kappa$.

Figure 5.3 compares the numerical density fields with experiments (Cenedese *et al.* 2016) having the same array geometries. Two typical flow structures for a gravity current propagating past a submerged array under a submergence ratio of $H/h = 4$ are shown. For the sparse array (figure 5.3a, c), the vast majority of the gravity current propagates along the channel bed which resembles the classical case for a smooth bottom. The turbulent cylinder wakes are the main contributor to the dilution of the gravity current. In contrast, for the dense array (figure 5.3b, d), the array drag is large enough such that a new, well-defined current nose is found to propagate along the array top. The over-current nose is well mixed with the underlying lighter fluid via vertical convective instability.

Within the laboratory illuminated section ($x = 77.9 \sim 128.1$ cm), the gravity current was found to be propagating at a nearly-constant speed. The corresponding time-averaged Froude number is

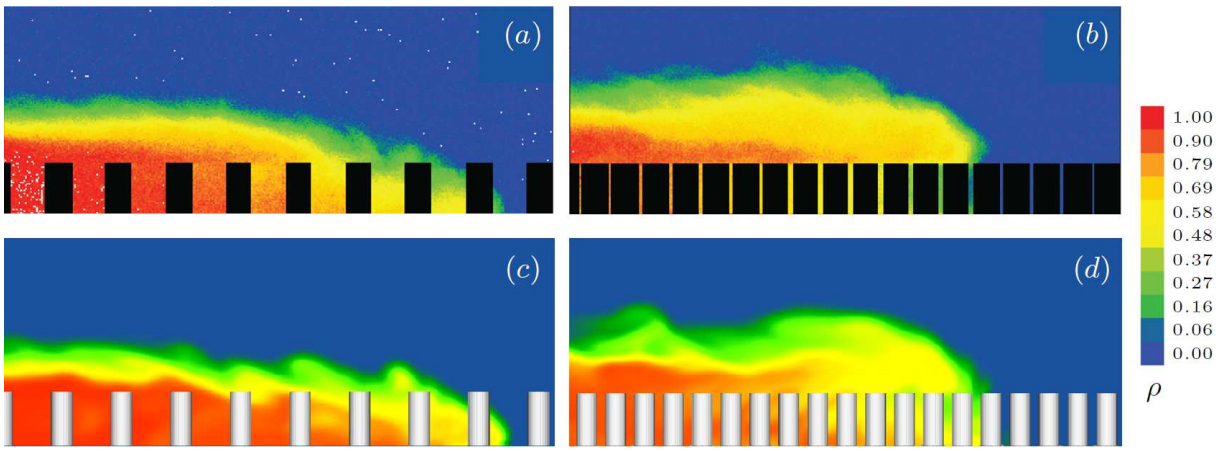

Figure 5.3: Comparison of experimental and numerical instantaneous density fields of a gravity current propagating past a sparse and a dense array. The submergence condition is fixed at $H/h = 4$. (a) sparse, experimental; (b) dense, experimental; (c) sparse, LES; (d) dense, LES. For the sparse array, $\mu_x = 0.361$, $\mu_y = 0.313$, and $\phi = 0.09$. For the dense array, $\mu_x = 0.722$, $\mu_y = 0.626$ and $\phi = 0.36$. The experimental density fields are from Cenedese *et al.* (2016).

given by

$$\overline{Fr} = \overline{U_f}/u_b, \tag{5.7}$$

where $\overline{U_f}$ is the time-averaged front velocity that was calculated through a linear interpolation to the variation of the front position, x_f, as a function of time, t. It can be seen in figure 5.4 that the values of $\overline{Fr}$ for the numerical simulations and the laboratory experiments are in excellent agreement to up to $\phi = 0.36$, except for the case with $\phi = 0.181$ and $H/h = 7$. Starting from the canonical case of gravity currents propagating over a flat bottom, $\overline{Fr}$ is initially seen to decrease as the array becomes denser, which is consistent with gravity current front speeds in emergent canopies (Zhang & Nepf 2008) and sparse submerged canopies (Cenedese *et al.* 2016). As ϕ increases further, our laboratory experiments indicate for the first time a non-monotonic dependence of $\overline{Fr}$ on ϕ, which was confirmed by the numerical simulations. However, the detailed $\overline{Fr} \sim \phi$ relationship and the underlying flow physics beyond $\phi = 0.36$ are still unknown. This serves as one of the motivations of the present study.

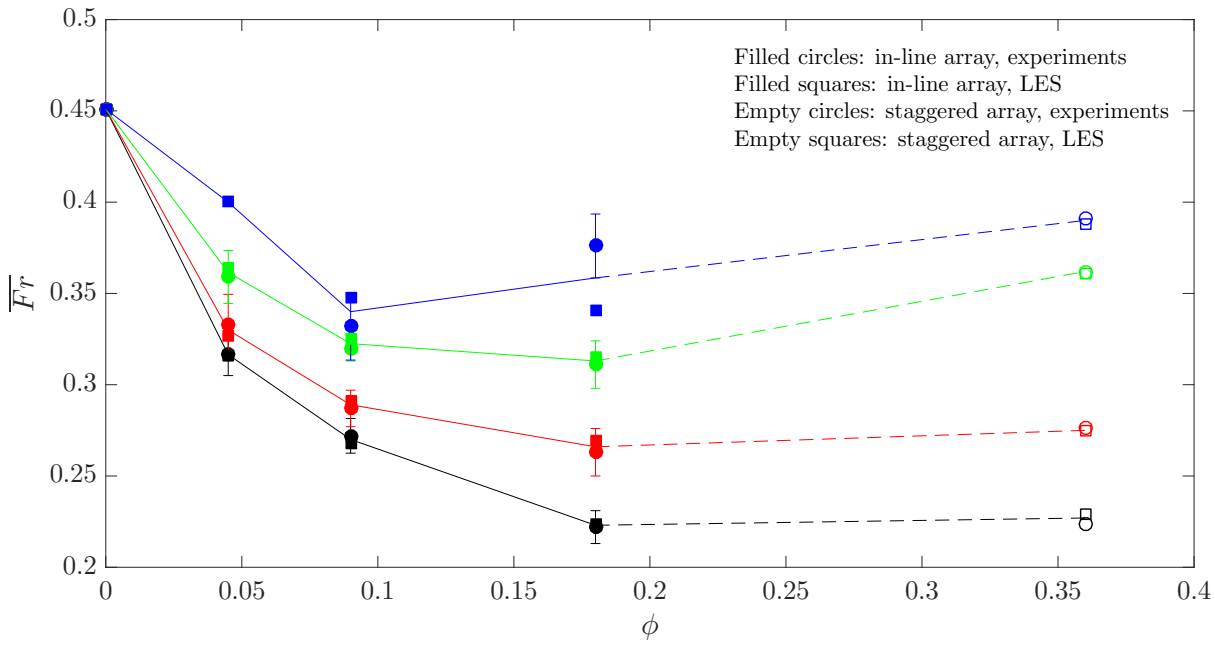

Figure 5.4: Comparison of the time-averaged Froude number between the laboratory experiments and the numerical simulations for different array densities and submergence conditions (black: $H/h = 3$; red: $H/h = 4$; green: $H/h = 5.4$; blue: $H/h = 7$). Error bars are included to account for the range of $\overline{Fr}$ in 4-6 different experimental methods for measuring the front velocity for each case due to the highly unsteady nature of the flow. For in-line arrays, the mean values of experimental and LES results are linearly interpolated by solid lines. The data between in-line and staggered arrays are interpolated using dashed lines. Experimental data of the smooth ($\phi = 0$) and the densest cases ($\phi = 0.36$) are from Cenedese *et al.* (2016).

5.2.3 Matrix of Parametric Study

A broad-range parametric study is performed using the array characterization method as described in §5.1 and given by equations (5.2) and (5.3). All the large eddy simulations were conducted in a channel with a flat bottom wall and lateral vertical endwalls. The top boundary is modeled as a free surface. The initial lock-gate position is at $x = 0$, as shown in figure 5.1. An array of vertical cylinders with an aspect ratio of 2.5 is mounted on the channel bed, with the upstream face of the first row of cylinders located at $x = 0$ so that the interaction between the gravity current and the array occurs immediately after the gate removal. The streamwise dimension of the array is determined in each simulation to ensure a negligible effect from the downstream boundary of the computational domain. The reduced gravity is fixed at g' = 5 $\mathrm{cm/s^2}$.

The simulation runs performed in this study are summarized in table 5.1. The unobstructed flat-bed case ($\phi = 0$) and the fully-blocked solid-slab case ($\phi = 1$) under a submergence ratio of $H/h = 5.4$ are regarded as two baseline simulations with the notation

$$\text{F-}0\text{-}5.4 \quad \text{and} \quad \text{F-}1\text{-}5.4, \tag{5.8}$$

respectively. The simulations with cylinders at a fixed submergence raio of $H/h = 5.4$ are denoted as

$$\text{I(S)-}\boldsymbol{\mu_x}\text{-}\boldsymbol{\mu_y}\text{-}5.4, \tag{5.9}$$

where I indicates in-line arrays and S indicates staggered arrays. The value of μ_y is varied across a 10-element set of 0.181, 0.272, 0.363, 0.454, 0.545, 0.636, 0.727, 0.818, 0.909 and 1.000. The value set of μ_x is identical to that of μ_y with an additional value of $\mu_x = 0.090$. In order to investigate the effect of array non-equidistance on the current propagation, μ_x and μ_y are varied independently such that 110 simulations are conducted for in-line and staggered arrangements, respectively (220 in total). As μ_x and μ_y vary, the corresponding solid volume fraction, ϕ, ranges from 0 to $\pi/4$ according to equation (5.3), which covers the whole range of possible aquatic and terrestrial conditions (note that arrays with $\phi > \pi/4$ is unachievable for circular cylinders due to their curvature).

In addition, instead of varying the planar array configuration, a equidistant staggered array with a fixed geometry ($\mu_x = \mu_y = 0.636$) is used to study the effect of submergence ratio. This last set of LES runs are denoted as

$$\text{S-}0.636\text{-}0.636\text{-}\boldsymbol{H/h}, \tag{5.10}$$

where the submergence ratio H/h varies as 1, 2, 3, 4, 6, 10 respectively. The array is initially emergent ($H/h = 1$), and eventually becomes deeply submerged ($H/h = 10$) as the flow depth rises.

Most of the LES runs with a submergence ratio of $H/h = 5.4$ were performed with a channel Reynolds number $Re_H > 30000$ which is typical for exchange flows within aquatic canopies

Simulation group	Comments	μ_x	μ_y	ϕ	H/h	# of runs
F-0-5.4	Flat bed	0	0	0	5.4	1
F-1-5.4	Solid slab	1	1	1	5.4	1
I-$\boldsymbol{\mu_x}$-$\boldsymbol{\mu_y}$-5.4	In-line arrays	$(0, 1]$	$(0, 1]$	$(0, \pi/4]$	5.4	110
S-$\boldsymbol{\mu_x}$-$\boldsymbol{\mu_y}$-5.4	Staggered arrays	$(0, 1]$	$(0, 1]$	$(0, \pi/4]$	5.4	110
S-0.636-0.636-$\boldsymbol{H/h}$	Submergence ratio	0.636	0.636	0.318	[1,10]	6

Table 5.1: List of simulations performed showing the parameter space covered. The boldfaced characters indicate the varying parameters in each simulation group.

where $Re \sim 10^4$ because the current is driven by a small amount of temperature difference due to differential shading. In atmospheric and geophysical settings, however, the Reynolds number is higher (e.g. $Re = 10^5 \sim 10^8$) due to the increase of the characteristic length and velocity scales. However, we expect the bulk propagation dynamics to be similar, and the Re-scaling effects are left to future studies. For most of the simulations, the cylinder Reynolds number $Re_d = \overline{U}_f d/\nu$ was between 500 and 1000 such that the flow can be considered as turbulent and three-dimensional (Williamson 1996).

The total number of simulations conducted in the present study is 228, in order to provide a comprehensive understanding of the various flow regimes and transitions when a gravity current encounters a submerged array of obstacles. This extensive parametric study is made possible at the cost of sacrificing some of the grid resolution. The uniform mesh size of $0.2d$ that was used for comparison with the experimental data as shown in figures 5.3 and 5.4 is applied to the whole computational domain. A grid-independence study was performed where the grid size was halved to $0.1d$, and the difference of the front velocity was found to be less than 5%. For most simulations, the number of grid points was $1300 \times 60 \times 80$ in the streamwise ($L_x = 23H$), spanwise ($L_y = 0.9H$) and vertical ($L_z = 1.2H$) directions, respectively. The fact that L_z is slightly larger

than H is to ensure that free surface fluctuations are accurately modeled by our numerical solver. For the simulations focusing on the self-similar propagation in §5.3.1, the streamwise length of the domain is increased as needed. No-slip boundary conditions were employed on the velocity field at the bottom boundary, the upstream and downstream vertical endwalls, and on the surfaces of the cylinders. Symmetry boundary conditions are applied to the lateral endwalls. The time step was automatically adjusted by the solver to be as large as possible without exceeding the stability limits and affecting accuracy, with a mean value of $0.003t_0$.

5.3 Front Velocity

In this section, we discuss the propagating properties of the front of the gravity current, with the temporal evolution in §5.3.1 and the time-averaged front velocity during the slumping-phase in §5.3.2, respectively. Six representative simulation cases with different array geometries under a fixed submergence ratio of $H/h = 5.4$ are analyzed and compared. Detailed flow structures of these simulations will be discussed in more detail in §5.4. For ease of interpretation here, flow regimes corresponding to the six cases are respectively: F-0-5.4 (flat-bed, figure 5.9a), S-0.363-0.363-5.4 (through-flow, figure 5.9b), S-0.636-0.636-5.4 (over-flow, figure 5.9c), S-1.000-1.000-5.4 (over-flow, figure 5.9d), I-0.090-1.000-5.4 (plunging-flow, figure 5.9e) and I-1.000-0.272-5.4 (skimming-flow, figure 5.9f). For the two over-flow cases, only the over-nose position is plotted.

5.3.1 Temporal Evolution of the Gravity Current Front

The trajectories of the dimensionless front position x_f/H versus the dimensionless time t/t_0 are shown in figure 5.5. The position of the nose is determined by inspection of the cross-sectionally (laterally) averaged density fields, which can be considered arguably to be more robust than the center-line velocity captured in the laboratory experiments in §5.2.1. As expected, in all simulations, after a short initial acceleration, the gravity current reaches a slumping phase in which the front trajectories can be well approximated by lines with constant slopes. This constant-speed phase has been observed in lock-exchange gravity currents propagating over a smooth surface

(Rottman & Simpson 1983), through an emergent canopy (Tanino *et al.* 2005), and over a series of submerged two-dimensional obstacles (Tokyay *et al.* 2011a). The vertical gray line in figure 5.5 indicates the time before which time-averaged Froude number can be appropriately calculated. For the flat-bed case, $\overline{Fr} = 0.451$, which agrees well with previous studies of full-depth lock release for similar order of Reynolds number (Keulegan 1958; Härtel *et al.* 2000; Shin *et al.* 2004; Cantero *et al.* 2007). The laboratory experiments of Cenedese *et al.* (2016) report an almost identical value of $\overline{Fr}$ (see figure 5.4).

It is evident in figure 5.5 that except for case I-1.000-0.272-5.4, the presence of the array slows down the advancement of the gravity currents in all other simulations compared with the flat-bed case. However, the array with the lowest solid volume fraction (I-0.090-1.000-5.4) results in the slowest gravity current propagation, which is contrary to the prediction of $\overline{Fr}$ variation with ϕ for equidistant arrays (e.g. Zhang & Nepf 2008). At later stages of all the cases, the front speed starts to decrease. A thorough discussion of $\overline{Fr}$ averaged over $t = 2t_0 \sim 21.5t_0$ across a broad range of array configurations is provided in §5.3.2, where we focus on the current propagation in the slumping phase before any decelerating effects become significant. The fact that the current nose in case I-1.000-0.272-5.4 is initially slightly ahead of that in case F-0-5.4 but overtaken around $t = 60t_0$ is discussed later in §5.5.2.1.

For a better interpretation of the self-similar propagation of the gravity current for these representative simulations, figure 5.5 is replotted using log-log scale in figure 5.6. For case F-0-5.4, due to the finite volume of the release, a disturbance with the appearance of an internal hydraulic drop generated at the lock endwall eventually overtakes the current front and causes it to decelerate. Consequently, after a transitional phase, the gravity current reaches a buoyancy-inertial self-similar phase (black line in figure 5.6a). The corresponding front trajectory follows a power law, $x_f \sim t^{2/3}$ (or equivalently $U_f \sim t^{-1/3}$ where t is the time since release), which is consistent with the theoretical value proposed by Rottman & Simpson (1983). The buoyancy-viscous phase was not observed due to the high Re in the time frame considered.

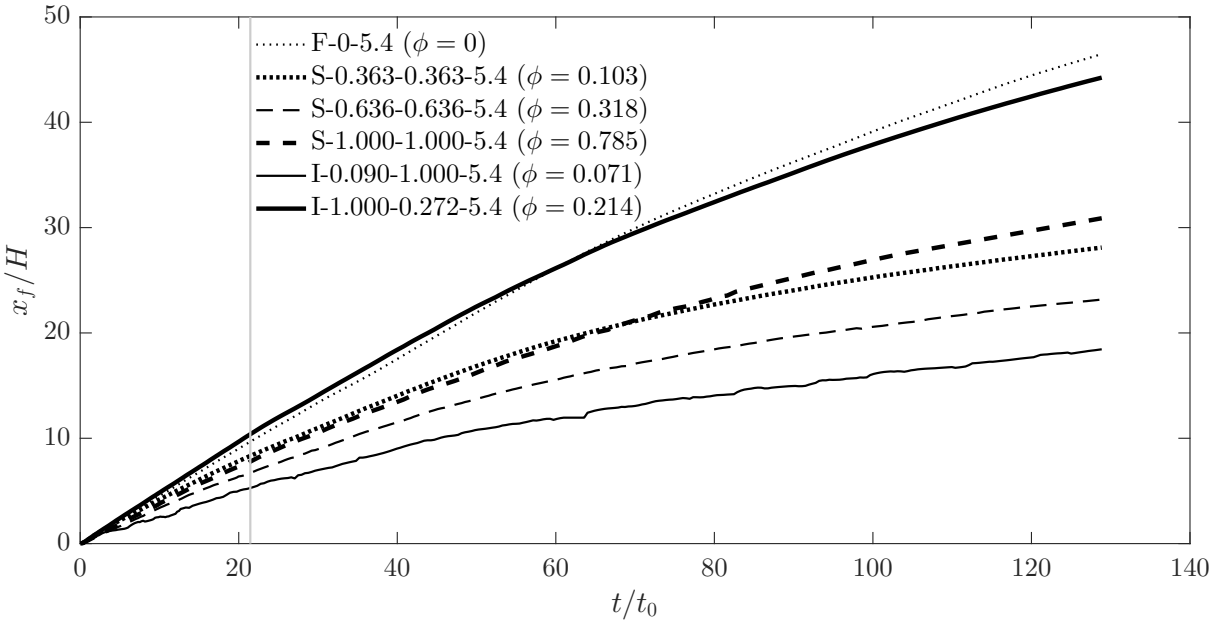

Figure 5.5: Time variation of the dimensionless front position x_f/H as a function of the dimensionless time t/t_0 for six representative simulation cases. The vertical gray line indicates the time ($t = 21.5t_0$) before which the front trajectories can be well approximated by lines with constant slopes.

Compared with the flat-bed case, the presence of obstacles alters the self-similar property of the gravity current propagation after the slumping phase because of different mechanisms. In case S-0.363-0.363-5.4 (blue line in figure 5.6a), the gravity current is within the through-flow regime. Initially the current adjusts to the uniformly-distributed array drag until $t \approx 10t_0$ when the deviation of the front trajectory from the flat-bed case occurs. Later on, the array drag becomes increasingly significant as more obstacles are immersed in the current body, and finally the gravity current transitions to a turbulent drag-dominated phase ($x_f \sim t^{1/2}$) in which the front velocity decreases faster than that of the buoyancy-inertia phase in case F-0-5.4, which is consistent with the analytical model for a finite release proposed by Hatcher *et al.* (2000).

Comparison between the two dense cases within the over-flow regime, i.e. S-0.636-0.636-5.4 and S-1.000-1.000-5.4, reveals their different propagating dynamics. In case S-0.636-0.636-5.4 (figure 5.9c), the clear-cut over-nose controls the bulk propagation and the vertical convection is the main contributor to the dilution of the over-current. However, the relatively large volume of dense fluid trapped within the array due to the high porosity of the array ($p = 1 - \phi = 0.682$),

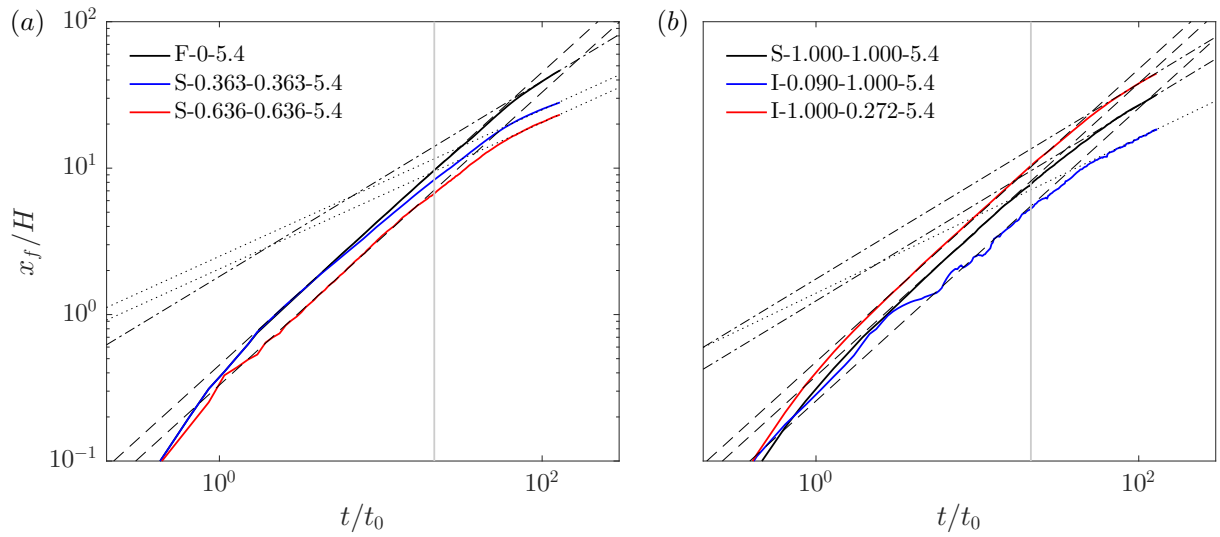

Figure 5.6: Representation of figure 5.5 using log-log scale. The vertical gray line demarcates the constant-speed slumping phase and the subsequent self-similar phases. Best fitting lines in the form of $x_f \sim t^k$ are plotted for $k = 1$ (- - -), $k = \frac{2}{3}$ (-·-·-) and $k = \frac{1}{2}$ (·····), respectively. For ease of visualization: (a) front positions corresponding to figure 5.9(a, b, c); (b) front positions corresponding to figure 5.9(d, e, f).

together with the drag exerted by the turbulent cylinder wakes, albeit small, still result in a power dependence of $x_f \sim t^{1/2}$ similar to case S-0.363-0.363-5.4. In contrast, the longitudinal current propagation in case S-1.000-1.000-5.4 is completely above the array top boundary, with the fluid motion within the array being purely subject to vertical convective instability (figure 5.9d). As a result, the gravity current exhibits another self-similar property in which $x_f \sim t^{2/3}$. The possible mechanism accounting for this power dependence is the overtaking of the reflected bore due to the finiteness of the lock-release that is similar to the flat-bed case. This slower decrease of the front velocity in case S-1.000-1.000-5.4 as compared to the $x_f \sim t^{1/2}$ relationship of the turbulent drag-dominated phase in case S-0.363-0.363-5.4 can also explain the fact that the front position of the former case slightly lags behind but overtakes the latter around $t = 70t_0$ in figure 5.5.

The two cases with non-equidistant arrays in figure 5.6(b) are also found to have different post-slumping self-similarities in current propagation. In case I-0.090-1.000-5.4 (plunging-flow regime in figure 5.9e), the gravity current decelerates when moving upwards on encountering the upstream face of each row of obstacles, and accelerates when moving downwards after it passes the cylinder free ends. Consequently, the front trajectory is subject to large-amplitude temporal

variations. After a transitional phase, the current enters a turbulent drag-dominated regime where $x_f \sim t^{1/2}$. A similar array geometry (ribs with $\mu_x = 0.05 \sim 1$, $\mu_y = 1$) was studied by Tokyay *et al.* (2014) and the same drag-dominated regime was found. On the other hand, the current in case I-1.000-0.272-5.4 is within the skimming-flow regime (figure 5.9f) where the array drag is largely reduced. The flow dynamics of each sub-current is basically the same as in the flat-bed case (compare figures 5.9a and 5.9f) such that the front position evolves as the buoyancy-inertial self-similarity, $x_f \sim t^{2/3}$.

5.3.2 Time-averaged Front Velocity in the Slumping Phase

As shown in figures 5.5 and 5.6, within the range of $t = 2t_0 \sim 21.5t_0$ demarcated by the gray line, the gravity current is propagating in the slumping phase or around the beginning of transition to subsequent self-similar phases, and thus a constant-speed approximation is appropriate. In what follows, we briefly discuss the time-averaged Froude number of the frontmost nose (either through or above the array) in this time frame, which is defined as

$$\overline{Fr}^* = \max\left\{\overline{Fr}_{ON}, \overline{Fr}_{TN}\right\}, \tag{5.11}$$

where $\overline{Fr}_{ON}$ and $\overline{Fr}_{TN}$ are the Froude numbers of the over-nose (ON) and the through-nose (TN), respectively. The submergence ratio is fixed at $H/h = 5.4$.

Figure 5.7 shows the variation of $\overline{Fr}^*$ with μ_x or μ_y with the other being fixed, for both in-line and staggered arrangements. As will be discussed in §5.5, the two acceleration mechanisms of the gravity current are the transition to skimming-flow and over-flow, respectively. For in-line arrays in figure 5.7(a), the value of $\overline{Fr}^*$ first decreases and then increases with increasing μ_x at any fixed μ_y. For low-to-moderate μ_y, based on the flow-regime classification in §5.4, the increase of $\overline{Fr}^*$ with increasing μ_x is the consequence of a through-to-skimming transition (see §5.5.2.1). On the other hand, for large μ_y, the streamwise densification of the array results in a much earlier increase of $\overline{Fr}^*$, which is caused by a plunging-to-over transition (see §5.5.2.2).

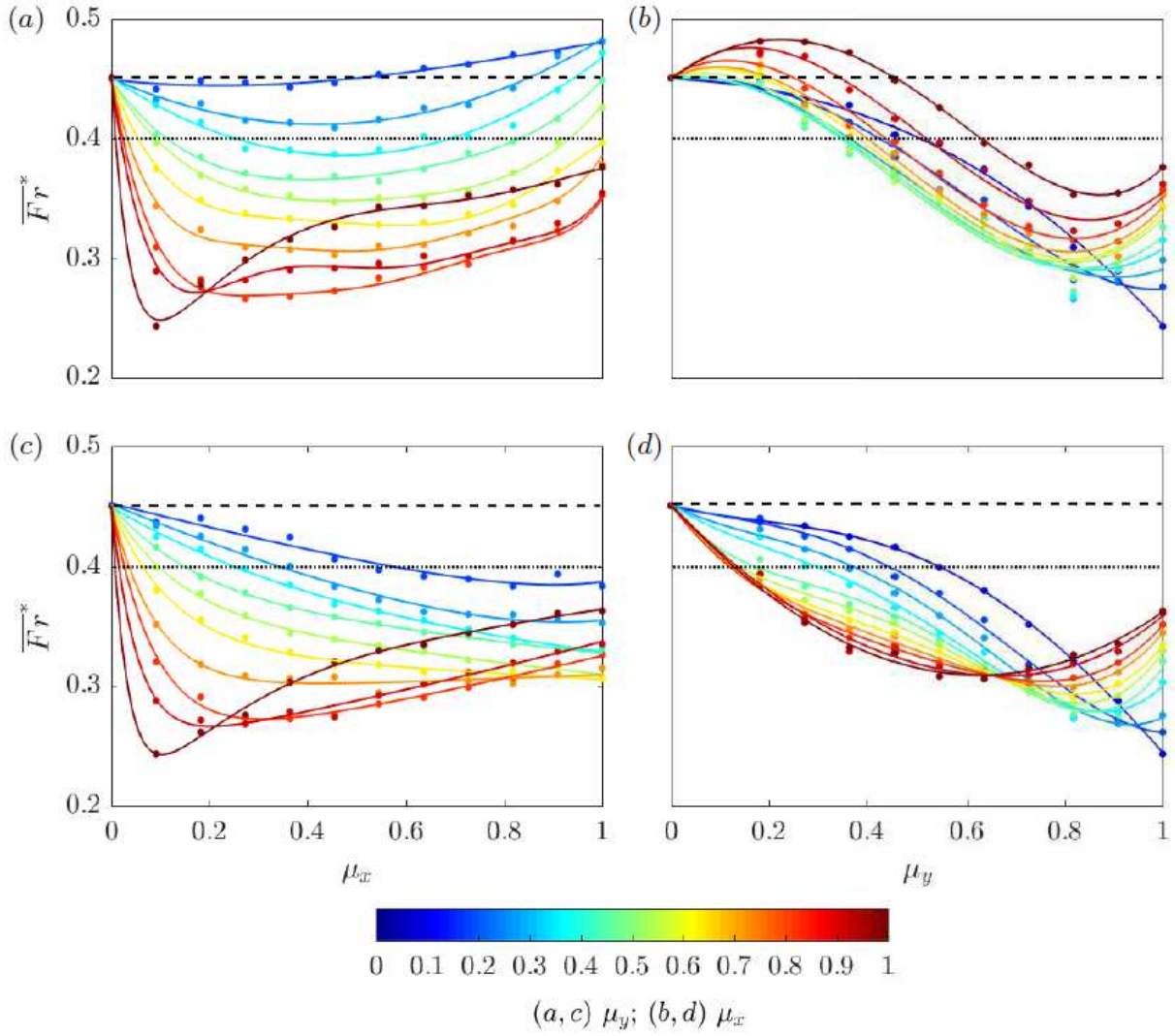

Figure 5.7: Froude number versus streamwise (spanwise) array density at fixed spanwise (streamwise) array densities under a submergence ratio of $H/h = 5.4$. (a, b) in-line arrays; (c, d) staggered arrays. Circles show the values of $\overline{Fr}^*$ averaged over the interval $t = 2t_0 \sim 21.5t_0$ and solid lines are the best fitting curves with $R^2 \geq 0.98$. The two limiting cases are included in each panel: flat-bed case F-0-5.4 (- - -); solid-slab case F-1-5.4 (·····).

The independent effects of μ_y on $\overline{Fr}^*$ are shown in Figure 5.7(b). For very small μ_x, increasing μ_y leads to a monotonic decreases of $\overline{Fr}^*$ due to the net increase of drag without any accelerating mechanism present. At a fixed moderate-to-large μ_x, as μ_y increases, initially the through-to-skimming transition accelerates the current even faster than the flat-bed limit ($\overline{Fr}^*$=0.45, the dashed line). Successive increase of μ_y causes the current to decelerate because of the increasing array drag. Finally, as μ_y is increased further, the gravity current is accelerated again due to the transition to over-flow.

Two major differences are observed for the staggered arrays shown in figure 5.7(c, d). Firstly, the through-to-skimming accelerating mechanism is absent due to the interruption of interstitial flow by the offset rows (see §5.5.2.1). In figure 5.7(c), the increase of μ_x at a fixed μ_y leads to a monotonic decrease of $\overline{Fr}^*$ except for the cases with $\mu_y \geqslant 0.818$ where the plunging-to-over transition accelerates the current motion (see §5.5.2.2). Secondly, in figure 5.7(d), the critical value of μ_y beyond which $\overline{Fr}^*$ starts to increase becomes smaller for contours with larger μ_x, which is not the case for in-line arrays (figure 5.7b). At a fixed μ_x, as μ_y increases, there is a more remarkable growth of the array drag promoting the transition to over-flow due to the offset interruption.

5.4 Flow Regimes

Now, we discuss in detail the the various flow regimes mentioned in §5.3. In the spirit of using the new two-dimensional parameter space to predict the current-array interaction as outlined in §5.1, an interpolated recast of figure 5.7 in the μ_x-μ_y space is shown in figure 5.8. We define a dimensionless parameter,

$$\epsilon = \overline{Fr}^* / \overline{Fr}^*_{\phi=0}, \tag{5.12}$$

where $\overline{Fr}^*_{\phi=0}$ is the base value from the flat-bed case. In consequence, Figure 5.8 represents the *net effects* of the array with a specific μ_x-μ_y combination on the gravity current propagation with respect to the unobstructed flat-bed condition. By allowing for the independent variation of μ_x and μ_y with the corresponding ϕ-contours embedded, figure 5.8 facilitates a convenient and

unambiguous interpretation of the parametric dependence of the various flow regimes and their mutual transitions on array geometry. The key message is that there is an infinite number of possible states of flow along a single contour of ϕ, emphasizing the inappropriateness of using the conventional ϕ-parameterization of array geometry whenever their is a nonnegligible degree of array non-equidistance.

The density structures corresponding to different flow regimes are shown in figure 5.9. In the flat-bed case F-0-5.4 (figure 5.9a), the classic gravity current interface and the lobe-and-cleft structures are clearly observed. Once the array is present, the flow structure starts to differ from the flat-bed case to varying degrees. Depending on the specific combination of μ_x and μ_y, four distinct flow regimes of an obstructed gravity current are possible:

- *Through-flow* (figure 5.9b). For in-line arrays with small μ_x and small μ_y or staggered arrays with arbitrary μ_x and small μ_y, the gravity current propagates along the channel bed, finding its way through the pore regions between individual obstacles, which is referred to as the through-nose (TN). The isolated cylinder wakes and their interferences act as the major turbulence-energy dissipator (Cenedese *et al.* 2016). This regime bears some similarities to gravity currents in sparse emergent canopies (Tanino *et al.* 2005) or gravity currents propagating inside a highly porous medium over a solid boundary (Ozan *et al.* 2015) where the current interface resembles that of a classic flat-bed gravity current (figure 5.9a).

- *Over-flow* (figures 5.9c, d). For arrays with large μ_x and large μ_y, due to the excessive drag of a dense array with respect to the horizontal pressure gradient, a well-defined over-nose (ON) propagates along the top boundary of the array and controls the overall current propagation. Significant vertical convection (VC) occurs between the over-nose and the underlying lighter ambient fluid, leading to intense turbulent mixing (Cenedese *et al.* 2016). The volume of dense fluid trapped within the array increases with propagated distance of the current. Therefore, the advancement of the over-current is accompanied by a continuous loss of the effective buoyancy that drives its propagation, which scales as

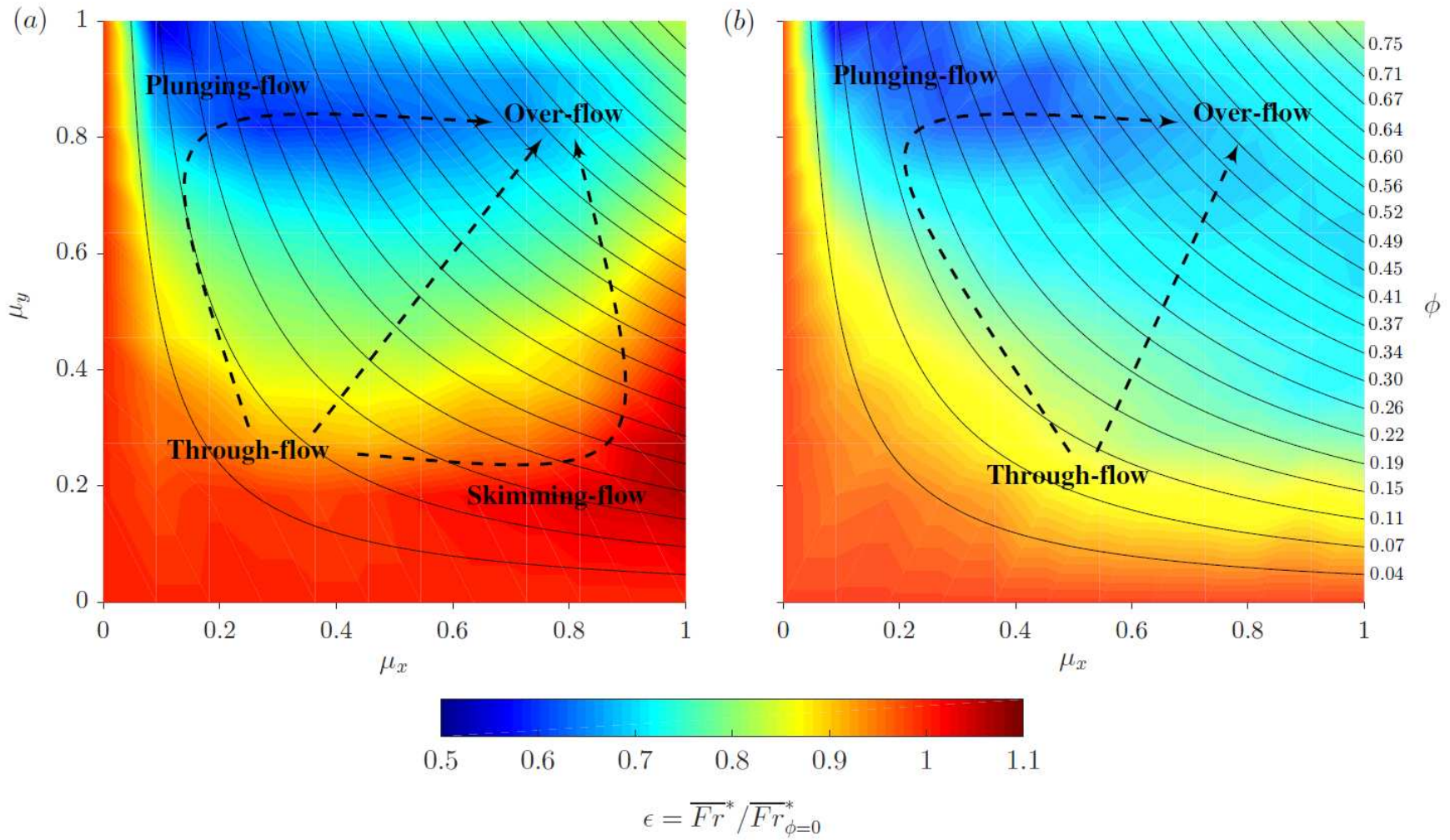

Figure 5.8: Variation of ϵ as defined in equation (5.12) in μ_x-μ_y space under a submergence ratio of $H//h = 5.4$. (a) in-line arrays; (b) staggered arrays. Solid curves indicate contours of $\phi = (\frac{\pi}{4})\mu_x\mu_y$ with their values marked on the right hand side of (b). Approximate regions corresponding to different flow regimes are annotated in both panels. Different paths of flow transition are shown by dashed arrows. The time-averaging period is $t = 2t_0 \sim 21.5t_0$.

$$\mathcal{B}_e \sim g'_e \mathcal{V}_e, \tag{5.13}$$

where g'_e is the effective reduced gravity of the gradually diluted over-nose ($g'_e \leqslant g'_{e,t=0} = g\left(\rho_{max} - \rho_{min}\right)/\rho_{max}$), and $\mathcal{V}_e$ is the gradually reduced volume of dense fluid above the array top boundary ($\mathcal{V}_e \leqslant \mathcal{V}_{e,t=0} = WL_{lock}(H-h)$), using the notation in figure 5.1. This flow regime is similar to gravity currents over a porous boundary (Ungarish & Huppert 2000) or particle-driven gravity currents (An *et al.* 2012) in the sense that the dense current system undergoes a continuous loss of effective buoyancy as it advances. The through-current, albeit weakened, still persists (figure 5.9c) until the maximum array density for circular cylinders ($\phi = \pi/4 \approx 0.785$) is achieved where no longitudinal propagation is permitted within the array (figure 5.9d). In this case, the fluid motion within the pores is purely convective, and the shape of the over-nose evolves closer to the flat-bed limit.

- *Plunging-flow* (figure 5.9e). For arrays with small μ_x and large μ_y, array non-equidistance greatly affect the current propagation dynamics. Due to the strong blocking effect by each spanwise row of obstacles, the nose of the gravity current is projected upwards when it reaches the upstream face of each spanwise row, and then plunges towards the bed between two adjacent rows. This is similar to the k-type roughness reviewed by Jimenez (2004) for constant-density flows. The large-eddy simulations of a gravity current over a series of submerged 2-D obstacles by Tokyay *et al.* (2011a) fall within this category.

- *Skimming-flow* (figure 5.9f). For in-line arrays with large μ_x and small μ_y, the cylinder wakes are greatly suppressed, and the gravity current is separated into several highly independent sub-currents that pass through the array interior along the streamwise direction, with minimal cross-stream interactions. Here, we follow the nomenclature of Oke (1988) where the mesoscale atmospheric boundary-layer flow is almost decoupled from the recirculation region within urban canopies when buildings are closely spaced, corresponding to the d-type roughness in Jimenez (2004), if applied to the spanwise direction. This is the only regime

that is absent in staggered arrays where streamwise channelizing is always interrupted by the next offset rows (compare figure 5.8a, b).

In figure 5.8, starting from the flat-bed case, as one moves along the 45°-diagonal (equidistant array), ϵ is seen to first decrease and then increase, signifying the through-over transition. However, when moving along the detours of the through-plunging (skimming)-over transitions, array non-equidistance starts to significantly influence the flow dynamics. In the plunging-flow regime, the current can be heavily impeded by fairly sparse arrays. whereas in the skimming-flow regime, the gravity current may be propagating even faster than the flat-bed case, i.e. $\epsilon > 1$. The three pathways of flow transition, i.e. the through-over, through-plunging-over and through-skimming-over transitions, will be discussed in detail is §5.5.

The most remarkable difference between the the in-line and staggered cylinder arrangements is the nonexistence of the skimming-flow regime in figure 5.8(b) due to the offset interruption. The blue zone with low values of ϵ in figure 5.8(b) appears more diffused than that in figure 5.8(a). This can be interpreted using the one-dimensional plots shown in figure 5.7 where either of the two parameters, μ_x and μ_y, is fixed: (i) streamwise densification: in figure 5.7(c), except along contours of very large μ_y, the increase of μ_x is accompanied by a decrease of $\overline{Fr}^*$, signifying a net increase of resistance to the through-current as opposed to the case of in-line arrays (figure 5.7a). This extends the zone of low ϵ to the lower right portion of figure 5.8(b); and (ii) spanwise densification: in figure 5.7(d), $\overline{Fr}^*$ starts to increase at smaller value of μ_y along contours of larger μ_x, signifying an earlier transition to the over-flow as compared to the almost unchanged threshold value of μ_y in figure 5.7(b). This causes a less prominent deep-blue zone in the upper right portion of figure 5.8(b).

5.5 Flow Transitions

In what follows, we discuss three possible paths of flow-regime transitions annotated by the dashed arrows in figure 5.8. The direct through-over transition for equidistant arrays ($T \Rightarrow O$) is discussed in §5.5.1. We then follow with the assessment of the effects of array non-equidistance

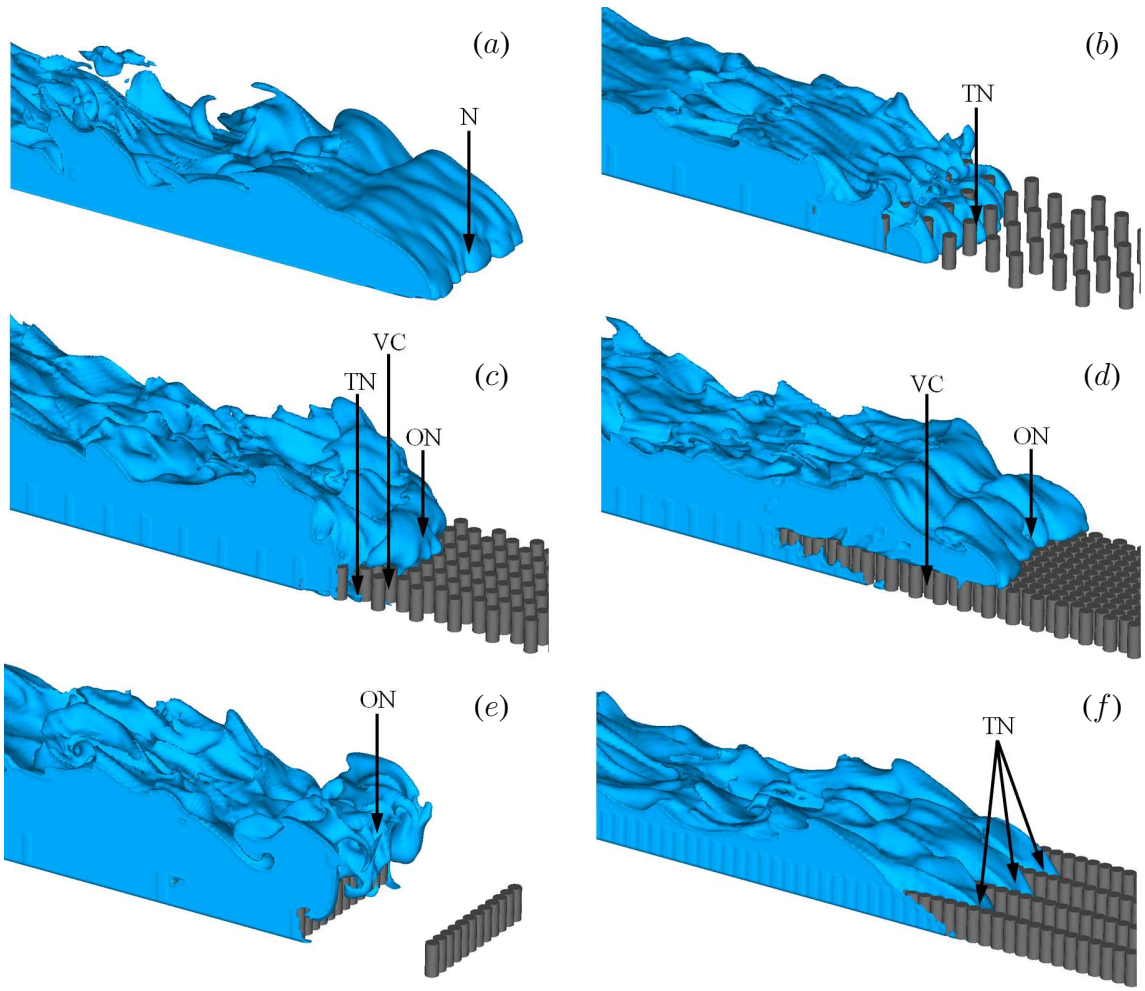

Figure 5.9: Visualization of representative flow structures using instantaneous density isosurfaces, $\rho \geqslant 0.5$. (a) F-0-5.4 (unobstructed flat bed, $\phi = 0$); (b) S-0.363-0.363-5.4 (equidistant and sparse, $\phi = 0.103$); (c) S-0.636-0.636-5.4 (equidistant and dense, $\phi = 0.318$); (d) S-1.000-1.000-5.4 (highest density achievable for circular cylinders, $\phi = \pi/4$); (e) I-0.090-1.000-5.4 (impermeable fences, $\phi = 0.071$); (f) I-1.000-0.272-5.4 (channelization, $\phi = 0.214$). The arrows mark the unobstructed nose (N), through-nose within the array (TN), over-nose above the array (ON) and the vertical convection within the pore regions (VC), respectively.

in §5.5.2. The through-skimming-over flow transition ($T \Rightarrow S \Rightarrow O$) is discussed in §5.5.2.1, and the through-plunging-over flow transition ($T \Rightarrow P \Rightarrow O$) is discussed in §5.5.2.2.

5.5.1 Equidistant Array: Through-over Flow Transition

5.5.1.1 Density and Velocity Structures

In this section, we analyze the flow transition dynamics from the through-flow regime directly to the over-flow regime without the effects of array non-equidistance. Figure 5.10 depicts the instantaneous fluid density fields with ϕ ranging from 0 to 1. Figure 5.10(a) shows the classic structure of a gravity current propagating on a smooth bottom. In figure 5.10(b), the array is sparse such that the gravity current propagates along the channel bed, finding its way either between or over the cylinders. Compared with the flat-bed case, the net increase of array drag slows down the gravity current mainly by the turbulent dissipation in the cylinder wakes. Denser arrays tend to divert the current above the array, and a discernible over-current gradually emerges (figure 5.10c). The over-current is diluted mainly due to the exchanged flow coming from underneath. In case S-1.000-1.000-5.4 (figure 5.10d), through-flow is completely blocked and the current fills the space between cylinders with dense fluid as it advances. The vertical convection is stronger and thus enhancing the current dilution as compared with that in figure 5.10(c). Eventually, in the solid-slab case (figure 5.10e), the dense fluid only exists and propagates above the solid obstacle with a height of h placed on the channel bed. The density structure again resembles that of the flat-bed case but with smaller flow depth ($H - h$).

It is evident from figures 5.8 and 5.10 that as the gravity current transitions from through-flow to over-flow, its time-averaged front velocity begins to increase with array densification. This $T \Rightarrow O$ transition is the first possible acceleration mechanism for a gravity current past a submerged array. For this flow transition path, the pore regions between the cylinders behave like a "void roughness" in the sense that the over-current is subject to less momentum loss as it approaches the solid-slab limit F-1-5.4 with a porosity $p = 0$ (i.e. $\phi = 1$). In case F-1-5.4, according to equation (5.13), $\mathcal{V}_e \equiv \mathcal{V}_{e,t=0}$ since no trapping of dense fluid within the array occurs after the gate removal.

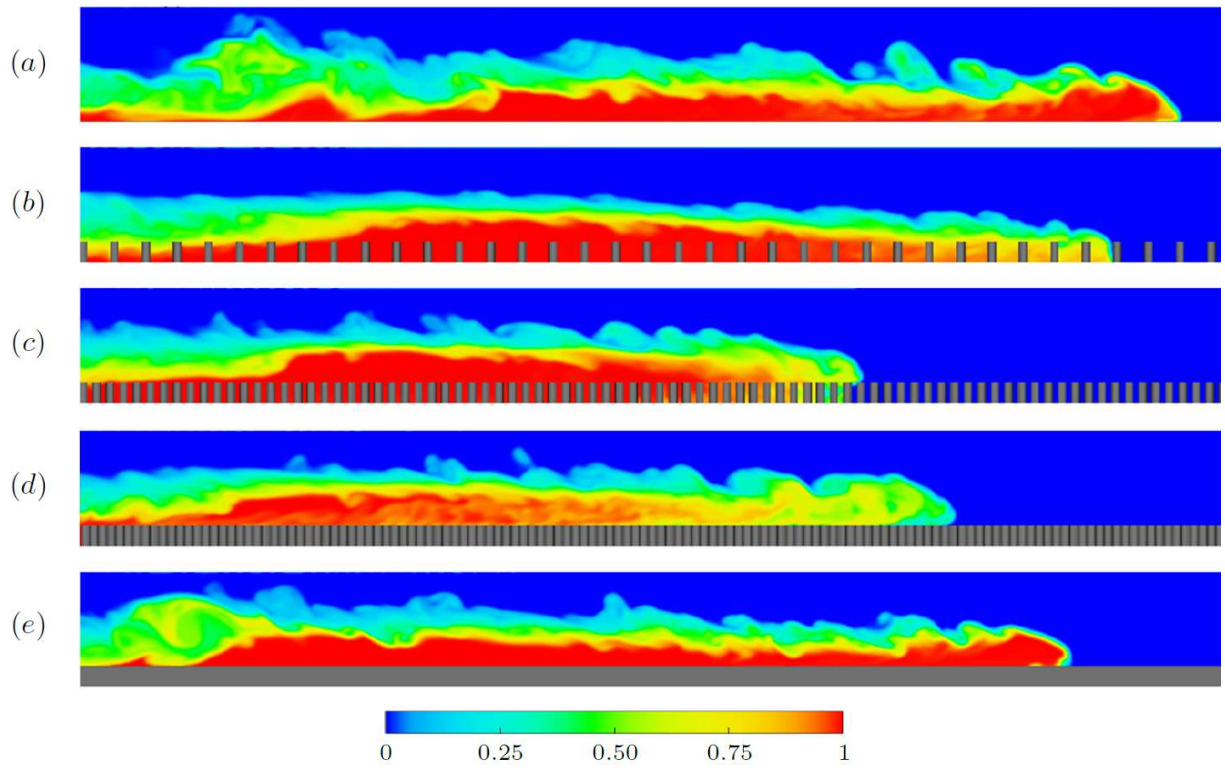

Figure 5.10: Instantaneous fluid density fields along the channel centerline at $t = 21.5t_0$ showing the $T \Rightarrow O$ transition. (a) F-0-5.4; (b) S-0.272-0.272-5.4; (c) S-0.636-0.636-5.4; (d) S-1.000-1.000-5.4; (e) F-1-5.4. Roughness elements are shown in dark gray. The lock region ($-L_{lock} \leqslant x < 0$) is not shown.

Assuming negligible effects of the abrupt elevation of the channel bottom at the lock gate, an estimate of the Froude number can be obtained as

$$\overline{Fr}^*_{\phi=1} = \overline{Fr}^*_{\phi=0}\sqrt{\frac{H-h}{H}}, \tag{5.14}$$

where $H - h$ is the effective lock height which is time-invariant due to zero array porosity. The resulting $\overline{Fr}^*_{\phi=1}$ for $H/h = 5.4$ is calculated to be 0.406 ($\epsilon = 90\%$), which is slightly larger than the LES value of 0.401 ($\epsilon = 89\%$), presumably because of the energy loss near the leading edge of the slab at $x = 0$. For case S-1.000-1.000-5.4, $\overline{Fr}^*_{\phi=\pi/4} = 0.363$ ($\epsilon = 81\%$). The reason is that the presence of the pores between cylinders results in an additional reduction of $\mathcal{V}_e$ which increases with time because of the array porosity, $p = 0.215$. Besides, the effective density difference, g'_e, is also reduced due to the enhanced dilution of the over-current with respect to the solid-slab case.

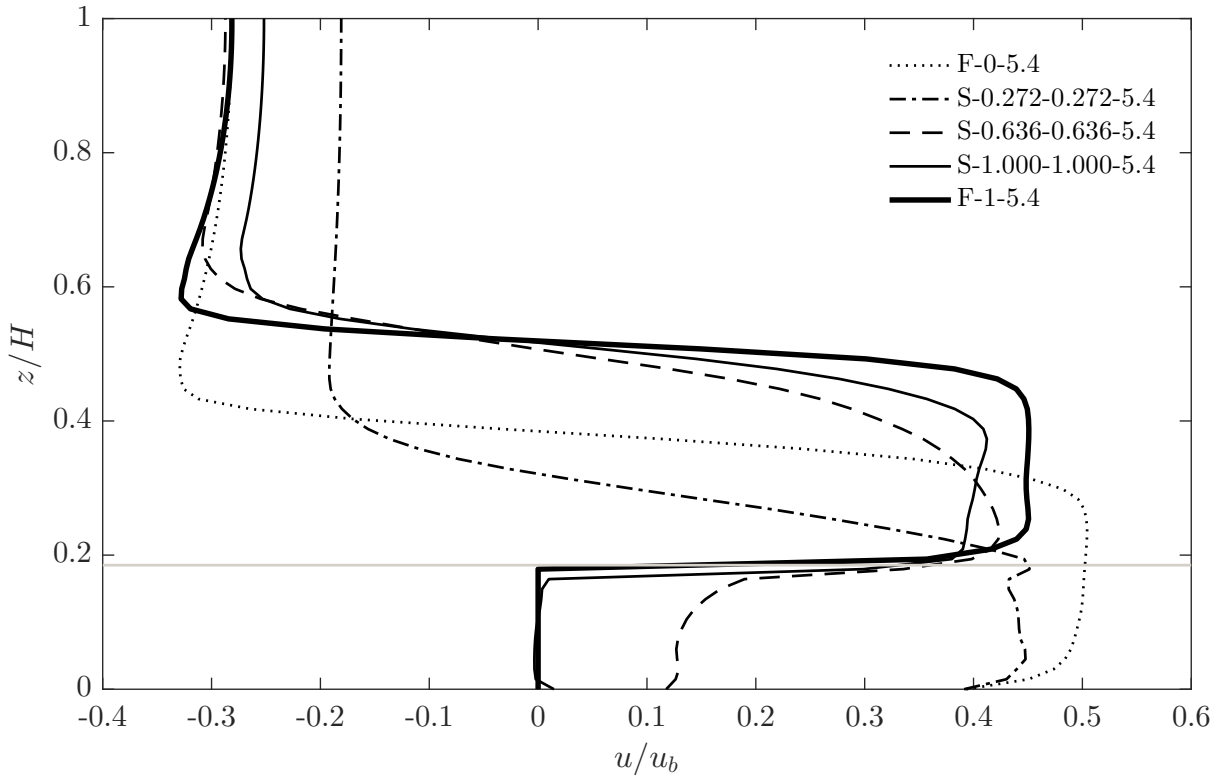

Figure 5.11: Time-averaged and laterally-averaged horizontal velocity profiles showing the $T \Rightarrow O$ transition for equidistant arrays. The velocity data are recorded at a distance of $H/2$ behind the current nose by moving with the gravity current frame. The time-averaging period is $2t_0 \sim 21.5t_0$. The horizontal gray line marks the array top.

Consequently, this continuous decay of $\mathcal{B}_e$ that is absent in the solid-slab case results in a 9.5% difference between $\overline{Fr}^*_{\phi=\pi/4}$ and $\overline{Fr}^*_{\phi=1}$.

Figure 5.11 shows the time-averaged and laterally-averaged horizontal velocity profiles corresponding to the cases in figure 5.10. The velocity data are taken from the cross section at a distance of $H/2$ behind the current leading edge as we move with the current frame. The time-averaging is performed over $2t_0 \sim 21.5t_0$ as in §5.3.2. Starting from the flat-bed case, a clear transition from through-flow to over-flow can be observed. The velocity profile of the through-flow case, S-0.272-0.272-5.4, resembles that of case F-0-5.4 but with smaller mean magnitude. As ϕ increases further, the average horizontal velocity within the array decreases, and reaches zero in cases S-1.000-1.000-5.4 and F-1-5.4 as expected, which implies a gradual suppression of longitudinal propagation. Meanwhile, above the array, the horizontal momentum of the over-current

recovers as the array is densified, and eventually reaches the solid-slab case where all the dense fluid is propagating along the array top.

The array density ϕ is observed to influence the driving mechanism of the flow within the array, which is similar to that of constant-density barotropic flows over a submerged canopy despite of the difference in flow forcing. For example, Nepf (2012) suggested that for a sparse array, the velocity follows a turbulent boundary-layer profile, while for a dense array, suppression of the downward penetration of the vertical turbulent stress leads to enhanced shear below and above the array top. Similarly, in the context of gravity currents, for sparse arrays, the velocity follows a hyperbolic-tangent profile as with the classic flat-bed case (compare velocity profiles of F-0-5.4 and S-0.272-0.272-5.4 in figure 5.11). As the array becomes denser, there is a gradual suppression of through-current propagation and acceleration of the over-current, which strengthens the horizontal shear layer at the array top boundary.

Figure 5.12 sheds some light on the dilution of the over-current observed in figure 5.10. We define the lower region of the array as the "longitudinal propagation zone" ($0 \leqslant z < \delta$) where the flow communicates with the surrounding water predominantly through longitudinal current propagation. The remaining upper array is defined as the "vertical convection zone" ($\delta \leqslant z < h$) where turbulent buoyancy fluxes dominate the flow behavior. The vertical convection zone (if it exists) is only prominent near the over-nose, and weakens upstream of the nose due to the gradual homogenization of the water column after the passage of the over-current. In figure 5.12(a), the gravity current is in the through-flow regime and no vertical convection zone exists. The in-array flow is purely due to longitudinal advection driven by the pressure gradient. In figure 5.12(b), the increase of array drag results in the coexistence of over- and through-currents interconnected by a vertical convection zone. One portion of the light fluid between the cylinders is vertically exchanged with the denser over-current, while the remaining favors a horizontal propagation below $z = \delta$, forming the longitudinal propagation zone. However, for the case in which horizontal propagation is fully blocked (figure 5.12c), despite the smaller amount of lighter fluids initially within the array at higher ϕ, they are all forced to exchange with the overlying denser over-current,

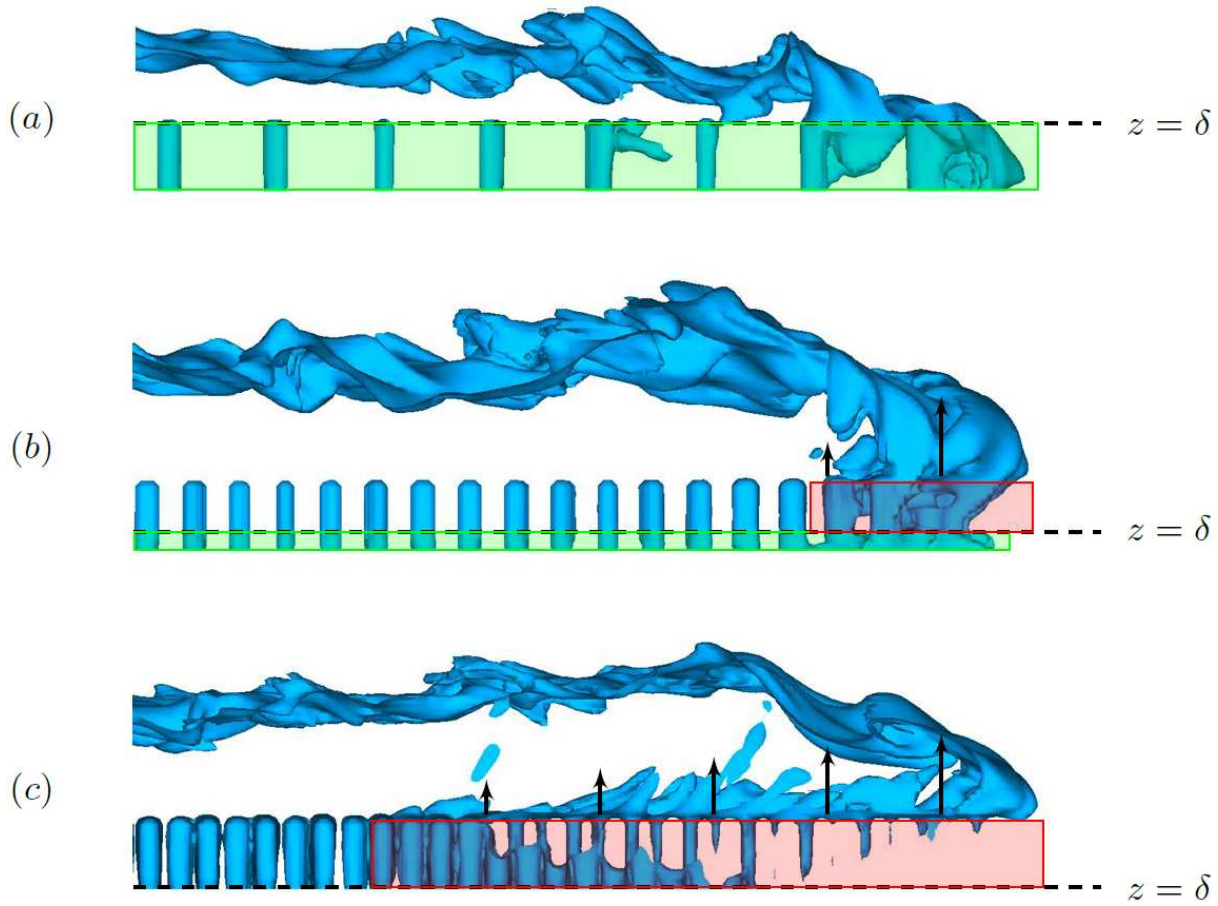

Figure 5.12: Instantaneous density isosurface at $\rho = 0.5$ for different array densities. (a) S-0.272-0.272-5.4; (b) S-0.636-0.636-5.4; (c) S-1.000-1.000-5.4. The horizontal dashed lines roughly divides the in-array region into a longitudinal propagation zone ($0 \leqslant z < \delta$, encompassed by the green window) and a vertical convection zone ($\delta \leqslant z < h$, encompassed by the red window). Arrows indicate the ejection of the lighter ambient fluid from underneath, with their length signifying the strength of the vertical exchange. Note, the vertical convection is more pronounced near the over-nose, and vanishes far upstream where the water column is largely homogenized.

resulting in an enhanced dilution of the over-current as shown in figure 5.10(d) in comparison with that in figure 5.10(c).

5.5.1.2 Dilution of the Over-current

Figure 5.13 shows the variation of mixing pattern of the gravity currents in the over-flow regime by visualizing the evolution of fluid density with time along a fixed horizontal line located slightly above the array top. Consistent with §5.3.1, the over-nose is initially propagating at a constant speed and then begins to mildly slow down which leads to smaller angles between the front trajectory and the time axis. Both the passage of the interfacial billows over the $0.03H$ line and the vertical mixing with the lighter fluid within the array contribute to the dilution of the gravity current. As ϕ increases, despite the smaller volume of ambient fluids within the array pores, they favor a vertical exchange other than longitudinal propagation due to the growing array drag. As a consequence, the dilution of the gravity current becomes stronger for denser arrays. Around $t = 5.2t_0$ in case S-1.000-1.000-5.4 (figure 5.13c), the vertical buoyancy forcing is so strong that a large-scale ejection of the underlying light fluid into the over-current occurs, leading to a significant amount of turbulent mixing. This ejection event is found to be intermittent also at later times (not shown here), which is analogous to the case of constant-density flows in the context of quadrant-hole analysis (e.g. Finnigan 2000).

5.5.1.3 Global Energy Budget

In essence, a density-driven gravity current can be interpreted as a conversion of potential energy into kinetic energy, which subsequently is dissipated into heat by viscous friction. To better understand the through-to-over transition, a global energy budget is performed using the approaches by Necker *et al.* (2005), Ooi *et al.* (2009) and Ozan *et al.* (2015) for compositional gravity currents. The differential equation relating the rates of change of the potential and kinectic energy can be expressed as

$$\frac{\mathrm{d}}{\mathrm{d}t}\left(E_k + E_p\right) = -\varepsilon, \tag{5.15}$$

where E_k and E_p is the total kinetic energy and excess potential energy over the flow domain Ω,

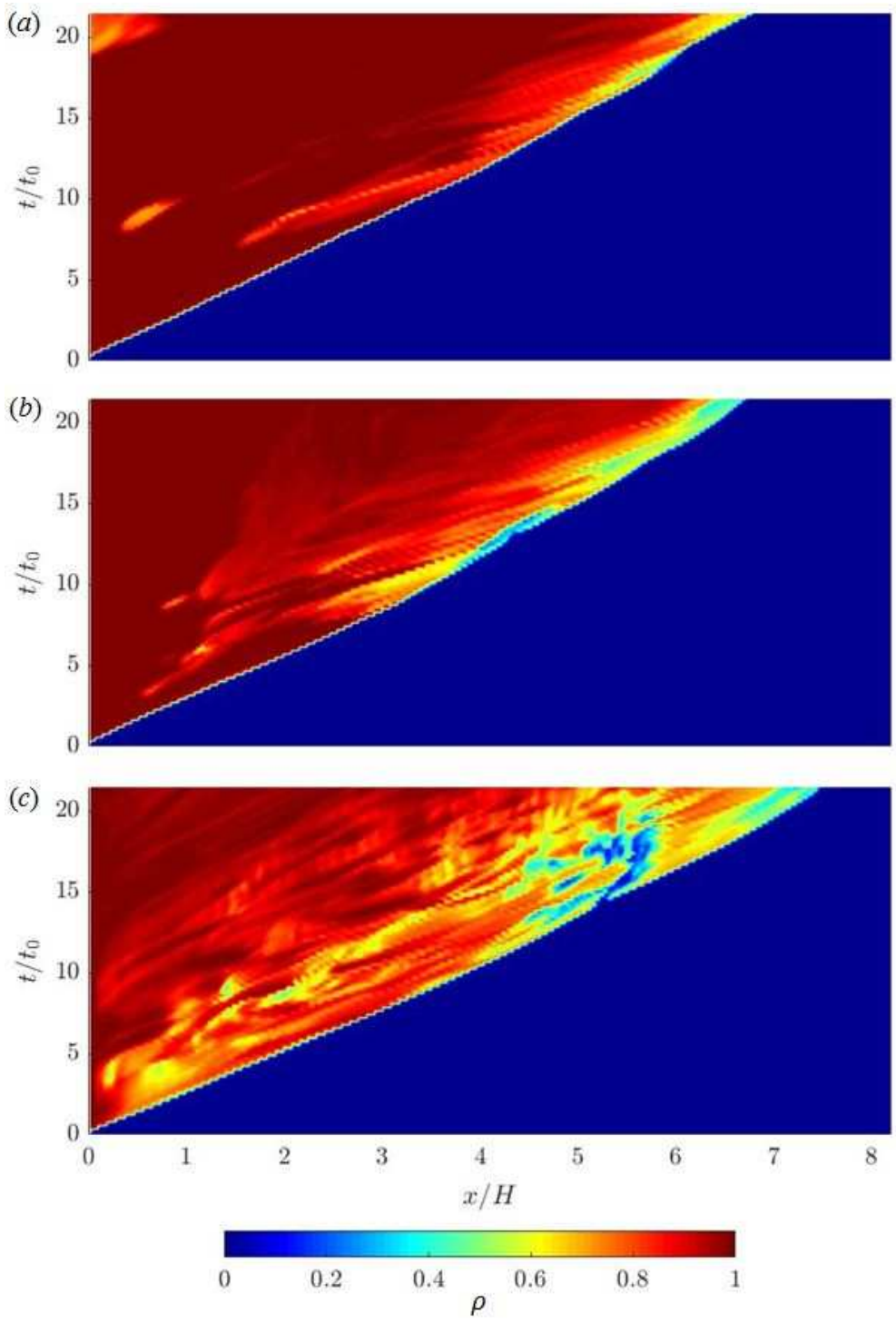

Figure 5.13: Evolution of fluid density with time along the x-axis which is located $0.03H$ above the array top ($z = h_a + 0.03H$). (a) case S-0.636-0.636-5.4; (b) S-0.818-0.818-5.4; (c) S-1.000-1.000-5.4.

$$E_k(t) = \int_\Omega \frac{1}{2} u_i u_i dV, \tag{5.16}$$

$$E_p(t) = \int_\Omega \rho z dV, \tag{5.17}$$

and ε is the total dissipation rate. Integrating equation (5.15) with respect to time yields the balance equation for the mechanical energy,

$$E_k + E_p + E_d = E_{k0} + E_{p0}, \tag{5.18}$$

where E_{k0} and E_{p0} are the total initial ($t = 0$) kinetic and potential energy, and $E_d(t) = \int_0^\tau \varepsilon(\tau) d\tau$ is the time integral of the total dissipation rate. For the lock-release configuration in this study which starts from rest, $E_{k0} = 0$. The variation of the terms in equation (5.18) with time is plotted in figure 5.14 for the simulations of submerged arrays with ϕ ranging from 0 to 1 with equidistant and staggered configurations. In all the simulations, a first regime characterized by a rapid conversion of potential energy into kinetic energy is present until $t \approx 8t_0$. Afterwards, the rate of decay of E_p becomes smaller, whereas E_k starts to decrease due to the growing effect of dissipation.

The transition process from through flow to over flow can be easily analyzed from the energy-conversion perspective using figure 5.14, where the global energy budget is observed to be a strong function of the array density. The introduction of a sparse array with small ϕ results in a considerable increase of E_d compared with the flat-bed case ($\phi = 0$). In the range of ϕ up to 0.1, the gravity current is propagating within the through-flow regime, and E_d increases with ϕ mainly because of the turbulent dissipation in the cylinder wakes. As the array becomes further denser, the closeness between cylinders begins to give rise to wake sheltering effects which suppress E_d. The average potential energy undergoes a monotonic increase with increasing ϕ. The reason for this trend is the increasing occupation of space by solids that forces the mass center of the flow to shift upwards, which is consistent with the studies of gravity currents through sparse arrays, either submerged or (Tokyay *et al.* 2011*a*) or emergent (Ozan *et al.* 2015). The rate of increase of E_p becomes smaller as ϕ exceeds 0.3, which implies that the turbulent cylinder wakes are almost completely suppressed

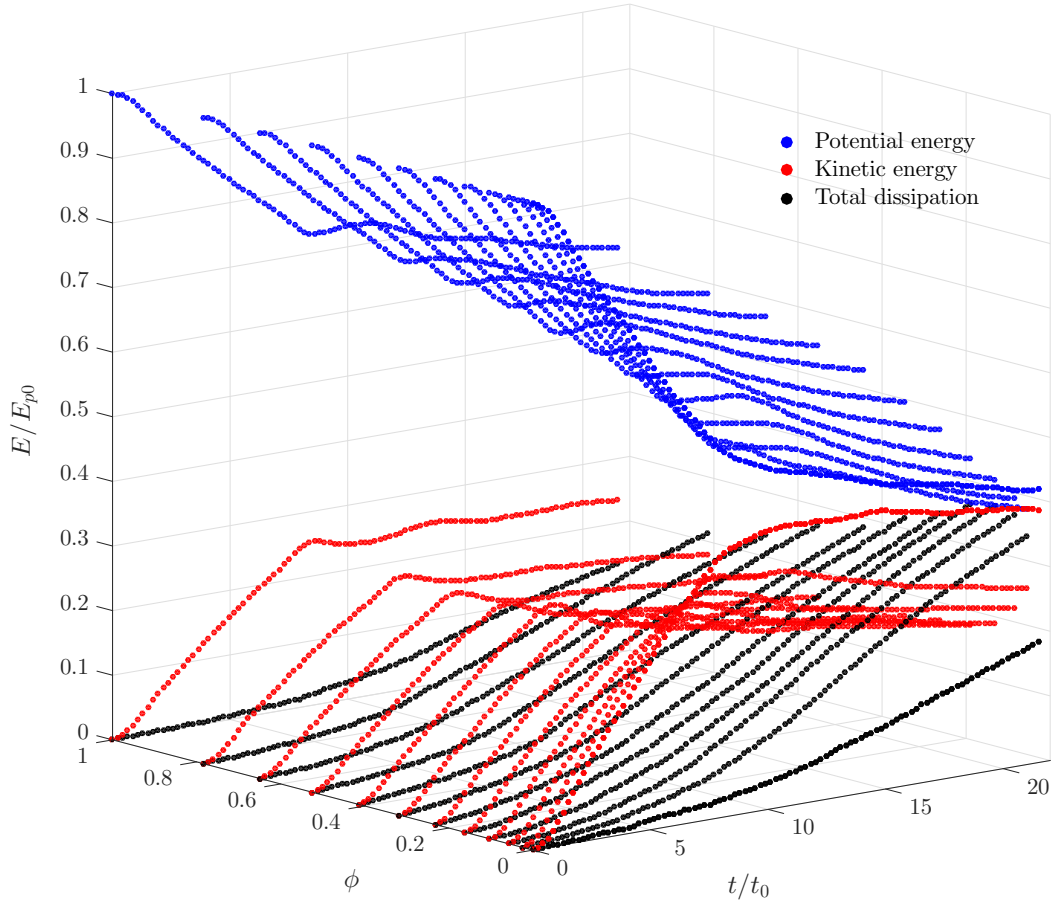

Figure 5.14: Time history of the potential energy E_p (blue lines), kinetic energy E_k (red lines) and integral of the total dissipation E_d (black lines) in the simulations of submerged equidistant arrays with ϕ ranging from 0 to 1, including the flat-bed and solid-slab cases. The submergence ratio is fixed at $H/h = 5.4$. All the terms are non-dimensionalized by the initial potential energy, E_{p0}.

beyond this threshold, and further densification of the array only reduces the energy loss associated with the vertical convective instability. This is accompanied by a slower decay of E_k around the same value of ϕ, and a subsequent increase of E_k at $\phi > 0.4$, consistent with the variation of front velocity in figure 5.8. The turning point of average E_d with ϕ is at $\phi = 0.1$, which occurs earlier than that of E_p and E_k. The energy loss associated with the vertical convective instability is found to be smaller than that of the turbulent wakes. The smallest average E_d is reached for the solid-slab case ($\phi = 1$), where both of these two mechanisms of energy dissipation are missing and the flow is less turbulent with respect to the flat-bed case due to a reduction of the effective water depth by h_a. Based on figures 5.8 and 5.14, it follows that the gravity current is propagating within the through-flow regime at $\phi = 0 \sim 0.1$ and the over-flow regime at $\phi = 0.4 \sim 1$, which is connected by a transitional regime in the range of $\phi = 0.1 \sim 0.4$.

5.5.2 Non-equidistant Array

We discuss in this section under what circumstances the μ_x-μ_y characterization is necessary. As indicated in figure 5.8, in addition to a direct transition from through-flow to over-flow, there are two other possible detours that lead to the same destination. We discuss the through-skimming-over flow transition path ($T \Rightarrow S \Rightarrow O$) in §5.5.2.1, and the through-plunging-over flow transition path ($T \Rightarrow P \Rightarrow O$) path in §5.5.2.2, respectively.

5.5.2.1 Through-skimming-over Flow Transition

The through-skimming flow transition is another accelerating mechanism of the gravity current regardless of the array submergence, in contrast to the $T \Rightarrow O$ acceleration which is only possible for a submerged array. Figures 5.15 and 5.16 show the density and velocity structures during the through-skimming-over flow transition, respectively. It is obvious that the information provided by the array density ϕ about the current propagation for non-equidistant arrays is fairly misleading. For the case I-0.636-0.272-5.4 (figure 5.15b, g), all the cylinders are subject to strong wake interferences due to their streamwise closeness. Three discernible sub-currents can be observed but with enhanced dilution with respect to the flat-bed case, due to the still persisting wake-induced

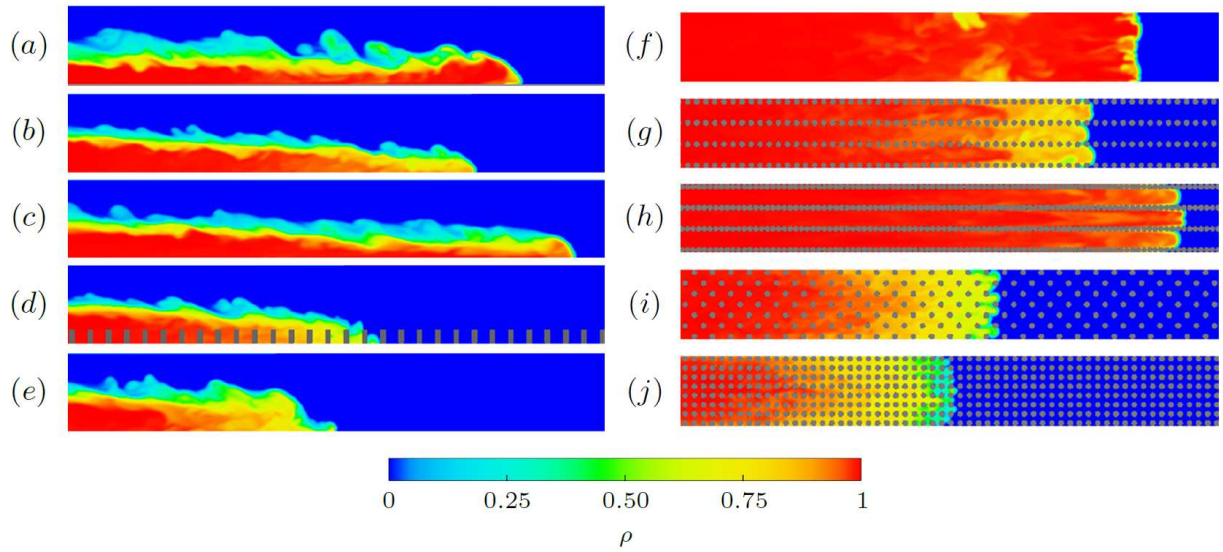

Figure 5.15: Instantaneous fluid density fields at $t = 21.5t_0$ showing the $T \Rightarrow S \Rightarrow O$ transition. (a, f) F-0-5.4; (b, g) I-0.636-0.272-5.4; (c, h) I-1.000-0.272-5.4; (d, i) S-0.636-0.272-5.4; (e, j) I-0.636-0.636-5.4. The left panels are plotted in the x-z plane along the array centerline, and the right panels are plotted in the x-y plane located $0.2h$ above the channel bed. Roughness elements are shown in dark gray. Note that in (d) the centerline density data are not available at every other cylinder in the streamwise direction due to the staggered arrangement.

mixing. The current is within a transitional stage between through-flow and skimming-flow where cross-stream interaction between sub-currents is weak but nonnegligible. The wake sheltering effect results in a significant drop of form drag per cylinder upon the incoming flow with this specific configuration. Therefore, when moving along the contour of $\phi = 0.136$ in figure 5.8(a), the current in case I-0.636-0.272-5.4 has a much larger ϵ as compared to other array configurations with the same array density. As μ_x increases to 1 (figure 5.15c, h), the cylinder wakes have been completely suppressed and the array has been fully channelized. The three sub-currents only communicate with each other in the above-array area ($z > h$), and thus a sudden contraction of the channel cross-sectional area below $z = h$ accelerates the currents due to the conservation of mass principle. The current in this particular configuration even propagates faster than the unobstructed case in the slumping phase, which appears as the peaks of ϵ in figure 5.8(a) and the velocity profile in figure 5.16 as well. This is a phenomenon similar to the skimming flows observed in wind passing building clusters (Oke 1988), as well as the d-type roughness in turbulent flows over rough

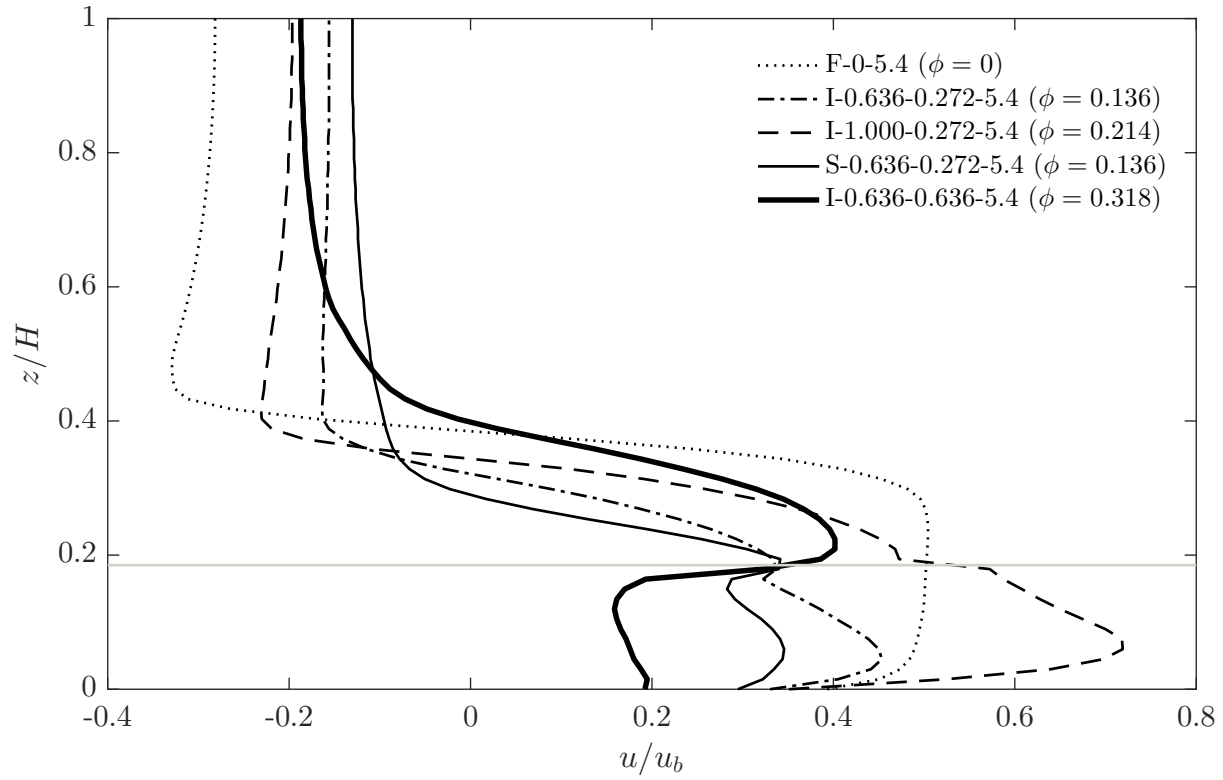

Figure 5.16: Time-averaged and laterally-averaged horizontal velocity profiles showing the $T \Rightarrow S \Rightarrow O$ transition. The velocity data are recorded at a distance of $H/2$ behind the current nose by moving with the gravity current frame. The time-averaging period is $2t_0 \sim 21.5t_0$. The horizontal gray line marks the array top.

walls (Jimenez 2004), where the main streams are separated from the smaller-scale flows within the closely-packed roughness elements.

A point worth noting is that in figure 5.5, the leading current front in case I-1.000-0.272-5.4 is overtaken by the front in case F-0-5.4 after $t \approx 60t_0$. Inspection of the density structure (not shown) indicates that the overtaking occurs shortly after the time when the height of this finite-volume gravity current is reduced below the array top. Therefore, the inner link between the sub-currents above $z = h$ is lost, and so is the $T \Rightarrow S$ acceleration mechanism due to the sudden contraction of the flow cross section. The added friction drag of the cylinders then begins to decelerate the current with respect to the flat-bed case.

The $T \Rightarrow S$ transition is exclusive for in-line arrangements, and thus there is no skimming-flow regime in figure 5.8(b). In a staggered array (figure 5.15d, i), the high-velocity interstitial

jets between the spanwise gaps are always obstructed by the offset rows immediately downstream such that the channelizing is heavily interrupted. Comparison between cases I-0.636-0.272-5.4 and S-0.636-0.272-5.4 indicates that the difference in cylinder arrangement alone may result in a significant change of the gravity current propagation dynamics for arrays with high values of μ_x/μ_y.

Along the contours of $\mu_x = 1$ in figure 5.7(b), the value of $\overline{Fr}^*$ first increases beyond the flat-bed limit and peaks around $\mu_y = 0.25$. Further increase of μ_y results in a considerable increase of array drag such that the gravity current is unable to squeeze into the sub-channels. The $T \Rightarrow S$ acceleration is compensated by a significant reduction of flow rate, and $\overline{Fr}^*$ starts to drop. In figure 5.16, the velocity profile of case I-0.636-0.636-5.4 indicates that the current is shifting from skimming-flow to the over-flow regime due to the increase of μ_y when compared with case I-0.636-0.272-5.4. With even larger μ_y, the current transitions from skimming-flow to the over-flow, and $\overline{Fr}^*$ increases again due to the $S \Rightarrow O$ acceleration.

5.5.2.2 Through-plunging-over Flow Transition

In this section, we briefly discuss the third path of flow transition depicted in figure 5.8(a), focusing on the configurations with large μ_y. Again, relevant density fields and velocity profiles are shown in figures 5.17 and 5.18, respectively. According to figure 5.17(a), case I-0.090-0.636-5.4 is within the through-flow regime where the gravity current mainly propagates between the cylinders. The values of μ_y for the remaining cases are all unity for each row of cylinders to be felt as impermeable by the current, and we assess the effect of streamwise array densification. As μ_y is increased to 1 (case I-0.090-1.000-5.4 in figure 5.17b), the current is right within the plunging-flow regime and its propagation is greatly impeded. For all the simulation cases shown, the streamwise spacing between the cylinders, if normalized by the water depth H, is comparable or small with respect to the vertical dimension of the current due to the deep submergence of the array. Therefore, even with μ_x as low as 0.090, the corresponding velocity profile in figure 5.18 indicates that the contact time of the current nose with the channel bed is very limited. Time history of the current propagation (not shown) indicates that after the nose reattaches to the bed, it hardly

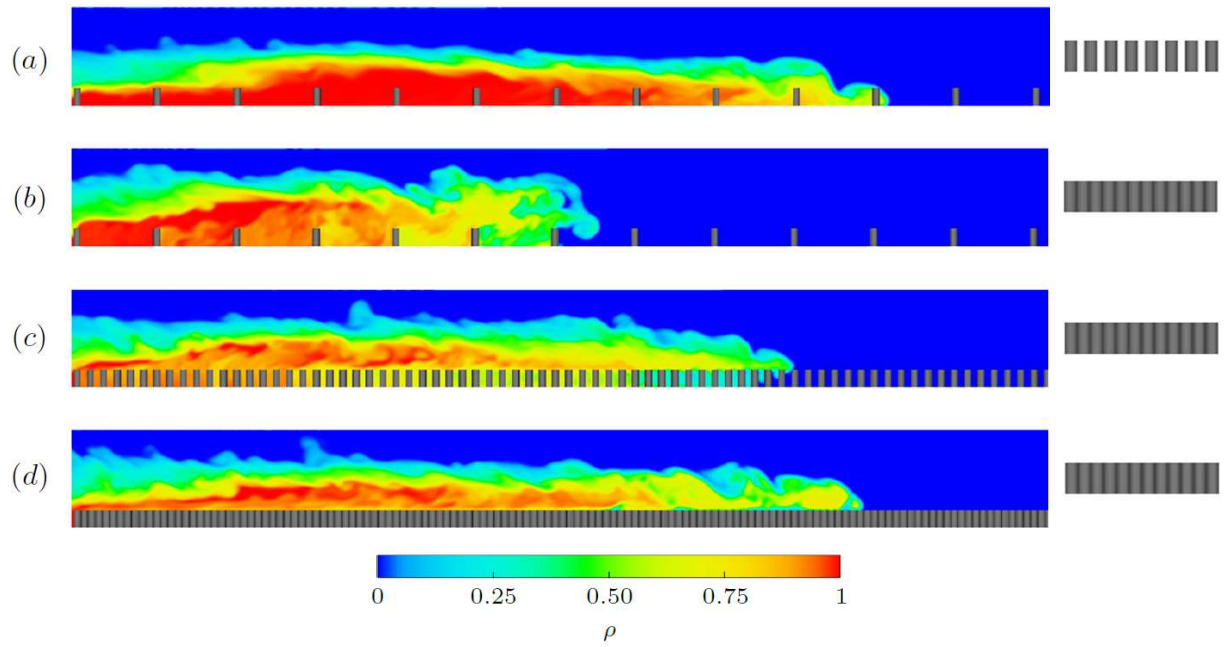

Figure 5.17: Instantaneous fluid density fields along the channel centerline at $t = 21.5t_0$ showing the $T \Rightarrow P \Rightarrow O$ transition. (a) I-0.090-0.636-5.4; (b) I-0.090-1.000-5.4; (c) I-0.545-1.000-5.4 (d) I-1.000-1.000-5.4. Frontal cylinder configurations as seen by the current are shown on the right.

favors a horizontal propagation but rather begins to climb the next row of cylinders. The gravity current undergoes significant mixing and energy dissipation during this climbing and plunging motions. We expect more contact of the current nose with the channel bed as the submergence ratio H/h decreases. Consistent with figure 5.7, the transition from plunging-flow to the over-flow regime occurs immediately after μ_x is increased beyond 0.090. Along the path of the through-plunging-over flow transition, the gravity current is first greatly impeded by the $T \Rightarrow P$ transition, reaching the region with lowest ϵ in figure 5.8, and then accelerates again because of the $P \Rightarrow O$ transition.

5.6 Effect of Submergence Ratio

In the foregoing sections, the effects of array configuration on the gravity current propagation have been discussed under a fixed submergence ratio of $H/h = 5.4$. In what follows, orthogonal to the two-dimensional parameter space in figure 5.8, the array geometry is fixed with $\mu_x = \mu_y =$

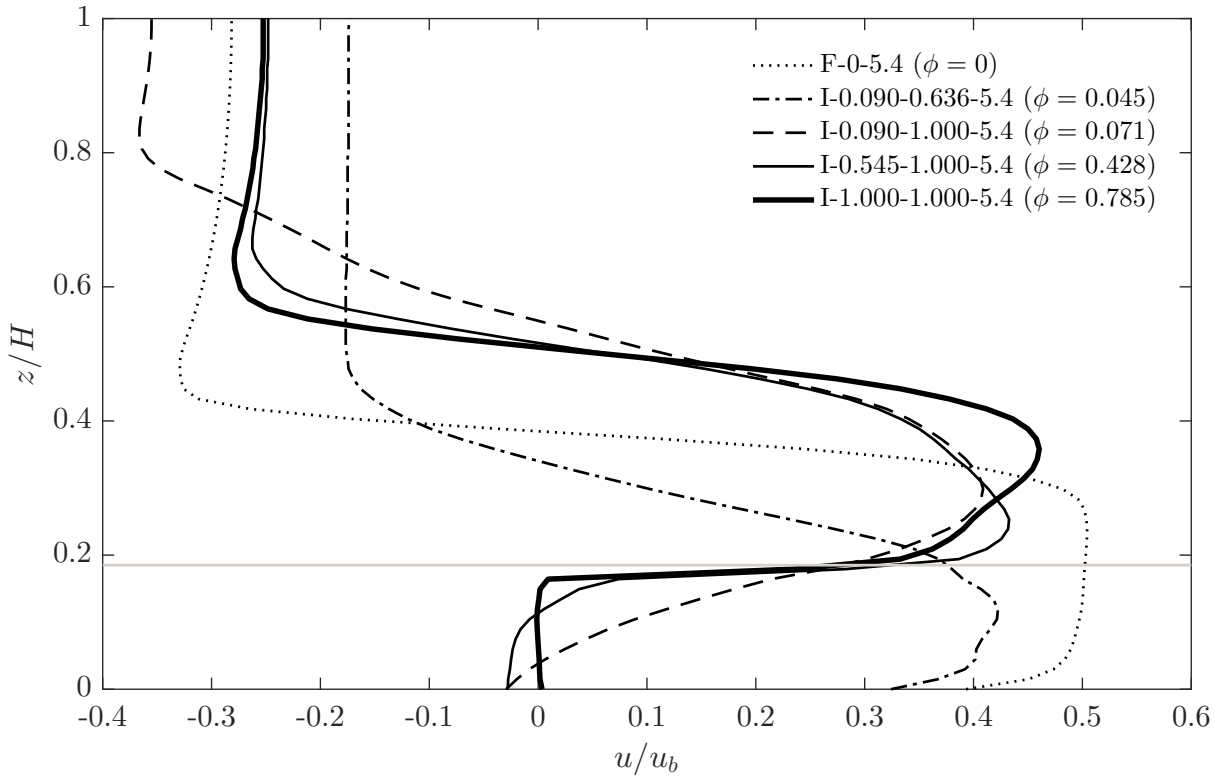

Figure 5.18: Time-averaged and laterally-averaged horizontal velocity profiles showing the $T \Rightarrow P \Rightarrow O$ transition. The velocity data are recorded at $H/2$ behind the current nose by moving with the gravity current frame. The time-averaging period is $2t_0 \sim 21.5t_0$. The horizontal gray line marks the array top.

0.636 (staggered) and the water depth is varied to investigate the effect of submergence ratio in the range of $1 \leqslant H/h \leqslant 10$.

It can be seen in figure 5.19 that the increased of H/h acts as another mechanism that promotes the through-to-over flow transition other than the increase of array drag as described in §5.5.1. When the array is emergent (figure 5.19a), due to the uniformly-distributed drag exerted by this dense canopy ($\phi = 0.318$) on the gravity current over its whole depth, the current propagation is dominated by the cylinder drag such that the interface is nearly triangular, which is consistent with Tanino *et al.* (2005). As H/h increases to 2, the current interface within the canopy is still triangular due to the still overwhelming drag with respect to the horizontal current momentum. The vertical convection zone is almost negligible. Starting from $H/h = 3$ and onwards, a increasingly well-defined over-nose can be identified that propagates along the array top. Due to the gradual

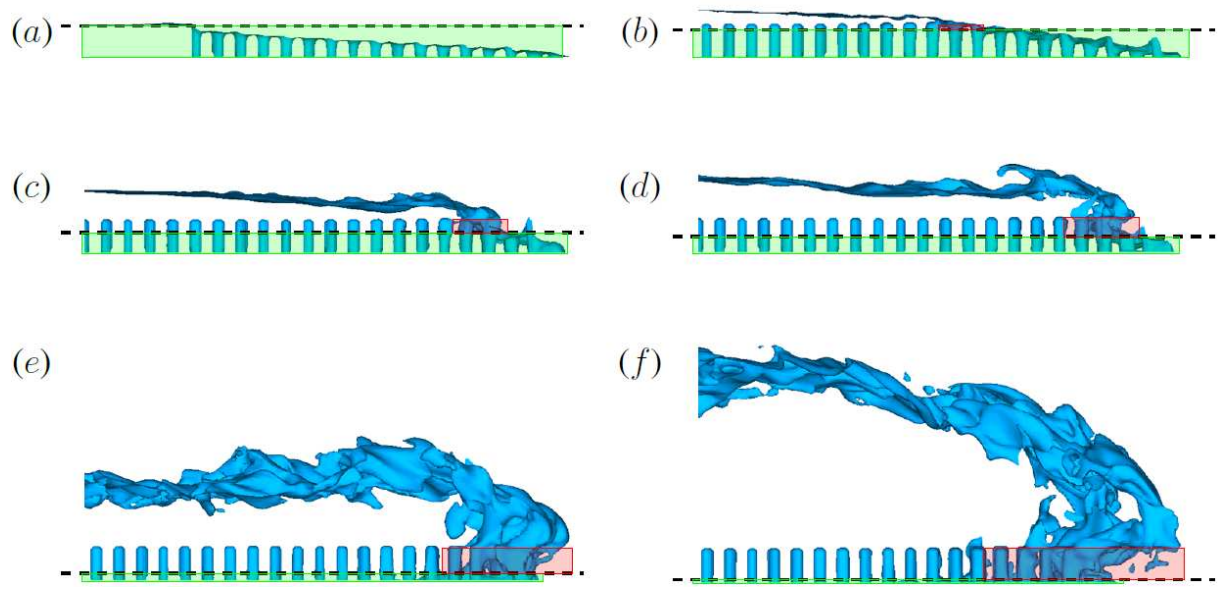

Figure 5.19: Instantaneous density isosurface at $\rho = 0.5$ under different submergence conditions for a fixed array geometry ($\mu_x = \mu_y = 0.636$, staggered). (a) $H/h = 1$; (b) $H/h = 2$; (c) $H/h = 3$; (d) $H/h = 4$; (e) $H/h = 6$; (f) $H/h = 10$. The horizontal dashed lines roughly divides the in-array region into a longitudinal propagation zone (encompassed by the green window) and a vertical convection zone (encompassed by the red window) as in figure 5.12.

flooding of dense fluid with increasing water depth, a through-over flow transition occurs during which the vertical convection zone gradually deepens into the lower canopy, accompanied by the suppression of longitudinal advection (figure 5.19$a \sim f$).

Figure 5.20 shows the time-averaged and laterally-averaged horizontal velocity profiles at different submergence ratios corresponding to those in figure 5.19. Since the gravity current propagation in the emergent ($H/h = 1$) and the shallowly-submerged case ($H/h = 2$) is governed by the array drag, the increase in water depth only results in faster current propagation within the array while the shape of the velocity profiles are similar. However, as H increases further, the emergence of the over-nose brings about a distinctly different flow behavior. The over-current propagates faster as the array poses a progressively smaller resistance with respect to the total horizontal momentum of the gravity current. Meanwhile, the in-array current propagation recedes with rising water depth. The transition to over-flow at higher submergence ratios leads to the growing dominance of vertical buoyancy fluxes within the array over the longitudinal current propagation

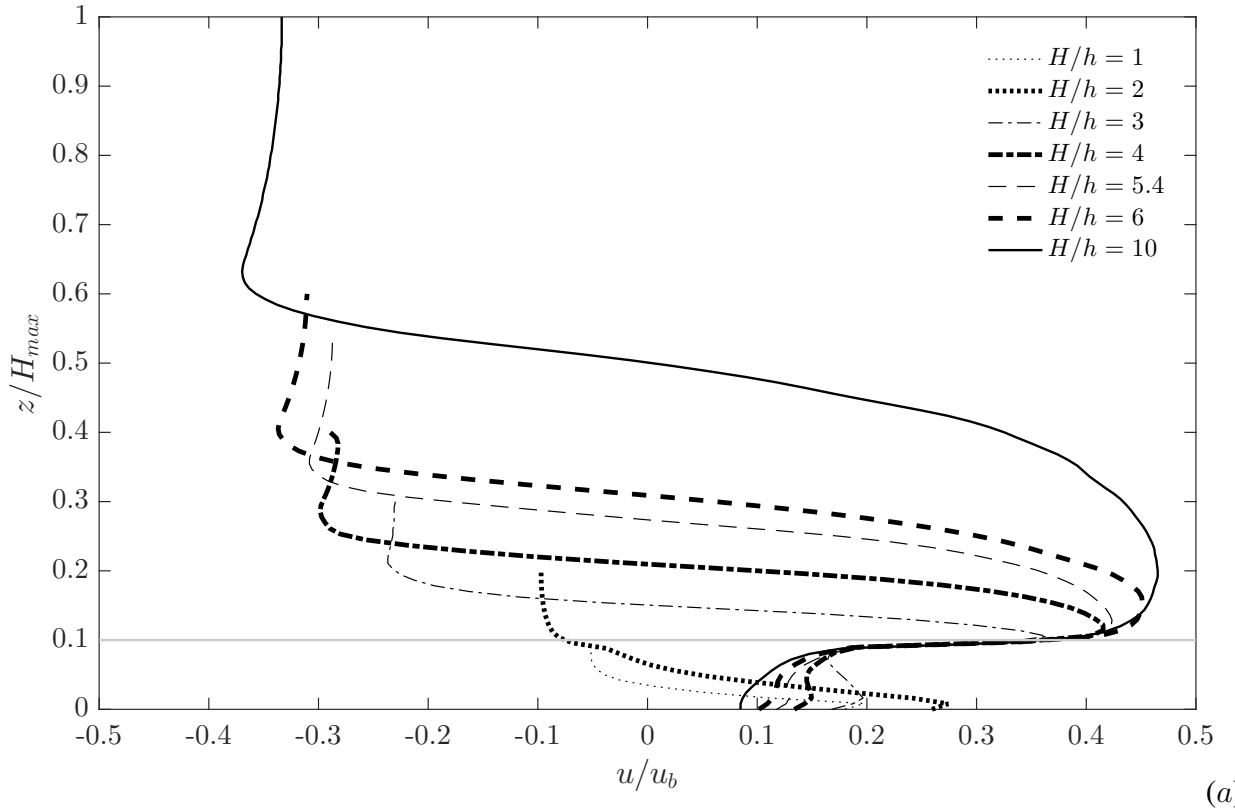

(a)

Figure 5.20: Time-averaged and laterally-averaged horizontal velocity profiles for a staggered array with $\mu_x = \mu_y = 0.636$ under different submergence conditions. The velocity data are recorded at $H/2$ behind the current nose by moving with the current frame. The z coordinate is normalized by the maximum water depth, $H_{max} = 10h$, and u is normalized by $u_b = \sqrt{g'H}$ corresponding to different flow depths, respectively. The time-averaging period is $2t_0 \sim 21.5t_0$ with $t_0 = H/u_b$. The gray line marks the array top.

driven by the horizontal pressure gradient, which is consistent with the deeper penetration of vertical convection zone in figure 5.19. This is opposite to what has been observed for constant-density flows over a submerged canopy, where deeper array submergence enhances the downward transfer of horizontal momentum via vertical turbulent stress, and thus gives rise to faster in-array flows (e.g. Nepf & Vivoni 2000).

5.7 Conclusions

Submerged canopies are ubiquitous in aquatic flows and even more commonly seen in oceanic and atmospheric environments. Laboratory experiments and large eddy simulations were used to study lock-exchange gravity currents propagating over and through an infinite array of submerged

circular cylinders. After validating our numerical model with experimental data, we performed an extensive parametric study to account for as many possible array geometries as possible (over 200 numerical simulations), in order to provide a comprehensive understanding of the influences of array density (ϕ) and non-equidistance ($\mu_x \neq \mu_y$) that have not been adequately addressed in previous studies. The discussions in §5.3, §5.4 and §5.5 fix the submergence ratio at $H/h = 5.4$. The effect of H/h is presented in §5.6.

In order to investigate the behavior of the gravity current over the full possible range of ϕ, the array density was varied from the unobstructed flat-bed case ($\phi = 0$) continuously towards the fully-blocked solid-slab case ($\phi = 1$). When a gravity current encounters a dense array submerged in the fluid ($H/h > 1$) with excessive drag, the existence of the additional flow pathway outside the array brings about the fundamental difference in current propagation with that of an emergent array. Staring from the flat-bed case, the time-averaged Froude number $\overline{Fr}$ was initially seen to decrease as ϕ increases, which is consistent with current propagation in emergent canopies. However, as ϕ increases further, our experiments indicated for the first time a non-monotonic dependence of $\overline{Fr}$ on ϕ which is confirmed by the numerical simulations (figure 5.4). As the array gradually approaches a solid-slab, the diminishing individual cylinder wakes together with the smaller amount of dense fluid trapped within the pore regions, jointly result in a less momentum loss of the over-current. This through-over flow transition associated with the densification of an equidistant array was observed to be the first mechanism of gravity current acceleration as ϕ increases (figures 5.10 and 5.11).

Strictly speaking, it is rare that an array is absolutely equidistant. When $\mu_x \approx \mu_y$, the conventional array characterization using the horizontally-averaged parameter ϕ can be applied with acceptable error. However, judging from the front velocity and flow structure of the gravity current when it encounters a highly non-equidistant array, we demonstrated that the flow condition cannot be uniquely determined by ϕ at all. Instead, its orthogonal components are individually important. Consequently, we proposed a new geometrical framework consisting of the streamwise and spanwise array densities, μ_x and μ_y, to provide a more convenient and unambiguous prediction of the

gravity current propagation under the impact of array non-equidistance. Physically, μ_x controls the wake sheltering and μ_y controls the current intrusion. It is highlighted that an infinite number of flow conditions are possible along a single contour of ϕ in figure 5.8, emphasizing the breakdown of the equidistant-array assumption.

Depending on the specific μ_x-μ_y combination, four dynamically different flow regimes and their transitions are identified. The flow falls into the through-flow regime with small μ_x and small μ_y (in-line array, figure 5.8a) or arbitrary μ_x and small μ_y (staggered array, figure 5.8b) where the gravity current propagates along the bed with strong cylinder wakes. With sufficiently large μ_x and μ_y, a well-defined over-current emerges and rides on the array top (i.e. over-flow regime) irrespective of the cylinder arrangement. As one moves away from the 45°-diagonal (increasing array non-equidistance), two extreme conditions can occur: (i) in the energy-consuming plunging-flow regime (small μ_x and large μ_y), the gravity current reattaches to the bed before it is projected upwards by the next row of cylinders; and (ii) for the skimming-flow exclusively occurring in in-line arrays with large μ_x and small μ_y, high-speed channelized gravity current may even propagate faster than the flat-bed case due to the abrupt contraction of the flow cross section within the array (note that $\epsilon_{max} = 1.1$ in the colorbar of figure 5.8). This through-skimming flow transition is identified as the second mechanism of gravity current acceleration as ϕ increases. It is absent for staggered arrays with offset interruption (figures 5.15 and 5.16), highlighting the effect of cylinder arrangement pattern (note the difference between figures 5.8a and 5.8b).

The self-similar properties of current propagation after the slumping phase ($x_f \sim t$) are found to vary among different flow regimes. Gravity currents in the through-flow and plunging-flow regimes transition to the turbulent drag-dominated phase where $x_f \sim t^{1/2}$ due to strong cylinder drag. The highly independent sub-currents in the skimming-flow regime are subject to negligible streamwise obstacle resistance, and hence the front velocity decays as $x_f \sim t^{2/3}$ which resembles the buoyancy-inertial phase of the flat-bed condition. The front velocity in the over-flow regime decays as $x_f \sim t^{1/2}$ if the through-current still exists (red line in figure 5.6a), but exhibits another

power dependence of $x_f \sim t^{2/3}$ if the cylinder wakes are completely suppressed with the gravity current evolving closer to the flat-bed limit (black line in figure 5.6b).

Hydrologic storage occurs in regions of diminished flow in which water can remain in contact with biologically and geochemically active surfaces for an extended time before moving downstream (Harvey *et al.* 2003). Longer periods of hydrologic retention in submerged canopies contributes to the nutrient removal for water quality applications, and more broadly, hydrologic storage (Nepf *et al.* 2007). However, the true retention time associated with dense partial-depth canopies in field conditions is often much shorter than what is estimated based on the through-current propagation (Ozan *et al.* 2016). The possible explanation is that as the array becomes denser, the over-current gradually accelerates and overtakes the underlying through-current (figure 5.10), and thus the water renewal in the canopy region downstream of the through-current is mainly accomplished by vertical exchange due to the unstable stratification at the array-ambient interface (figure 5.12). On the other hand, this increased canopy flushing rate prevents the nutrient uptake of the submerged vegetation from being supply-limited, partly compensating the declined growth rate caused by the weakened longitudinal transport of nutrients within a dense array. In this regard, the effect of the through-over flow transition on the retention time in submerged canopies is a key part of our understanding of how fluid mechanics influences the ecology of lotic ecosystems.

The fast-spreading destructive gravity current flows (e.g. snow avalanches, haboobs and pyroclastic flows) pose a significant threat to lives and properties, emphasizing the effectiveness of the preventative measures to weaken their power as well as accurate precaution systems. The region with the slowest front velocities (plunging flow) in figure 5.8 well explains the fact that snow fences are always built perpendicular to the mountain slope. Since an very early transition to overflow is possible for an array with large μ_y (figure 5.7c), special attention should be paid to the gaps between rows to prevent unexpected acceleration of the avalanche due to the plunging-over flow transition (figures 5.17 and 5.18). Meanwhile, in urban canopies where the streets may be highly channelized, the inclusion of the directional information of atmospheric gravity fronts (e.g. haboobs and sea breezes) in weather forecasting models is necessary. These propagating fronts may

be heavily impeded if their path is perpendicular to the streets (plunging-flow), or on the contrary, accelerated if they advance along the streets (skimming-flow).

Chapter 6

Intrusive Gravity Currents Interacting with a Submerged Obstacle[3]

6.1 Introduction

Dense water formed in semi-enclosed seas often has to flow through narrow straits or down continental slopes before it reaches the open ocean. These regions of dense water flowing over topography are known as dense overflows. The dense water can be formed through a variety of processes including surface cooling, the addition of salt in the form of brine from freezing pack ice in high-latitude seas, and evaporation in enclosed subtropical seas. The dense overflows are regions of significant mixing, which modifies the temperature and salinity signal of the dense water. Many of the deep water-masses of the ocean originate in these overflows and have their properties set by the mixing that occurs therein (refer to Chassignet *et al.* (2012) for a complete review). Figure 6.1 shows schematically the common formation process of deep water masses in the continuously stratified midocean. A dense overflow moves down topography, accelerating under gravity. This acceleration leads to the development of strong shear between the dense water and the lighter overlying water column. There is also strong shear in the friction layer at the bottom boundary (especially when bottom roughness is present). These two shear layers may lead to turbulence-generating instability, which dilutes the descending dense current. Finally, the initially very dense overflow may separate from the topography at its level of neutral buoyancy and intrudes into the open ocean in the form of an intrusive gravity current. Note that compared

[3]The research presented in this chapter has been published in substantial part in *Environmental Fluid Mechanics* under the title "Numerical simulation of intrusive gravity currents past obstacles in a continuously stratified ambient" (J. Zhou and S. K. Venayagamoorthy 2017). Background information and literature relevant to this chapter are presented again so the chapter may be read as a stand-alone work. The chapter is written in a collective "we" voice to acknowledge collaboration with the co-author.

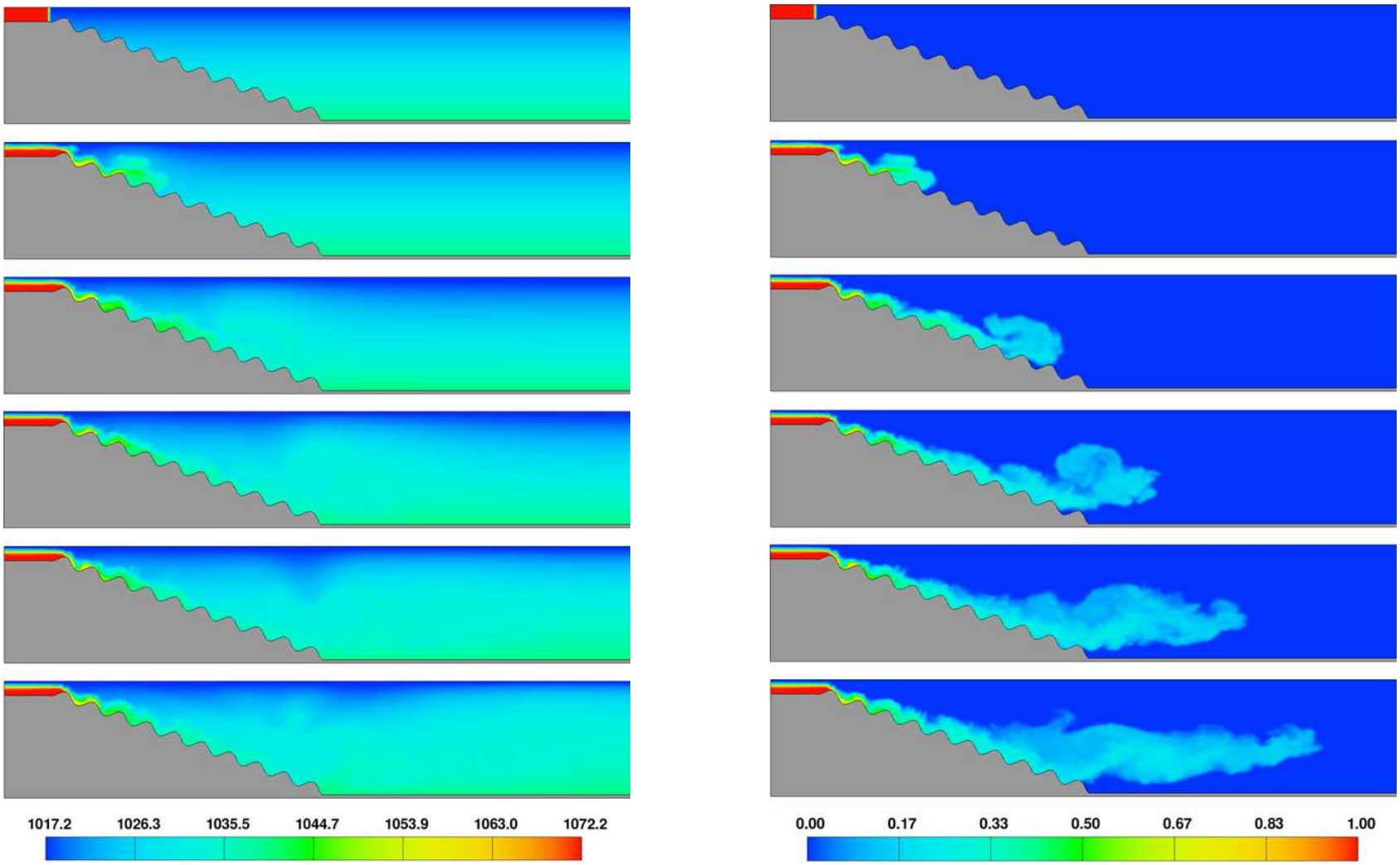

Figure 6.1: Large eddy simulation showing the formation process of deep water masses. A constant flux of dense current is prescribed at the left boundary. Left panel: density contours. Right panel: dye concentration contours.

with the density contours, the dye-concentration contours are much more helpful in identifying the intrusion.

There are numerous studies on the dynamics and structure of gravity currents given their broad geophysical and engineering relevance. A bottom-boundary gravity current (hereafter called BBGC) forms when the current is denser than the ambient fluid, and an intrusive gravity current (hereafter called IGC) forms when a fluid is released into a non-homogeneous (i.e. stably stratified) ambient and travels at its level of neutral buoyancy. Both of these types of gravity currents have been reviewed in the monograph by Simpson (1997). The most commonly studied case is the BBGC in a homogeneous fluid (Benjamin 1968; Simpson & Britter 1979; Klemp *et al.* 1994; Shin *et al.* 2004; Nogueira *et al.* 2014; Lombardi *et al.* 2015). Maxworthy *et al.* (2002) was the first to experimentally investigate BBGC in a continuously stratified ambient. They found that the front speed of the BBGC is given by $U = FNH$, where F is the Froude number, H is the total fluid depth, N is the buoyancy frequency given by $N = \sqrt{(g/\rho_0)\,(-\mathrm{d}\rho/\mathrm{dz})}$ (z is the vertical coordinate, g is the acceleration due to gravity, ρ is the local fluid density, and ρ_0 is the reference density). They suggested that $F \approx 0.266$, which lies in close agreement with the analytical prediction of $F = 0.25$ by Ungarish & Huppert (2002).

For intrusive gravity currents at arbitrary depths, Bolster *et al.* (2008) developed a model based on energy arguments to predict the front speed U as

$$U = \frac{1}{2}FNH\left[12\left(\frac{h_N - \frac{1}{2}H}{H}\right)^2 + 1\right]^{1/2}, \tag{6.1}$$

where h_N is the level of neutral buoyancy at which the intrusion density matches the ambient density. Munroe *et al.* (2009) examined the generation of internal waves by asymmetric intrusions and the consequent current-wave interaction. They demonstrated that even though the energy associated with the internal waves is not so large to have a leading-order effect on the front speed, it is large enough to affect non-negligibly the consequent evolution of the IGC.

Topographic features are ubiquitous in natural and engineered flows, and hence it is important to understand the interaction of stratified flows such as gravity currents with such topographic features for practical reasons such as mitigation of pollutants transported by the current (see Baines (1995) for a complete review). When a BBGC encounters an isolated bottom-mounted obstacle, a proportion of the flow may continue over the obstacle while the remaining flow may be reflected back as a hydraulic jump. On encountering the obstacle, the gravity current head is deflected upwards and then reattaches to the bottom boundary. Eventually a similar but smaller current re-establishes downstream of the obstacle. Armi (1986) constructed a comprehensive theoretical framework to study two-layer flows interacting with an isolated bottom-mounted obstacle. Lane-Serff *et al.* (1995) theoretically predicted the proportion of the over-passing flux, the speed of the reflected jump, and the depth of the reflected flow. Gonzalez-Juez & Meiburg (2009) extended the shallow-water theory to predict the height and front speed of the downstream re-established current as functions of the upstream Froude number and the ratio of obstacle height to current height. La Rocca *et al.* (2013) used Lattice Boltzmann simulations to simulate the interaction of 3D gravity currents with an emerging cylinder. Tokyay & Constantinescu (2015) investigated the flow induced by a compositional gravity current propagating over a fixed non-erodible triangular bottom-mounted obstacle using 3-D large eddy simulations. Several studies have investigated the time-varying forces on obstacles that result from the impact of gravity currents. The magnitude of the drag increases monotonically with time in an exponential fashion towards a maximum when the current impinges on the obstacle, and goes through a transient phase and eventually reaches a quasi-steady value (Gonzalez-Juez & Meiburg 2009; Gonzalez-Juez *et al.* 2009, 2010). The structure and evolution of a bottom-propagating compositional gravity current over a series of obstacles were analyzed by a series of efforts of Tokyay *et al.* (2011*a*, 2012, 2011*b*). They classified the flow into a low-drag case where the front speed is close to constant, and a high-drag case where the current transitions to a drag-dominated regime in which the front speed decays with time. Recently there is a growing interest in studying sediment-driven turbidity currents over bottom topography for sedimentation-control (Nasr-Azadani & Meiburg 2014*a*,*b*).

However, there are only a limited number of studies in the refereed literature that focus on the interaction of BBGC with obstacles in a continuously stratified ambient. Ozgokmen *et al.* (2006) were the first to consider a bottom-boundary gravity current interacting with sloping topography in the presence of ambient stratification, albeit over a smooth surface. Their results showed that, with constant slope angle and linear ambient stratification, the gravity current separates from the slope bottom which causes the entrained mass flux to depend only on the ambient stratification while the slope angle is irrelevant. Ozgokmen *et al.* (2007) also performed a large eddy simulation of stratified mixing in a two-dimensional dam-break problem within a rectangular enclosed domain. Ozgokmen & Fischer (2008) further extended this line of investigation by incorporating rough sloping beds. They considered the interaction between a bottom-boundary saline current and rough seafloor topography within a temperature-stratified ambient fluid. They presented results on the front speed using a parameter matrix consisting of the amplitude of bottom roughness and the strength of ambient stratification.

As shown in figure 6.1, the post-separation deep water masses may encounter large-scale topography mounted on the ocean floor. To our knowledge, no studies on the interaction of IGC with bottom-mounted obstacles in a continuously stratified ambient have been conducted to date. As such, an overarching objective of the present study is to explore the dynamics of a symmetric IGC interacting with a bottom-mounted obstacle using the non-hydrostatic FLOW-3D computational fluid dynamics (CFD) code. The capability of the numerical model to capture the essential dynamics of a classical IGC without obstacle effect is first assessed by comparison with available experimental and theoretical results, in order to lay the foundation for analyzing and parameterizing the properties of a topography-affected IGC. An overview of the problem configuration and a summary of simulations that were performed in this study are described in §6.2. We then present and discuss the simulation results in §6.3. In §6.3.1, we present the results and analysis of classical IGC without obstacle effect for validation purpose. In §6.3.2, we present new results from a series of simulations of a symmetric IGC interacting with an obstacle to gain insights into the downstream flow pattern, and highlight the effect of the obstacle height on the downstream propagation

speed of IGC. We finally draw some conclusions and provide some suggestions for future work in §6.4.

6.2 Simulation Setup

Two series of simulations for two problem configurations were performed in this study. The first series of simulations for the first problem configuration were performed to validate the capability of FLOW-3D to capture the flow dynamics of IGC in a continuously stratified ambient in the absence of an obstacle and are discussed in more detail in §6.2.1. The second series of simulations for the second problem configuration were done to investigate the effects of a bottom-mounted obstacle with varying non-dimensional height $\tilde{D}$ on a symmetric IGC propagating at mid-depth as discussed in §6.2.2. A massless scalar (dye) is added to the lock fluid for enhancing flow visualizations similar to that in figure 6.1. All the simulations reported in this study are two-dimensional, based on observations from previous studies which indicate that no considerable differences between 2-D and 3-D simulations for gravity current flows were apparent (Ozgokmen *et al.* 2006; Bolster *et al.* 2008; An *et al.* 2012).

The schematic for the numerical setup is shown in figure 6.2. In this lock-release configuration, the density of the intruding fluid ρ_i lies between the minimum and maximum densities of the ambient stratified fluid, ρ_U and ρ_L, respectively. The stratification is uniform and the density of the ambient fluid is given by $\rho_s(z) = \rho_L + (z/H)(\rho_U - \rho_L)$, where H is the total flow depth and z is vertically upwards. Once the lock gate is removed, the fluid of density ρ_i will travel along its level of neutral buoyancy h, where $\rho_s(z = h) = \rho_i$. The downstream bottom-mounted obstacle has a height D and thickness W. The level of neutral buoyancy, obstacle width and height can be non-dimensionalized using the total fluid depth as $\tilde{h} = h/H$, $\tilde{W} = W/H$ and $\tilde{D} = D/H$, respectively.

No-slip boundary conditions are employed at left, right, and bottom walls as well as at the obstacle surface, while the tank is left open to the atmosphere at the top. For all simulation cases the Reynolds number defined as $Re = NH^2/\nu$ is sufficiently large (i.e. $> 10^4$) so that viscous

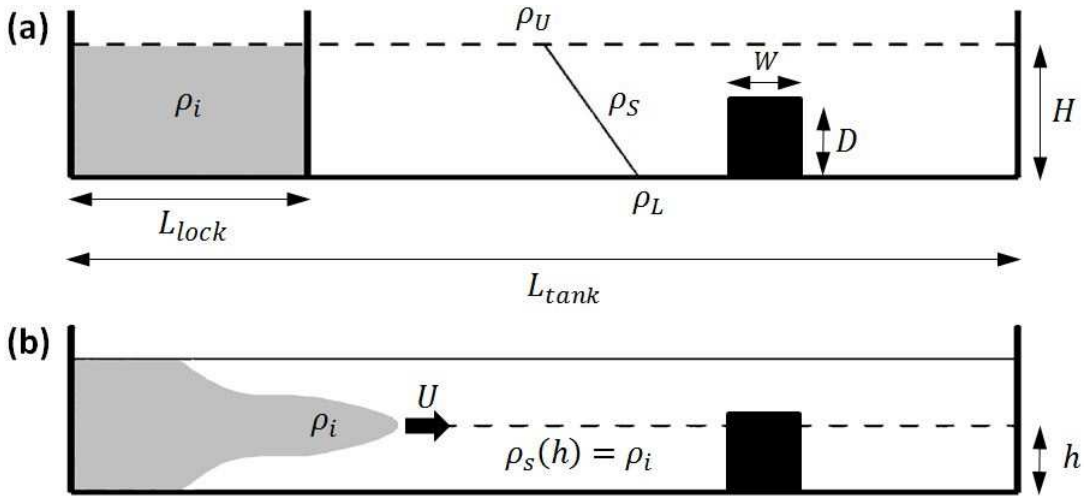

Figure 6.2: (a) A schematic of the initial setup for a full-depth lock-release flow; (b) a schematic of an IGC propagating at its level of neutral buoyancy.

effects are negligible. Details of the simulations for the two problem configurations discussed above are provided separately in what follows.

6.2.1 IGC without the Obstacle

The simulations of IGC without the obstacle's effect correspond to the condition with D = 0 in figure 6.2, i.e. the obstacle is absent. The results using the two-dimensional LES model in FLOW-3D are compared with the theoretical, experimental and DNS data from Bolster *et al.* (2008), Munroe *et al.* (2009) and Maxworthy *et al.* (2002):

- Bolster *et al.* (2008) focuses on the propagation speed of an IGC through the whole range of dimensionless level of neutral buoyancy ($\tilde{h}$), in order to assess the suitability of FLOW-3D for simulating an IGC in a quantitative sense. The numerical setup is identical with that of Bolster *et al.* (2008). The tank dimensions are: L_{tank} = 182 cm, L_{lock} = 30 cm, and H = 20 cm. The density of the lock fluid is varied in a manner such that $\tilde{h}$ varies from 0 to 1 in 0.1 increments. The parameter matrix consists of two different values of buoyancy frequency ($N = 1\ s^{-1}$ and 0.5 s^{-1}) and eleven different values of $\tilde{h}$. The number of grid points used

for all simulations are 840 in the horizontal (streamwise) direction and 230 in the vertical direction, resulting in a grid resolution of 1 mm.

- The comparison with the experimental and DNS results of Munroe *et al.* (2009) is used to further validate the numerical model by visualizing the evolution dynamics of a symmetric IGC ($\tilde{h}$ = 0.5) and the associated internal wave field. The numerical setup is identical with that of Munroe *et al.* (2009), with L_{tank} = 197.1 cm, L_{lock} = 18.5 cm, and H = 30 cm. The buoyancy frequency is fixed at $N = 2\ s^{-1}$. The number of grid points is 1991 in the streamwise direction and 320 in the vertical direction, again resulting in a grid resolution of 1 mm.

- The data from the experimental study of bottom gravity currents in a linearly stratified ambient by Maxworthy *et al.* (2002) is used to validate the numerical model in terms of temporal evolution of the gravity current front location. The tank dimensions are: L_{tank} = 240 cm, L_{lock} = 20 cm, and H = 15 cm. The gravity current is generated using a partial-depth lock release where the ratio of lock height to the flow depth is $1/3$. An additional dimensionless parameter, R, is introduced to measure the relative strength of the current and the ambient stratification, i.e. $R = (\rho_i - \rho_U)/(\rho_L - \rho_U)$. Three representative runs are simulated: (i) run 11 where $N = 1.422\ s^{-1}$, $R = 1.000$; (ii) run 19 where $N = 1.941\ s^{-1}$, $R = 1.397$; and (iii) run 22: $N = 2.000\ s^{-1}$, $R = 1.189$. The same mesh resolution is used.

6.2.2 IGC with the Obstacle

The numerical simulations of an IGC interacting with a bottom-mounted obstacle were undertaken in a domain depicted by the schematic in figure 6.3(a) with L_{tank} = 2.8 m, L_{lock} = 1 m, and H = 0.2 m. The lock length is selected so as to guarantee sufficient supply of upstream intrusion fluid. The obstacle is located 0.4 m downstream of the lock gate, which is two times the flow depth to ensure that a fully-developed IGC is achieved before reaching the obstacle. Two types of obstacles are used, i.e. a thick obstacle with W = 0.1 m ($\tilde{W} = 0.5$) and a thin obstacle with W = 0.01 m ($\tilde{W} = 0.05$). For each obstacle thickness, its height is varied from 0.02 m ($\tilde{D} = 0.1$) to

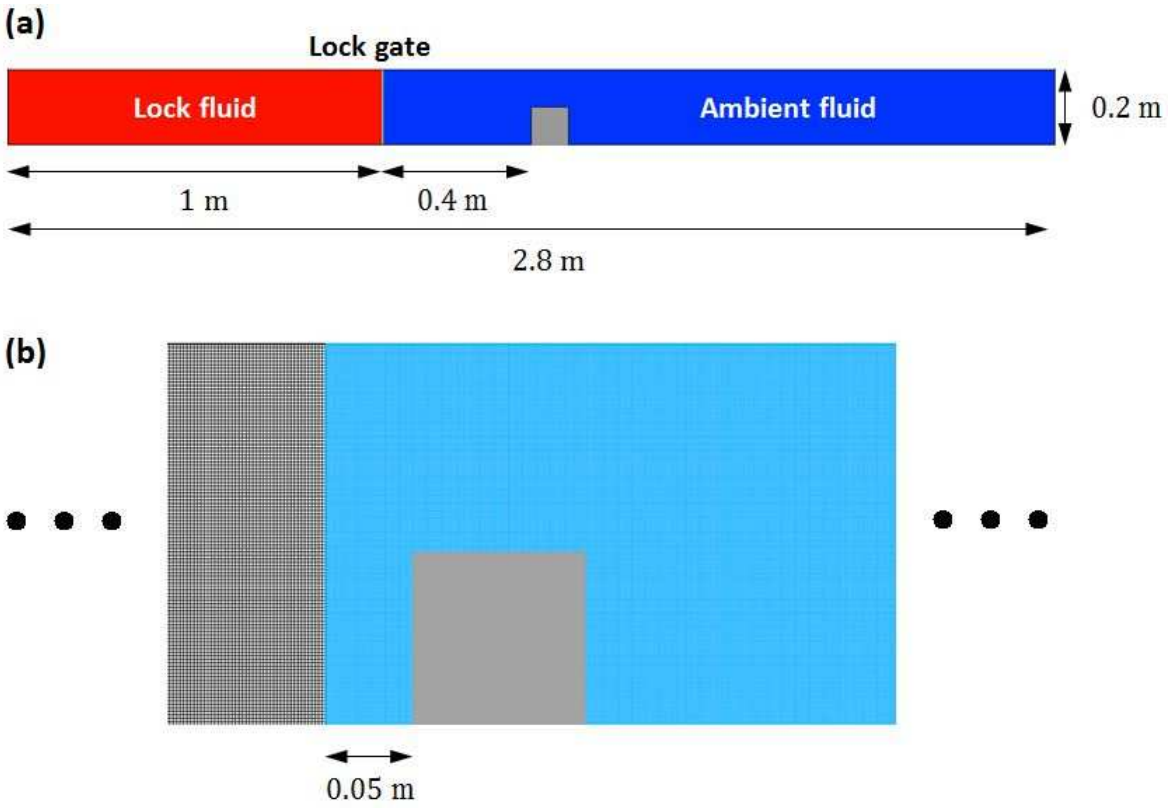

Figure 6.3: (a) Computational domain depicting the lock-release simulations of an IGC interacting with a bottom-mounted obstacle; (b) a zoomed-in view highlighting the grid refinement near and downstream of the obstacle.

0.18 m ($\tilde{D} = 0.9$), in order to investigate the effect of obstacle height on the flow dynamics. The buoyancy frequency is fixed at $N = 1\ s^{-1}$. The lock fluid density is the mean of the ambient stratified fluid, which implies that only a symmetric IGC propagating at mid-depth is simulated in this study. In this manner no dominating mode-1 internal wave controls the motion of IGC and hence the pulsating feature of asymmetric intrusions reported by Maxworthy *et al.* (2002) and Munroe *et al.* (2009) are eliminated. Also, since the mode-2 long wave is locked to the intrusion head, the disturbance of the density field only occurs at the vicinity of the intrusion. This allows us to focus on the intrusion-obstacle interaction, with interferences from wave-obstacle interaction minimized. As shown in figure 6.3(b), the grid size of the region ranging from the left end of the tank to 0.05 m upstream of the obstacle is 2 mm, and is refined to 1 mm further downstream, in order

to adequately resolve the flow field in the vicinity of the obstacle as well as further downstream of the obstacle.

6.3 Results and Discussion

6.3.1 IGC without the Obstacle

In this section we first provide a quantitative validation of the time-averaged propagation speed of a classical IGC outlined in §6.2.1 by comparing with the theoretical and experimental data from Bolster *et al.* (2008), followed by the flow field of a free-propagating symmetric IGC to provide a qualitative comparison with the experimental and DNS results of Munroe *et al.* (2009). Next, the results of the temporal evolution of a bottom gravity current nose in a linearly stratified ambient is compared with the experimental data from Maxworthy *et al.* (2002).

6.3.1.1 Time-averaged IGC Front Speed versus Level of Neutral Buoyancy

The propagation speed of the front of a gravity current is perhaps one of the most discussed quantity in the study of gravity currents. Figure 6.4 compares the simulated propagation speed of the front of an IGC with the experimental results of Bolster *et al.* (2008). The theoretical predictions given by equation (6.1) with F = 0.25 and 0.266 are also shown. It can be seen that the front speeds predicted by the numerical simulations from FLOW-3D are in good agreement with both the theoretical predictions and the experimental measurements. Consistent with discussion presented in Bolster *et al.* (2008), three important conclusions that can be drawn from figure 6.4 are: (1) for a given stratification, the mid-depth intrusion travels the slowest, and the maximum front speed is attained by either the top or the bottom boundary current intrusion; (2) for a given level of neutral buoyancy, the intrusion speed is directly proportional to the buoyancy frequency. The dimensionless intrusion velocities (U/NH) collapse over the range of $N = 0.5\ s^{-1} \sim 1\ s^{-1}$ over the entire range of $\tilde{h}$; (3) noting that the mode-n long-wave speed is given by $NH/n\pi$ (note, the speeds of the first three modes are plotted in figure 6.4), it is clear that intrusions at any depth

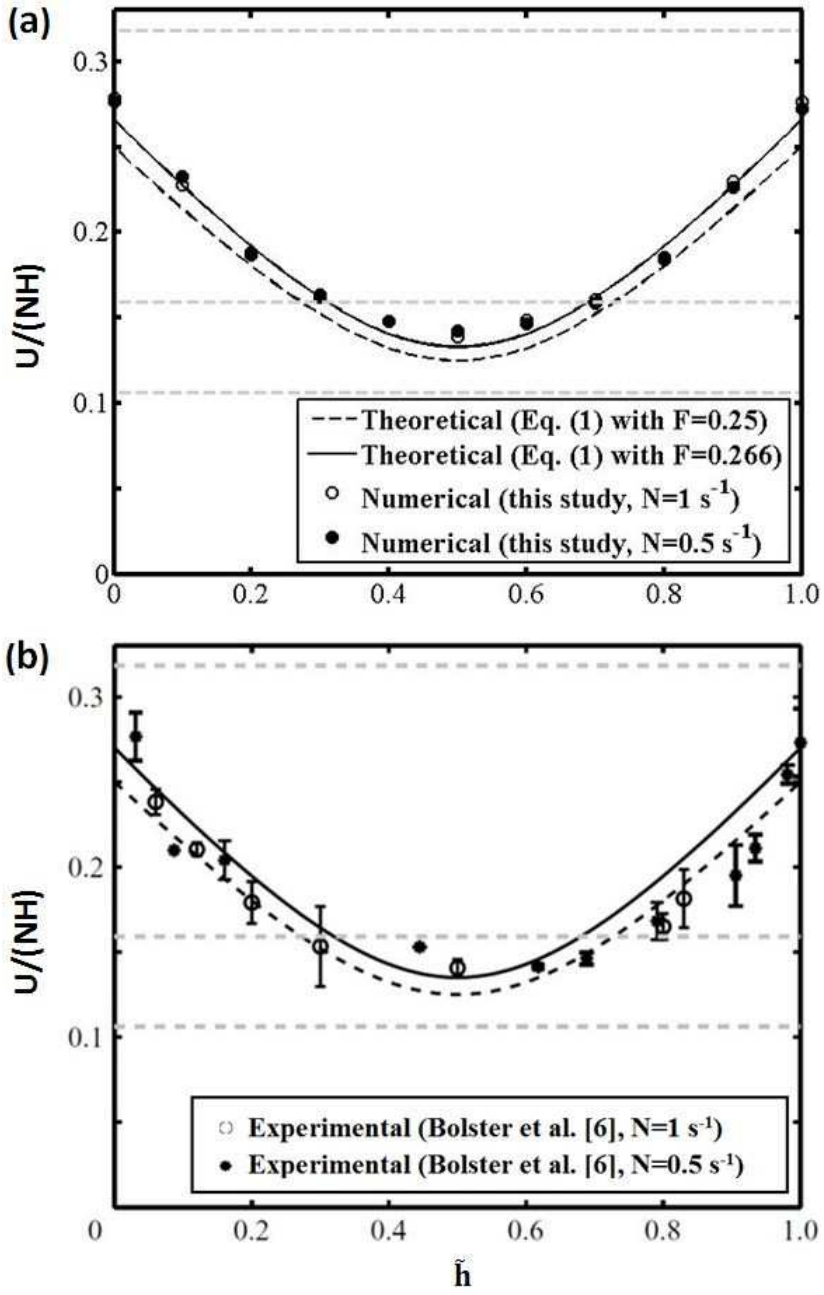

Figure 6.4: The dimensionless IGC propagation speed as a function of level of neutral buoyancy: (a) comparison of numerical simulations to theoretical predictions; (b) comparison of experiments Bolster *et al.* (2008) to theoretical predictions. The horizontal grey dashed lines represent from top to bottom the first-, second-, and third-mode long-wave speed, respectively.

are subcritical to mode-1 waves, subcritical to mode-2 waves for approximately $0.3 < \tilde{h} < 0.7$, and supercritical to all higher modes.

The agreement of the numerical results is further assessed using the coefficient of variation of the root-mean-square deviation of the intrusion speed, i.e. CV_{RMSD}, which is usually used to compare differences between two data sets and is given by

$$CV_{RMSD} = \sqrt{\frac{\sum_{i=1}^{n}(x_i - \hat{x}_i)^2}{n}} \Bigg/ \bar{x} \,, \tag{6.2}$$

where x_i is the standard data, $\hat{x}_i$ is the predicted data, n is the number of data points, and $\bar{x}$ is the mean of the standard data. The theoretical prediction given by equation (6.1) are considered as the standard data herein, with F taking the mean of 0.25 and 0.266. Throughout the whole range of $\tilde{h}$, the maximum value of CV_{RMSD} was 6.0% for the case with $N = 1\ s^{-1}$, and 5.6% for the case with $N = 0.5\ s^{-1}$, which are sufficiently small.

6.3.1.2 Flow Structure of a Mid-depth IGC

Figure 6.5 demonstrates the characteristic behavior of a symmetric IGC ($\tilde{h}$ = 0.5) for a background ambient stratification with a buoyancy frequency of $N = 2\ s^{-1}$. For the times shown in the plots, the IGC is within the slumping phase and is propagating at a constant speed. The intrusion head continuously becomes thinner but the front speed stays unchanged. Sutherland & Nault (2007) also noted this phenomenon and stated that a symmetrical IGC was found to propagate at a constant speed up to 20 lock lengths with no indication of a decelerating self-similar phase, although the intrusion thickness decreases as it propagates. The supposition that the IGC has evolved into a closed-core solitary wave may account for this behavior. An entrapment of ambient fluid can be observed due to the roll-up of Kelvin-Helmholtz billows behind the intrusion head. Throughout the evolution of this symmetric IGC, the leading mode-2 internal wave is locked to the intrusion head, and the disturbances of the density field is only limited within the near-intrusion region. The density contours near the IGC head are displaced upward and downward within the

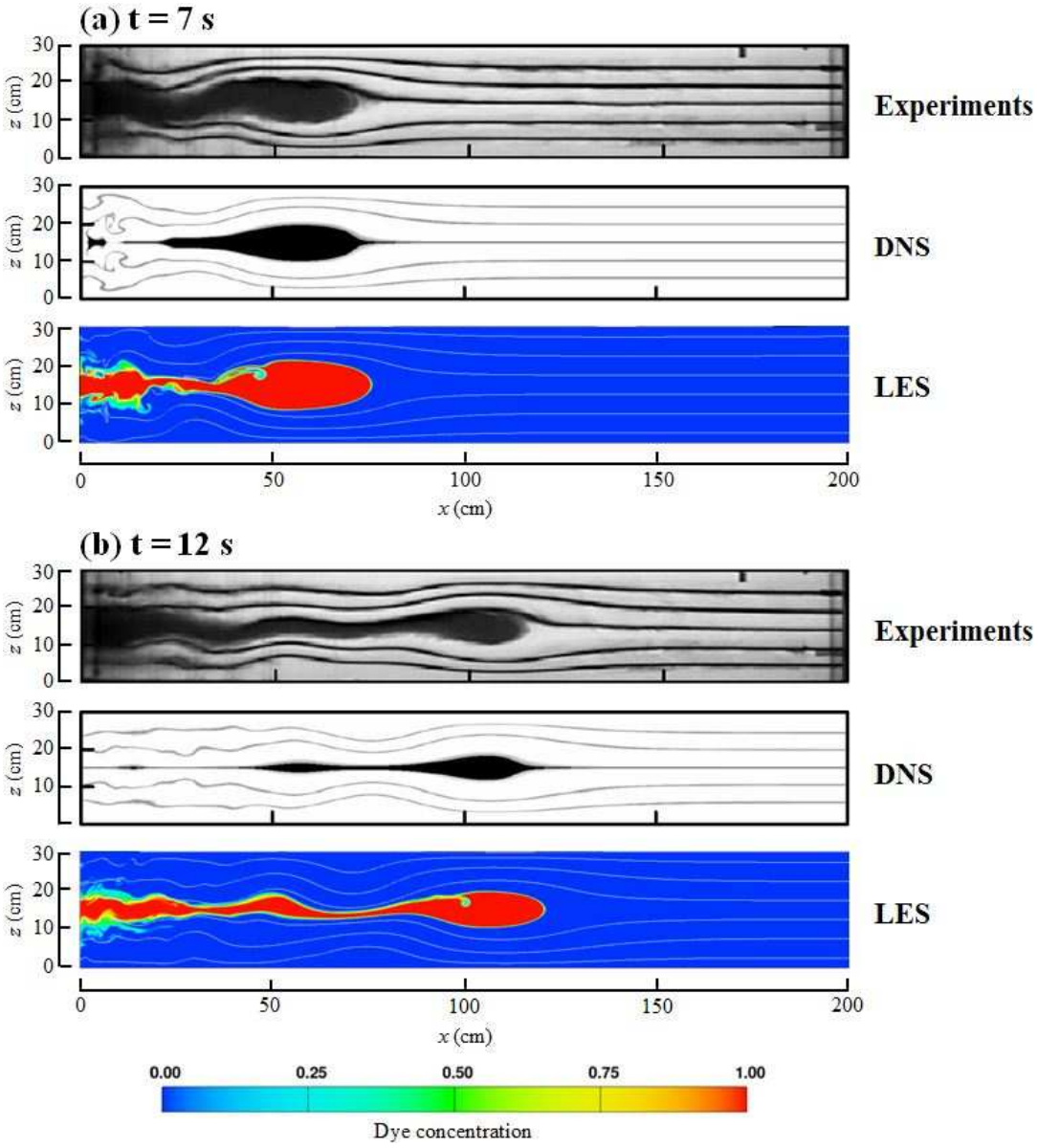

Figure 6.5: Snapshots of a symmetric IGC ($\tilde{h}$ = 0.5) with $N = 2\ s^{-1}$, at times (a) t = 7 s and (b) t = 12 s. The LES results from this study are compared with the experimental and DNS data from Munroe *et al.* (2009). The white lines denote density contours and the dye concentration contours provides a visualization of the intrusion.

upper and lower half of the tank respectively. Overall, the simulation results from the LES model in FLOW-3D match well with the experiments and DNS data from Munroe *et al.* (2009).

6.3.1.3 Positional History of the Nose of a Bottom IGC

Figure 6.6 shows the x_f versus t trajectory of a bottom propagating gravity current in a linearly stratified environment, where the current is denser than the ambient fluid. For all the three simulations, after a very short initial acceleration phase, the gravity current reaches a constant-speed slumping phase where the x_f-t curves can be well approximated by lines of constant slopes. The dimensionless time-averaged front velocities, $F = U/NH$ are observed to be 0.131, 0.264 and 0.210 for Run 11, Run 19 and Run 22, respectively, which are almost the same with the experimental measurements of Maxworthy *et al.* (2002). Moreover, the transitional distance X_{tr} after which the internal wave starts to control the gravity current propagation is predicted as 0.189 m, 0.768 m and 0.442 m for Run 11, Run 19 and Run 22, respectively, which are also in excellent agreement with the experiments. Together with the discussions in §6.3.1.1 and §6.3.1.2, it can be

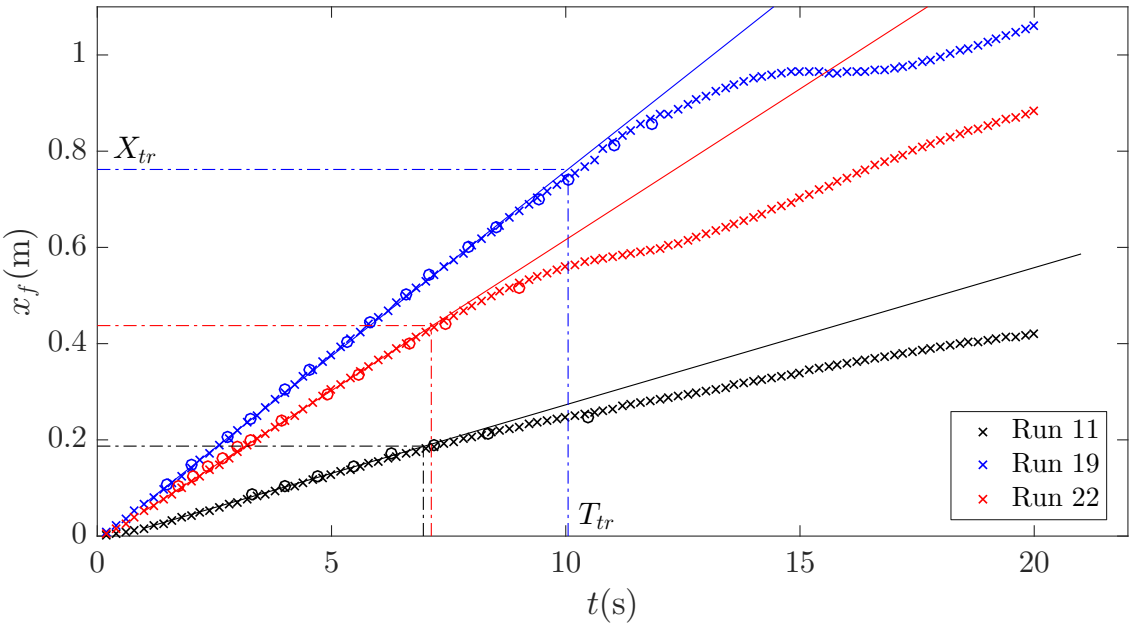

Figure 6.6: Positional history of the bottom gravity current nose in a linearly stratified ambient for three representative runs: (×) the present LES; (○) the experimental data of Maxworthy *et al.* (2002). The transitional distance (X_{tr}) and time (T_{tr}) mark the end of the constant-speed slumping phase, and the solid lines represent the time-averaged front velocities therein.

seen that the FLOW-3D solver is capable of capturing the temporal and spatial evolution of IGC propagating in a continuously stratified ambient fluid, either free from or along the boundary.

6.3.2 IGC with the Obstacle

6.3.2.1 General Description

Figures 6.7 and 6.8 depict the temporal evolution of a passive scalar concentration of two representative simulation cases with a short obstacle ($\tilde{W} = 0.5$, $\tilde{D} = 0.3$) and a taller obstacle ($\tilde{W} = 0.5$, $\tilde{D} = 0.5$) respectively. It is immediately apparent from these figures that the obstacle height significantly impacts the downstream flow behavior, and taller obstacles lead to more intense mixing.

In the short-obstacle case, initially the flow is a classical symmetric IGC propagating at mid-depth (figure 6.7a). On encountering the obstacle, the intrusion below the obstacle top is blocked and reflected back. The remaining part separates from the top left corner of the obstacle, quickly re-establishes itself and propagates further downstream. The slanted upper and lower surfaces of the intrusion result from the restoring buoyancy forces. Due to the obstacle's cutting effect and the flow separation which pushes the intrusion upward, the particles have a relatively small deviation from their position of equilibrium, thus no obvious overshoot-and-springback feature is observed in this case. However, for even shorter obstacle, e.g. $\tilde{D} = 0.1$ (see figure 6.11b), the deviation is large enough to overshoot and a concave-downward intrusion head emerges.

For the case of a taller obstacle (figure 6.8), when the intrusion encounters the obstacle, a major portion of the intrusion head below the obstacle top is blocked and reflected back, while the upper portion flows over the obstacle. A high-velocity jet-like flow plunges into the downstream stratified fluid. Given that the jet fluid has the same density as the mid-depth ambient fluid and hence heavier than its immediate ambient fluid, the jet will gain downward momentum from buoyancy forces as it migrates towards its level of neutral buoyancy. Combined with the forward momentum due to the horizontal pressure gradient (which also stems from buoyancy forces), the jet is expected to travel in a damping sinusoidal path, which is consistent with figure 6.11($f \sim j$). There is a

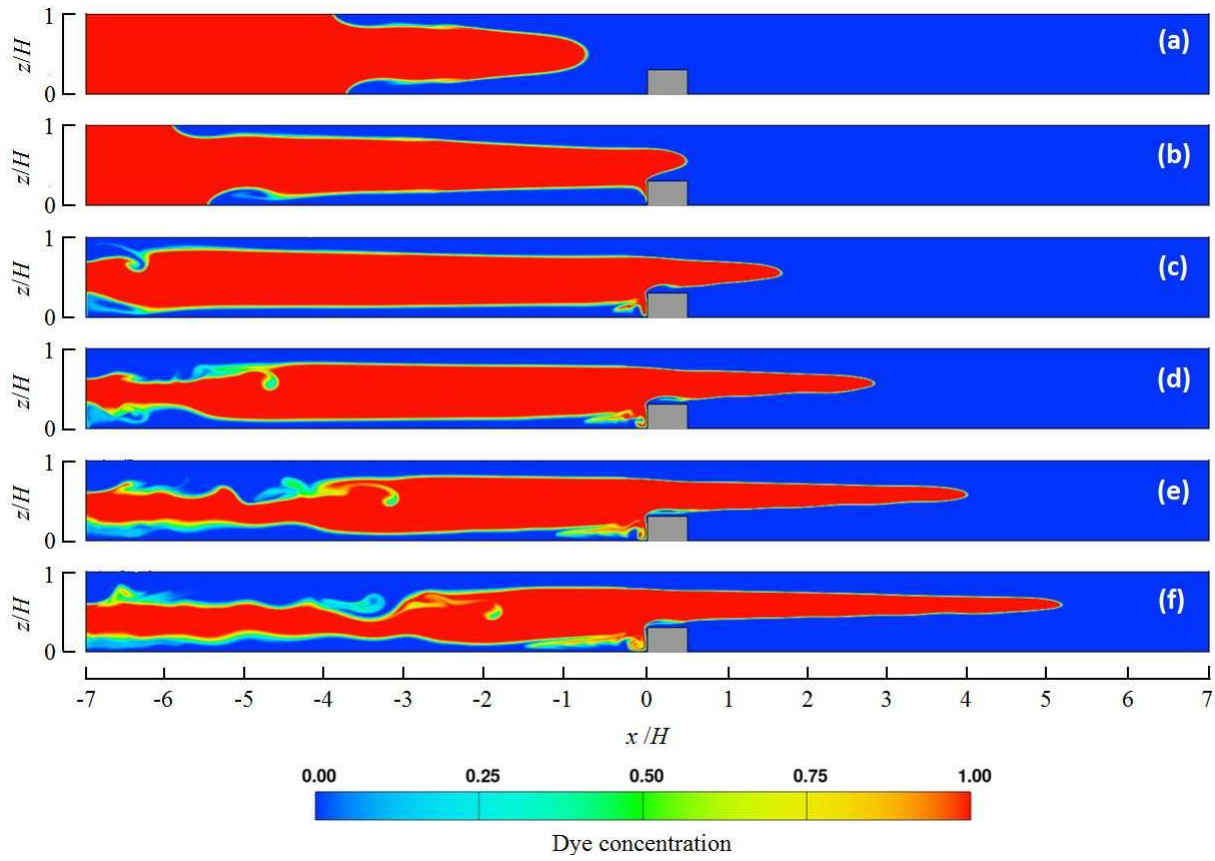

Figure 6.7: Time evolution of scalar concentration depicting the interaction of an IGC interacting with a thick ($\tilde{W} = 0.5$) and short ($\tilde{D} = 0.3$) obstacle at different times: (a) t = 10 s; (b) t = 20 s; (c) t = 30 s; (d) t = 40 s; (e) t = 50 s; (f) t= 60 s.

gradual rise in the vertical level at which the downstream intrusion travels due to dilution mainly caused by lighter ambient fluid. Figure 6.9(a) shows a zoom-in view highlighting the flow structure immediately downstream of the obstacle for a simulation case of a very tall obstacle (i.e. $\tilde{D} = 0.7$) at t = 28 s. The opposite flow directions of the downstream intrusion and the associated return flow leads to enhanced local shear that results in the rolling up of the fluid interface in lumped vortices. The entrapment of ambient fluid by the intrusion indicates the existence of the Kelvin-Helmholtz instability. A classic Kelvin-Helmholtz instability from Price (2008) is shown in figure 6.9(b) for comparison.

Based upon the observations discussed above, the flow of a symmetric IGC past a bottom-mounted obstacle in a continuously stratified ambient can be classified into two major types de-

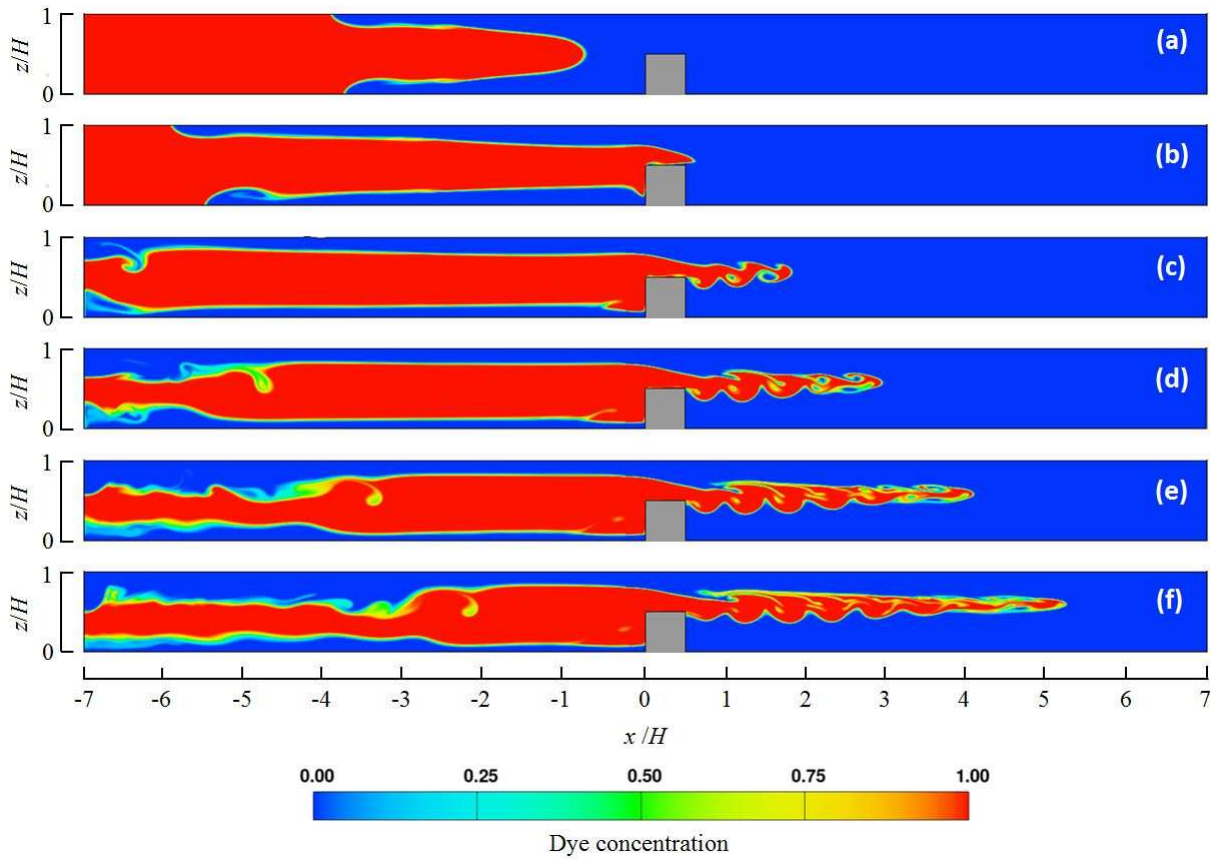

Figure 6.8: Time evolution of scalar concentration depicting the interaction of an IGC interacting with a thick ($\tilde{W} = 0.5$) and tall $\tilde{D} = 0.5$) obstacle at different times: (a) t = 10 s; (b) t = 20 s; (c) t = 30 s; (d) t = 40 s; (e) t = 50 s; (f) t= 60 s.

pending on the obstacle height. For a short obstacle, the intrusion is simply cut by an amount slightly larger than the obstacle height and propagates downstream in a similar form. On the other hand, for a tall obstacle, a richer set of phenomena occur, and the downstream flow pattern is a combined effect of three major mechanisms: (1) horizontal advection driven by horizontal pressure gradients; (2) overshoot-and-springback phenomenon when a fluid parcel is disturbed away from its state of equilibrium in a continuously stratified fluid; and (3) the Kelvin-Helmholtz instability generated by local velocity shear (i.e. vertical gradients of horizontal velocities). Thus, the completely-altered downstream flow dynamics highlights how the interaction of a IGC with an obstacle is quite different to that of a BBGC interacting with an obstacle.

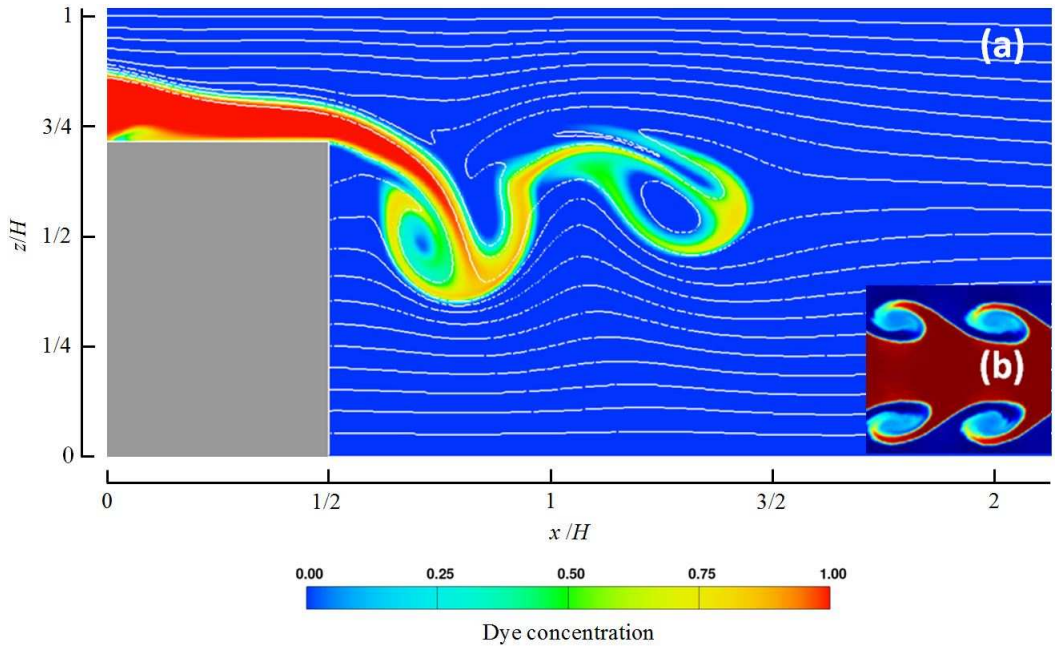

Figure 6.9: (a) A zoom-in view of the scalar concentration field immediately downstream of the obstacle for a simulation case with a very tall obstacle ($\tilde{W} = 0.5$, $\tilde{D} = 0.7$) at t = 28 s. The *white solid lines* indicate the density contours; (b) a depiction of a classical Kelvin-Helmholtz instability (Price 2008).

6.3.2.2 Effect of Obstacle Size

Figure 6.10 shows the temporal evolution of scalar concentration for a simulation case with a relatively thin but tall obstacle ($\tilde{W} = 0.05$, $\tilde{D} = 0.5$). Compared with figure 6.8, which is for a simulation case with the same obstacle height but 10 times the width, it can be seen that there are some changes in the fine structure of the downstream flow. However, the bulk features of the downstream intrusions are remarkably similar despite an order of magnitude difference in the width of the obstacle. This indicates that the obstacle thickness appears to have a negligible effect on the bulk downstream propagation distance (at least for the thicknesses explored here). This issue is further explored in §6.3.2.3.

Snapshots of downstream scalar concentration fields at a selected time t = 50 s for a series of 10 simulations cases for a fixed obstacle width ($\tilde{W} = 0.5$,) and varying obstacle heights in the range $\tilde{D}$ = 0 $\sim$ 0.9, are shown in figure 6.11. It is clear that the obstacle height is a key factor in determining downstream motion. Very short obstacles (e.g. $\tilde{D} = 0.1$) have no direct contact

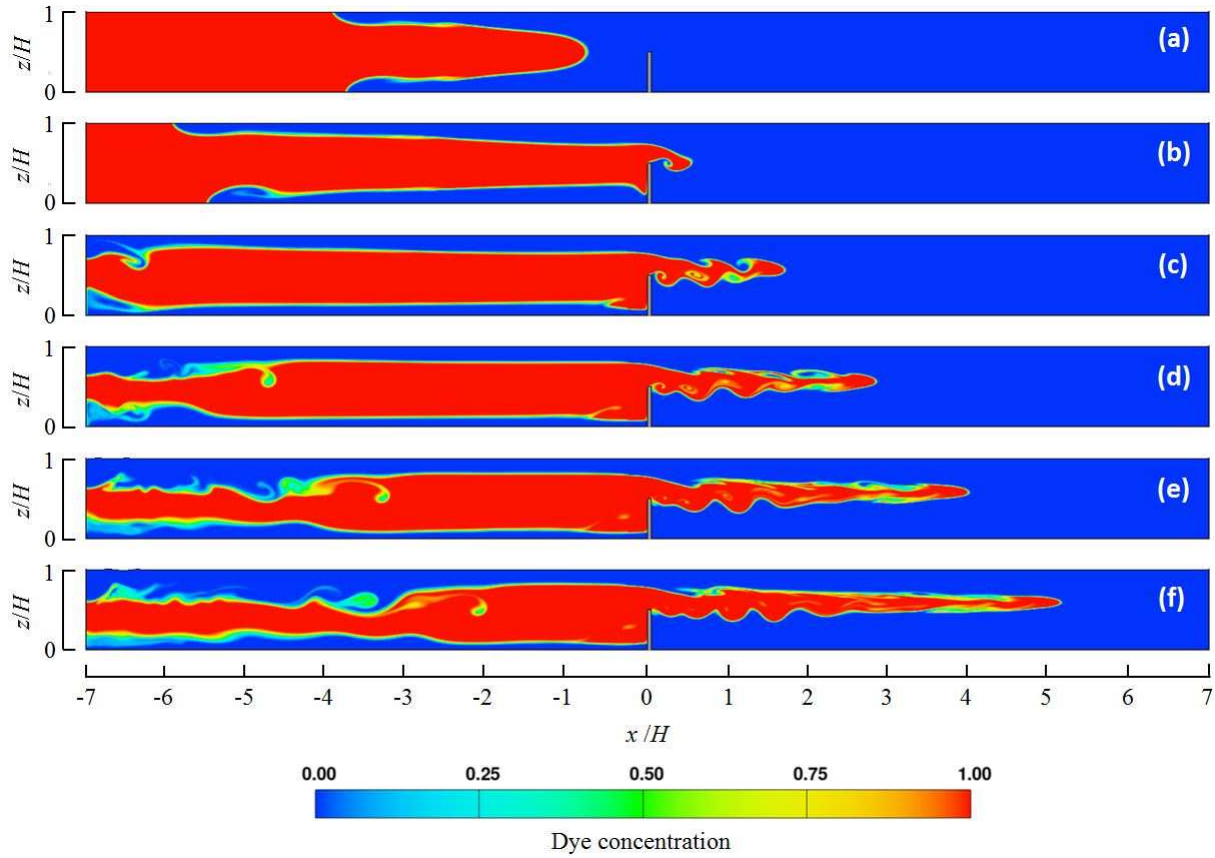

Figure 6.10: Time evolution of scalar concentration depicting the interaction of an IGC interacting with a thin ($\tilde{W} = 0.05$) and tall $\tilde{D} = 0.5$) obstacle at different times: (a) t = 10 s; (b) t = 20 s; (c) t = 30 s; (d) t = 40 s; (e) t = 50 s; (f) t= 60 s.

with the IGC, and only influence the motion downstream through interaction with the return flow. The propagation distance of the IGC is only slightly reduced compared to the classical IGC (see figure 6.11a, b). The concave-downward intrusion head forms as a result of particle overshoot and springback phenomenon discussed earlier. As the obstacle height increases to $\tilde{D} = 0.2$, it directly touches the intrusion and thus poses a more noticeable retarding effect on the propagation of the intrusion as seen in figure 6.11(c). For obstacles heights $\tilde{D} \geq 0.5$, the overshoot-springback feature can be easily seen in the downstream oscillations, given that the intrusion for these cases are forced to rise above their equilibrium mid-depth level.

For obstacle heights in the range $\tilde{D}$ = 0.3 $\sim$ 0.6 (figure 6.11$d \sim g$), increase in the obstacle height generates no obvious corresponding reduction in downstream propagation distance. The

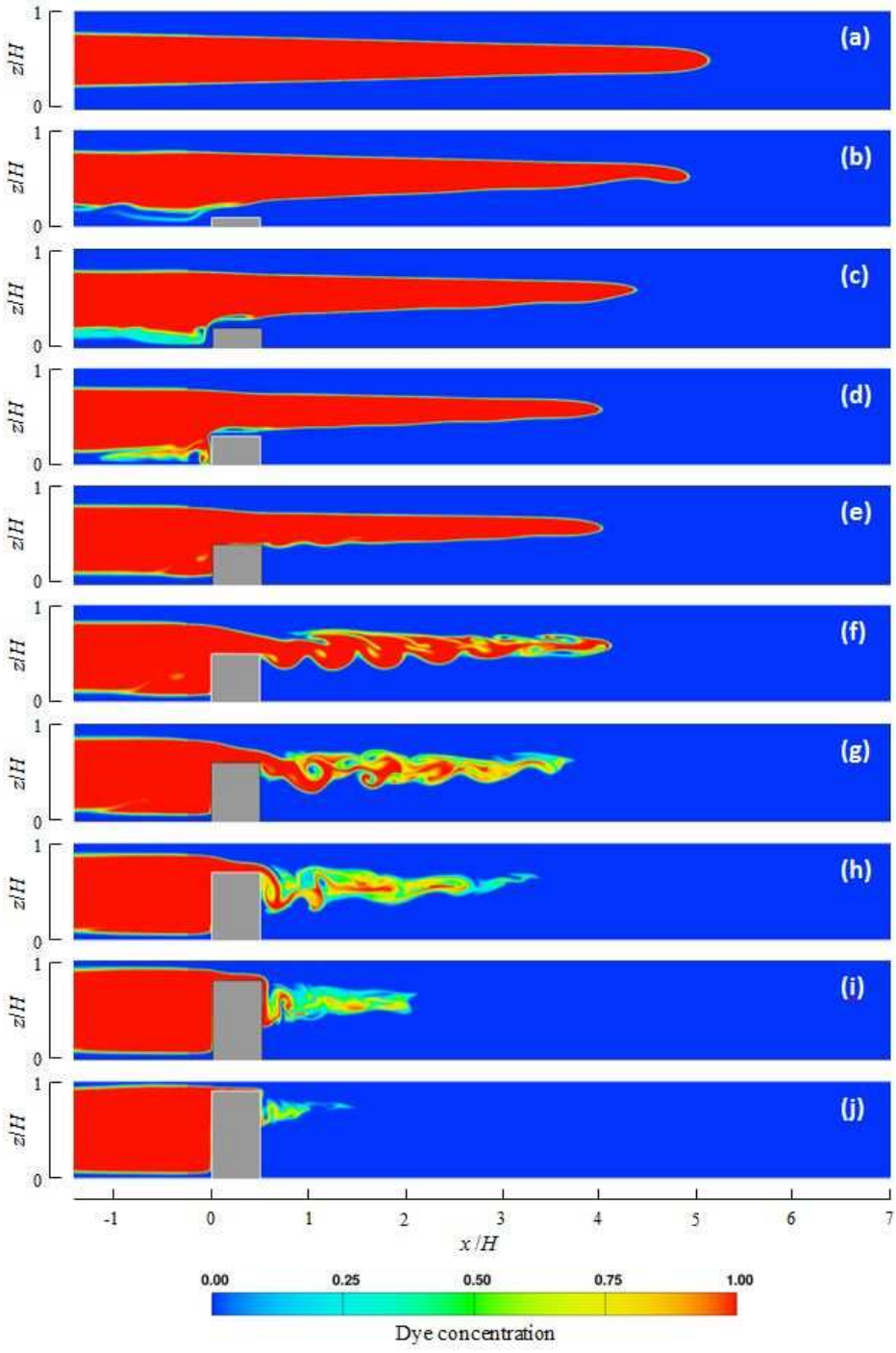

Figure 6.11: Visualizations of the downstream intrusions at t = 50 s for simulation cases with different obstacle heights: (a) $\tilde{D} = 0$ (no obstacle); (b) $\tilde{D} = 0.1$; (c) $\tilde{D} = 0.2$; (d) $\tilde{D} = 0.3$; (e) $\tilde{D} = 0.4$; (f) $\tilde{D} = 0.5$; (g) $\tilde{D} = 0.6$; (h) $\tilde{D} = 0.7$; (i) $\tilde{D} = 0.8$; (j) $\tilde{D} = 0.9$. The upstream regions have been truncated for clarity.

reason for this behavior is likely two-fold viz: (1) upstream impoundment which introduces additional kinetic energy into the downstream flow; and (2) taller obstacles lead to greater mixing with lighter fluid which makes the intrusion propagate at a higher level and hence at a larger speed (see equation (6.1)). Both of these two factors likely compensate the obstacle's retarding effect on the propagation speed. However, as the obstacle height increases even further (see figure 6.11$h \sim j$), the retarding effect becomes increasingly predominant and the intrusion loses its kinetic energy rapidly. For the case of $\tilde{D} = 0.9$, the over-passing fluid travels almost in the vertical direction and propagates downstream very slowly.

6.3.2.3 Propagation Speed

The propagation distance of the intrusion front as a function of time for all the simulation cases discussed in figure 6.11 are shown in figure 6.12. Three interaction phases can be identified by inspecting this figure, namely: (1) an upstream slumping phase ($t = 0 \sim 16$ s) that occurs before encountering the obstacle noting that the IGC in all the simulation cases accelerate from rest and propagate at exactly the same speed, regardless of the obstacle height; (2) a transient phase ($t = 16 \sim 28$ s) where the IGC encounters the obstacle and the retarding effect of the obstacle is noticeable depending on the obstacle height and the propagation distance diverges with no clear time dependence; and (3) a downstream constant-speed phase ($t = 28 \sim 60$ s) when the intrusion has gone past the obstacle and propagates further downstream. The slopes of the fitted straight lines indicates a constant downstream front speed which depends on the obstacle height. The overall varying trend, i.e. taller obstacle generally leads to larger retarding effect and thus smaller propagation speed, is observed as expected.

In order to cast the results seen in figure 6.12 in a generalizable form, we plot the non-dimensional front speed U/NH of the downstream intrusion as a function of the non-dimensional obstacle height, D/H in figure 6.13. Given the previous comparison of propagation distances of a symmetric IGC interacting with both thin and wider obstacles (see figures 6.8 & 6.10) showed that the downstream intrusion speed has no obvious dependence on the streamwise dimension of the obstacle, the obstacle height is plotted as the predominant independent variable that controls

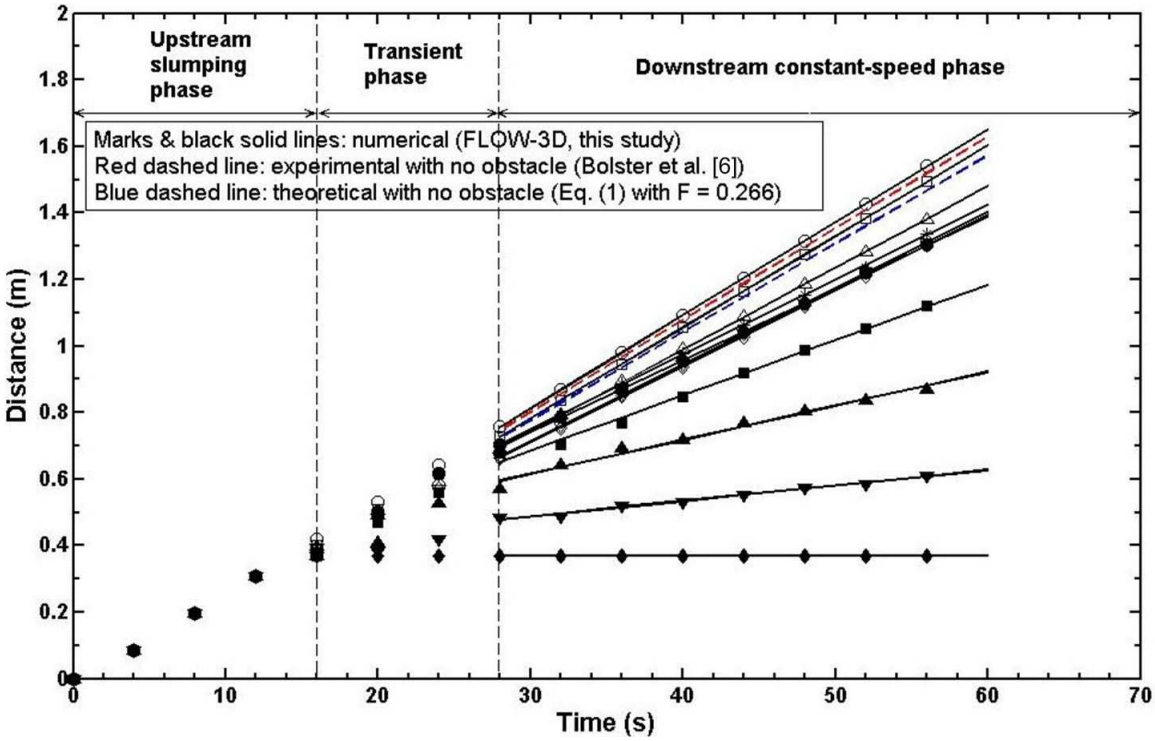

Figure 6.12: Simulated temporal evolution of an IGC past a thick obstacle ($\tilde{W} = 0.5$), for cases with $\tilde{D} = 0 \sim 1$. The symbols indicate varying non dimensional obstacle heights $\tilde{D}$ as follows: *empty circles*, $\tilde{D}$ = 0 (no obstacle);*empty squares*, $\tilde{D}$ = 0.1; *empty upward triangles*, $\tilde{D}$ = 0.2; *empty downward triangles* $\tilde{D}$ = 0.3; *empty diamonds*, $\tilde{D}$ = 0.4; *stars*, $\tilde{D}$ = 0.5; *filled circles*, $\tilde{D}$ = 0.6; *filled squares*, $\tilde{D}$ = 0.7; *filled upward triangles*, $\tilde{D}$ = 0.8; *filled downward triangles*, $\tilde{D}$ = 0.9; *filled diamonds*, $\tilde{D}$ = 1.0, respectively. The *solid lines* are the fitted straight lines for cases with different values of $\tilde{D}$, with the slope denoting the corresponding propagation speed. The *red dashed line* indicates the experimental results for the case of $\tilde{D}$ = 0 (no obstacle) from Bolster *et al.* (2008), and the *blue dashed line* indicates the theoretical results for the case of $\tilde{D}$ = 0 according to equation (6.1) with F = 0.266.

the downstream propagation of a symmetric IGC past the obstacle. Note, we have also plotted the front speeds for the thin obstacle simulations in figure 6.13 (shown in triangular symbols). For the parameter range considered in this study, the flow pattern of a symmetric IGC past an obstacle in a continuously stratified ambient can be subdivided into three regimes:

- *A retarding regime* ($\tilde{D} \approx 0 \sim 0.3$): The front speed of the intrusion experiences a 20 % reduction when compared with the case of $\tilde{D} = 0$, simply due to the retarding effect of the obstacle;

- *An impounding regime* ($\tilde{D} \approx 0.3 \sim 0.6$): An additional 30% increase in the obstacle height only leads to a negligible 5% reduction in front speed;

- *A choking regime* ($\tilde{D} \approx 0.6 \sim 1.0$): The intrusion loses its forward momentum quickly and accounts for the remaining 75% front-speed reduction.

This proportional distribution of the front-speed reduction among different ranges of obstacle height provides a preliminary guidance for the engineering design of retarding facilities for a symmetric IGC in a continuously stratified ambient. However, it is important to note that we have only varied the obstacle size in this study, while keeping all other pertinent parameters fixed, such as the strength of the ambient stratification and the depth of neutral equilibrium of the lock fluid (see figure 6.2). It is well known that an IGC in a stratified fluid will get thinner as it propagates. Hence, the lock length will affect the long time evolution of the intrusion (e.g. the rate at which intrusion thickness decreases), although it is irrelevant to the initial dynamics. Since the vertical scale of the intrusion when it hits the obstacle tends to determine the existence of upstream impoundment as well as the direct contact of the obstacle with the intrusion (otherwise the return flow), it is expected that the downstream intrusion speed to be a function of multiple factors, such as the stratification, lock length, distance between the release position and the obstacle. Such a comprehensive study that endeavors to cover a wider parameter space is beyond the scope of this initial study where our goal is simpler with the primary focus being on the effect of the obstacle

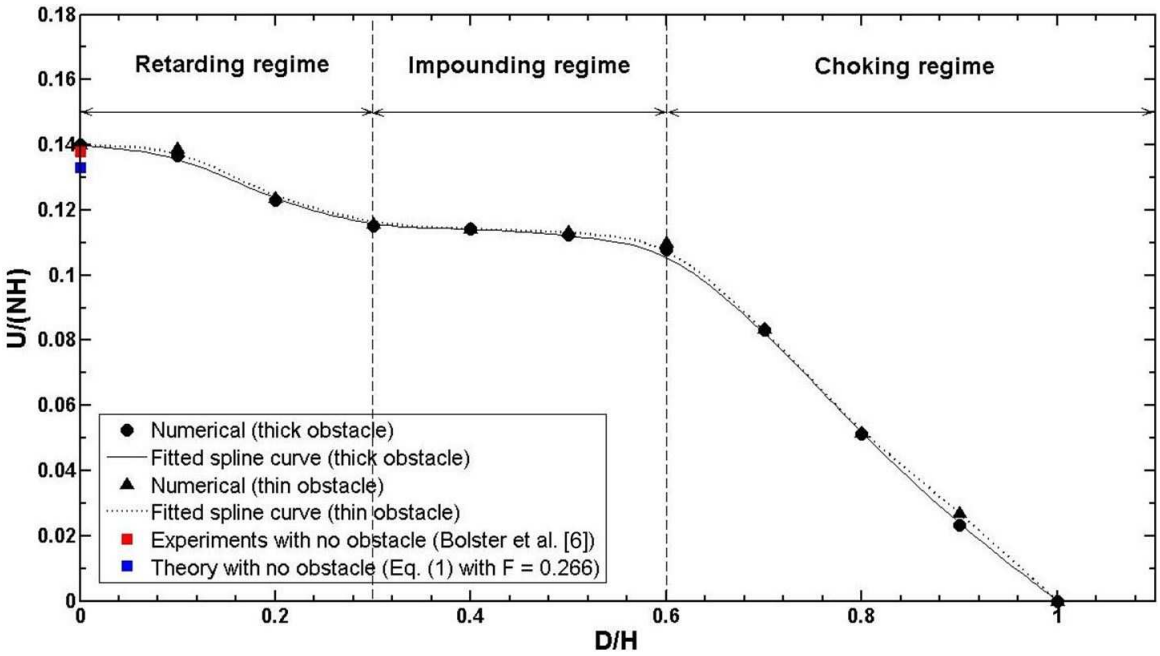

Figure 6.13: The downstream dimensionless front speed as a function of dimensionless obstacle height. The *black circles* correspond to the slope of the fitted solid lines for $\tilde{D}$ = 0 to 1 in figure 6.12. The *red* and *blue squares* correspond to the slope of the *red* and *blue dashed lines* in figure 6.12. The results for a thin obstacle ($\tilde{W} = 0.05$) are also plotted for comparison and are denoted by the *black upward triangles*.

height, given that it is one of the key variables that influences the interaction dynamics of an IGC with an obstacle.

6.4 Conclusions

The focus of the present study was on the dynamics of a 2D symmetric IGC past a bottom-mounted obstacle in a continuously stratified ambient fluid. Two series of LES simulations using the FLOW-3D non-hydrostatic numerical model were performed. The first series of simulations were used to validate the capability of the numerical model to capture the essential spatial-temporal evolution dynamics of IGC in a continuously stratified ambient without topographic effects. The propagation speed for IGC at arbitrary depths and the internal wave field for a symmetric IGC were simulated and compared with analytical, experimental and DNS data, and good agreement were found.

The main findings of this study are based on the second series of simulations that included a bottom-mounted obstacle in order to investigate the interaction dynamics of a symmetric IGC with the obstacle. The obstacle height was found to significantly impact the downstream flow behavior, while the obstacle width appears to only have a minor effect. For short obstacles, the intrusion was simply distorted minimally by the obstacle and propagated further downstream in a similar form to the classical IGC. For taller obstacles, the downstream flow was determined to be a joint effect of horizontal advection, overshoot-springback phenomenon, and the Kelvin-Helmholtz instability. The most remarkable difference between a topographically-affected BBGC and IGC is that while the downstream BBGC still possesses the same dynamics after encountering tall obstacles, the downstream IGC may evolve quite differently further downstream.

On encountering the obstacle, the intrusion enters a transient phase where its speed oscillates, and then propagates further downstream far from the obstacle at a constant speed. The relationship between the downstream (constant) intrusion speed and obstacle height can be subdivided into three regimes: (1) a retarding regime ($\tilde{D} \approx 0 \sim 0.3$) where a 30% increase in obstacle height leads to a 20% reduction in intrusion speed, simply due to obstacle's retarding effect; (2) an impounding regime ($\tilde{D} \approx 0.3 \sim 0.6$) where an additional 30% increase in obstacle height only leads to a rather negligible additional 5% reduction in intrusion speed, presumably due to the accelerating effect of upstream impoundment and downstream enhanced mixing; and (3) a choking regime ($\tilde{D} \approx 0.6 \sim 1.0$) where the remaining 40% increase in obstacle height accounts for the remaining 75% reduction in intrusion speed as a direct result of the dominance of the obstacle's blocking effect. Overall, this study is a first step towards understanding the dynamics of IGC at arbitrary depths past complex terrain in continuous stratified ambients. Future work focusing on asymmetric intrusions interacting with multiple and irregular obstacles is required to gain more insights into the internal wave field and its influence on the intrusion-obstacle interaction. It will also be desirable to perform a limited number of 3D simulations to investigate the lateral instability of the coherent structures such as the Kelvin-Helmholtz billows, in order to obtain a complete understanding of turbulent mixing.

Chapter 7

Summary & Conclusions

7.1 Summary of Investigation

In this dissertation, an in-depth investigation of constant-density/density-driven environmental flows interacting with single/multiple obstacles has been carried out using large eddy simulations. The governing equations were solved using the finite-volume CFD software, FLOW-3D, developed by Flow Science, Inc. The main results of the research are presented in chapters 4, 5, and 6, respectively.

In chapter 4, the mean three-dimensional hydrodynamics in the vicinity of a suspended cylindrical canopy patch was investigated. High-resolution three-dimensional large eddy simulations were conducted to study the effects of patch density ($0.16 \leq \phi = N_c(d/D)^2 \leq 1$, by varying N_c) and patch aspect ratio ($0.25 \leq AR = h/D \leq 1$, by varying h) on the near-field flow properties (a total of 16 simulations). The respective effects of ϕ or AR on the bleeding flow through the patch surface area were analyzed based on visualization of the velocity fields. A close look at the flow dynamics inside the patch provides an explanation for the observed dependence of vertical bleeding on these two parameters. Next, the three-dimensional flow-bleeding dynamics was quantitatively assessed using a flow-rate budget. Finally, the interlinks between the patch geometry (ϕ and AR), the bleeding flows perpendicular to the main stream, and the proportional redistribution of the steamwise flow rate were discussed in detail.

In chapter 5, the propagation dynamics of a bottom-boundary gravity current over a submerged array of cylinders was investigated using laboratory experiments and large eddy simulations. Excellent agreement between experiments and LES was found. A new geometrical framework (μ_x-μ_y) was proposed to better characterize the planar array geometry. Firstly. to investigate the front velocity of gravity currents across the whole range of array density ϕ (i.e. the volume fraction of solids), the array was densified from a flat-bed ($\phi = 0$) towards a solid-slab ($\phi = 1$) under a partic-

ular submergence ratio H/h. Next, the streamwise array density μ_x and the spanwise array density μ_y were varied independently to explore the effect of array non-equidistance. Furthermore, for a constant array geometry, the flow depth was varied to result in different submergence conditions. Both in-line and staggered arrays are considered. A total of 228 simulations were performed for this extensive parametric study. The time-averaged front speed in the slumping phase was used to identify four dynamically different flow regimes. Based on density and velocity structures, the transitions between different flow regimes were then analyzed.

In chapter 6, the interaction of a mid-depth intrusion with an isolated bottom-mounted obstacle was investigated using high-resolution two-dimensional large eddy simulations. We focused on the effect of ambient stratification without including the obstacle's grouping effects. After validating the numerical model with a free-propagating intrusion, the obstacle was introduced. Both thick and thin obstacles are considered. The submergence ratio D/H was varied between 0 to 0.9 in 0.1 increments. The downstream intrusion density structure and propagation speed were then analyzed.

7.2 Conclusions on Key Findings

The following is a brief description of the main outcomes of this study:

- The near-field hydrodynamics of a suspended finite canopy patch strongly depends on the patch geometry, and is much more complex than the case of emergent infinite canopies, emergent finite canopies, and partial-depth infinite canopies. The resulting flow field is highly three-dimensional: an increase in either ϕ or AR decreases/increases/increases bleeding velocity along the streamwise/lateral/vertical direction. A close look at the flow inside the patch reveals that despite the similar dependence of vertical bleeding on ϕ and AR, the underlying physics are different. However, in contrast to the bleeding velocity, a flow-rate budget shows that the proportion of the vertical bleeding flow leaving the patch in the total flow entering the patch (i.e. relative vertical bleeding) decreases with increasing AR. The interlinks between patch geometry, flow bleeding and flow diversion are identified: the patch

influences the flow diversion not only directly by its real geometrical dimensions, but also indirectly by modifying flow bleeding which enlarges the size of the near-wake. While loss of flow penetrating the patch increases monotonically with increasing ϕ, its partition into flow diversion around and beneath the patch shows a non-monotonic dependence.

- There is a wide range of possible states of flow along a single contour of ϕ, emphasizing the inappropriateness of using the conventional ϕ-parameterization of array geometry for nonequidistant arrays ($\mu_x \neq \mu_y$). Instead, the newly proposed two-dimensional parameter space allows for the independent variation of μ_x and μ_y, and thus provides a more quantitative and unambiguous description of the dynamics of canopy flows compared with the array density given by $\phi = \left(\frac{\pi}{4}\right) \mu_x \mu_y$. In terms of bottom gravity currents, four dynamically different flow regimes are identified: (i) through-flow propagating in the array interior subject to individual cylinder wakes (μ_x: small for in-line array and arbitrary for staggered array; μ_y: small); (ii) over-flow propagating on the top of the array subject to vertical convective instability (μ_x: large; μ_y: large); (iii) plunging-flow climbing sparse close-to-impermeable rows of cylinders with minor streamwise intrusion (μ_x: small; μ_y: large); and (iv) skimming-flow channelized by an in-line array into several sub-currents with strong wake sheltering (μ_x: large; μ_y: small). The most remarkable difference between in-line and staggered arrays is the nonexistence of skimming-flow in the latter due to the flow interruption by the offset rows. Our analysis reveals that as ϕ increases, the transition from through-flow towards over- or skimming-flow is responsible for increasing the gravity current front velocity.

- Compared with gravity current's propagation in a homogeneous ambient, a richer set of flow phenomena is possible in the case of a continuously stratified ambient. For short obstacles, the intrusion re-established itself downstream without much distortion. However, for tall obstacles, the downstream flow was found to be a joint effect of horizontal advection, overshoot-springback phenomenon, and associated Kelvin-Helmholtz instabilities. Analysis of the numerical results show that the relationship between the downstream propagation speed and the obstacle height can be subdivided into three regimes: (1) a retarding regime ($\tilde{D}$

$\approx 0 \sim 0.3$) where a 30% increase in obstacle height leads to a 20% reduction in propagation speed, simply due to the obstacle's retarding effect; (2) an impounding regime ($\tilde{D} \approx 0.3 \sim 0.6$) where the additional 30% increase in obstacle height only leads to a further (negligible) 5% reduction in propagation speed, due to the accelerating effect of upstream impoundment and downstream enhanced mixing; and (3) a choking regime ($\tilde{D} \approx 0.6 \sim 1.0$) where the propagation speed is dramatically reduced due to the dominance of the obstacle's blocking effect. The obstacle thickness was found to be irrelevant in determining the downstream propagation speed at least for the parameter range explored in this study.

- There are fundamental differences in the flow dynamics between porous canopies and their solid counterpart, that is to say, one should not assume a monotonic variation of flow dynamics as ϕ is increased from 0 continuously to 1. Relevant evidences include: (i) In figure 4.12(c), the decrease of $|\Delta Q_a|/|\Delta Q_t|$ with increasing ϕ is governed by the dominance of lateral bleeding over vertical bleeding. However, the value of $|\Delta Q_a|/|\Delta Q_t|$ associated with the limiting case of a solid patch ($\phi = 1$) turns out to be much larger compared with all the porous patches, due to the absence of bleeding flow; (ii) In figure 4.13, the patch drag coefficient $\overline{C}_D$ increases as ϕ increases from 0.16 to 0.31, and reaches a plateau between $\phi = 0.31$ and 0.50. However, as ϕ increases further, the $\overline{C}_D$ drops abruptly towards the solid-patch case ($\phi = 1$), which is even smaller than that of the sparsest patch with $\phi = 0.16$. This can be attributed to the absence of internal resistance and/or the bleeding flows which enlarges the effective patch dimensions; (iii) In figure 5.8, it seems that as ϕ increases, the time-averaged front speed of the gravity current first decreases and then increases towards the flat-bed condition. However, in figure 5.10, as ϕ increases, dilution of the over-current riding on top of the array was strengthened as ϕ increases from 0 to 0.785, but a much weaker dilution occurs at the limiting case of a solid slab, due to the absence of the vertical convection between the over-current and the underlying lighter ambient fluid. Based on the above, there clearly exists a turning point between very dense canopies and their solid counterpart after which

the dependence of flow parameters on ϕ are reversed. Further research which is beyond the scope of this study is required to quantitatively define the transition.

7.3 Suggestions for Future Research

The research presented in this dissertation provides fundamental insights into the physics of environmental flows driven by difference forcing mechanisms interacting with obstacles of different geometries, with or without density stratification. From a practical point of view, the results can aid in the development of better parameterizations of such processes in engineering applications. Given the limitations of this study, several directions of future research are suggested below:

- It would be interesting to introduce density stratification (either multi-layered or continuously stratified) into the problems presented in chapters 4 and 5 to better mimic the oceanic and atmospheric conditions. For chapter 4, the stratification could suppress vertical bleeding, while at the same time, prevent the bottom shear layer from intruding into the wake region. The resultant effect of these two contradictory processes on the wake structures is intriguing. For chapter 5, stronger ambient stratification tends to increase the gravity current front speed due to stronger buoyancy forcing, but also tends to decrease the current motion because it inhibits the through-to-over transition. Again, the resultant effect is unknown and could be investigated using an analogous parametric study to that presented in chapter 5.

- In chapter 5, not only the array drag, but also the incoming buoyancy forcing (i.e. g' and H), determines the propagation properties of gravity currents. Although we are aware that the flow-regime diagram in figure 5.8 is only proposed for a particular submergence ratio, it is conceivable that it can also be applied to other submergence conditions as long as the array is submerged. However, the transition thresholds between different regimes would require some modifications. For example, there will be an earlier transition to over-flow since that deeper submergence tends to promote the through-over transition (figures 5.19 and 5.20), presumably the plunging-over and the skimming-over transitions as well. Besides, this study

only considered a particular cylinder aspect ratio $h/d = 2.5$. A future direction of study will be to investigate how the variation of h/d modify the gravity current propagation.

- For the problem presented in chapter 6, future work focusing on asymmetric intrusions interacting with multiple and irregular obstacles is required to gain more insights into the internal wave field and its influence on the intrusion-obstacle interaction. It will also be desirable to perform a limited number of 3D simulations to investigate the lateral instability of the coherent structures such as the Kelvin-Helmholtz billows, in order to obtain a complete understanding of turbulent mixing.

- The gap of data between dense and solid patches calls for future study on the detailed flow dynamics within this range. To date, no studies have been done on this issue. To achieve this, a significant separation of the lengthscales between the canopy and its constituent element, D/d, will be needed to approach the solid-canopy limit ($\phi = 1$) as close as possible. Obviously, this will require more computational effort to fully resolve the flow at the much smaller element-scale.

Bibliography

Afgan, I., Moulinec, C., Prosser, R. & Laurence, D. 2007 Large eddy simulation of turbulent flow for wall mounted cantilever cylinders of aspect ratio 6 and 10. *Intl. J. Heat Fluid Flow* **28**, 561–574.

Allen, J. 1985 *Principles of Physical Sedimentology*. Allen & Unwin.

An, S., Julien, P. Y. & Venayagamoorthy, S. K. 2012 Numerical simulation of particle-driven gravity currents. *Environ. Fluid Mech.* **12**, 495–513.

Armi, L. 1986 The hydraulics of two flowing layers with different densities. *J. Fluid Mech.* **163**, 27–58.

Ashby, S. F., Manteuffel, T. A. & Saylor, P. E. 1990 A taxonomy for conjugate gradient methos. *SIAM J. Numer. Anal.* **27(6)**, 1542–1568.

Aure, J., Strohmeier, T. & Strand, Ø. 2007 Modelling current speed and carrying capacity in long-line blue mussel (*Mytilus edulis*) farms. *Aquacult. Res.* **38**, 304–312.

Baines, P. G. 1995 *Topographic effects in stratified flows*. Cambridge University Press.

Ball, D. J. & Hall, C. D. 1980 Drag of yawed pile groups at low reynolds number. *ASCE J. R. Aero. Soc.* **90**, 128–138.

Ball, D. J., Stansby, P. K. & Albertson, J. D. 1996 Modelling shallow water flow around pile groups. *Proc. Inst. Civ. Eng.-Water* **118**, 223–236.

Barkley, D. & Henderson, B. D. 1996 Three-dimensional floquet stability analysis of the wake of circular cylinder. *J. Fluid Mech.* **322**, 215–241.

Belcher, S., Jerram, N. & Hunt, J. 2003 Adjustment of a turbulent boundary layer to a canopy of roughness elements. *J. Fluid Mech.* **488**, 369–398.

Belcher, S. E., Harman, I. N. & Finnigan, J. J. 2012 The wind in the willows: flows in forest canopies in complex terrain. *Annu. Rev. Fluid Mech.* **44**, 479–504.

Benjamin, T. B. 1968 Gravity currents and related phenomena. *J. Fluid Mech.* **31**, 05014004.

Birman, V. K., Meiburg, E. & Ungarish, M. 2007 On gravity currents in stratified ambients. *Phys. Fluids* **19**, 086602.

Blanco, J., Zapata, M. & Morono, A. 1996 Some aspects of the water flow through mussel rafts. *Sci. Mar.* **60(2-3)**, 275–282.

Bolster, D., Hang, A. & Linden, P. F. 2008 The front speed of intrusions into a continuously stratified medium. *J. Fluid Mech.* **594**, 369–377.

Bonnecaze, R. & Lister, J. 1993 Particle-driven gravity currents. *J. Fluid Mech.* **250**, 339–369.

Bourgeois, J. A., Sattari, P. & Martinuzzi, R. J. 2011 Alternating half-loop shedding in the turbulent wake of a finite surface-mounted square cylinder with a thin boundary layer. *Phys. Fluids* **23**, 095101.

Boyd, A. J. & Heasman, K. G. 1998 Shellfish mariculture in the Benguela system: Water flow patterns within a mussel farm in Saldanha Bay, South Africa. *J. Shellfish Res.* **17(1)**, 25–32.

Britter, R. E. & Simpson, J. E. 1981 A note on the structure of the head of an intrusive gravity current. *J. Fluid Mech.* **112**, 459–466.

Cantero, M. I., Lee, J. R., Balachandar, S. & Garcia, M. H. 2007 On the front velocity of gravity currents. *J. Fluid Mech.* **586**, 1–39.

Cassiani, M., Katul, G. G. & Albertson, J. D. 2008 The effects of canopy leaf area index on airflow across forest edges: large-eddy simulation and analytical results. *Boundary-Layer Meteorol.* **126**, 433–460.

Cenedese, C., Nokes, R. & Hyatt, J. 2016 Lock-exchange gravity currents over rough bottoms. *Environ. Fluid Mech.* **doi:10.1007/s10652-016-9501-0**.

Chang, C. C., Yang, S. H. & Chu, C. C. 2008 A many-body force decomposition with applications to flow about bluff bodies. *J. Fluid Mech.* **600**, 95–104.

Chang, K. & Constantinescu, G. 2015 Numerical investigation of flow and turbulence structure through and around a circular array of rigid cylinders. *J. Fluid Mech.* **776**, 161–199.

Chassignet, E. P., Cenedese, C. & Verron, J. 2012 *Buoyancy-Driven Flows*. Cambridge University Press.

Chen, Z., Jiang, C. & Nepf, H. 2013 Flow adjustment at the leading edge of a submerged aquatic canopy. *Water Resour. Res.* **49**, 5537–5551.

Chen, Z., Ortiz, A., Zong, L. & Nepf, H. 2012 The wake structure begind a porous obstruction and its implications for deposition near a finite patch of emergent vegetation. *Water Resour. Res.* **48**, W09517.

Cheong, H.-B., Kuenen, J. J. P. & Linden, P. F. 2006 The front speed of intrusive gravity currents. *J. Fluid Mech.* **552**, 1–11.

Chimney, M. J., Wenkert, L. & Pietro, K. C. 2006 Patterns of vertical stratification in a subtropical constructed wetland in south florida (USA). *Ecol. Engng* **27**, 322–330.

Coceal, O. & Belcher, S. 2004 A canopy model of mean winds through urban areas. *Q. J. R. Meteorol. Soc.* **130**, 1349–1372.

de Rooij, F., Linden, P. F. & Dalziel, S. B. 1999 Saline and particle-driven interfacial intrusions. *J. Fluid Mech.* **389**, 303–334.

Duarte, C. M. 1991 Seagrass depth limits. *Aquat. Bot.* **40**, 363–377.

Eames, I., Hunt, J. C. R. & Belcher, S. E. 2004 Inviscid mean flow through and around groups of bodies. *J. Fluid Mech.* **515**, 371–389.

Felix, M. 2002 Flow structure of turbidity currents. *Sedimentology* **49**, 397–419.

Finnigan, J. 2000 Turbulence in plant canopies. *Annu. Rev. Fluid Mech.* **32**, 519–571.

Flynn, M. R. & Linden, P. F. 2006 Intrusive gravity currents. *J. Fluid Mech.* **568**, 193–202.

Flynn, M. R. & Sutherland, B. R. 2004 Intrusive gravity currents and internal gravity wave generation in stratified fluid. *J. Fluid Mech.* **514**, 355–383.

Garcia-Villalba, M., Palau-Salvador, G. & Rodi, W. 2014 Forced convection heat transfer from a finite-height cylinder. *Flow Turb. Combust.* **93**, 171–187.

Ghisalberti, M. 2009 Obstructed shear flows: similarities across systems and scales. *J. Fluid Mech.* **641**, 51–61.

Ghisalberti, M. & Nepf, H. 2004 The limited growth of vegetated shear layers. *Water Resour. Res.* **40**, W07502.

Ghisalberti, M. & Nepf, H. 2006 The structure of the shear layer over rigid and flexible canopies. *Environ. Fluid Mech.* **6**, 277–301.

Gonzalez-Juez, E. & Meiburg, E. 2009 Shallow-water analysis of gravity-current flow past isolated obstacles. *J. Fluid Mech.* **635**, 415–438.

Gonzalez-Juez, E., Meiburg, E. & Constantinescu, G. 2009 Gravity currents impinging on submerged cylinders: flow fields and associated forces. *J. Fluid Mech.* **631**, 65–102.

Gonzalez-Juez, E., Meiburg, E., Tokyay, T. & Constantinescu, G. 2010 Gravity current flow past a circular cylinder: forces and wall shear stresses and implications for scour. *J. Fluid Mech.* **649**, 69–102.

Gray, W. G. & Lee, P. C. Y. 1977 On the theorems for local volume averaging of multiphase systems. *Int. J. Multiphase Flow* **3**, 333–340.

Griffiths, R. W. 1986 Gravity currents in rotating systems. *Annu. Rev. Fluid Mech.* **18**, 59–89.

Hain, R., Kahler, C. J. & Michaelis, D. 2008 Tomographic and time resolved piv measurements on a finite cylinder mounted on a flat plate. *Exp. Fluids* **45**, 715–724.

Hamed, A. M., Sadowski, M. J., Nepf, H. M. & Chamorro, L. P. 2017 Impact of height heterogeneity on canopy turbulence. *J. Fluid Mech.* **813**, 1176–1196.

Harlow, F. H. & Welch, J. E. 1965 Numerical calculation of time-dependent viscous incompressible flow of fluid with free surface. *Phys. Fluids* **8(12)**, 2182–2189.

Härtel, C., Meiburg, E. & Necker, F. 2000 Analysis and direct numerical simulation of the flow at a gravity-current head. Part 1. Flow topology and front speed for slip and no-slip boundaries. *J. Fluid Mech.* **418**, 189–212.

Hartstein, N. D. & Stevens, C. L. 2005 Deposition beneath long-line mussel farms. *Aquacult. Eng.* **33**, 192–213.

Harvey, J. W., Conklin, M. H. & Koelsch, R. S. 2003 Predicting changes in hydrologic retention in an evolving semi-arid alluvial stream. *Adv. Water Resour.* **26**, 939–950.

Hatcher, L., Hogg, A. J. & Woods, A. W. 2000 The effects of drag on turbulent gravity currents. *J. Fluid Mech.* **416**, 297–314.

Henderson, B. D. & Barkley, D. 1996 Secondary instability in the wake of a circular cylinder. *Phys. Fluids* **8**, 1683–1685.

Hirt, C. W. 1993 Volume-fraction techniques: power tools for wind engineering. *J. Wind Eng Ind Aerodyn* **46&47**, 327–338.

Hirt, C. W., Amsden, A. A. & Cook, J. L. 1974 An arbitrary lagrangian-eulerian computing method for all flow speeds. *J. Comp. Phys.* **135**, 203–216.

Hirt, C. W., Cook, J. L. & Butler, T. D. 1970 A lagrangian method for calculating the dynamics of an incompressible fluid with free surface. *J. Comp. Phys.* **5(1)**, 103–124.

Hirt, C. W. & Nichols, B. D. 1981 Volume of fluid (vof) method for the dynamics of free boundaries. *J. Comput. Phys.* **39**, 201–225.

Hogg, A. J., Hallworth, M. A. & Huppert, H. E. 2005 On gravity currents driven by constant fluxes of saline and particle-laden fluid in the presence of a uniform flow. *J. Fluid Mech.* **539**, 349–385.

Holdsworth, A. M. & Sutherland, B. R. 2013 Influence of lock aspect ratio upon the evolution of an axisymmetric intrusion. *J. Fluid Mech.* **735**, R3.

Holyer, J. Y. & Huppert, H. E. 1980 Gravity currents entering a two-layer fluid. *J. Fluid Mech.* **100**, 739–767.

Hopfinger, E. J. 1983 Snow avalanche motion and related phenomena. *Annu. Rev. Fluid Mech.* **15**, 47–76.

Hoult, D. P. 1972 Oil spreading on the sea. *Annu. Rev. Fluid Mech.* **4**, 341–368.

Huang, J., Cassiani, M. & Albertson, J. D. 2011 Coherent turbulent structures across a vegetation discontinuity. *Boundary-Layer Meteorol.* **140**, 1–22.

Hunt, J. C. R. & Eames, I. 2002 The disappearance of laminar and turbulent wakes in complex flows. *J. Fluid Mech.* **457**, 111–132.

Huppert, H. E. 2006 Gravity currents: a personal perspective. *J. Fluid Mech.* **554**, 299–322.

Huppert, H. E. & Simpson, J. E. 1980 The slumping of gravity currents. *J. Fluid Mech.* **99**, 785–799.

Inoue, O. & Sakuragi, A. 2008 Vortex shedding from a circular cylinder of finite length at low reynolds numbers. *Phys. Fluids* **20**, 033601.

Irvine, M. R., Gardiner, B. A. & Hill, M. K. 1997 The evolution of turbulence across a forest edge. *Boundary-Layer Meteorol.* **84**, 467–496.

Jackson, G. A. 1998 Currents in the high drag environment of a coastal kelp stand off California. *Cont. Shelf Res.* **17(15)**, 1913–1928.

Jamali, M., .Zhang, X & Nepf, H. M. 2008 Exchange flow between a canopy and open water. *J. Fluid Mech.* **611**, 237–254.

Jimenez, J. 2004 Turbulent flows over rough walls. *Annu. Rev. Fluid Mech.* **36**, 173–196.

Kaimal, J. & Finnigan, J. 1994 *Atmospheric Boundary Layer Flows*. Oxford University Press.

Keulegan, G. H. 1954 Ninth progress report on model laws for density currents. An example of density current flow in permeable media. *Tech. Rep.* Natl. Bur. Stand. Rep. 3411. U.S. Dep. of Commerce, Washington, D. C.

Keulegan, G. H. 1958 The motion of saline fronts in still water. *Natl Bur. Stand. Rep.* **99**, 785–799.

Kinzel, M., Araya, D. B. & Dabiri, J. O. 2015 Turbulence in vertical axis wind turbine canopies. *Phys. Fluids* **27**, 115102.

Klemp, J. B., Rotunno, R. & Skamarock, W. C. 1994 On the dynamics of gravity currents in a channel. *J. Fluid Mech.* **269**, 169–198.

Knippertz, P. & Todd, M. C. 2010 The central west saharan dust hot spot and its relation to african easterly waves and extratropical disturbances. *J. Geophys. Res.* **115**, D12117.

Krajnovic, S. 2011 Flow around a tall finite cylinder explored by large eddy simulation. *J. Fluid Mech.* **676**, 294–317.

La Rocca, M., Prestininzi, P., Adduce, C., Sciortino, G. & Hinkelmann, R. 2013 Lattice boltzmann simulation of 3d gravity currents around obstacles. *Int. J. Offshore and Polar Eng.* **23(3)**, 178–185.

Lane-Serff, G. F., Beal, L. M. & Hadfield, T. D. 1995 Gravity current flow over obstacles. *J. Fluid Mech.* **292**, 39–53.

Lee, B. & Wilhelmson, R. 1997*a* The numerical simulation of non-supercell tornadogenesis. Part I. Initiation and evolution of pretornadic misocyclone circulation along a dry outflow boundary. *J. Atmos. Sci.* **54**, 32–60.

Lee, B. & Wilhelmson, R. 1997*b* The numerical simulation of non-supercell tornadogenesis. Part II. Evolution of a family of tornadoes along a weak outflow boundary. *J. Atmos. Sci.* pp. 2387–2415.

van Leer, B. 1977 Towards the ultimate conservative difference scheme. iv. a new approach to numerical convection. *J. Comput. Phys.* **23**, 276–299.

Lei, J. & Nepf, H. 2016 Impact of current speed on mass flux to a model flexible seagrass blade. *J. Geophys. Res. Oceans* **121**, 4763–4776.

Lightbody, A. F. & Nepf, H. 2006 Prediction of near-field shear dispersion in an emergent canopy with heterogeneous morphology. *Environ. Fluid Mech.* **6(5)**, 477–488.

Lombardi, V., Adduce, C., Sciortino, G. & La Rocca, M. 2015 Gravity currents flowing upslope: laboratory experiments and shallo-water simulations. *Phys. Fluids* **27**, 016602.

Lowe, R. J., Linden, P. F. & Rottman, J. W. 2002 A laboratory study of the velocity structure in an intrusive gravity current. *J. Fluid Mech.* **456**, 33–48.

Manins, P. 1976 Intrusion into a stratified fluid. *J. Fluid Mech.* **74**, 547–560.

Maurer, B. D., Bolster, D. T. & Linden, P. F. 2010 Intrusive gravity currents between two stably stratified fluids. *J. Fluid Mech.* **647**, 53–69.

Maurer, B. D. & Linden, P. F. 2014 Intrusion-generated waves in a linearly stratified fluid. *J. Fluid Mech.* **752**, 282–295.

Maxworthy, T., Leilich, J., Simpson, J. E. & Meiburg, E. H. 2002 The propagation of a gravity current into a linearly stratified fluid. *J. Fluid Mech.* **453**, 371–394.

Meiburg, E. & Kneller, B. 2010 Turbidity currents and their deposits. *Annu. Rev. Fluid Mech.* **42**, 135–156.

Monaghan, J. J. 2007 Gravity currents interaction with interfaces. *Annu. Rev. Fluid Mech.* **39**, 245–261.

Munroe, J. R., Voegeli, C., Sutherland, B. R., Birman, V. & Meiburg, E. H. 2009 Intrusive gravity currents from finite-length locks in a uniformly stratified fluid. *J. Fluid Mech.* **635**, 245–273.

Nasr-Azadani, M. M. & Meiburg, E. 2014*a* Influence of seafloor topography on the depositional behavior of bi-disperse turbidity currents: a three-dimensional, depth-resolved numerical investigation. *Environ. Fluid Mech.* **14**, 319–342.

Nasr-Azadani, M. M. & Meiburg, E. 2014*b* Turbidity currents interacting with three-dimensional seafloor topography. *J. Fluid Mech.* **745**, 409–443.

Necker, F., Härtel, C., Kleiser, C. & Meiburg, L. 2002 High-resolution simulations of particle-driven gravity currents. *Intl J. Multiphase Flow* **28**, 279–300.

Necker, F., Härtel, C., Kleiser, L. & Meiburg, E. 2005 Mixing and dissipation in particle-driven gravity currents. *J. Fluid Mech.* **545**, 339–372.

Nepf, H., Ghisalberti, M., White, B. & Murphy, E. 2007 Retention time and dispersion associated with submerged aquatic canopies. *Water Resour. Res.* **43**, W04422.

Nepf, H., Mugnier, C. G. & Zavistoski, R. A. 1997 The effects of vegetation on longitudinal dispersion. *Estuarine Coastal Shelf Sci.* **44**, 675–684.

Nepf, H. M. 2012 Flow and transport in regions with aquatic vegetation. *J. Fluid Mech.* **44**, 123–142.

Nepf, H. M. & Vivoni, E. R. 2000 Flow structure in depth-limited, vegetated flow. *Water Resour. Res.* **105(12)**, 28,547–28,557.

Newell, C. R. & Richardson, J. 2014 The effects of ambient and aquaculture structure hydrodynamics on the food supply and demand of mussel rafts. *J. Shellfish Res.* **33**, 257–272.

Nichols, B. D. & Hirt, C. W. 1971 Calculating three-dimensional free surface flows in the vicinity of submerged and exposed structures. *J. Comp. Phys.* **12**, 234–246.

Nicolle, A. & Eames, I. 2011 Numerical study of flow through and around a circular array of cylinders. *J. Fluid Mech.* **679**, 1–31.

Noack, B. R. 1999 On the flow around a circular cylinder. part i: laminar and transitional regime; part ii: turbulent regime. *Z. Angew. Math. Mech.* **79**, S223–S226; S227–S230.

Nogueira, H. I. S., Adduce, C., Alves, E. & Franca, M. J. 2014 Dynamics of the head of gravity currents. *Environ. Fluid Mech.* **14**, 519–540.

Nokes, R. 2016 *Streams 2.05 - System Theory and Design*. University of Canterbury.

O'Donncha, F., Hartnett, M. & Nash, S. 2013 Physical and numerical investigation of the hydrodynamic implications of aquaculture farms. *Aquacult. Eng.* **52**, 14–26.

Oke, T. R. 1988 *Boundary Layer Climates, 2nd edn.*. Methuen.

Oldham, C. & Sturman, J. 2001 The effect of emergent vegetation on convective flushing in shallow wetlands: Scaling and experiments. *Limnol. Oceanogr.* **46(6)**, 1486–1493.

Ooi, S. K., Constantinescu, G. & Weber, L. 2009 Numerical simulations of lock-exchange compositional gravity current. *J. Fluid Mech.* **635**, 361–388.

Ozan, A. Y., Constantinescu, G. & Hogg, A. J. 2015 Lock-exchange gravity currents propagating in a channel containing an array of obstacles. *J. Fluid Mech.* **765**, 544–575.

Ozan, A. Y., Constantinescu, G. & Nepf, H. 2016 Free-surface gravity currents propagating in an open channel containing a porous layer at the free surface. *J. Fluid Mech.* **809**, 601–627.

Ozgokmen, T. M. & Fischer, P. F. 2008 On the role of bottom roughness in overflows. *Ocean Modell.* **20**, 336–361.

Ozgokmen, T. M., Fischer, P. F., Duan, J. & Iliescu, T. 2004 Three-dimensional turbulent bottom density currents from a high-order nonhydrostatic spectral element model. *J. Phys. Oceanogr.* **34**, 2006–2026.

Ozgokmen, T. M., Fischer, P. F. & Johns, W. E. 2006 Product water mass formation by turbulent density currents from a high-order nonhydrostatic spectral element model. *Ocean Modell.* **12**, 237–267.

Ozgokmen, T. M., Iliescu, T., Fischer, P. F., Srinivasan, A. & Duan, J. 2007 Large eddy simulation of stratified mixing in two-dimensional dam-break problem in a rectangular enclosed domain. *Ocean Modell.* **16**, 106–140.

Palau-Salvador, G., Stoesser, T., Frohlich, J., Kappler, M. & Rodi, W. 2010 Large eddy simulations of flow around finite-height cylinders. *Flow Turb. Combust.* **84**, 239–275.

Plew, D.R., Spigel, R. H., Stevens, C. L., Nokes, R. I. & Davidson, M. J. 2006 Stratified flow interactions with a suspended canopy. *Environ. Fluid Mech.* **6**, 519–539.

Plew, D.R., Stevens, C. L., Spigel, R. H. & Hartstein, N. D. 2005 Hydrodynamic implications of large offshore mussel farms. *IEEE J. Ocean. Eng.* **30(1)**, 95–108.

Plew, D. R. 2011 Depth-averaged coefficient for modeling flow through suspended canopies. *J. Hydraul. Eng.* **137(2)**, 234–247.

Poggi, D., Porporato, A., Ridolfi, L., Albertson, J. D. & Katul, G. G. 2004 The effect of vegetation density on canopy sub-layer turbulence. *Boundary-Layer Meteorol.* **111(3)**, 565–587.

Pope, S. B. 2000 *Turbulent flows*. Cambridge University Press.

Price, D. J. 2008 Modelling discontinuities and kelvin-helmholtz instabilities in sph. *J. Comput. Phys.* **227**, 10040–10057.

Qiao, J. D., Delavan, S. K., Nokes, R. I. & Plew, D. R. 2016 Flow structure and turbulence characteristics downstream of a spanwise suspended linear array. *Environ. Fluid Mech.* **16**, 1021–1041.

Raupach, M., Finnigan, J. & Brunet, Y. 1996 Coherent eddies and turbulence in vegetation canopies: the mixing-layer analogy. *Boundary-Layer Meteorol.* **60**, 375–395.

Raupach, M. & Shaw, R. 1982 Averaging procedures for flow within vegetation canopies. *Boundary-Layer Meteorol.* **22**, 79–90.

Van Dyke, M. 1982 *An Album of Fluid Motion*. The Parabolic Press.

Roh, S. C. & Park, S. O. 2003 Vortical flow over the free end surface of a finite circular cylinder mounted on a flat plate. *Exp. Fluids* **34**, 63–67.

Rominger, J. T. & Nepf, H. 2011 Flow adjustment and interior flow associated with a rectangule porous obstruction. *J. Fluid Mech.* **680**, 636–659.

Roshko, A. 1961 Expriments on the flow past a circular cylinder at very high reynolds numbers. *J. Fluid Mech.* **10**, 345–356.

Roshko, A. 1993 Perspectives on bluff body aerodynamics. *J. Wind Ind. Aerodyn* **49**, 70–100.

Rosman, J. H., Koseff, J. R., Monismith, S. G. & Grover, J. 2007 A field investigation into the effects of a kelp forest (*Macrocystis pyrifera*) on coastal hydrodynamics and transport. *J. Geophys. Res. Oceans* **112**, C02016.

Rostamy, N., Sumner, D., Bergstrom, D. J. & Bugg, J. D. 2012 Local flow field of a surface-mounted finite circular cylinder. *J. Fluids Struct.* **34**, 105–122.

Rottman, J. W. & Simpson, J. E. 1983 Gravity currents produced by instantaneous releases of a heavy fluid in a retangular channel. *J. Fluid Mech.* **135**, 95–110.

Schooley, A. & Hughes, B. 1972 An experimental and theoretical study of internal waves generated by the collapse of a two-dimensional mixed region in a density gradient. *J. Fluid Mech.* **51**, 159–175.

Shin, J. O., Dalziel, S. B. & Linden, P. F. 2004 Gravity currents produced by lock exchange. *J. Fluid Mech.* **521**, 1–34.

Simpson, J. E. 1997 *Gravity currents: in the environment and laboratory, 2nd edn.*. Cambridge University Press.

Simpson, J. E. & Britter, R. E. 1979 The dynamics of the head of a gravity current advancing over a horizontal surface. *J. Fluid Mech.* **94**, 477–495.

Smagorinsky, J. 1963 General circulation experiments with the primitive equations: I. the basic experiments. *Mon. Weather Rev.* **91**, 99–164.

Sparrow, E. M. & Samie, F. 1981 Measured heat transfer coefficients at and adjacent to the tip of a wall-attached cylinder in crossflowâĂŤapplication to fins. *J. Heat Transfer* **103(4)**, 778–784.

Strouhal, V. 1878 Uber eine besondere art der tonerregung. *Ann. Phys. Chem. (Liepzig),* Neue Folge Bd. **5(10)**, 216.

Sumner, D. 2013 Flow above the free end of a surface-mounted finite-height circular cylinder: A review. *J. Fluids Struct.* **43**, 41–63.

Sumner, D., Heseltine, J. L. & Dansereau, O. J. P. 2004 Wake structure of a finite circular cylinder of small aspect ratio. *Exp. Fluids* **37**, 720–730.

Sumner, D., Rostamy, N., Bergstrom, D. J. & Bugg, J. D. 2015 Influence of aspect ratio on the flow above the free end of a surface-mounted finite cylinder. *Int. J. Heat Fluid Flow* **28**, 561–574.

Sutherland, B. R., Chow, A. N. F. & Pittman, T. P. 2004 Interfacial gravity currents in two-layer fluids. *J. Fluid Mech.* **514**, 327–353.

Sutherland, B. R., Chow, A. N. F. & Pittman, T. P. 2007 The collapse of a mixed patch in stratified fluid. *Phys. Fluids* **19**, 116602.

Sutherland, B. R. & Nault, J. T. 2007 Intrusive gravity currents propagating along thin and thick interfaces. *J. Fluid Mech.* **586**, 109–118.

Taddei, S., Manes, C. & Ganapathisubramani, B. 2016 Characterisation of drag and wake properties of canopy patches immersed in turbulent boundary layers. *J. Fluid Mech.* **798**, 27–49.

Tanino, Y. & Nepf, H. M. 2008*a* Laboratory investigation of mean drag in a random array of rigid, emergent cylinders. *J. Hydraul. Eng.* **134(1)**, 34–41.

Tanino, Y. & Nepf, H. M. 2008*b* Lateral dispersion in random cylinder arrays at high reynolds number. *J.Fluid Mech.* **600**, 339–371.

Tanino, Y., Nepf, H. M. & Kulis, P. S. 2005 Gravity currents in aquatic canopies. *Water Resour. Res.* **41**, W12402.

Testik, F. Y. & Ungarish, M. 2016 On the self-similar propagation of gravity currents through an array of emergent vegetation-like obstacles. *Phys. Fluids* **28**, 056605.

Testik, F. Y. & Yilmaz, N. A. 2015 Anatomy and propagation dynamics of continuous-flux release bottom gravity currents through emergent aquatic vegetation. *Phys. Fluids* **27**, 056603.

Thompson, M., Hourigan, K. & Sheridan, J. 1996 Three-dimensional instabilities in the wake of a circular cylinder. *Exp. Therm. Fluid Sci.* **12(2)**, 190–196.

Tokyay, T. & Constantinescu, G. 2015 The effects of a submerged non-erodible triangular obstacle on bottom propagating gravity currents. *Phys. Fluids* **27**, 056601.

Tokyay, T., Constantinescu, G., Gonzales-Juez, E. & Merburg, E. 2011*a* Gravity currents propagating over periodic arrays of blunt obstacles: effect of the obstacle size. *J. Fluid Struct.* **27**, 798–806.

Tokyay, T., Constantinescu, G. & Meiburg, E. 2012 Tail structure and bed friction velocity distribution of gravity currents propagating over an array of obstacles. *J. Fluid Mech.* **694**, 252–291.

Tokyay, T., Constantinescu, G. & Merburg, E. 2011*b* Lock-exchange gravity currents with a high volume of release propagating over a periodic array of obstacles. *J. Fluid Mech.* **672**, 570–605.

Tokyay, T., Constantinescu, G. & Merburg, E. 2014 Lock-exchange gravity currents with a low volume of release propagating over an array of obstacles. *J. Geophys. Res. Oceans* **119**, 2752–2768.

Tseung, H. L., Kikkert, G. A. & Plew, D. 2016 Hydrodynamics of suspended canopies with limited length and width. *Environ. Fluid Mech.* **16**, 145–166.

Ungarish, M. 2006 On gravity currents in a linearly stratified ambient: a generalization of Benjamin's steady-state propagation results. *J. Fluid Mech.* **548**, 49–68.

Ungarish, M. 2009 *An Introduction to Gravity Currents and Intrusions*. Chapman and Hall/CRC.

Ungarish, M. & Huppert, H. E. 2000 High-reynolds number gravity currents over a porous boundary: shallow-water solutions and box-model approximations. *J. Fluid Mech.* **418**, 1–23.

Ungarish, M. & Huppert, H. E. 2002 On gravity currents propagating at the base of a stratified ambient. *J. Fluid Mech.* **458**, 283–301.

Venayagamoorthy, S. K., Ku, H., Fringer, O. B., Chiu, A., Naylor, R. L. & Koseff, J. R. 2011 Numerical modeling pf aquaculture dissolved waste transport in a coastal embayment. *Environ. Fluid Mech.* **11**, 329–352.

Vennell, R. 2010 Tuning turbines in a tidal channel. *J. Fluid Mech.* **663**, 235–267.

Vennell, R. 2011 Tuning tidal turbines in-concert to maximise farm efficiency. *J. Fluid Mech.* **671**, 587–604.

von Karman 1912 Uber den mechanismus den widrstandsm, den ein bewegter korper in einer flussigkeit erfahrt. *Göttingen Nachr. Math. Mech.* **12**, 509–546.

von Karman, T. 1940 The engineer grapples with nonlinear problems. *Bull. Am. Math. Soc.* **46**, 615–683.

Wang, H. F. & Zhou, Y. 2009 The finite-length square cylinder near wake. *J. Fluid Mech.* **638**, 453–490.

Wang, H. F., Zhou, Y., Chan, C. & Lam, K. S. 2006 Effect of initial conditions on interaction between a boundary layer and a wall-mounted finite-lengthcylinder wake. *Phys. Fluids* **18**, 065106.

Wang, H. F., Zhou, Y. & Mi, J. 2012 Effects of aspect ratio on the drag of a wallmounted finite-length cylinder in subcritical and critical regimes. *Exp. Fluids* **53**, 423–436.

Wetzel, R. G. 2001 *Light in inland water, 3rd ed*. Academic Press.

White, B. & Nepf, H. 2007 Shear instability and coherent structures in a flow adjacent to a porous layer. *J. Fluid Mech.* **593**, 1–32.

White, B. L. & Helfrich, K. R. 2008 Gravity currents and internal waves in a stratified fluid. *J. Fluid Mech.* **616**, 327–356.

Williamson, C. H. K. 1996 Vortex dynamics in the cylinder wake. *J. Fluid Mech.* **28**, 477–539.

Winant, C. & Browand, F. 1974 Vortex pairing: the mechanism of turbulent mixing-layer growth at moderate reynolds number. *J. Fluid Mech.* **63**, 237–255.

Wooding, R., Bradley, E. & Marshall, J. 1973 Dray due to regular arrays of roughness elements. *Boundary-Layer Meteorol.* **5**, 285–308.

Wu, J. 1969 Mixed region collapse with internal wave generation in a density stratified medium. *J. Fluid Mech.* **35**, 531–544.

Wu, J., Ma, H. & Zhou, M. 2006 *Vorticity and Vortex Dynamics*. Springer.

Yao, G. F. 2004 Development of new pressure-velocity solvers in FLOW-3D. *Tech. Rep.* FSI-04-TN68. Flow Science, Inc.

Zdravkovich, M. M. 1997 *Flow Around Circular Cylinders. VOL 1: Fundamentals*. Oxford University Press.

Zdravkovich, M. M. 2003 *Flow Around Circular Cylinders. VOL 2: Applications*. Oxford University Press.

Zhang, X. & Nepf, H. M. 2008 Density-driven exchange flow between open water and an aquatic canopy. *Water Resour. Res.* **44**, W08417.

Zhang, X. & Nepf, H. M. 2009 Thermally driven exchange flow between open water and an aquatic canopy. *J. Fluid Mech.* **632**, 227–243.

Zhang, X. & Nepf, H. M. 2011 Exchange flow between open water and floating vegetation. *Environ. Fluid Mech.* **11**, 531–546.

Zhou, J., Cenedese, C., Williams, T., Ball, M., Venayagamoorthy, S. K. & Nokes, R. 2017 On the propagation of gravity currents over and through a submerged array of circular cylinders. *J. Fluid Mech.* **in press**.

Zong, L. & Nepf, H. 2012 Vortex development behind a finite porous obstruction in a channel. *J. Fluid Mech.* **691**, 368–391.